

AD-A062 730

PHILIPS LABS BRIARCLIFF MANOR N Y
OPTIMIZED PYROELECTRIC VIDICON THERMAL IMAGER. VOLUME II. IMPRO--ETC(U)
JUL 78 W A SMITH

F/G 17/5

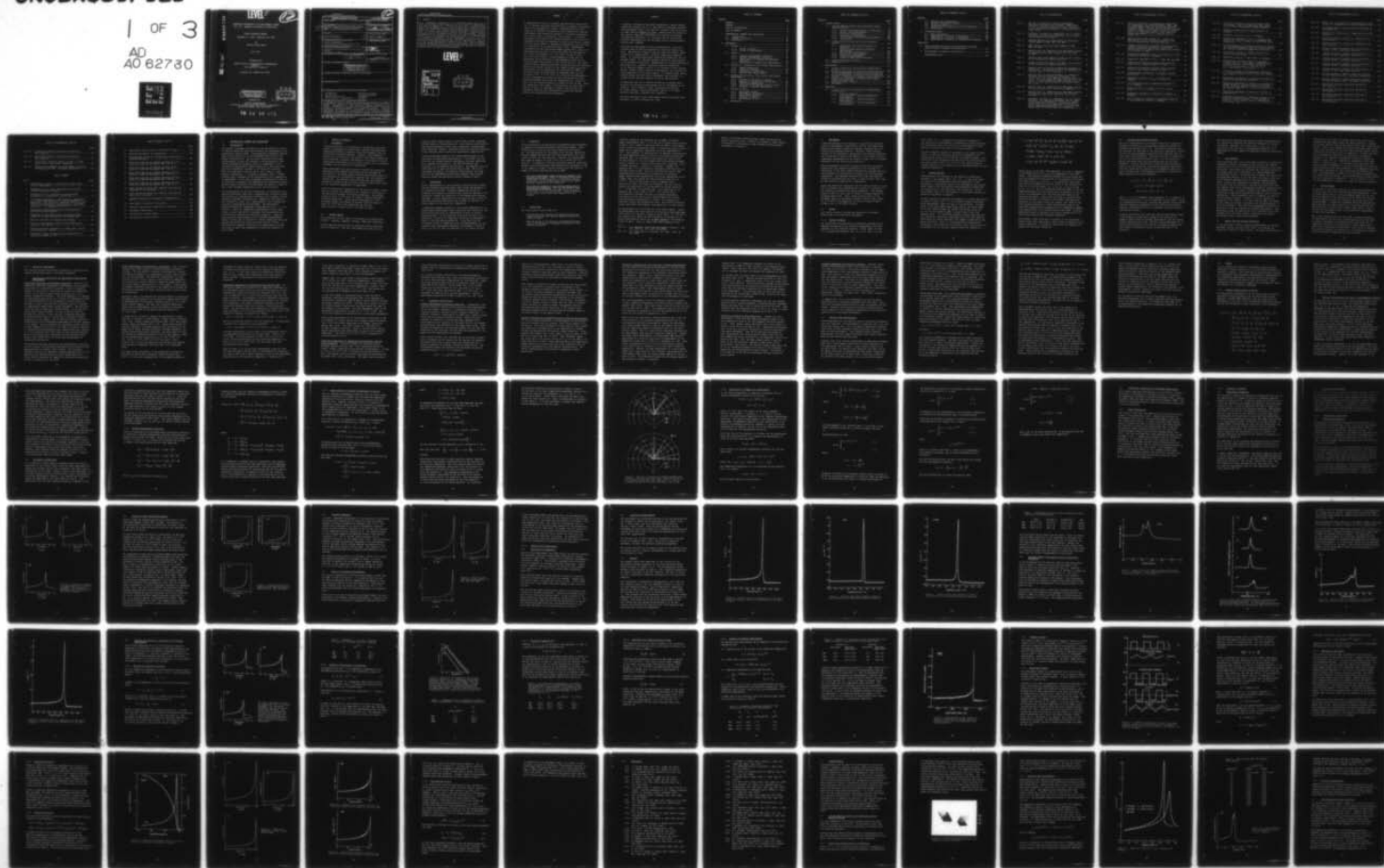
DAA653-76-C-0053

NL

UNCLASSIFIED

1 OF 3

AD
A0 62730



ADA062730

DDC FILE COPY

LEVEL *II*

12
B.S.

OPTIMIZED PYROELECTRIC VIDICON THERMAL IMAGER
Vol. II: Improper Ferroelectric Materials

FINAL TECHNICAL REPORT

September 1, 1976 - February 28, 1978

by

Wallace Arden Smith

July 1978

Prepared for

NIGHT VISION & ELECTRO-OPTICS LABORATORIES
USAECOM
Fort Belvoir, Virginia

Contract No. DAAG53-76-C-0053

DISTRIBUTION STATEMENT A

**Approved for public release;
Distribution Unlimited**

Prepared by

PHILIPS LABORATORIES
A Division of North American Philips Corporation
Briarcliff Manor, New York 10510

DDC
RECEIVED
DEC 21 1978
RECEIVED
D

78 12 13 012

UNCLASSIFIED

SECURITY CLASSIFICATION OF THIS PAGE (When Data Entered)

REPORT DOCUMENTATION PAGE		READ INSTRUCTIONS BEFORE COMPLETING FORM
1. REPORT NUMBER	2. GOVT ACCESSION NO.	3. RECIPIENT'S CATALOG NUMBER
4. TITLE (and Subtitle) OPTIMIZED PYROELECTRIC VIDICON THERMAL IMAGER. VOL. II. IMPROPER FERROELECTRIC MATERIALS.		5. TYPE OF REPORT & PERIOD COVERED Final Technical Report 1 Sep 1976 - 28 Feb 1978
7. AUTHOR(s) Wallace Arden/Smith		8. CONTRACT OR GRANT NUMBER(s) DAAG53-76-C-0053
9. PERFORMING ORGANIZATION NAME AND ADDRESS PHILIPS LABORATORIES A Division of North American Philips Corp. Briarcliff Manor, New York 10510		10. PROGRAM ELEMENT, PROJECT, TASK AREA & WORK UNIT NUMBERS
11. CONTROLLING OFFICE NAME AND ADDRESS Night Vision & Electro-Optics Laboratories USAECOM Ft. Belvoir, Virginia		12. REPORT DATE July 1978
14. MONITORING AGENCY NAME & ADDRESS (if different from Controlling Office) 12 224p		13. NUMBER OF PAGES 229
		15. SECURITY CLASS. (of this report) UNCLASSIFIED
		15a. DECLASSIFICATION/DOWNGRADING SCHEDULE
16. DISTRIBUTION STATEMENT (of this Report) <div style="border: 1px solid black; padding: 5px; text-align: center;"> DISTRIBUTION STATEMENT A Approved for public release; Distribution Unlimited </div>		
17. DISTRIBUTION STATEMENT (of the abstract entered in Block 20, if different from Report)		
18. SUPPLEMENTARY NOTES		
19. KEY WORDS (Continue on reverse side if necessary and identify by block number) Ferroelectrics Pyroelectrics Improper Ferroelectrics Phase transition: ferroelectrics Ferroelectric sulfates Rare-earth molybdates Propionates Boracites		
20. ABSTRACT (Continue on reverse side if necessary and identify by block number) A comprehensive survey of improper ferroelectrics was carried out to identify materials with potential to enhance the performance of the pyroelectric vidicon. Representatives of four families of improper ferroelectrics were selected for detailed experimental and theoretical analysis: rare-earth molybdates, the sulfate family, propionates, and boracites. A thorough experimental and theoretical characterization of the rare-earth molybdates confirmed the expectation that the dielectric anomaly could be nearly absent in improper ferroelectrics and thus lead to a high value of the figure-of-merit.		

DD FORM 1 JAN 73 1473 EDITION OF 1 NOV 65 IS OBSOLETE

UNCLASSIFIED

SECURITY CLASSIFICATION OF THIS PAGE (When Data Entered)

UNCLASSIFIED

SECURITY CLASSIFICATION OF THIS PAGE(When Data Entered)

20. ABSTRACT

p/e.c. Experimental confirmation of the theoretical models allows one to obtain an optimized figure-of-merit₂ of $10 \times 10^3 \text{ cm}^2/\text{C}$ for materials of this family as compared to $3 \times 10^3 \text{ cm}^2/\text{C}$ for TGS at 40°C). From the sulfate family, lithium ammonium sulfate and its deuterated analog exhibited a room-temperature value of the figure-of-merit about equal to that of TGS at 40°C . The other analog sulfates examined exhibited a characteristically different behavior and smaller values for the figure-of-merit. Initial measurements on the propionates were analyzed and lead to a projected₃ figure of merit which is unbounded above and was estimated to be $7.3 \times 10^3 \text{ cm}^2/\text{C}$ for dicalcium lead propionate. Initial measurements on boracites were consistent with data measured elsewhere which give the expectation of a figure of merit for the boracites greatly in excess of that of TGS. Thus, the expectation that improper ferroelectrics can have large figures of merit is confirmed in detail; the boracite and propionate families were identified as having the greatest promise for enhanced device performance.

LEVEL II

ACCESSION NO.	
DTIC	Write Section <input checked="" type="checkbox"/>
DDO	Diff Section <input type="checkbox"/>
UNANNOUNCED	
JUSTIFICATION	
Per DDC Form 50	
on file	
DISTRIBUTION/AVAILABILITY CODE	
Dist.	AVAIL. and/or SPECIAL
A	

DDC
RECEIVED
DEC 21 1978
D

UNCLASSIFIED

SECURITY CLASSIFICATION OF THIS PAGE(When Data Entered)

10,000
SUMMARY
10³ cm
epsilon

A comprehensive survey of improper ferroelectrics was carried out to identify materials with potential to enhance the performance of the pyroelectric vidicon. Representatives of four families of improper ferroelectrics were selected for detailed experimental and theoretical analysis: rare-earth molybdates, the sulfate family, propionates, and boracites. A thorough experimental and theoretical characterization of the rare-earth molybdates confirmed the expectation that the dielectric anomaly could be nearly absent in improper ferroelectrics and thus lead to a high value of the figure-of-merit $p/\epsilon c$. Experimental confirmation of the theoretical models allows one to obtain an optimized figure-of-merit of $10 \times 10^3 \text{ cm}^2/\text{C}$ for materials of this family as compared to $3 \times 10^3 \text{ cm}^2/\text{C}$ for TGS at 40°C . From the sulfate family, lithium ammonium sulfate and its deuterated analog exhibited a room-temperature value of the figure-of-merit about equal to that of TGS at 40°C . The other analog sulfates examined exhibited a characteristically different behavior and smaller values for the figure-of-merit. Initial measurements on the propionates were analyzed and lead to a projected figure of merit which is unbounded above and was estimated to be $7.3 \times 10^3 \text{ cm}^2/\text{C}$ for dicalcium lead propionate. Initial measurements on boracites were consistent with data measured elsewhere which give the expectation of a figure of merit for the boracites greatly in excess of that of TGS. Thus, the expectation that improper ferroelectrics can have large figures of merit is confirmed in detail; the boracite and propionate families were identified as having the greatest promise for enhanced device performance.

3,000
10³ cm

PREFACE

A program to develop an optimized pyroelectric vidicon thermal imager was issued by the U. S. Army Mobility Equipment Research and Development Center, Fort Belvoir, Virginia, and was initiated under Contract DAAG53-76-C-0053. Modification No. P00002 to the contract added the requirement for research of improper ferroelectric materials; Dr. Lynn Garn was the Contracting Officer's Representative for the Night Vision & Electro-Optics Laboratories, USAECOM.

This work was performed by Philips Laboratories, a Division of North American Philips Corporation, Briarcliff Manor, New York. The materials research task was under the overall supervision of Dr. Stewart Kurtz, Director, Exploratory Research Group. Dr. Wallace Arden Smith, Theoretical Physicist, was the Program Leader. Dr. Gertrude Neumark, Physicist, participated in the theoretical analysis. Measurements at Philips Laboratories were made by Dr. Joseph P. Dougherty, Material Scientist; Mr. M. Delfino, Chemist; and Mr. G. M. Loiacono, Senior Program Leader, Crystal Growth & Materials Technology. Mr. Loiacono was also responsible for materials growth. Dr. Edward Stupp, Senior Program Leader for Solid State Components, was available in a consulting and advisory capacity on device implications.

A subcontract was let to Yeshiva University to perform pyroelectric and dielectric measurements and to collaborate on the analysis. Prof. Michael I. Bell, Principal Investigator, Dr. Avner Shaulov, Visiting Scientist, and Mr. Y. H. Tsuo, Research Assistant, conducted this research.

The work described in this Final Report covers the period from September 1, 1976 to February 28, 1978.

TABLE OF CONTENTS

<u>Section</u>	<u>Page</u>
SUMMARY.....	3
PREFACE.....	5
LIST OF ILLUSTRATIONS.....	10
LIST OF TABLES.....	14
1. INTRODUCTION, SUMMARY AND CONCLUSIONS.....	17
1.1 Introduction.....	17
1.2 Summary of Results.....	18
1.3 Conclusions.....	20
2. MOLYBDATES.....	23
2.1 Review.....	23
2.1.1 Review of Theory.....	23
2.1.2 Review of Measurements.....	29
2.2 Theory.....	41
2.2.1 Complete Thermodynamic Potential.....	41
2.2.2 Reduced Thermodynamic Potential.....	44
2.2.3 Approximation to Reduced Thermodynamic Potential.....	46
2.2.4 Expressions to Compare with Experiments....	50
2.3 Dielectric, Pyroelectric and Thermal Measurements..	54
2.3.1 Sample Preparation.....	54
2.3.2 Dielectric Constant.....	55
2.3.3 Pyroelectric Coefficient.....	56
2.3.4 Specific Heat Measurements.....	62
2.4 Analysis of Dielectric, Pyroelectric and Thermal Measurements.....	72
2.4.1 Analysis of Dielectric Constant.....	72
2.4.2 Analysis of Pyroelectric Coefficient.....	74
2.4.3 Transition Temperatures.....	76
2.4.4 Influence of an Applied Electric Field.....	77
2.4.5 Analysis of Thermal Measurements.....	78
2.5 Figures of Merit.....	81
2.5.1 Measurement Method.....	81
2.5.2 Experimental Techniques.....	84
2.5.3 Experimental Results.....	85
2.5.4 Analysis of Results.....	85
2.5.5 Optimization of M(1).....	89
2.6 References.....	91

TABLE OF CONTENTS (Cont'd)

<u>Section</u>	<u>Page</u>
3. SULFATE FAMILY.....	93
3.1 Lithium Ammonium Sulfate and Deuterated Lithium Ammonium Sulfate.....	93
3.1.1 Growth and Characterization of Materials....	93
3.1.2 Specific Heat Measurements.....	95
3.1.3 Dielectric Measurements.....	98
3.1.4 Pyroelectric Measurements.....	100
3.1.5 Second Harmonic Generation Measurements.....	106
3.1.6 Conclusions.....	106
3.2 Lithium Cesium Sulfate and Lithium Potassium Sulfate.....	109
3.2.1 Preparation and Characterization of Materials.....	109
3.2.2 Optical Second Harmonic Generation Measurements.....	109
3.2.3 Specific Heat Measurements.....	110
3.2.4 Pyroelectric Measurements.....	111
3.2.5 Dielectric Measurements.....	112
3.2.6 Figure of Merit and Conclusions.....	112
3.3 Lithium Trihydrogen Selenite.....	114
3.4 References.....	117
4. PROPIONATES.....	118
4.1 Initial Pyroelectric and Dielectric Measurements on DLP.....	118
4.2 Annealing Experiments on Dicalcium Lead Propionate..	122
4.3 Initial Measurements of Specific Heat on Dicalcium Strontium Propionate and Dicalcium Lead Propionate..	122
4.4 Analysis of Pyroelectric Behavior of DLP above T_c ...	123
4.5 Analysis of Propionates as Second-Order Pseudo-Proper Ferroelectrics.....	124
4.6 Projected Figure of Merit.....	127
4.7 References.....	129
5. BORACITES.....	130
5.1 Initial Dielectric and Pyroelectric Measurements on Boracites.....	130
5.1.1 Poling of Samples.....	130
5.1.2 Ni-Br Boracite: Initial Pyroelectric Measurements.....	132
5.1.3 Ni-Br Boracite: Initial Dielectric Measurements.....	134
5.1.4 Cu-Cl Boracite: Initial Dielectric Measurements.....	134

TABLE OF CONTENTS (Cont'd)

<u>Section</u>	<u>Page</u>
5.2 Specific Heat Measurements.....	137
5.3 Infrared Vibrational Spectra.....	150
5.4 Electronic Spectra.....	154
5.5 Second Harmonic Generation in Ni-Br Boracite.....	155
5.6 References.....	158
6. LITERATURE SURVEY.....	159
6.1 Basic References.....	159
6.2 Experimental Literature on Boracites.....	161
6.3 Experimental Literature on Molybdates.....	167
6.4 Experimental Literature on Ferroelectric Sulfates..	171
 Appendices	
A Intuitive Physical Overview of Theoretical Concepts used in Study of Improper Ferroelectrics.....	179
B Bibliography of Improper Ferroelectrics.....	203
DISTRIBUTION LIST.....	229

LIST OF ILLUSTRATIONS

	Page
Fig. 1: The loci of minima for reduced thermodynamic potential involving only soft mode. These plots are for an isotropic sixth-order term, $2\chi E(a_1/g) = 1$, and indicated anisotropies in second and fourth-order terms.....	49
Fig. 2: Dielectric constant vs. temperature for (a) terbium molybdate, (b) gadolinium molybdate, and (c) gadolinium-dysprosium molybdate.....	57
Fig. 3: Measured pyroelectric coefficients of fully-electroded samples of GMO, TMO, and GDMO.....	59
Fig. 4: Ratio p/c for fully-electroded samples of GMO, TMO, and GDMO.....	61
Fig. 5: Specific heat vs. temperature for TMO sample exhibiting multiple peaks after annealing for 24 hours at 960°C.....	64
Fig. 6: Isobaric molar heat capacity of GMO in the vicinity of the ferroelectric phase transition.....	65
Fig. 7: Isobaric molar heat capacity of GDMO in the vicinity of the ferroelectric phase transition.....	66
Fig. 8: Specific heat of gadolinium dysprosium molybdate vs. temperature. This sample exhibits the phenomenon of multiple peaks at the transition.....	68
Fig. 9: Specific heat of terbium molybdate vs. temperature following various mechanical processings: (a) initial scan, (b) after applying finger pressure for 5 sec., (c) after applying finger pressure for 5 sec more, (d) after pressing between two glass slides for 10 sec.....	69
Fig. 10: Specific heat vs. temperature for TMO sample exhibiting multiple peaks near transition temperature.....	70
Fig. 11: Specific heat vs. temperature for TMO sample exhibiting multiple peaks after annealing for 24 hours at 960°C.....	71
Fig. 12: Dielectric constant vs. temperature for (a) terbium molybdate, (b) gadolinium molybdate, and (c) gadolinium-dysprosium molybdate. Crosses are experimental data; solid line represents theoretical expected temperature-dependence fit to only the data points which lie below transition temperature.....	73

LIST OF ILLUSTRATIONS (Cont'd)

	Page
Fig. 13: Square of reciprocal of pyroelectric coefficient vs. temperature for terbium molybdate (TMO), gadolinium molybdate (GMO) and gadolinium-dysprosium molybdate (GDMO). Crosses are data points; straight lines are theoretically expected linear relationship fit to these data points. Data comes from dynamic measurements of p/c combined with our results for c.....	75
Fig. 14: Specific heat of TMO (Isomet #1). Crosses are experimental values previously reported; solid line is theoretically calculated behavior.....	80
Fig. 15: Schematic description of steady state pyroelectric current and voltage responses to rectangular radiation pulses of period much shorter than thermal time constant of sample.....	82
Fig. 16: Temperature dependence of M(1) and ratio p/c in TGS as measured by dynamic technique.....	86
Fig. 17: Temperature dependence of M(1) in GMO, TMO and GDMO..	87
Fig. 18: Comparison of measured (crosses) and calculated values of M(1) figure-of-merit for TMO.....	88
Fig. 19: Comparison of measured (crosses) and calculated values of $M(\frac{1}{2})$ figure-of-merit for TMO.....	88
Fig. 20: Pseudohexagonal morphology of LiNH_4SO_4 (crossed polarizers).....	94
Fig. 21: Temperature behavior of c_p in LiNH_4SO_4 and LiND_4SO_4	96
Fig. 22: High resolution scan of temperature behavior of c_p in LiNH_4SO_4	97
Fig. 23: Hysteresis loop of LiNH_4SO_4 at 437 K (c-axis; 60 Hz).....	99
Fig. 24: Temperature dependence of dielectric constant in LiNH_4SO_4	99
Fig. 25: Fit of dielectric constant to Curie-Weiss behavior in high temperature phase of LiNH_4SO_4	101

LIST OF ILLUSTRATIONS (Cont'd)

	Page
Fig. 26: Dielectric constant of fully electroded sample of LiNH_4SO_4 . Near low temperature phase transition ($\sim 4-6^\circ\text{C}$) measurement becomes unstable.....	101
Fig. 27: Temperature dependence of figure-of-merit in LiNH_4SO_4	102
Fig. 28: Temperature behavior of p/c in LiNH_4SO_4	102
Fig. 29: Temperature dependence of p/c, in LiNH_4SO_4 upon heating and cooling through low temperature phase transition.....	104
Fig. 30: Multiple peaking in pyroelectric current of partially electroded LiND_4SO_4 as seen during both heating and cooling through low temperature transition.....	105
Fig. 31: Pyroelectric current of LiND_4SO_4 measured on a fully electroded sample.....	105
Fig. 32: Temperature behavior of SHG signal in LiND_4SO_4	107
Fig. 33: Ferroelectric hysteresis loop for $\text{LiH}_3(\text{SeO}_3)_2$. Vertical axis is $1 \mu\text{C}/\text{division}$; horizontal axis is $200/\text{V}_2/\text{division}$. For samples of area $A_2 = 0.227 \text{ cm}^2$ and thickness $t = 0.50 \text{ mm}$, $P_s = 12.1 \mu\text{C}/\text{cm}^2$ and $E_c = 3.8 \text{ kV}/\text{cm}$	114
Fig. 34: Dielectric constant and pyroelectric coefficient of lithium trihydrogen selenite from room temperature to 80°C	116
Fig. 35: Pyroelectric coefficient of as-grown DLP sample as measured by Byer-Roundy technique.....	119
Fig. 36: Temperature dependence of ratio p/c as measured by dynamic method in as-grown sample of DLP, under various dc fields applied in direction opposite to the internal bias.....	120
Fig. 37: Temperature dependence of dielectric constant of as-grown DLP.....	121
Fig. 38: Temperature dependence of dielectric constant of as-grown DLP under dc field of $3 \text{ kV}/\text{cm}$ applied in direction of the internal bias (+) and opposite to the internal bias (-).....	121

LIST OF ILLUSTRATIONS (Cont'd)

	Page
Fig. 39: Square root of reciprocal of the pyroelectric coefficient vs. temperature for as-grown sample of DLP...	124
Fig. 40: Electroded sample of Ni-Br boracite fabricated by the Plessey Co.....	131
Fig. 41: Pyroelectric coefficient vs. temperature for Ni-Br boracite.....	133
Fig. 42: Relative dielectric constant vs. temperature for Ni-Br boracite.....	135
Fig. 43: Relative dielectric constant vs. temperature for Cu-Cl boracite.....	136
Fig. 44: Isobaric molar heat capacity of Cr-Cl boracite in vicinity of $\bar{4}3m$ - $mm2$ phase transition.....	138
Fig. 45: Isobaric molar heat capacity of Fe-I boracite in vicinity of $\bar{4}3m$ - $mm2$ phase transition.....	139
Fig. 46: Isobaric molar heat capacity of Cu-Cl boracite in vicinity of $\bar{4}3m$ - $mm2$ phase transition.....	140
Fig. 47: Isobaric molar heat capacity of Ni-Br boracite in vicinity of $\bar{4}3m$ - $mm2$ phase transition.....	141
Fig. 48: Isobaric molar heat capacity of Zn-Br boracite in vicinity of $\bar{4}3m$ - $mm2$ phase transition.....	142
Fig. 49: Multiple peaking of isobaric molar heat capacity in Cr-Cl boracite at $\bar{4}3m$ - $mm2$ phase transition.....	145
Fig. 50: Multiple peaking of isobaric molar heat capacity in Ni-Br boracite at $\bar{4}3m$ - $mm2$ phase transition.....	145
Fig. 51: Solid-state infrared vibrational spectrum of $\bar{4}3m$ $Cr_3B_7O_{13}Cl$	151
Fig. 52: Solid-state infrared vibrational spectrum of $mm2$ $Fe_3B_7O_{13}I$	151
Fig. 53: Solid-state infrared vibrational spectrum of $mm2$ $Zn_3B_7O_{13}Br$	152
Fig. 54: Solid-state infrared vibrational spectrum of $mm2$ $Ni_3B_7O_{13}Br$	152

LIST OF ILLUSTRATIONS (Cont'd)

	Page
Fig. 55: Solid-state infrared vibrational spectrum of mm2 $\text{Cu}_3\text{B}_7\text{O}_{13}\text{Cl}$	153
Fig. 56: Solid-state infrared vibrational spectrum of $\bar{4}3\text{m}$ $\text{Cr}_3\text{B}_7\text{O}_{13}\text{Cl}$	153
Fig. 57: Solid-state electronic spectra of mm2, a) "light green" and b) "dark green" $\text{Cu}_3\text{B}_7\text{O}_{13}\text{Cl}$	156
Fig. 58: Temperature dependence of second harmonic intensity of $\text{Ni}_3\text{B}_7\text{O}_{13}\text{Br}$ at $\bar{4}3\text{m}$ - mm2 phase transition.....	157

LIST OF TABLES

Table	Page
1 Thermodynamic values for ferroelectric phase transition in molybdates.....	67
2 Parameters ϵ_p , K_1 , and T_1 obtained by fitting the observed dielectric constant.....	74
3 Parameters K and T_1 obtained by fitting dynamic measurements of pyroelectric coefficient.....	75
4 Curie-Weiss temperature T_C and transition temperature T_1 as determined from Eq. (15) and the maximum of ϵ , respectively. Also given for comparison is T_1 as found from fitting pyroelectric coefficient p or dielectric constant ϵ . All temperatures are in $^{\circ}\text{C}$	76
5 Parameters determined previously from pyroelectric and dielectric measurements.....	78
6 Comparison of calculated values and measured upper bounds for entropy discontinuity and latent heat.....	79
7 Specific heat data for LiNH_4SO_4 and LiND_4SO_4	97
8 Optical second harmonic powder analysis data (particle size: 212-300 μm).....	107
9 Isobaric molar heat capacities of LiKSO_4 (MW = 142.10) and LiCsSO_4 (MW = 235.91).....	111
10 Comparison of easy and hard poling directions for a $\text{LiH}_3(\text{SeO}_3)_2$ sample at 24°C	115

LIST OF TABLES (Cont'd)

	Page
11 Experimental values used in calculation of M_{\max}	128
12 Projected parameters for propionates.....	128
13 Thermodynamic values for 43m-mm2 phase transition in boracite crystals.....	144
14 Molar heat capacity at constant pressure of Cr-Cl boracite in mm2 and $\bar{4}3m$ phases (MW = 475.10).....	146
15 Molar heat capacity at constant pressure of Fe-I boracite in mm2 and $\bar{4}3m$ phases (MW = 578.10).....	147
16 Molar heat capacity at constant pressure of Cu-Cl boracite in mm2 and $\bar{4}3m$ phases (MW = 509.75).....	147
17 Molar heat capacity at constant pressure of Ni-Br boracite in mm2 and $\bar{4}3m$ phases (MW = 539.69).....	148
18 Molar heat capacity at constant pressure of Zn-Br boracite in mm2 and $\bar{4}3m$ phases (MW = 559.70).....	148
19 Least squares fit molar heat capacity functions for boracites in the mm2 phase.....	149
20 Least squares fit molar heat capacity functions for boracites in $\bar{4}3m$ phase.....	149
21 Infrared absorptions of boracites (fundamentals in cm^{-1}).....	154
22 Experimental literature on boracites.....	162
23 Observed ferroelectric transition in boracites.....	166
24 Molybdates experiments.....	168
25 Ferroelectric sulfate family.....	172
26 Ferroelectric sulfate family.....	173

1. INTRODUCTION, SUMMARY AND CONCLUSIONS

1.1 Introduction

This study of improper ferroelectrics was motivated by a desire to identify materials which would enhance the performance of the pyroelectric vidicon (PEV). The pyroelectric materials commonly used in this device are in the TGS-DTGFB family and are all proper ferroelectrics. The principle limitation with proper ferroelectrics is that the increase in the pyroelectric coefficient obtained by operating closer in temperature to the ferroelectric-paraelectric phase transition is more than overcome by a concomitant increase in the dielectric constant. Thus, the material's figure of merit, $p/\epsilon c$, where p = pyroelectric coefficient, ϵ = dielectric constant, and c = volume specific heat, decreases as the ferroelectric Curie temperature is approached. In the case of improper ferroelectrics, there is no dielectric divergence upon approaching the ferroelectric-paraelectric phase transition, and therefore one obtains a figure of merit that increases dramatically up to the Curie point.

The investigations at Philips Laboratories, in conjunction with Yeshiva University, began with a comprehensive literature survey and selection of representative materials from a number of known classes of improper ferroelectrics. Samples of each material were obtained or grown, and a comprehensive set of thermal and electrical measurements was performed. The measurements program consisted of independent determinations of p , ϵ , c , p/c and $p/\epsilon c$. With five independent measurements of three quantities, we were thus able to eliminate the discrepancies and artifacts that obscured the published literature. Combining these precision measurements with an extended thermodynamic theory, we were able to confirm our initial expectation that the improper ferroelectrics would have high figures of merit. In every class of improper ferroelectrics investigated, we found the figure of merit was comparable or distinctly superior to that of TGS.

1.2 Summary of Results

(1) Molybdates

A detailed analysis of the dielectric, pyroelectric and heat capacity measurements on gadolinium, terbium, and gadolinium-dysprosium molybdate revealed an excellent agreement with the theoretically expected behavior. Moreover, these separate analyses of the dielectric, pyroelectric and thermal properties can be combined to predict the behavior of the figure of merit. Independent measurements of the figure of merit are in excellent agreement with the theoretical projections.

These measurements and their analysis confirm the theoretical expectation that improper ferroelectrics can overcome the limitations in the usual proper ferroelectrics brought about by the divergence of the dielectric constant near the transition temperature. The improper ferroelectrics have well-behaved dielectric constants and thus have a figure of merit that rises as the transition temperature is approached.

Using the theoretical expression for the figure of merit, we are able to optimize this expression with respect to variations in the difficult-to-assess free energy parameters. The optimum figure of merit is then given in terms of readily measured or estimated quantities. Using values characteristic of the molybdate family, we estimate an optimum figure of merit of about $10 \times 10^3 \text{ cm}^2/\text{C}$ (for comparison, we find the figure of merit of TGS to be $3 \times 10^3 \text{ cm}^2/\text{C}$ at 40°C).

(2) Sulfate Family

Five materials from the family of ferroelectric sulfates were studied: LiNH_4SO_4 , LiND_4SO_4 , LiCsSO_4 , LiKSO_4 and $\text{LiH}_3(\text{SeO}_3)_2$.

Lithium ammonium sulfate and its deuterated analog exhibited similar properties. The high room-temperature value for the

figure of merit (about equal to that of TGS at 40°C) suggested further study of related materials. Both lithium cesium sulfate and lithium potassium sulfate were consequently investigated; these materials, however, exhibited distinctly different behaviors which eliminate them for practical pyroelectric applications.

Lithium trihydrogen selenite was investigated because of its high value of spontaneous polarization ($\sim 15 \mu\text{C}/\text{cm}^2$), and the fact that the related material $\text{RbH}_3(\text{SeO}_3)_2$ has been identified as an improper ferroelectric. We find no evidence that $\text{LiH}_3(\text{SeO}_3)_2$ is an improper ferroelectric. The measured value of that ratio p/ϵ is about one-fourth that of TGS. While this eliminates $\text{LiH}_3(\text{SeO}_3)_2$ for practical applications, the large value of the spontaneous polarization suggests that related materials might have potentially useful figures of merit.

(3) Propionates

Initial measurements of the pyroelectric and dielectric properties of dicalcium lead propionate (DLP) reveal the presence of an internal bias field. Annealing samples of DLP did not eliminate the effects of internal bias fields as reported in the literature; indeed the properties of the samples were severely degraded. Initial measurements on the specific heat of DLP and dicalcium strontium propionate (DSP) showed, as expected, no large anomaly at the transition temperature.

A theoretical analysis based on a free energy appropriate to a second-order pseudo-proper phase transition was carried out; the predictions agree with our measurements as well as certain published data. In this analysis, the figure of merit has a maximum as a function of temperature which can be expressed in terms of the free-energy parameters. Using data from the literature (which is compatible with our measurements), we can estimate these free-energy parameters and project a figure of merit of $4.2 \times 10^3 \text{ cm}^2/\text{C}$ for DSP and $7.3 \times 10^3 \text{ cm}^2/\text{C}$ for DLP.

(4) Boracites

Initial dielectric and pyroelectric measurements were performed on samples of boracites obtained from Plessey Company. Major difficulties in fully poling these samples were encountered. The measurements are consistent with the data reported by Plessey Company and with the resulting expectations of a high figure of merit for the boracites. Specific heat measurements were made on samples of Zn-Br, Cr-Cl, Fe-I, Ni-Br and Cu-Cl boracite. In addition, infrared vibrational spectra, electronic spectra, and second-harmonic measurements were performed on some of the samples in order to better characterize the material. A number of initial observations can be made:

- The cubic-orthorhombic phase transition appears to be strongly first-order. This is indicated by the large latent heat of the transition, a detectable thermal hysteresis, and the discontinuous jump in the second harmonic intensity at the transition.
- The different members of the boracite family may be structurally dissimilar. This is indicated by large differences in the molar heat capacity of Fe-I and Cr-Cl boracite in the cubic phase. Large differences in the molar latent heats also support this conclusion.

1.3 Conclusions

The conclusions of this study are:

- Confirmation that improper ferroelectrics have the expected potential for greatly improved pyroelectric figure of merit.
- Identification of the boracite and propionate materials as the families of improper ferroelectrics with greatest potential.

Interest focuses on the boracites for a number of reasons. First, measurements (Ref. 1-1) of the Fe-I boracite show a figure of merit, $p/\epsilon c$, which is one-fourth that of TGS at room temperature, and which subsequently rises to exceed the figure of merit of DTGFB as the temperature approaches the Curie temperature at 72°C. This behavior is characteristic of improper ferroelectrics. The room-temperature figure of merit of the Ni-Br boracite was measured (Ref. 1-1) and found to be larger than that of TGS; one would expect it to rise dramatically with increasing temperature to result in a figure of merit distinctly superior to that of DTGFB (estimate: a factor of 3 greater). Second, the measured (Ref. 1-2) piezoelectric constants of the boracites are one-tenth those of TGS. This will substantially aid in tube ruggedization by decreasing the sensitivity to vibration. Third, pedestal-noise suppression, when fully implemented in the vidicon tube, will change the figure-of-merit from $p/\epsilon c$ to $p/\epsilon^{3/2} c$. Since the principle virtue of improper ferroelectrics is their low dielectric constant, this will further enhance the superiority of the boracites by another factor of 1.7. In addition, the measured (Ref. 1-1) resistance of the boracites are in the range of $10^{10} - 10^{12}$ ohm-cm, which could possibly eliminate the need for pedestal generation. Elimination of this noise source should improve the overall tube performance significantly. Finally, the boracites are chemically stable and mechanically hard. This should facilitate target fabrication and simplify tube operation in a hard vacuum.

The propionates are of interest for three major reasons. First, the measurements and their analysis for dicalcium lead propionate (DLP) allow us to project a figure of merit about $7.3 \times 10^3 \text{ cm}^2/\text{C}$. Our analysis also shows that DLP belongs to a sub-class of improper ferroelectrics which has no upper bounds on the potential figure of merit. Thus, we expect that other members of this

Ref. 1-1. R.W. Whatmore, Annual Research Report, Plessey C. Ltd., Nov. 1976-Oct. 1977, Ref. CD.6500088.

Ref. 1-2. A.S. Sonin and I.S. Zheludev, Sov. Phys. Cryst. 8, 217 (1963).

family, or suitably substituted DLP, might have distinctly higher figures of merit. Finally, the growth of large crystals of materials in this family, using standard solution-growth techniques, is possible.

2. MOLYBDATES

A detailed analysis of the dielectric, pyroelectric and heat capacity measurements on gadolinium, terbium, and gadolinium-dysprosium molybdate reveals an excellent agreement with the theoretically expected behavior. Moreover, these separate analyses of the dielectric, pyroelectric and thermal properties can be combined to predict the behavior of the figure of merit. Independent measurements of the figure of merit are in excellent agreement with the theoretical projections.

These measurements and their analysis confirm the theoretical expectation that improper ferroelectrics can overcome the limitations in the usual proper ferroelectrics brought about by the divergence of the dielectric constant near the transition temperature. The improper ferroelectrics have well-behaved dielectric constants and thus have a figure of merit that rises as the transition temperature is approached.

Using the theoretical expression for the figure of merit, we are able to optimize this expression with respect to variations in the difficult-to-assess free energy parameters. The optimum figure of merit is then given in terms of readily measured or estimated quantities. Using values characteristic of the molybdate family we estimate an optimum figure of merit about $10 \times 10^3 \text{ cm}^2/\text{C}$ (for comparison we find the figure of merit of TGS to be $3 \times 10^3 \text{ cm}^2/\text{C}$ at 40°C).

2.1 Review

This section reviews the previous theoretical and experimental work on the rare-earth molybdates.

2.1.1 Review of Theory

The theoretical interpretation of gadolinium molybdate as an improper ferroelectric was advanced independently and simultaneously by four different sources: Dvorak (Refs. 2-1 and 2-2), Levanyuk and Sannikov (Ref. 2-3), Aizu (Ref. 2-4) and

Pytte (Ref. 2-5). A subsequent interesting discussion of the theory for the molybdates is presented in a paper by Dorner, Axe and Shirane (Ref. 2-6) as part of a description of their neutron scattering experiment on terbium molybdate.

The most complete analysis is contained in the works of Dvorak (Refs. 2-1 and 2-2) which are based on a knowledge of the precise space groups of the high and low symmetry phases. This evaluation is not intended to detract from the contributions of the other workers (Refs. 2-3, 2-4, 2-5) who inferred the essential features in the behavior of the molybdates based on less complete information.

(1) Dvorak Analysis

Dvorak presents his analyses of the behavior of gadolinium molybdate in two papers (Refs. 2-1, 2-2). In the first paper the form of the thermodynamic potential applicable to the molybdates is determined, based on the knowledge of the precise space groups in the ferroelectric and paraelectric phases and the observation of cell doubling at the transition. In the second paper (Ref. 2-2), the dielectric and elastic behavior of gadolinium molybdate is deduced.

Dvorak's analysis of gadolinium molybdate is a direct application of Landau's theory (Ref. 2-7) of continuous phase transitions. Three experimental facts are used in this analysis: the space group of the high symmetry phase D_{2d}^3 ($P\bar{4}2_1m$); the space group of the low symmetry phase C_{2v}^8 ($Pba2$); the volume of the unit cell in the low symmetry phase is double that of the high symmetry phase. In a detailed argument, Dvorak shows that only one physically irreducible representation of the high symmetry space group can induce precisely this symmetry reduction at the phase transition. This is a two-dimensional representation belonging to the M point of the brillouin zone. The form of the free-energy (in his notation) deduced from this analysis is,

$$\begin{aligned}
F = F_0 &+ \frac{1}{2}\alpha(T) (q_1^2 + q_2^2) + \frac{1}{4}\beta_1 (q_1^4 + q_2^4) + \frac{1}{2}\beta_2 q_1^2 q_2^2 + \beta_3 q_1 q_2 (q_1^2 - q_2^2) + \\
&+ \frac{1}{6}\zeta(q_1^2 + q_2^2)^3 + \frac{1}{2}\chi_{33}^{-1} P_z^2 + \frac{1}{2}c_{11} (u_{xx}^2 + u_{yy}^2) + \frac{1}{2}c_{33}u_{zz}^2 + \\
&+ \frac{1}{2}c_{66}u_{xy}^2 + c_{12}u_{xx}u_{yy} + c_{13}(u_{xx} + u_{yy})u_{zz} + a_{36}'P_z u_{xy} + \\
&+ \gamma_1 P_z q_1 q_2 + \gamma_2 P_z (q_1^2 - q_2^2) + \delta_1 u_{zz}(q_1^2 + q_2^2) + \\
&+ \delta_2(u_{xx} + u_{yy})(q_1^2 + q_2^2) + \delta_3 u_{xy} q_1 q_2 + \delta_4 u_{xy}(q_1^2 - q_2^2)
\end{aligned}$$

where (q_1, q_2) is the soft mode amplitude, P_z is the z component of the polarization and u_{ij} are the components of the strain tensor. The essential difference between this free energy and the form advanced by other workers is the presence of the terms with coefficient β_3 , γ_2 and δ_4 . It is precisely these terms that cause the minimum of the free energy in the ferroelectric phase to lie off the lines: $q_1 = \pm q_2$; $q_1 = 0$, $q_2 \neq 0$; and $q_1 \neq 0$, $q_2 = 0$. That the physically realized states in the low temperature phase occur off these lines is essential to get the correct correspondence with the observed space group of the ferroelectric phase. These terms can lead to a qualitatively different behavior for certain of the elastic and dielectric properties at the phase transition, namely, such terms in the free energy would produce a small discontinuous jump at the transition temperatures superimposed on the temperature dependence expected from a free energy without such terms. Existing experimental data on dielectric and elastic properties do not reveal such effects with reasonable magnitude.

Nevertheless, these terms must be present in the free-energy - however small their magnitude or their effect on dielectric and elastic properties - to properly account for the reduction in symmetry at the phase transition.

(2) Levanyuk and Sannikov Analysis

The first interpretation of the phase transition in gadolinium molybdate as driven by a zone boundary phonon was offered by Levanyuk and Sannikov (Ref. 2-3). The authors recognized that the observed cell doubling at the transition temperature indicated that the order parameter describing the transition must be other than the polarization. They were then able to apply their earlier more generalized analysis (Ref. 2-8) of ferroelectric phase transitions where the polarization was not the order parameter. Without carrying out a detailed group theoretical analysis of the transition, Levanyuk and Sannikov hypothesized that the transition was driven by a two-component order parameter and wrote down a thermodynamic potential to describe the phase transition (in their notation):

$$\begin{aligned}\Phi = & \frac{\alpha}{2} (\eta^2 + \zeta^2) + \frac{\beta_1}{4} (\eta^2 + \zeta^2)^2 + \frac{\beta_2}{2} (\eta\zeta)^2 \\ & + \frac{\gamma}{6} (\eta^2 + \zeta^2)^3 + \frac{\chi}{2} P^2 + \frac{c}{2} u^2 + \\ & \lambda Pu + a\eta\zeta P + b\eta\zeta u - PE - \sigma u\end{aligned}$$

where (η, ζ) = two component order parameter, P = z component of the polarization and u = the x-y component of the strain. Using this hypothesized potential, Levanyuk and Sannikov calculated the expected temperature dependence of the elastic and dielectric constants and found them to be in agreement with the available experimental results.

Levanyuk and Sannikov did note that there are many phase transitions between the known point groups of the high and low symmetry phases which are exactly described by just the thermodynamic potential they used. However, without knowledge of the precise space groups of the high and low symmetry phases they were unable to determine a priori the precise form of the potential.

The form of the potential analyzed by Levanyuk and Sannikov has the substantial advantage that analytic solutions are readily calculated. Moreover, as we shall argue in Par. 2.2, it is plausible to use just such a thermodynamic potential as an approximation to the complete thermodynamic potential derived by Dvorak.

(3) Aizu Analysis

Aizu's analysis (Ref. 2-4) of the phase transition in gadolinium molybdate is based on knowledge of the high and low symmetry space groups, as well as the observed cell doubling at the phase transition. Aizu correctly concludes that the phase transition is brought about by an instability in a doubly-degenerate zone-boundary phonon. The method used to deduce the form of the thermodynamic potential is not the usual calculation involving the irreducible representations of the high symmetry space group. Rather Aizu enumerates the symmetry transformations which must leave the potential invariant and then writes down the simplest form of the thermodynamic potential consistent with these symmetries. In order to simplify the computation Aizu introduces an additional hypothetical symmetry, while carefully emphasizing: "This assumption serves to simplify the form of the free-energy function. However, it is not essentially requisite to the theory. If it were found to make the results of the theory too roughly coincident with the observations, it would be withdrawn." The resulting thermodynamic potential is equivalent to the one analyzed by Levanyuk and Sannikov. Aizu demonstrates that the predictions of his analysis are in good agreement with the extant elastic, dielectric and optical measurements made on gadolinium molybdate.

(4) Dorner, Axe and Shirane Discussion

In reporting their neutron scattering measurements on terbium molybdate, Dorner, Axe and Shirane (Ref. 2-6) discuss the theoretical analysis of their result. The major contribution of

this work is, of course, the direct observation of the zone-boundary soft mode which causes the phase transition. However, the authors make two useful observations which help illuminate the theory. First, they include the complete anisotropic sixth order term in the potential for the soft mode; previous workers had included only an isotropic term for simplicity. Second, they note that the essential difficulty in carrying out an analytic solution of the complete thermodynamic potential advanced by Dvorak is that there is a temperature dependence in the phase angle $\phi = \arctan (q_1/q_2)$. To circumvent this difficulty the authors append the hypothesis that this angle does not vary very much and analyze their data according to a thermodynamic potential essentially equivalent to that of Levanyuk and Sannikov and Aizu. The experiment is found to be in excellent agreement with the theoretical expressions. This provides post-hoc justification for their hypothesis of constant ϕ . (In our analysis in Par. 2.2 the hypothesis of constant ϕ is shown to be quite plausible.)

(5) Pytte Analysis

An analysis of the phase transition in gadolinium molybdate is given by Pytte (Ref. 2-5) from the soft mode perspective. Using the known space group of the high symmetry phase and the cell doubling observed at the transition, Pytte identifies the mode whose instability causes the transition as one of three zone boundary modes. Introducing a phenomenological Hamiltonian which describes both the phase transition in this mode and the soft mode coupling to a polar and an elastic mode, Pytte is able to account for the extant elastic and ferroelectric measurements on gadolinium molybdate.

While Pytte observes that this soft mode is doubly degenerate, the Hamiltonian involves only the amplitude for this soft mode; no angular coordinate is introduced which would allow for a temperature variation in the particular linear combination of modes which constitutes the soft mode. Thus, while it captures the essential points, this analysis is not sufficiently detailed to give an analysis comparable to that of Dvorak.

2.1.2 Review of Measurements

This section reviews the previous pyroelectric, dielectric and thermal measurements made on rare-earth molybdates.

(1) Pyroelectric Coefficient and Spontaneous Polarization Measurements

Measurement Techniques and Boundary Conditions. There are two essentially different approaches to determining the pyroelectric coefficient of a ferroelectric material. One is to directly measure the pyroelectric current while varying the temperature either in a dc fashion (Byer-Roundy technique) or in an ac fashion (Chynoweth technique). The other approach is to measure the spontaneous polarization as a function of temperature either by analog integration of the pyroelectric current during dc heating, or from a ferroelectric hysteresis loop at a sequence of temperatures (Sawyer-Tower bridge technique). The resulting curve can then be numerically differentiated. All these techniques have inherent dangers. At low dc heating rates the pyroelectric current is small and hard to measure accurately; at higher heating rates it is difficult to maintain thermal equilibrium in the sample. The ac heating technique requires a normalization and an independent measurement of the heat capacity of the sample. Tracing ferroelectric hysteresis loops introduces many complexities involved in the domain switching; numerically differentiating experimental data requires even more courage. It is not surprising then that there are few precision measurements of the pyroelectric coefficient of the rare-earth molybdates, even though there are fairly many measurements of spontaneous polarization.

The mechanical boundary conditions for measurements of the pyroelectric current and spontaneous polarization are generally good approximations to constant (zero) stress. The electrical boundary conditions are generally constant applied field of zero magnitude, but some pyroelectric current measurement use a finite field to maintain the sample in a poled state especially during a cooling part of the cycle.

Direct Measurements of Pyroelectric Coefficient. The literature contains only three efforts to directly measure pyroelectric currents. The two efforts to measure the pyroelectric current from GMO were plagued by an experimental artifact that we shall call multiple peaking. The essential characteristic of this artifact is that in the vicinity of the transition temperature the pyroelectric current exhibits a number of spikes which are, in a given sample, reproducible to a fair degree. These spikes correspond to different portions of the sample going through the ferroelectric-paraelectric phase transition over a finite range of temperatures.

Rabinovich (Ref. 2-9) observed the multiple peaking in gadolinium molybdate and attributed it to the motion of domain walls caused by inhomogeneities ("inclusions, residual stress, etc.") in the single crystal sample. The only firm conclusion Rabinovich draws from his measurements is that the change in the polarization in the region of the phase transition amounts to $4 \times 10^{-8} \text{ C/cm}^2$.

A second effort to directly measure the pyroelectric current from GMO is reported in three papers: Ullman, Ganguly and Hardy (Ref. 2-10), Ullman, Ganguly and Zeidler (Ref. 2-11) and Ullman, Cheung, Rakes and Ganguly (Ref. 2-12). These works ascribe the multiple peaking to a thermal gradient near the surface of the sample which leads, through differential thermal expansion, to a stress-induced polarization switching. The data taken far from the transition temperature should be free of this effect; values for the pyroelectric coefficient of $1.4 \times 10^{-9} \text{ C/cm}^2 \text{ K}$ at 143 C and $2.5 \times 10^{-9} \text{ C/cm}^2 \text{ K}$ at 151°C are given. Their value at 151 C is just 9% below the value which can be deduced from the data of Sawaguchi and Cross (Ref. 2-13) described below.

The other direct measurement of the pyroelectric current was performed on TMO by Keve, Abrahams, Nassau and Glass (Ref. 2-14). In this case inhomogeneities in the sample probably so

broadened the phase transition region that it was not possible to resolve any discontinuities at the transition temperature (Ref. 2-15). In the region where the pyroelectric coefficient does not vary rapidly with temperature, this data should be quite reliable. Unfortunately no analysis of the data is presented.

Temperature Dependence of Spontaneous Polarization, GMO. Of the several papers which describe the temperature dependence of the spontaneous polarization of rare-earth molybdates, the most comprehensive study was performed by Sawaguchi and Cross (Ref. 2-13) on GMO from 4.2 K to 473 K with particular care near the phase transition. Low frequency (0.01 Hz) hysteresis loops were used to obtain the spontaneous polarization down to 75 K; below this temperature, the charge integration technique was used because the coercive field is too large to obtain saturated loops. The resulting data were subjected to a detailed analysis which included a fit to the form expected from Aizu's (Ref. 2-16) analysis of improper ferroelectrics, namely,

$$P(T) = [1.78 (433 - T)^{1/2} + 2.59] \times 10^{-6} \text{ C/cm}^2, T < 432.3 \text{ K.}$$

The fit is good only within 5 K of the transition. A significantly better fit is obtained to the expression,

$$P(T) = 3.68 (433.6 - T)^{1/3} \times 10^{-8} \text{ C/cm}^2, T < 432.3 \text{ K.}$$

A unique contribution of this work is the extrapolated value of the spontaneous polarization at absolute zero: $2.86 \pm 0.1 \times 10^{-7} \text{ C/cm}^2$. The value measured at 20°C, $2.01 \pm 0.15 \times 10^{-7} \text{ C/cm}^2$, and the discontinuity at the transition temperature of 432.3 K, $4.0 \pm 0.2 \times 10^{-8} \text{ C/cm}^2$, are also useful for comparisons with other works.

Only one (Ref. 2-17) of the other measurements using the loop tracing technique on GMO was able to distinguish the discontinuous jump to zero from a smooth decrease to zero of the spontaneous polarization at the transition temperature. Evidence for a

first order transition is reported by Kumada (Refs. 2-18, 2-19) who observed double hysteresis loops above the transition temperature. Sawaguchi and Cross (Ref. 2-20) expected to observe such double loops but were unable to find the phenomenon.

Cummins (Ref. 2-17) also finds a discontinuous jump of about $4.2 \times 10^{-8} \text{ C/cm}^2$ at the 159°C transition temperature. His measurements on GMO were made at "low frequency (hand traced)" and span from 25°C through the transition temperature. Cummins' value for the 20°C polarization, $2.0 \times 10^{-7} \text{ C/cm}^2$, also agrees with the measurements of Sawaguchi and Cross (Ref. 2-13).

In the first report of ferroelectricity in the rare-earth molybdates, Borchardt and Bierstedt (Ref. 2-21) measured the ferroelectric hysteresis loops of GMO at 60 Hz from 25°C through the phase transition at 159°C . The data has a scatter of about 10% around a smooth trend and no conclusion about the order of the transition can be drawn. The room temperature value of the spontaneous polarization is given as $1.7 \times 10^{-7} \text{ C/cm}^2$. This is the first report of ferroelectricity in rare-earth molybdates.

Other early measurements on the ferroelectric hysteresis of GMO are reported in a short note by Aizu, Kumada, Yumoto and Ashida (Ref. 2-22) and further elaborated on by Kumada, Yumoto and Ashida (Ref. 2-23). The data is taken at 1 MHz from 25°C through the phase transition. There is little scatter about a smooth trend which goes continuously to zero at the transition temperature. The value of $1.8 \times 10^{-7} \text{ C/cm}^2$ is reported for the polarization at 20°C .

Temperature Dependence of Spontaneous Polarization, TMO and Other Molybdates. Terbium molybdate was examined by Keve, Abrahams, Nassau and Glass (Ref. 2-14) using polarization reversal, charge integration and pyroelectric measurements. A value of $1.90 \pm 0.05 \times 10^{-7} \text{ C/cm}^2$ is obtained for the polarization at 25°C , this agrees with the earlier measurement by Borchardt and Bierstedt (Ref. 2-24) noted below. The report that the polari-

zation decreases continuously to zero at the phase transition is probably due to inhomogeneities broadening the transition region (Ref. 2-15).

In a survey of twelve ferroelectric rare-earth molybdates, Borchardt and Bierstedt (Ref. 2-24) give spontaneous polarization at two or three selected temperatures for each material. These data were probably taken from 60 Hz hysteresis loops as was described in the authors' earlier study (Ref. 2-21) of GMO. Values for the polarization at 25°C vary from 1.4 to 2.4×10^{-7} C/cm²; the value reported for GMO, 1.7×10^{-7} C/cm², is precisely the same as their earlier measurement. The 25°C spontaneous polarization of TMO is given as 1.8×10^{-7} C/cm².

(2) Dielectric Permittivity

Thermal and Mechanical Boundary Conditions. Conceptually, four distinct dielectric permittivities can be distinguished depending on the thermal (adiabatic or isothermal) and mechanical (constant stress or constant strain) boundary conditions. In practice, dielectric measurements are made with a small ac probe field with no external mechanical stress. Which dielectric constant is measured in a given experiment depends on the relationship of the frequency of the probe field to the thermal and mechanical time constants of the sample under study. These thermal and mechanical time constants depend not just upon the properties of the materials but also upon the dimensions of the sample and the experimental environment.

Since typical thermal time constants are on the order of magnitude of seconds, one may assume that the typical low-frequency experiment which uses a probe field with frequencies near a kilohertz measures an adiabatic dielectric permittivity. The relationship between the adiabatic and isothermal dielectric susceptibilities ($\epsilon = 1 + \chi$) is given by:

$$\chi^T/\chi^S - 1 = T_p^2/c^E \chi^S = T_p^2/c^P \chi^T,$$

where p is the pyroelectric coefficient, T is the absolute temperature and c^E and c^P are the specific heats at constant field and polarization respectively (the appropriate mechanical boundary condition being the same for every quantity). Thus the difference between them becomes significant only just below the phase transition where the pyroelectric coefficient becomes large.

With regard to mechanical boundary conditions, the value obtained at low frequencies (typically kHz) corresponds to the adiabatic dielectric permittivity at constant (zero) stress. It is only at very high frequencies (typically many MHz) that the crystal cannot equilibrate mechanically as fast as the field changes so that the resulting value measured is the adiabatic dielectric permittivity at constant (zero) strain. The permittivity at constant stress is higher than the value at constant strain, because, at constant stress, the applied field can electrostrictively cause a distortion in the lattice which enhances piezoelectrically the polarization already caused by the direct effect of the applied field.

Adiabatic, Mechanically Clamped Dielectric 'Constant' Measurements.

For the rare-earth molybdates, two measurements of the adiabatic dielectric permittivity at constant (zero) strain appear in the literature. Both were performed at 19 MHz and give values which are essentially unchanged even as the temperature is scanned through the paraelectric-ferroelectric phase transition. Cross, Fouskova and Cummins (Ref. 2-25) report a value of about 9.5 for GMO in the range from 25°C to 180°C. Keve, Abrahams, Nassau and Glass (Ref. 2-14) obtain a value of 9.2 ± 0.5 for TMO in the range from 25°C to 170°C. These observations on the mechanically clamped dielectric constant were the first indication that the rare-earth molybdates are truly special ferroelectrics. The correct understanding of this point is essential to their description.

Adiabatic, Mechanically Free Dielectric Constant Measurements.

All the reported low-frequency measurements on the rare-earth molybdates give essentially the same qualitative behavior for the temperature dependence of the adiabatic zero-stress dielectric constant. Namely, from a magnitude of about 10 at room temperature the permittivity increases in the vicinity of transition temperature to a peak value about 15-20% larger and then abruptly, at the transition temperature, drops back to essentially its room temperature value and remains constant in the paraelectric phase. Most measurements exhibit a small (1-2%) tailing which extends a few degrees above the transition; none of the papers offer an opinion as to whether this tail is an intrinsic property of the material or an experimental artifact.

The first measurement of the low frequency dielectric permittivity of gadolinium molybdate was given by Cross, Fouskova and Cummins (Ref. 2-25). They used a probe field of 20 V/cm at 1 kHz to scan from 25°C to 180°C. The background value of the dielectric constant is reported as 10.0 and the maximum value of 11.6 occurs at the transition temperature, 159 C.

These values are confirmed by Fousek and Konak (Ref. 2-26) who focus attention on an essential experimental point for all low-frequency dielectric measurements, namely the requirement that single domain samples be used so that domain wall motion does not spuriously enhance the measured value in the ferroelectric phase. This is a particularly important consideration for measurements made near the transition temperature. Fousek and Konak report measurements on single-domain GMO (poled by application of a 20 kV/cm field prior to measurement) in the temperature range 100°C to 190°C at a frequency of 1 kHz. They obtain a background value of 10.0 for the dielectric permittivity which rises to a peak of 11.6 at the 159°C transition temperature. However, the same measurements on a multi-domain sample give a peak value of 12.9; moreover, the permittivity is consistently higher than the single domain sample all the way down to 100°C. No differences between the two samples appear in the paraelectric phase, as expected.

Cummins (Ref. 2-17) summarizes verbally the result of his measurements on GMO at 1 kHz; the data is not displayed graphically. From a value of 10 at 25°C, he reports, the permittivity increases by about 10% through the transition at 159°C.

At variance with the above results is the measurements of Smith and Burns (Ref. 2-27). GMO was studied from 25°C to 170°C at a frequency of 1 kHz. A background value of 8.0 and a peak value of 10.7 were reported. These values were probably not determined with high precision as the authors only wanted the results to argue that the dielectric permittivity "is essentially temperature-independent". The principal goal of their work was the analysis of the electro-optic coefficients, so we do not regard this discrepancy as significant.

The only complete temperature dependence for the low frequency permittivity of terbium molybdate is reported by Keve, Abrahams, Nassau and Glass (Ref. 2-14) at 400 Hz from 25°C to 170°C. They reported that the background value of 10.0 ± 0.5 rises to a peak of about 15 at the transition temperature of $163 \pm 1^\circ\text{C}$.

Dielectric Constant at Room Temperature. Besides the cited measurements, there have been some measurements simply of the room temperature value of the low-frequency dielectric permittivity. Aizu, Kumada, Yumoto and Ashida (Ref. 2-22) obtain at 400 Hz a value of 10.5 for GMO at 25°C. Borchardt and Bierstedt (Ref. 2-24) give dielectric constants for twelve ferroelectric rare-earth molybdates. They do not describe the details of their measurements but we may plausibly expect that they are room temperature values obtained at a low frequency, since in an earlier work (Ref. 2-21) the same authors obtain a value of about 10 for the dielectric constant of GMO using a 60 Hz ferroelectric loop tracer. The reported values range from a low of 9.5 for europium molybdate to a high of 13 for europium-gadolinium and europium-terbium mixed crystals. The values of 10 for GMO and 11 for TMO are consistent with the results of other workers.

Pressure Dependence of Dielectric Constant. Shirokov, Mylov, Baranov and Prokhortseva (Ref. 2-28) performed an interesting study of the effect of hydrostatic pressure on the temperature dependence of the low-frequency dielectric permittivity of GdMO. They measure at 10 kHz for hydrostatic pressure up to 2.6 kbar and obtain a background value of 10 and a peak value of 11 for the permittivity. The shape of the temperature dependence does not change with increasing pressure except for an overall shift of the entire curve to higher temperatures. This shift varies linearly with hydrostatic pressure and has a magnitude of 29.5 ± 0.3 K/kbar. A similar study on $\text{Sm}_2(\text{MoO}_4)_3$ by Midorikawa, Ishibashi and Takagi (Ref. 2-29) finds a temperature shift of 29.4 K/kbar.

In summary then, all of the measurements on the rare-earth molybdates are in reasonable agreement with each other. Moreover they correspond qualitatively to what is expected from the theory. However, the literature contains no detailed quantitative analysis of the temperature dependence of the dielectric permittivity of rare-earth molybdates.

(3) Specific Heat Measurements

Three measurements of the specific heat of rare-earth molybdates have been reported. The measurements of Fouskova (Ref. 2-30) and Cheung and Ullman (Ref. 2-31) were made on gadolinium molybdate, while those of Keve, Abrahams, Nassau and Glass (Ref. 2-14) were made on terbium molybdate. Only Fouskova reports absolute measurements; the other papers calibrate their relative measurements by her absolute determination.

Fouskova (Ref. 2-30) reports measurements on gadolinium molybdate made with a Perkin-Elmer differential scanning calorimeter in the temperature 100°C to 200°C. From a value of about 0.104 cal/gK at 100°C, the specific heat gradually rise about 15% as the phase transition is approached and then shows a sharp peak at the phase transition at about 160°C. Above the transition the specific heat drops abruptly to 0.110 cal/gK and remains

essentially constant out to 200°C. Sample-to-sample variations of 1 K in the transition temperature are reported. The transition entropy is estimated to be 0.22 ± 0.08 cal/mol K and the transition heat (in a 0.5 K neighborhood of the transition) is estimated to be 0.048 cal/g $\pm 10\%$. No detailed analysis of the temperature dependence of the specific heat is reported. The author estimates a precision of $\pm 5\%$ in the absolute determination; the data exhibit a scatter of less than 1% about a smooth trend. The samples were silver plated on all sides to insure the electrical boundary condition of $E = 0$; mechanical boundary conditions are not mentioned.

Cheung and Ullman (Ref. 2-31) performed measurements on gadolinium molybdate in the temperature range from 50°C to 240°C using an ac heating technique. This technique produces a relative measurement whose scale is calibrated by setting the value of the specific heat just above the transition to the value reported by Fouskova (Ref. 2-30). The measurements are reproducible to within 0.1 K of the transition and no hysteresis effects appear between heating and cooling. The qualitative features of the specific heat temperature dependence are the same as reported by Fouskova; however, Cheung and Ullman carry out a much more detailed analysis of the data. The data fit well to linear temperature dependence both far below:

$$c_p = 2.43 \times 10^{-4} T - 6.28 \times 10^{-4} \text{ cal/gK}, 50^\circ\text{C} < T < 110^\circ\text{C}$$

and above:

$$c_p = 3.65 \times 10^{-5} T + 0.10 \text{ cal/gK}, 159^\circ\text{C} < T < 240^\circ\text{C}$$

the transition temperature, although the two linear regions do not join together smoothly. The data just below the transition were fitted to a number of different expressions. A power law divergence at the transition temperature gave an exponent of 2.1 but fit the data very poorly within 0.5 K of the transition. Fits to a logarithmic divergence at the transition were performed in two temperature ranges below the transition with the following results:

$$c_p = 0.09 - 0.0059 \ln[(432 - T)/432] \text{ cal/gK}, 110^\circ\text{C} < T < 157.4^\circ\text{C}$$

$$c_p = 0.0787 - 0.0077 \ln[(432 - T)/432] \text{ cal/gK}, 156.5^\circ\text{C} < T < 158.9^\circ\text{C}$$

The heat and entropy of transition are given as 0.108 cal/mol and 0.25 cal/mol K respectively. No quantitative estimate of the accuracy of the fits is presented, but the graphical display of data points versus fitted curve is impressive. Estimates of the accuracy of the experimental data is not made explicitly. However the authors convey the impression that they consider the data accurate to only a few percent, since they regard a 2% difference between c_p and c_v as negligible and employ an approximation good to 1% to calculate the transition entropy. The authors state that care has been exercised to eliminate thermal gradients and mechanical stresses, but do not comment on electrical boundary conditions.

Keve, Abrahams, Nassau and Glass (Ref. 2-14) report their measurements of the specific heat of terbium molybdate in arbitrary units. Quantitative estimates of the transition heat (38 cal/mol) and transition entropy (0.23 cal/mol K) are obtained by setting the magnitude of the specific heat of TMO at 100°C to the same value that Fouskova (Ref. 2-30) reported for GMO at that temperature. The qualitative temperature dependence of the specific heat differs from the reports of Fouskova (Ref. 2-30) and Cheung and Ullman (Ref. 2-31) in that the sharp peak in the specific heat at the transition temperature has an appreciable tail extending some 5 to 10 K into the high temperature phase. We regard the quantitative estimates as plausible and ascribe the qualitative discrepancy to an experimental artifact. Such an assesement merits explanation. First, the high temperature tail on the specific heat is not due to any gross inhomogeneities in the sample since there is no similar tailing in the pyroelectric coefficient (nor the dielectric constant and birefringence). There probably are inhomogeneities rounding out the measured values in the vicinity of the phase transition but

these probably extend over a range of 1 or 2 K. Second, just such a tailing effect can be produced by the inertia of the measuring apparatus during a scan with increasing temperature (measuring specific heat while heating is the standard experimental procedure). Thus this entire high temperature tail should be associated with the peak at the phase transition. From this interpretation it is also clear that the heat and entropy of transition can give reasonable values even though some of the contribution to them is shifted a few degrees towards higher temperatures. No estimate of the accuracy of the measurements is given. Neither the elastic nor the electrical boundary conditions are mentioned.

For the specific heats of rare-earth molybdates then, the reported measurements are in general agreement and have qualitatively the expected behavior. No attempt has been made to fit the measurements to the temperature dependence expected for an improper ferroelectric.

2.2 Theory

In this section the complete thermodynamic potential which describes the phase transition in the rare-earth molybdates is examined in detail. After reducing out the mechanical strains and introducing some reasonable approximations, expressions for the temperature dependence of the pyroelectric coefficient, dielectric constant and specific heat are derived. These expressions are subsequently compared with experimental results and found to be in excellent agreement.

2.2.1 Complete Thermodynamic Potential

The experimental determination of the space groups of both the paraelectric phase $D_{2d}^3(P\bar{4}2_1m)$ and the ferroelectric phase $C_{2v}^8(Pba2)$ in gadolinium molybdate allow the unequivocal determination of the form of the thermodynamic potential associated with the ferroelectric phase transition in the molybdates:

$$\begin{aligned} \Phi(q_1, q_2, P, u) = & \Phi_0(T) + \frac{\alpha(T)}{2} (q_1^2 + q_2^2) + \frac{\tilde{\beta}_1}{4} (2q_1q_2)^2 + \frac{\tilde{\beta}_2}{4} (q_1^2 - q_2^2)^2 \\ & + \frac{\tilde{\beta}_3}{4} (2q_1q_2)(q_1^2 - q_2^2) + \frac{\gamma_1}{6} (2q_1q_2)^2 (q_1^2 + q_2^2) \\ & + \frac{\gamma_2}{6} (q_1^2 - q_2^2)^2 (q_1^2 + q_2^2) + \frac{\gamma_3}{6} (2q_1q_2)(q_1^2 - q_2^2)(q_1^2 + q_2^2) \\ & + \frac{1}{2} \chi^{-1} P_z^2 + \frac{1}{2} C_{66} u_{xy}^2 + \frac{1}{2} C_{11} (u_{xx}^2 + u_{yy}^2) \\ & + \frac{1}{2} C_{33} u_{zz}^2 + C_{12} u_{xx} u_{yy} + C_{13} (u_{xx} + u_{yy}) u_{zz} \\ & + \tilde{a}_1 P_z (2q_1q_2) + \tilde{a}_2 P_z (q_1^2 - q_2^2) + d P_z u_{xy} \\ & + b_1 u_{xy} (2q_1q_2) + b_2 u_{xy} (q_1^2 - q_2^2) \\ & + b_4 u_{zz} (q_1^2 + q_2^2) + b_3 (u_{xx} + u_{yy}) (q_1^2 + q_2^2) \\ & - P_z E_z - \sigma_{xy} u_{xy} - \sigma_{xx} u_{xx} - \sigma_{yy} u_{yy} - \sigma_{zz} u_{zz}. \end{aligned}$$

where, (q_1, q_2) = two component order parameter describing the soft mode, P_z = component of the polarization along the ferroelectric z axis, E_z = component of the electric field along the z axis, u_{ij} = components of the strain tensor, and σ_{ij} = components of the stress tensor. The coefficients $\tilde{\beta}_1, \tilde{\beta}_2, \tilde{\beta}_3, \gamma_1, \gamma_2, \gamma_3, \chi^{-1}, d, c_{ij}, \tilde{a}_1, \tilde{a}_2, b_1, b_2, b_3$, and b_4 are all taken to be temperature independent, while the coefficient $\alpha = \alpha_0(T-T_0)$ is taken to have a linear temperature dependence. The thermodynamic potential is written in this form to emphasize the fact that the polarization and strain couple to two independent quantities which are quadratic in the order parameter, to wit $2q_1q_2$ and $q_1^2 - q_2^2$.

(1) Physical Interpretation of Terms in Thermodynamic Potential

The physical meaning of the various terms becomes apparent when one considers some special cases. The terms with coefficients $\tilde{\alpha}(T), \tilde{\beta}_1, \tilde{\beta}_2, \tilde{\beta}_3, \gamma_1, \gamma_2, \gamma_3$, describe the temperature dependence of the soft mode if the other displacements (strain u_{ij} and polarization P) were held constant. These terms would then describe a phase transition for the soft mode which is either first or second order depending on the sign of the $\tilde{\beta}$'s. The term with coefficient χ^{-1} describes the behavior of the polarization if the other displacements (strain u_{ij} and soft mode q_1, q_2) were held constant. In such a case the system would have a temperature independent electric susceptibility of χ . Similarly the terms with coefficients c_{ij} describe the behavior of the various strain components if the other displacements (polarization, P , and soft mode amplitude, q_1, q_2) were held constant. In such a case these terms would yield temperature independent elastic constants.

In most realizable experiments, it is not the displacements but rather the conjugate forces which are held constant. The force conjugate to the polarization is just the applied electric field and the forces conjugate to the strain components are just the corresponding stresses. However, the force conjugate to the

soft mode amplitude usually goes unnamed since there is no way to realize experimentally any value other than zero for this force. In describing the usual experiments performed with constant forces, one must take into account the couplings amongst the displacements. The terms with coefficient \tilde{a}_1 and \tilde{a}_2 describe the direct interaction of the soft mode with the polarization, while the terms with coefficients b_1 , b_2 , b_3 and b_4 describe the coupling of the soft mode and the various strain components. These terms are the lowest order interactions allowed by crystallographic symmetry; they are quadratic in the soft mode amplitude and linear in the polarization and strains. As the soft mode goes through its phase transition, these terms give rise to a spontaneous polarization and a spontaneous elastic distortion as well as introducing a temperature dependence in the dielectric susceptibility and elastic constants. Finally the usual bilinear piezoelectric coupling between the polarization P_z and the strain u_{xy} is given by the term with coefficient \tilde{d} .

Since the phase transition in the molybdates is caused by an instability in the soft mode, it is usual to regard the interaction terms as describing how the phase transition in the soft mode transmits its effect to the polarization and strains thereby causing a spontaneous polarization and elastic distortion. However, these coupling terms also mediate the effect of the polarization and strain (or their conjugate forces: electric field and stress) back on the soft mode itself.

(2) Estimates of Magnitudes

It is difficult to make general statements about the relative magnitudes of the various terms, since the usual experiments performed with constant forces give information only about various combinations of the terms. However, there is one experiment, viz., the high frequency dielectric permittivity, which corresponds to a constant displacement (strain). This enables one to directly assess the magnitude of the coefficients \tilde{a}_1 , and \tilde{a}_2 . The observation that the high frequency dielectric constant for the

rare-earth molybdates does not vary with temperature means that when the strain is held constant the polarization is essentially decoupled from the soft mode, so that $\tilde{a}_1 \approx \tilde{a}_2 \approx 0$. Since the polarization has only very weak direct coupling to the soft mode, the observed spontaneous polarization and temperature dependent dielectric permittivity must arise indirectly from the soft mode coupling to the strain u_{xy} which in turn couples piezoelectrically to the polarization.

One aspect of the interaction of the soft mode and the strain can be learned from the observed large pressure dependence of the transition temperature (Ref. 2-28). This result implies that the isotropic strains, u_{xx} , u_{yy} and u_{zz} , are fairly strongly coupled to the soft modes.

2.2.2 Reduced Thermodynamic Potential

Since our experiments are performed under stress-free conditions, we need only a reduced thermodynamic potential describing the polarization and the soft mode. Using the zero stress conditions, $\partial\Phi/\partial u_{ij} = 0$ while $\sigma_{ij} = 0$, allows one to express the strains in terms of the polarization and soft mode amplitude:

$$u_{xy} = -c_{66}^{-1} [b_1(2q_1q_2) + b_2(q_1^2 - q_2^2)]$$

$$u_{xx} = -[(s_{11} + s_{12})b_3 + s_{13}b_4](q_1^2 + q_2^2)$$

$$u_{yy} = -[(s_{11} + s_{12})b_3 + s_{13}b_4](q_1^2 + q_2^2)$$

$$u_{zz} = -[2s_{13}b_3 + s_{33}b_4](q_1^2 + q_2^2)$$

where, s_{ij} is the inverse of the matrix c_{ij} .

Inserting these into the complete thermodynamic potential yields the reduced thermodynamic potential corresponding to conditions of zero stress,

$$\begin{aligned}\Phi(q_1, q_2, P, T) = & \Phi_0(T) + \frac{\alpha(T)}{2} (q_1^2 + q_2^2) + \frac{\beta_1}{4} (2q_1 q_2)^2 + \frac{\beta_2}{4} (q_1^2 - q_2^2)^2 \\ & + \frac{\beta_3}{4} (2q_1 q_2) (q_1^2 - q_2^2) + \frac{\gamma_1}{6} (2q_1 q_2)^2 (q_1^2 + q_2^2) \\ & + \frac{\gamma_2}{6} (q_1^2 - q_2^2)^2 (q_1^2 + q_2^2) + \frac{\gamma_3}{6} (2q_1 q_2) (q_1^2 - q_2^2) (q_1^2 + q_2^2) \\ & + \frac{\chi^{-1}}{2} P^2 + a_1 P (2q_1 q_2) + a_2 P (q_1^2 - q_2^2) - PE\end{aligned}$$

where,

$$\begin{aligned}a_1 &= \tilde{a}_1 - db_1/c_{66} \\ a_2 &= \tilde{a}_2 - db_2/c_{66} \\ \beta_1 &= \tilde{\beta}_1 - 2b_1^2/c_{66} - 4(s_{11} + s_{12})b_3^2 - 8s_{13}b_3b_4 - 2s_{33}b_4^2 \\ \beta_2 &= \tilde{\beta}_2 - 2b_2^2/c_{66} - 4(s_{11} + s_{12})b_3^2 - 8s_{13}b_3b_4 - 2s_{33}b_4^2 \\ \beta_3 &= \tilde{\beta}_3 - 2b_1b_2/c_{66}\end{aligned}$$

It is important to remember that the interaction terms between the polarization and the soft mode amplitude give the effective coupling under stress-free conditions. Since we know that the direct interaction between the polarization and the soft mode is essentially negligible, the physical origin of this coupling lies in the piezoelectric coupling of the polarization to the strain which itself couples directly to the soft mode amplitude.

2.2.3 Approximation to Reduced Thermodynamic Potential

Even the reduced thermodynamic potential does not yield simple analytic expressions to compare with the measured temperature dependence of the polarization, dielectric permittivity and specific heat. However, as noted in Par. 2.1 a variety of apparently different approximations do yield analytic expressions which compare well with experiment. The common thread in all these approximations is that the phase angle $\phi = \arctan (q_1/q_2)$ is temperature independent. In this section we show why such an approximation is plausible.

As a first step it is convenient to express the thermodynamic potential in polar coordinates ($q_1 = \eta \cos \phi$, $q_2 = \eta \sin \phi$),

$$\begin{aligned} \Phi(\eta, \phi, P, T) = & \Phi_0(T) + \frac{\alpha(T)}{2} \eta^2 + [(\beta_1 + \beta_2) + (\beta_2 - \beta_1) \cos 4\phi \\ & + \beta_3 \sin 4\phi] \frac{\eta^4}{8} + [(\gamma_1 + \gamma_2) + (\gamma_2 - \gamma_1) \cos 4\phi + \gamma_3 \sin 4\phi] \frac{\eta^6}{12} \\ & + \frac{\chi^{-1}}{2} P^2 + P(a_1 \sin 2\phi + a_2 \cos 2\phi) \eta^2 - PE \end{aligned}$$

The polarization can be reduced out of this thermodynamic potential using the condition, $\partial \Phi / \partial P = 0$ to give the polarization in terms of the soft mode,

$$P = \chi \{ E - \eta^2 (a_1 \sin 2\phi + a_2 \cos 2\phi) \}$$

and yield the reduced thermodynamic potential involving only the soft mode,

$$\begin{aligned} \Phi(\eta, \phi, T) = & \Phi_0 + \frac{\eta^2}{2} [\alpha(T) + 2\chi E(a_1 \sin \phi + a_2 \cos \phi)] \\ & + \frac{\eta^4}{4} (f + g \cos 4\phi + h \sin 4\phi) \\ & + \frac{\eta^6}{12} [(\gamma_1 + \gamma_2) + (\gamma_2 - \gamma_1) \cos 4\phi + \gamma_3 \sin 4\phi] \\ & - \chi E^2 / 2 \end{aligned}$$

where

$$f = (1/2)(\beta_1 + \beta_2) - (a_1^2 + a_2^2)\chi$$

$$g = (1/2)(\beta_2 - \beta_1) + (a_1^2 + a_2^2)\chi$$

$$h = (1/2)\beta_3 - 2a_1a_2\chi$$

To determine the behavior of the soft mode amplitude one need only solve the equations $\partial\phi/\partial\phi = 0$ and $\partial\phi/\partial\eta = 0$ for $\eta(T)$ and $\phi(T)$. These equations take the form:

$$\eta^2 \left\{ \begin{aligned} &\eta^4[(\gamma_2 - \gamma_1)\sin 4\phi - \gamma_3\cos 4\phi]/3 \\ &+ \eta^2[g\sin 4\phi - h\cos 4\phi] + \\ &+ 2\chi E[a_1\cos 2\phi + a_2\sin 2\phi] \end{aligned} \right\} = 0$$

and

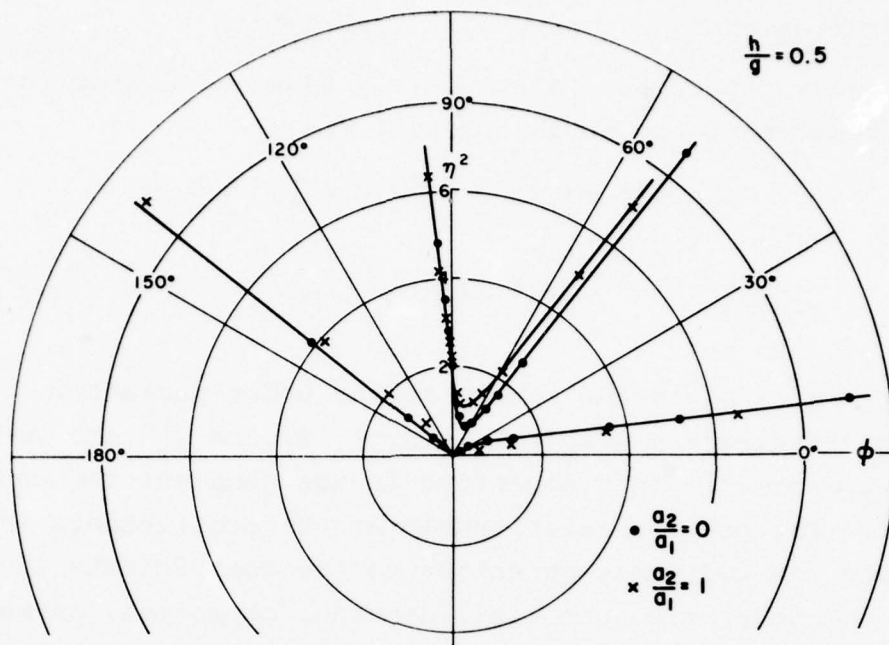
$$\eta \left\{ \begin{aligned} &\eta^4[(\gamma_1 + \gamma_2) + (\gamma_2 - \gamma_1)\cos 4\phi + \gamma_3\sin 4\phi]/2 \\ &+ \eta^2[f + g\cos 4\phi + h\sin 4\phi] \\ &+ \alpha(T) + 2\chi E[a_1\sin 2\phi + a_2\cos 2\phi] \end{aligned} \right\} = 0$$

For the solution to these equations to be a minimum of ϕ , one

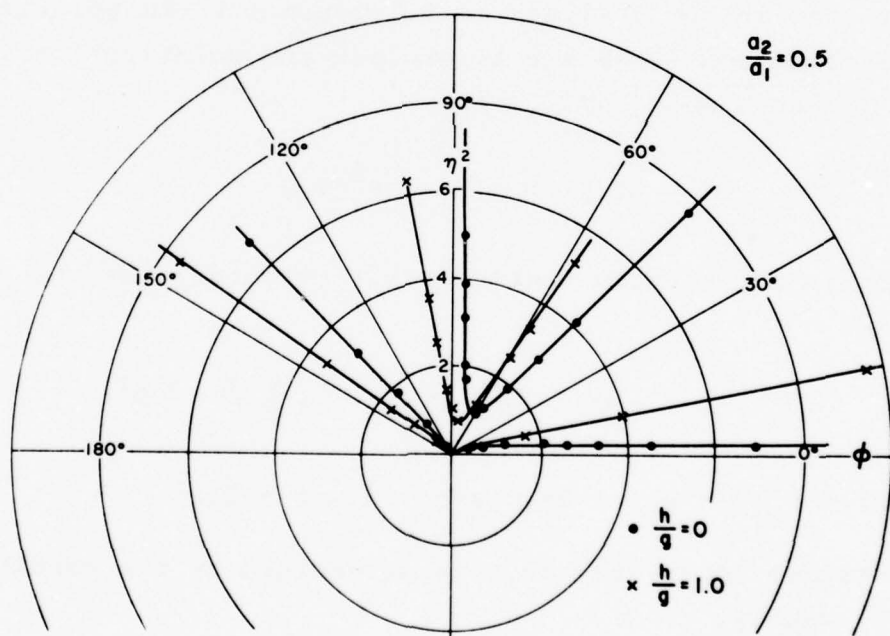
must also have that $\frac{\partial^2\phi}{\partial\phi^2} > 0$ and $\frac{\partial^2\phi}{\partial\eta^2} > 0$, since $\frac{\partial^2\phi}{\partial\phi\partial\eta} = 0$ at all extrema.

While detailed solutions to these equations require numerical computation, some general characteristics of the solutions can be discerned immediately. The first equation does not involve the temperature dependent coefficient $\alpha(T)$; the solution to this equation then gives the locus of points in the η - ϕ plane which are minima of ϕ . The temperature dependence of the actual minimum is determined by the solution to the second equation which involves $\alpha(T)$ explicitly. Thus the minimum of ϕ moves along the curve determined by the first equation at a rate determined by the second equation. To illustrate

the possible behaviors we have plotted in Figure 1a and 1b the solution to the first temperature-independent equation for a variety of values of the parameters ($\dot{\gamma}_1 = \gamma_2$ and $\gamma_3 = 0$ in all plots shown). These curves illustrate the point that, except for small values of η , there is essentially no variation in the angle ϕ . It is thus plausible to neglect any explicit angular dependence at the very onset.



(a)



(b)

Figure 1. The loci of minima for reduced thermodynamic potential involving only soft mode. These plots are for an isotropic sixth order term, $2\chi E(a_1/h) = 1$, and indicated anisotropies in second and fourth order terms.

2.2.4 Expressions to Compare with Experiments

If the angular dependence is completely eliminated from the reduced thermodynamic potential one obtains:

$$\begin{aligned}\Phi(\eta, P, T) = & \Phi_0(T) + \frac{\alpha(T)}{2} \eta^2 + \frac{\beta}{4} \eta^4 + \frac{\gamma}{6} \eta^6 \\ & + aP\eta^2 + \frac{\chi^{-1}}{2} P^2 - PE\end{aligned}$$

where, $\eta^2 = q_1^2 + q_2^2$ is the square of the order parameter and the coefficients $\alpha = \alpha_0(T - T_0)$, β , γ , a , and χ^{-1} are related to the coefficients appearing in the complete thermodynamic potential. The precise relationship of the coefficients in this approximate thermodynamic potential to the coefficients in the complete thermodynamic potential, depends, of course, on which approximation is adopted. We fit all of our experimental data to this form for the thermodynamic potential.

The first step in the analysis is to reduce out the polarization using the condition $\partial\Phi/\partial P = 0$ to express the polarization in terms of the soft mode amplitude,

$$P(T, E) = \chi[E - a\eta^2(T, E)]$$

and to obtain the reduced thermodynamic potential for the soft mode alone:

$$\Phi(\eta) = \Phi_0(T) + \frac{\alpha(T)}{2} \eta^2 + \frac{\beta}{4} \eta^4 + \frac{\gamma}{6} \eta^6 - \frac{\chi}{2} E^2$$

where $\alpha(T) = \alpha_0(T - T_0) + 2a\chi E$ and $\beta = \beta - 2\chi a^2$.

The temperature dependence of η is determined by the condition $\partial\Phi/\partial\eta = 0$, namely,

$$\eta[\alpha(T) + \beta\eta^2 + \gamma\eta^4] = 0.$$

We thus obtain explicitly the solution,

$$\eta^2(T, E) = \begin{cases} -\frac{\beta}{2\gamma} + \left(\frac{\alpha_0}{\gamma}\right)^{1/2} [T_1(E) - T]^{1/2} & T < T_c(E) \\ 0 & T > T_c(E) \end{cases}$$

where

$$T_1(E) = T_0 - \frac{2a\chi}{\alpha_0} E + \frac{\beta^2}{4\alpha_0\gamma}$$

and

$$T_c(E) = T_0 - \frac{2a\chi}{\alpha_0} E + \frac{3}{16} \frac{\beta^2}{\alpha_0\gamma}.$$

We have assumed in this solution that $\beta < 0$ so that a first order transition occurs at T_c , which is always less than T_1 .

The polarization is then,

$$P(T, E) = \begin{cases} P_1 + K(T_1 - T)^{1/2} & T < T_c \\ \chi E & T > T_c \end{cases}$$

where

$$P_1(E) = (\chi E - \frac{\chi a \beta}{2\gamma})$$

$$K = -a\chi \left(\frac{\alpha_0}{\gamma}\right)^{1/2}$$

Evidently the effect of an external electric field is merely to shift the transition temperature; it does not cause any smoothing of the discontinuities as occurs in a proper ferroelectric.

The pyroelectric coefficient is obtained by simply differentiating with the respect to T , to give

$$p(T,E) = \begin{cases} \frac{K}{2} (T_1 - T)^{-1/2} & T < T_c \\ 0 & T > T_c \end{cases}$$

A singularity in the measurements at the transition temperature is caused by the discontinuous jump in the polarization.

Similarly the dielectric constant is obtained by differentiating the polarization with respect to E , to give

$$\epsilon(T,E) = \begin{cases} 1 + \chi + K_1 (T_1 - T)^{-1/2} & T < T_c \\ 1 + \chi & T > T_c \end{cases}$$

where

$$K_1 = a^2 \chi / \alpha_o^{1/2} \gamma^{1/2}$$

Since T_c is always less than T_1 , there is no divergence in the dielectric constant, only a step discontinuity at the transition.

To find the specific heat, one must first derive the entropy from the thermodynamic potential,

$$S(\eta, P, T) = - \frac{\partial \Phi}{\partial T} [\eta, P, T] = - \frac{\partial \Phi_o}{\partial T} - \frac{2 \eta^2}{2}$$

and then differentiate to obtain the specific heat,

$$c(E, T) = T \frac{\partial S}{\partial T} (T, E) = T \frac{\partial S}{\partial T} [\eta(T, E), P(T, E), T]$$

$$c(T, E) = \begin{cases} c_o(T) + K_2 T [T_1 - T]^{-1/2} & T < T_c \\ c_o(T) & T > T_c \end{cases}$$

where

$$K_2 = \alpha_o^{3/2} / 4\gamma = K^2 / 4K_1$$

$$c_o(T) = T \frac{\partial^2 \phi_o}{\partial T^2}.$$

Here $c_o(T)$ is the other contribution to the specific heat and is assumed to vary only slowly with temperature.

2.3 Dielectric, Pyroelectric and Thermal Measurements

This section describes measurements of the dielectric constant ϵ , pyroelectric coefficient p , and specific heat c as functions of temperature performed on gadolinium molybdate (GMO), terbium molybdate (TMO) and gadolinium dysprosium molybdate (GDMO). The effect of an applied electric field on the dielectric properties is also investigated.

2.3.1 Sample Preparation

Thin slices of GMO, TMO, and GDMO were cut from single crystals normal to the pyroelectric axis. Samples were polished to thicknesses from 0.03 to 0.1 mm and electroded on both faces with evaporated antimony. In order to minimize edge effects, a special technique was used to obtain fully electroded samples. The technique is based on the observations that in GMO the ferroelastic domain boundaries consist of (110) and ($1\bar{1}0$) crystallographic planes which are also cleavage planes (Ref. 2-22). (We have confirmed that these observations apply to TMO and GDMO as well.) Samples were prepared using the following procedure: (1) identify (110) and ($1\bar{1}0$) planes by visual observation of the domain pattern through crossed polarizers, (2) evaporate electrodes, and (3) remove unelectroded regions by cleaving along (110) and ($1\bar{1}0$) planes. After preparation, samples were mounted freely on 3 mil diameter silver leads. Before each measurement samples were poled with a steady field of ~ 5 kV/cm applied during slow cooling through the Curie point and down to room temperature.

2.3.2 Dielectric Constant

(1) Experimental Apparatus

The dielectric constant was measured by determining the ratio of the capacitance of a sample to that of a reference capacitor placed in series with it. A small ac signal (at most 10 V/cm at 8 kHz) was applied to the sample and reference, and synchronous detection (i.e., a lock-in amplifier) was used to measure the voltage appearing across the reference capacitor. Measurements were made in the oven of a Deltatherm III differential thermal analyzer (DTA) which had been modified to provide additional feed-throughs and connections for the sample and thermocouple. To achieve good temperature uniformity, the sample was enclosed in a closed copper cylinder filled with inert gas (helium). A chromel-alumel thermocouple was used, and the thermocouple tip placed with 1 mm of the sample surface to ensure accurate temperature measurements. By connecting the outputs of the lock-in amplifier and thermocouple to an x-y recorder, we obtained continuous recordings of the dielectric constant as a function of temperature.

The capacitance of the reference was measured with an accuracy of 2%, and the sample dimensions determined to within 5%, so that the dielectric constant was obtained with an accuracy of better than 10%.

A second, completely independent, experimental apparatus was used to cross-check the measurements. This second apparatus employed a Boonton capacitance meter at 1 MHz and a Hewlett Packard 4270A capacitance bridge at 1 kHz, 10 kHz, 100 kHz and 1 MHz. The test signals for these instruments were less than 100 mV. In all cases the experimental data for both apparatuses agreed within better than 10%.

(2) Results of Measurements

The dielectric constants measured on samples prepared as described above are shown in Figure 2. The results for GMO and TMO are in general agreement with those reported by other investigators, although we obtain values consistently somewhat smaller than those reported elsewhere. The behavior of GDMO is very similar to that of the other two materials. No effect of applied electric field on the dielectric constant could be observed in any of these materials for fields up to 10 kV/cm.

2.3.3 Pyroelectric Coefficient

(1) Byer-Roundy Apparatus

The pyroelectric coefficient was measured by the direct technique of Byer and Roundy (Ref. 2-32), in which the crystal was connected to a microvolt ammeter (Keithley, Model 150B) and heated slowly at a constant rate, typically 2°C/min. The pyroelectric current produced by the sample was recorded directly as a function of temperature using an x-y recorder and the sample temperature was recorded separately as a function of time. The same samples and oven were used as for the dielectric constant measurements.

The major source of error in these measurements is nonlinearity of the sample temperature as a function of time. The measurements were repeated several times, and we were able in general to achieve a heating rate which was constant to better than 5%. On the few occasions when larger variations occurred they were taken into account by correcting the experimental data.

A second, completely independent, Byer-Roundy apparatus was used to cross-check these measurements. This second apparatus employed a Keithley 616 Digital Electrometer. In all cases the results of both apparatus agreed well within the experimental errors.

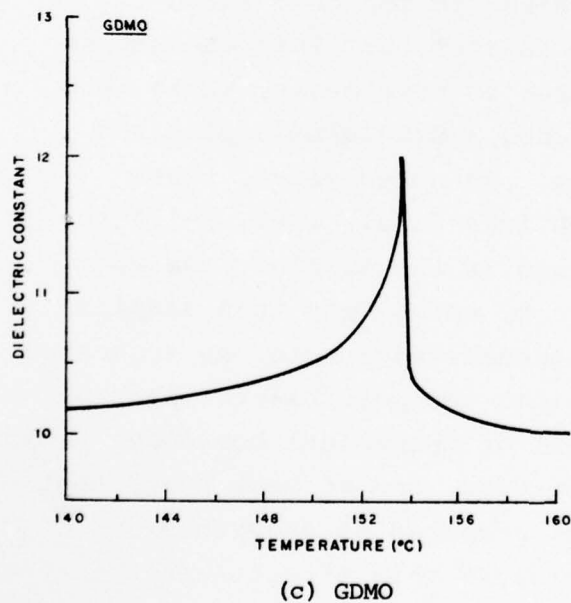
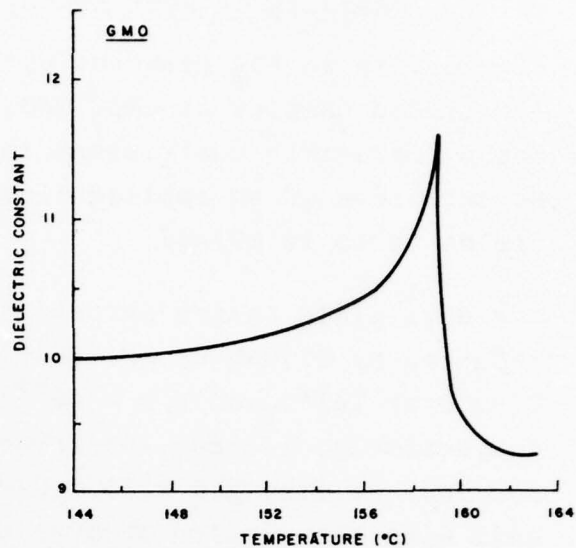
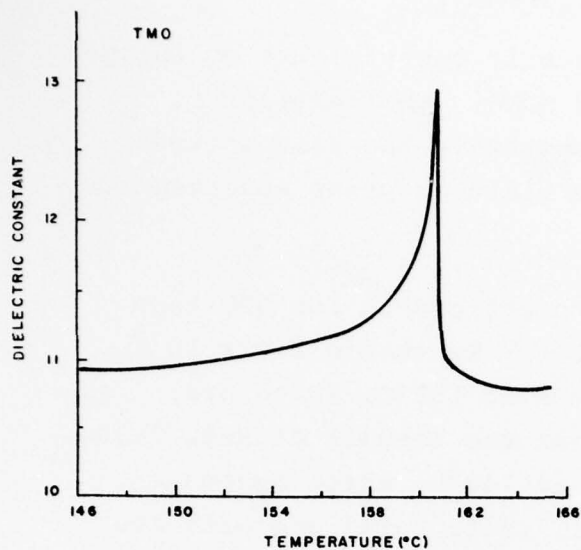


Figure 2. Dielectric constant vs. temperature for (a) terbium molybdate, (b) gadolinium molybdate, and (c) gadolinium-dysprosium molybdate.

(2) Results of Byer-Roundy Measurements

Figure 3 shows the measured pyroelectric coefficients of fully-electroded samples of GMO, TMO, and GDMO. The behavior of the pyroelectric coefficient is essentially the same in each. No influence of an applied electric field on p was observed for fields up to 10 kV/cm.

Our data yield larger pyroelectric coefficients for GMO than reported by Ullman et al. (Ref. 2-10). We obtain 2.0×10^{-9} C/cm²K at 143°C and 2.8×10^{-9} C/cm²K at 151°C, which are, respectively, 50% and 20% larger than the results of Ref. 2-10. For TMO, we find 1.8×10^{-9} C/cm²K at 140°C, which agrees well with the results of Keve et al. (Ref. 2-14) and with the value inferred from the dynamic measurements described below.

The importance of using fully-electroded samples when measuring the pyroelectric coefficient is demonstrated by the fact that partially-electroded samples exhibit multiple peaks in the pyroelectric current similar to those reported in Ref. 2-10. This structure is reproducible from run to run on a given sample, but varies from one sample to another. Thicker samples (100-200 μ m) frequently exhibit three or more peaks, while very thin samples (25-50 μ m) sometimes show a single main peak and one or more smaller, secondary ones. As noted above, these multiple peaks were attributed by Ullman et al. (Ref. 2-12) to the presence of temperature gradients in the samples. We were unable to eliminate this phenomenon by using very thin samples freely suspended in a strictly isothermal enclosure, as suggested in Ref. 2-12. This led us to consider the possibility that the multiple peaks are due to electrical or mechanical boundary conditions imposed by partial electrodes, and we have found that the use of fully-electroded samples prepared as described in Par. 2.3.1 greatly reduces or eliminates this effect. When full-surface electrodes are used, even samples several hundred microns in thickness show only a single current peak on both heating and cooling.

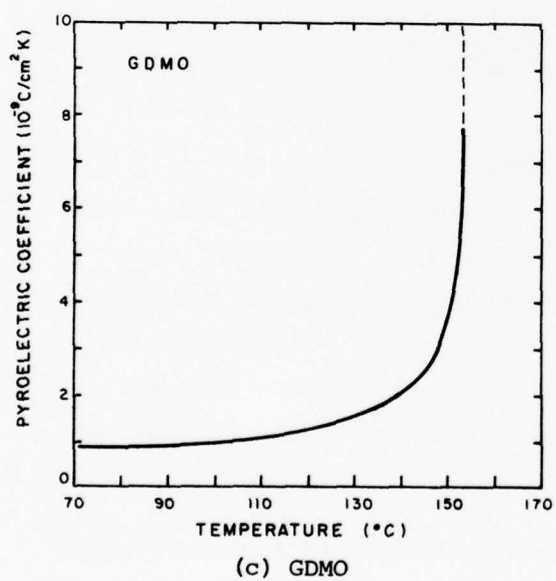
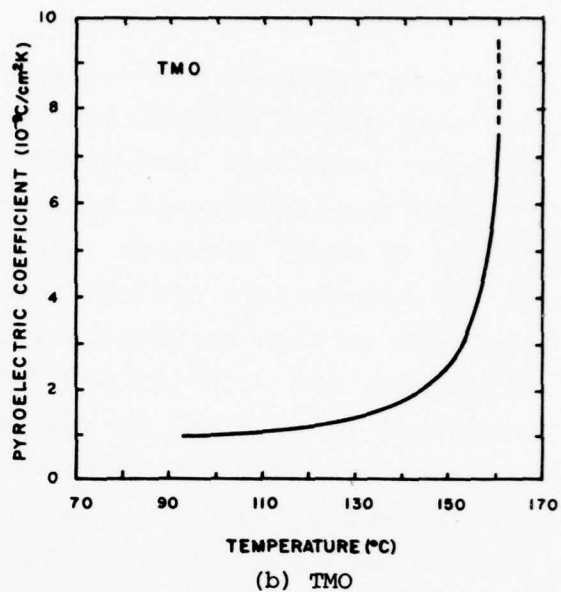
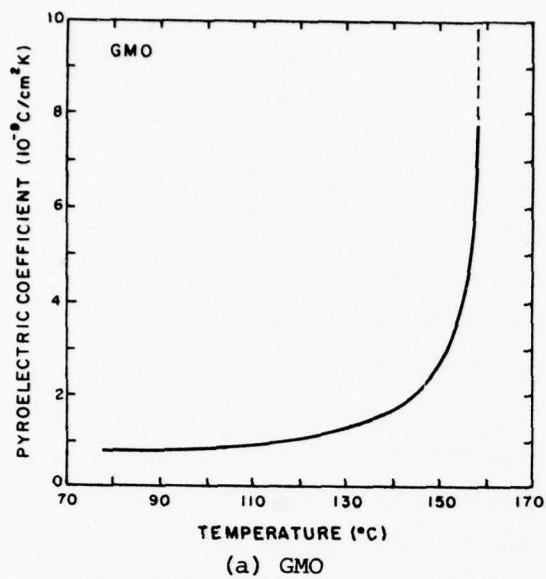


Figure 3. Measured pyroelectric coefficients of fully-electroded samples of GMO, TMO, and GDMO.

(3) Chynoweth Apparatus

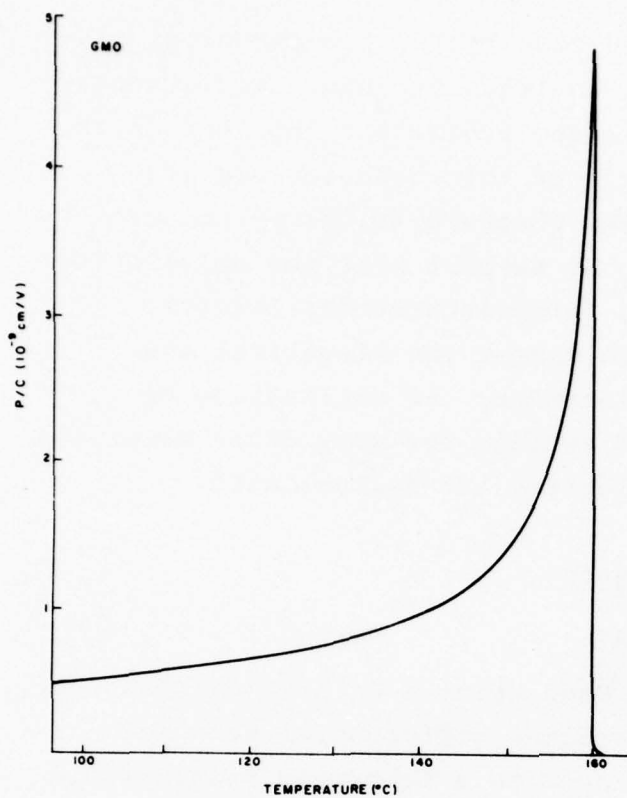
A second, independent measurement of the pyroelectric coefficient was obtained by determining the ratio p/c using the dynamic response technique introduced by Chynoweth (Ref. 2-33). The crystal was illuminated by a train of rectangular infrared pulses of short duration (typically 15 ms) so that the increase of its temperature did not exceed 0.01 K. The resulting pyroelectric voltage response was measured across a load resistor (typically $10^7 - 10^8 \Omega$) and FET source follower circuit connected in parallel to the sample (Ref. 2-34). The pyroelectric response voltages obtained were displayed on an oscilloscope, and the rms value of the voltage response was measured with a lock-in amplifier (Keithly Autolock 840). The outputs of the lock-in and thermocouple were recorded simultaneously on an x-y recorder.

This method yields relative, not absolute, values of p/c unless the radiation absorbed by the sample is known. It is not practical to measure the incident flux or sample absorption directly, so the system was calibrated by taking the values $p = 1.8 \times 10^{-9} \text{ C/cm}^2 \text{ K}$ and $c = 2.0 \text{ J/cm}^3 \text{ K}$ for TMO at 140°C .

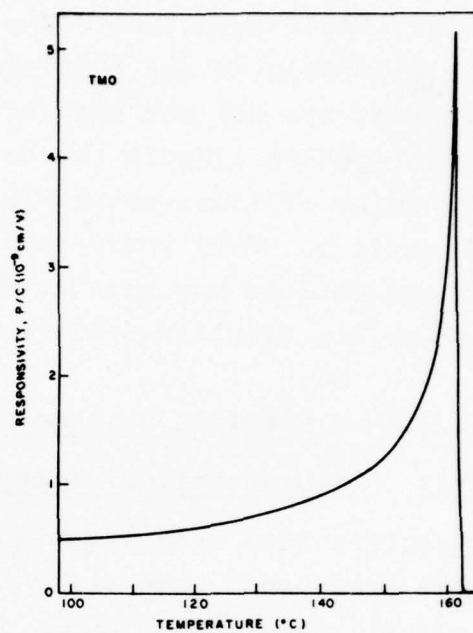
(4) Results of Chynoweth Measurements

The ratio p/c measured on fully-electroded samples of GMO, TMO, and GDMO is shown in Figure 4. It is readily seen that both the absolute magnitude and the temperature dependence of this ratio are very similar in the three materials. These results, taken together with the values of c reported in Par. 2.3.4, yield good agreement with the direct measurement of p reported above.

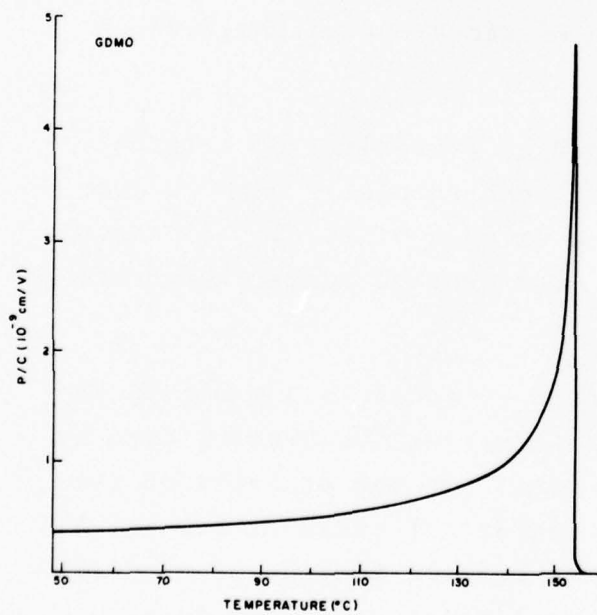
Effects due to the use of partially-electroded samples are also observable in the dynamic response measurements. Instead of the sharp maximum at the transition temperature reported above for



(a) GMO



(b) TMO



(c) GDMO

Figure 4. Ratio p/c for fully-electroded samples of GMO, TMO, and GDMO.

fully-electroded samples and predicted by the phenomenological theory (Section 4), we find that the response has a smaller peak than in the fully electroded case and exhibits a shoulder on the high-temperature side. The origin of this behavior and its relationship to the multiple peaks observed in the pyroelectric current are not yet understood. We suspect that the solution to this problem lies in the coupled ferroelectric-ferroelastic behavior of these materials which causes the electrical and elastic boundary conditions to interact. An explanation of these effects may also have implications for many other materials which are simultaneously ferroelectric and ferroelastic.

2.3.4 Specific Heat Measurements

(1) Description of Apparatus

Specific heat measurements were made using a dc heating technique. The instrument used was a Perkin-Elmer differential scanning calorimeter, Model DSC-2, interfaced to a Tektronix programmable calculator, Model 31. The system is equipped with an Autoscan Zero mini-computer for automatic baseline corrections. Single crystal samples, typically between 20 and 80 mg, were weighed with a precision of $1 (10^{-4})$ on a Perkin-Elmer autobalance, Model AD-2.

Open aluminum sample pans were used as crucibles; no external mechanical stresses were applied to the samples. Samples were flat plates about 1 mm thick and 3 mm on a side. In all cases, the flat side of the sample made good thermal contact with the crucible.

Typical data was taken using heating rates of 1.25 K/min in the vicinity of the phase transition. Lowering the heating rate by half did not effect the observed data. In the vicinity of the phase transition, data were recorded at intervals of 0.1 K. All reported data were taken during the heating portion of a cycle; the observations made during the cooling portion were in all cases superimposable on the heating curves to within 1%.

(2) Accuracy of Measurements

The calorimeter was calibrated relative to the melting point and the enthalpy of fusion of 5N indium metal; $T_M = 429.87$ K and $\Delta H_f = 3266.8$ J/mol, and of 6N lead metal; $T_M = 600.65$ K and $\Delta H_f = 4768.1$ J/mol. Both the melting points and the enthalpies of fusion were found to be independent of heating and cooling rates from 0.625 to 20 K/min and reproducible to 0.02% and 0.75%, respectively.

The raw data were further refined by normalization to the NBS values for sapphire (Ref. 2-35), corrected on a sapphire standard, run under the identical operating parameters.

The overall accuracy of the absolute value of the specific heats was better than 1%. Relative measurements on a single material are accurate to 0.25%.

(3) Results

The isobaric molar heat capacities in the vicinity of the ferroelectric phase transition of the three rare-earth molybdates are shown in Figures 5 to 7. The corresponding thermodynamic values are given in Table 1. The transition temperature is taken as the peak in the heat capacity. The heat of transition ΔH is obtained by graphical integration of the excess heat capacity.

The integration is performed by extrapolating a line from the heat capacity curve in the low temperature phase to a line in the high temperature phase. This is done over a temperature interval as small as 8 K in TMO and as large as 15 K in GDMO. The entropy of the transition is calculated by dividing ΔH by T_C . This assumes that the transition occurs over a small enough temperature interval so that the error in this approximation is minimal. Thus values of ΔH and ΔS are upper bounds on the true latent heat and entropy discontinuity at T_C as they contain contributions also from the rise in the specific heat just below the transition temperature.

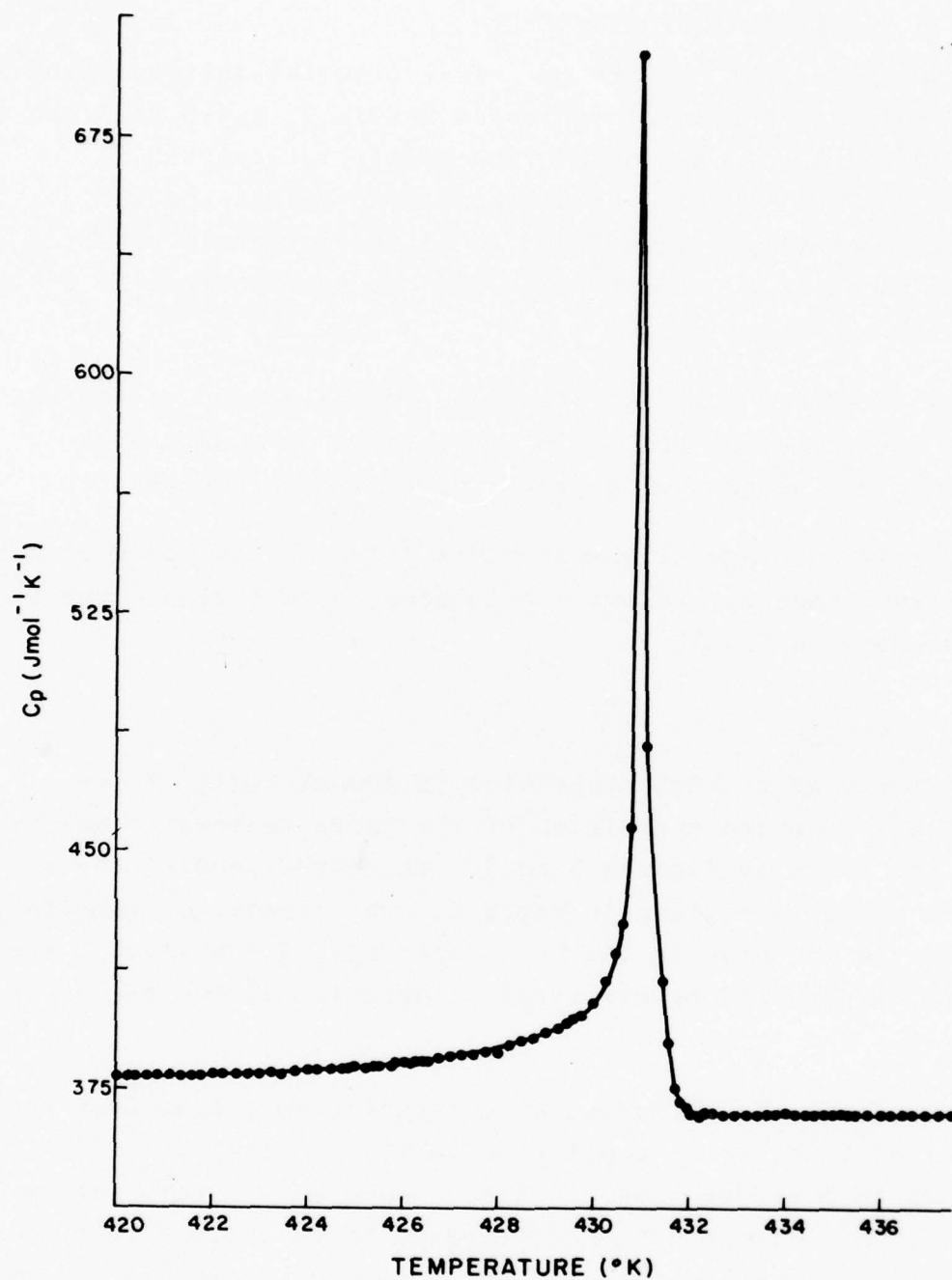


Figure 5. Specific heat vs. temperature for TMO sample exhibiting multiple peaks after annealing for 24 hours at 960°C.

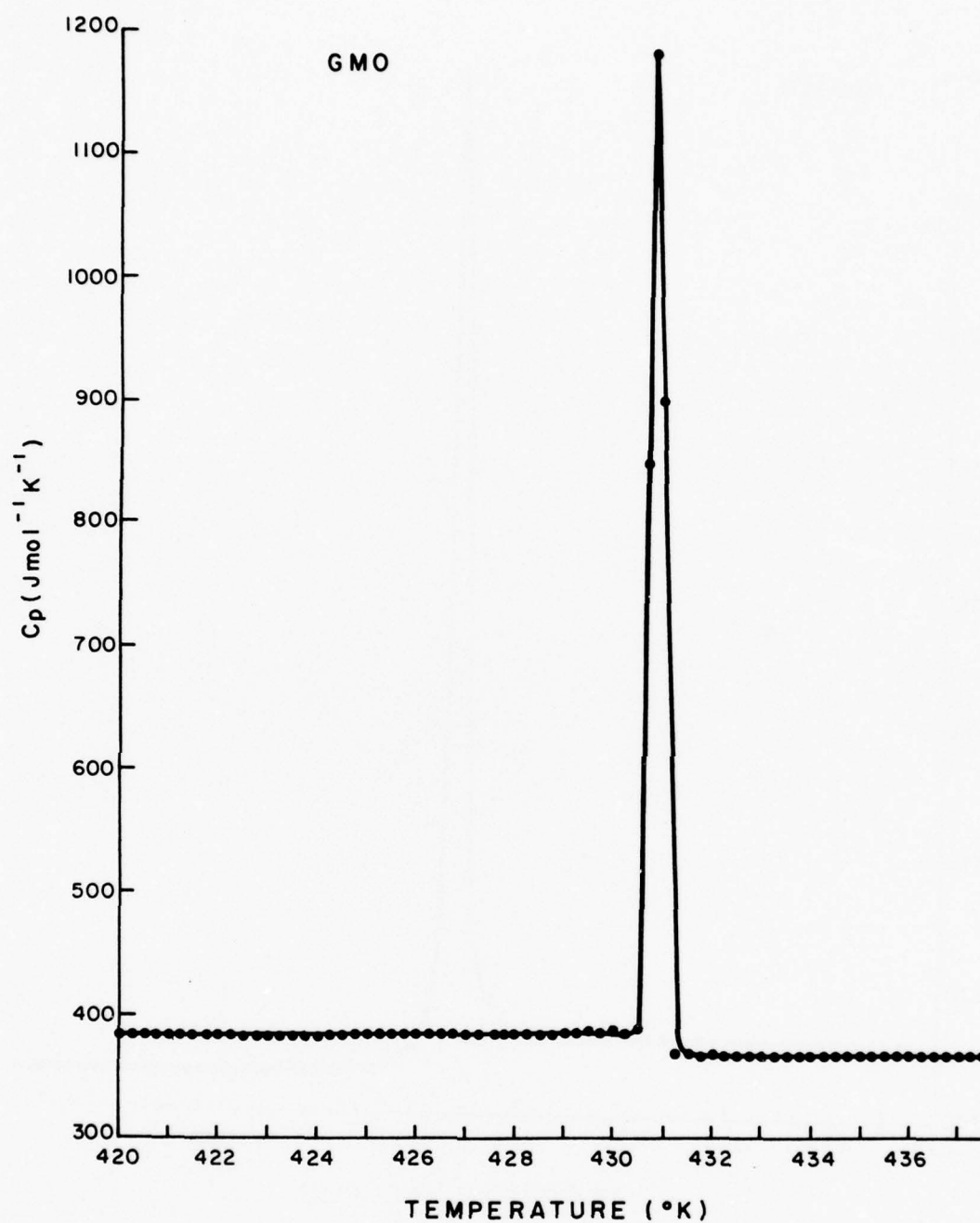


Figure 6. Isobaric molar heat capacity of GMO in the vicinity of the ferroelectric phase transition.

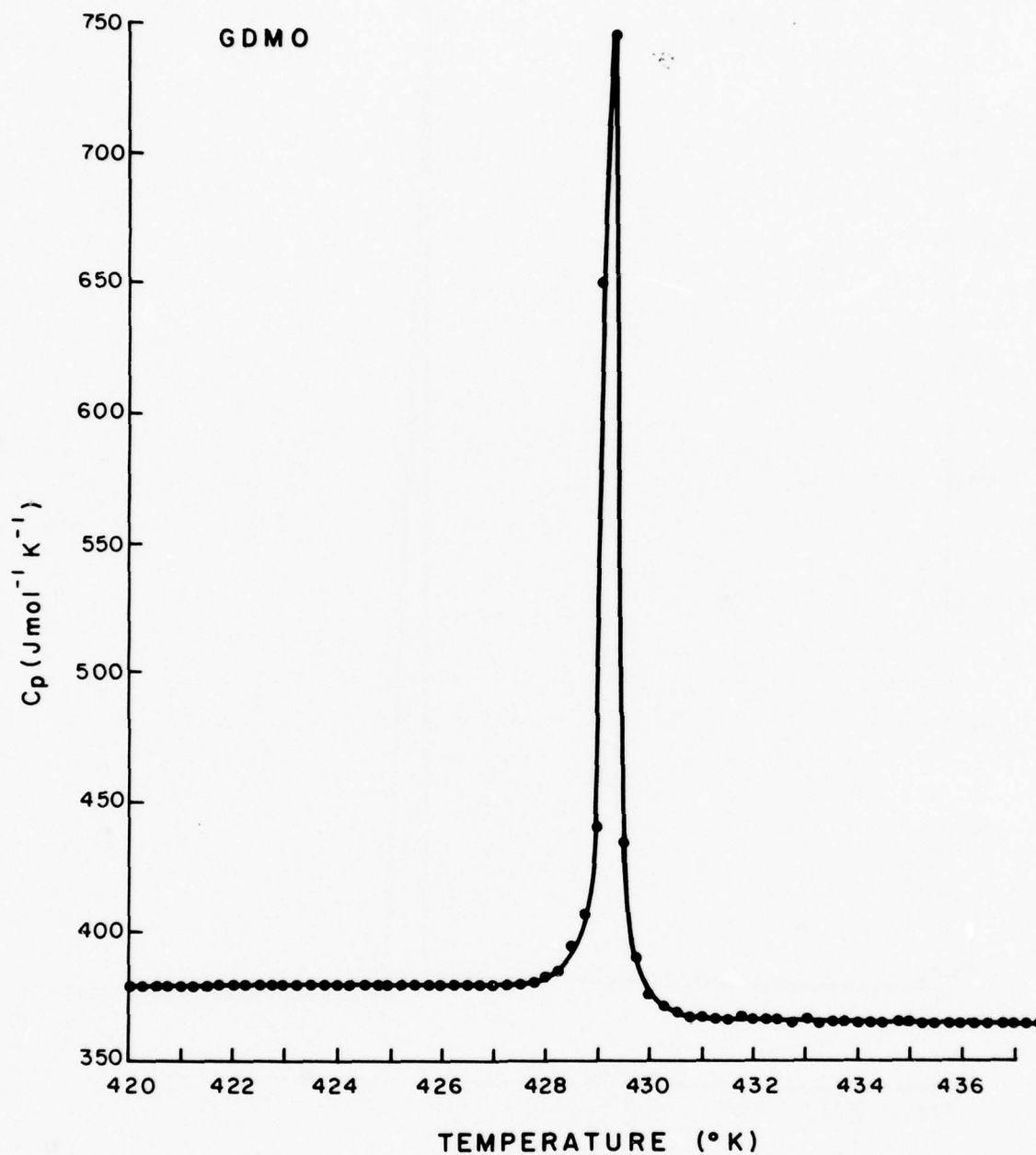


Figure 7. Isobaric molar heat capacity of GDMO in the vicinity of the ferroelectric phase transition.

TABLE 1. THERMODYNAMIC VALUES FOR THE FERROELECTRIC PHASE TRANSITION IN THE MOLYBDATES.

	T_c (K)	H (J/mol ⁻¹)	S (J/mol ⁻¹ K ⁻¹)	MW
TMO	431.7 \pm 0.2	255 \pm 26	0.59 \pm 0.06	797.66
GMO	430.8 \pm 0.2	304 \pm 30	0.71 \pm 0.07	794.31
GDMO	429.8 \pm 0.2	288 \pm 29	0.67 \pm 0.07	799.56

Two conclusions may be drawn from this data. First, the ferroelectric phase transition in the molybdates is strongly first order as evidenced by the large latent heat of transition and the sharp discontinuity in the heat capacity. Second, the position of the transition temperatures, the very similar heat capacities above and below the transition, and the similar heats of transition suggest that the effect of varying the rare-earth metal upon the crystal thermodynamics is quite small.

(4) Multiple Peaks in the Specific Heat of Rare-Earth Molybdates

In the measurements on the specific heats of rare-earth molybdates a number of samples exhibited multiple peaks in the specific heat near the phase transition (Fig. 8). Moreover, this phenomenon of multiple peaking can be induced in a sample by subjecting it to mechanical stresses (Fig. 9). The occurrence of multiple peaks is then interpreted to be caused by residual mechanical stresses in the samples. This interpretation is confirmed by annealing a sample which exhibited multiple peaks and noting the disappearance of the multiple peaks in the specific heat.

Three single crystal plates of TMO which exhibited multiple peaking of the heat capacity were wrapped in platinum foil and heated to 960°C in alumina crucibles under a flowing molecular oxygen atmosphere of 1.0 l/min. The temperature was maintained

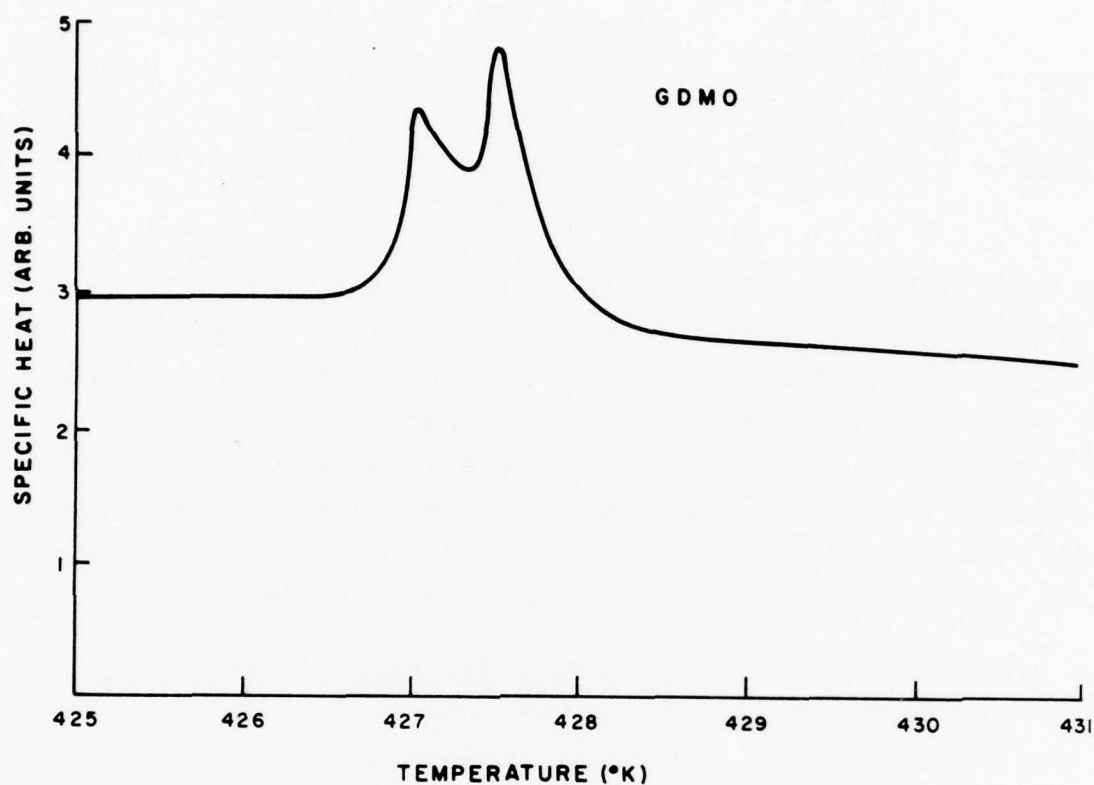


Figure 8. Specific heat of gadolinium dysprosium molybdate vs. temperature. This sample exhibits the phenomenon of multiple peaks at the transition.

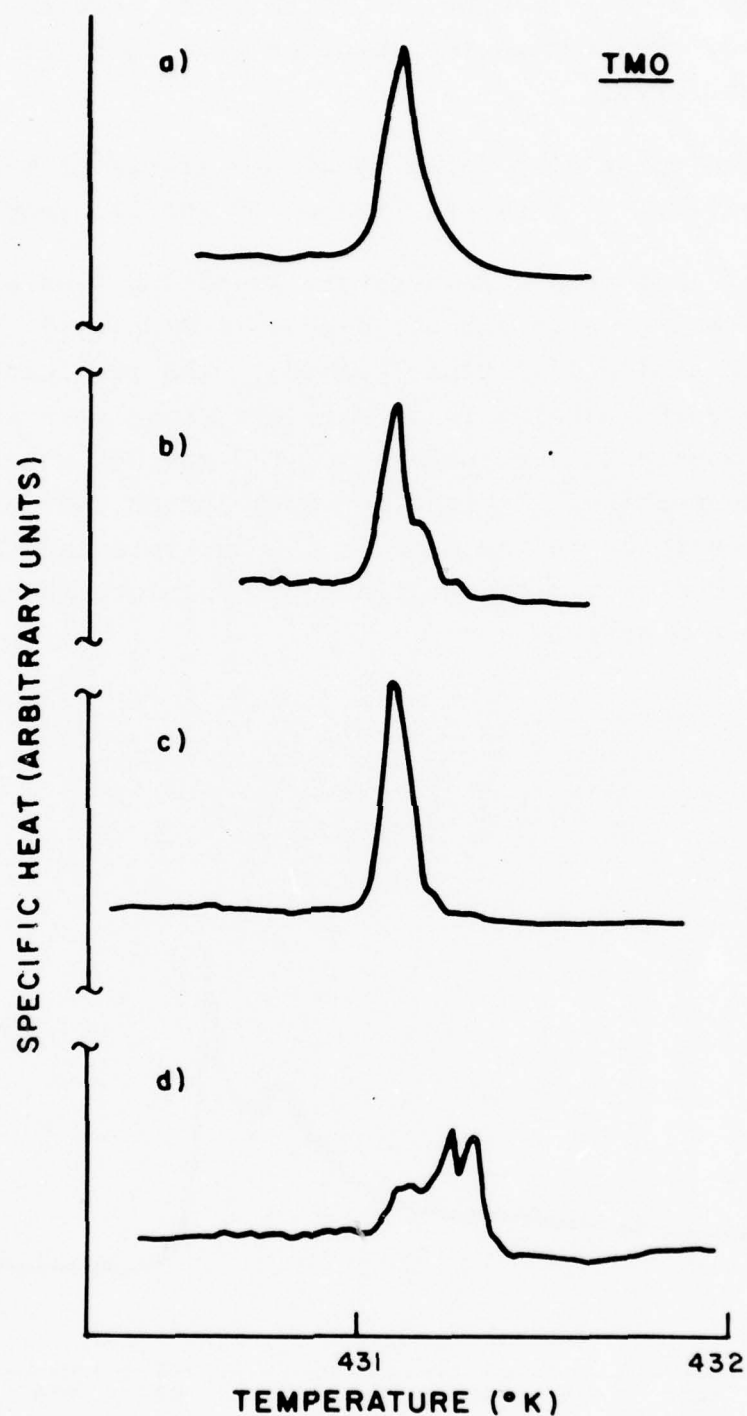


Figure 9. Specific heat of terbium molybdate vs. temperature following various mechanical processings: (a) initial scan, (b) after applying finger pressure for 5 sec., (c) after applying finger pressure for 5 sec more, (d) after pressing between two glass slides for 10 sec.

at $960^{\circ}\text{C} \pm 10^{\circ}\text{C}$ for 24 hours and cooled down to room temperature at a linear rate of 12°C/hr . Samples which were heated $1080 \pm 20^{\circ}\text{C}$ melted, even though the reported melting point for TMO is 1170°C (Ref. 2-36).

The measured molar heat capacity of one sample of TMO, before and after annealing, is shown in Figures 10 and 11, respectively.

It is clear that proper temperature annealing does eliminate the multiple peaking, although one sample of TMO still showed some evidence of residual multiple peaking. The magnitude of c_p for the annealed samples is in excellent agreement with our previous measurements on unannealed TMO samples which exhibited no multiple peaking. It is also worth noting that the measured heat of transition is the same in the multiple and single peaked samples, as one would expect since the multiple peaking is a strain induced effect.

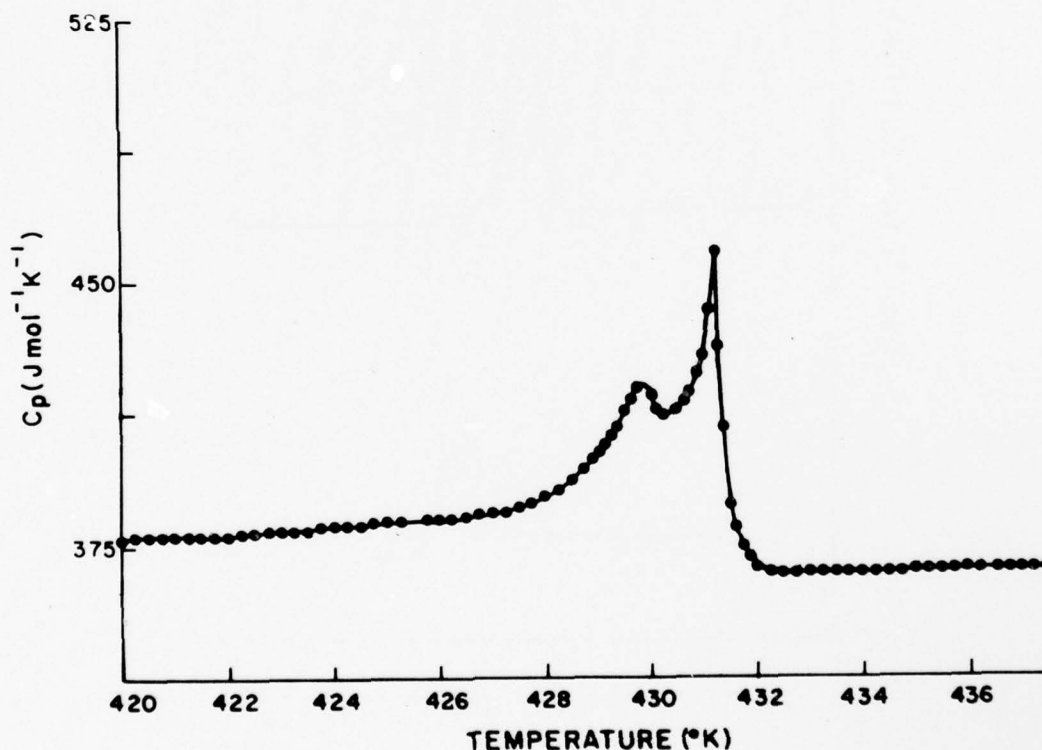


Figure 10. Specific heat vs. temperature for TMO sample exhibiting multiple peaks near transition temperature.

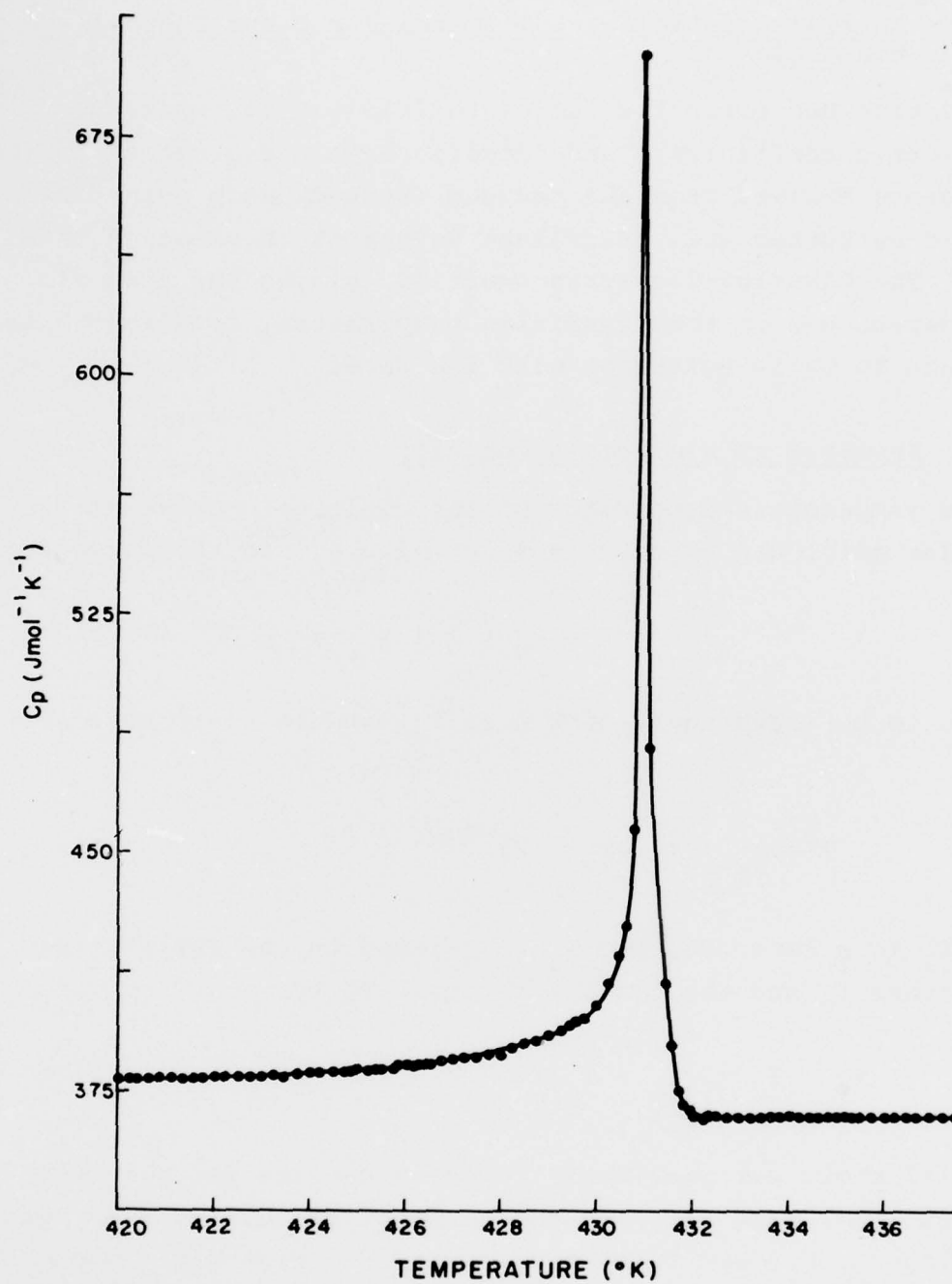


Figure 11. Specific heat vs. temperature for TMO sample exhibiting multiple peaks after annealing for 24 hours at 960°C .

2.4 Analysis of Dielectric, Pyroelectric and Thermal Measurements

This section describes the fit of the dielectric constant, pyroelectric coefficient, and specific heat measurements to the expressions derived from the reduced thermodynamic potential given in Paragraph 2.2. Excellent agreement is obtained in all cases. The Clausius-Clapeyron equation, giving the electric field dependence of the transition temperature, is also checked and found to be in agreement with the data.

2.4.1 Analysis of Dielectric Constant

For the temperature dependence of the dielectric constant along the polar axis, one expects (see Par. 2.2.4), in the paraelectric phase:

$$\epsilon = \epsilon_p = 1 + \chi$$

assumed to be independent of T near T_c ; and in the ferroelectric phase:

$$\epsilon = \epsilon_p + K_1 (T_1 - T)^{-1/2} \quad (1)$$

where K_1 is a constant, and T_1 is related to the Curie-Weiss temperature T_0 and the transition point T_c by:

$$T_1 - T_c = (T_c - T_0)/3. \quad (2)$$

Figure 12 shows our previously reported results for ϵ in GMO, TMO, and GDMO, together with the behavior calculated from Equation (1) using ϵ_p , K_1 , and T_1 chosen to give the best fit. The agreement is remarkably good below the transition temperature, and the error is less than 5% above it. The values of ϵ_p , K_1 , and T_1 obtained in this way are listed in Table 2.

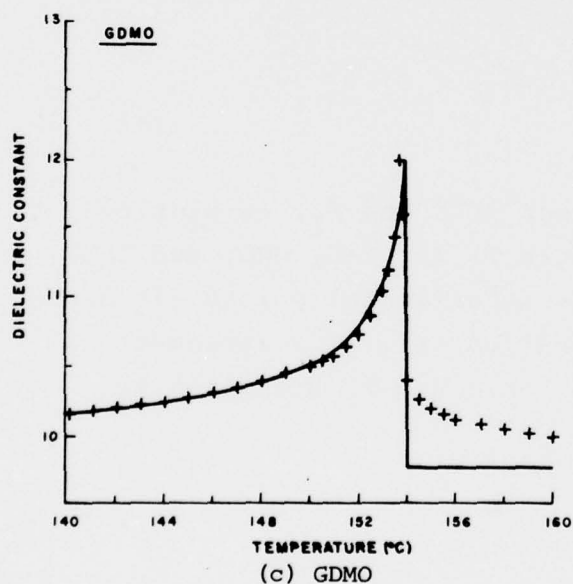
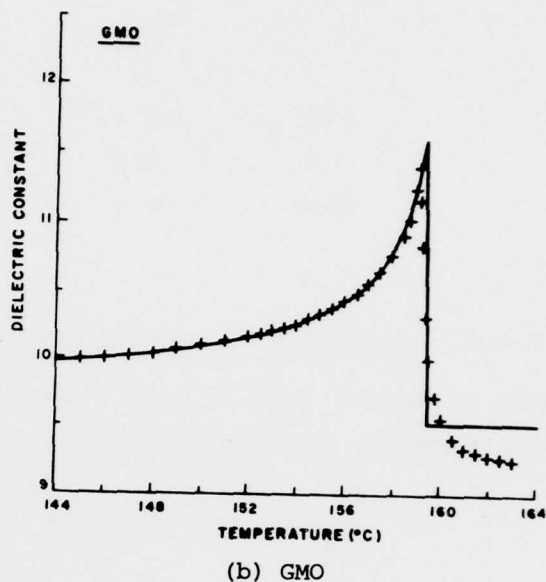
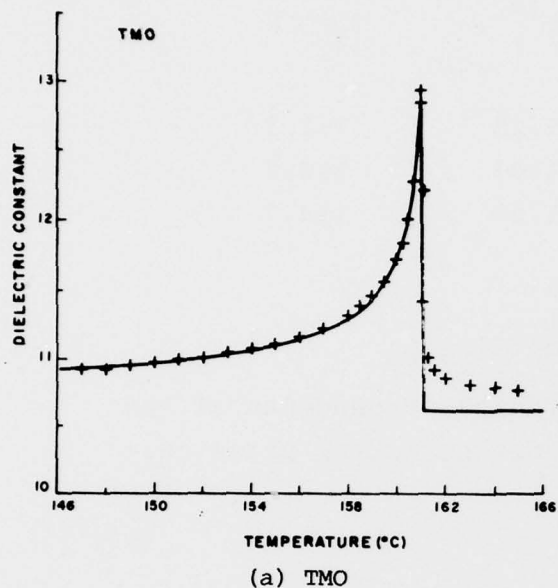


Figure 12. Dielectric constant vs. temperature for (a) terbium molybdate, (b) gadolinium molybdate, and (c) gadolinium-dysprosium molybdate. The crosses are the experimental data and the solid line represents the theoretical expected temperature dependence fit to only the data points which lie below the transition temperature.

TABLE 2. PARAMETERS ϵ_p , K_1 , AND T_1 OBTAINED BY FITTING THE OBSERVED DIELECTRIC CONSTANT.

	ϵ_p	$K_1(K^{1/2})$	$T_1(^{\circ}C)$
TMO	10.6	1.25	161.3
GMO	9.5	1.87	160.2
GDMO	9.8	1.57	154.7

2.4.2 Analysis of Pyroelectric Coefficient

The expected (see Par. 2.2.4) temperature dependence of the spontaneous polarization P_s in the ferroelectric phase is,

$$P_s = K (T_1 - T)^{1/2} + P_1, \quad (3)$$

where, K = a constant, T_1 = temperature above which no ferroelectric phase exists, and P_1 = hypothetical polarization at T_1 . The temperature T_1 is defined above.

From Equation (3) the pyroelectric coefficient $p = -dP_s/dT$ is given by:

$$p = (K/2) (T_1 - T)^{-1/2} \quad (4)$$

In order to find the numerical values of K and T_1 , we plotted $1/p^2$ as a function of the temperature T , for TMO, GMO, and GDMO (Fig. 13). It can be seen that the experimental points lie along straight lines as expected from Equation (4). The agreement is excellent, and the values obtained for K and T_1 are given in Table 3.

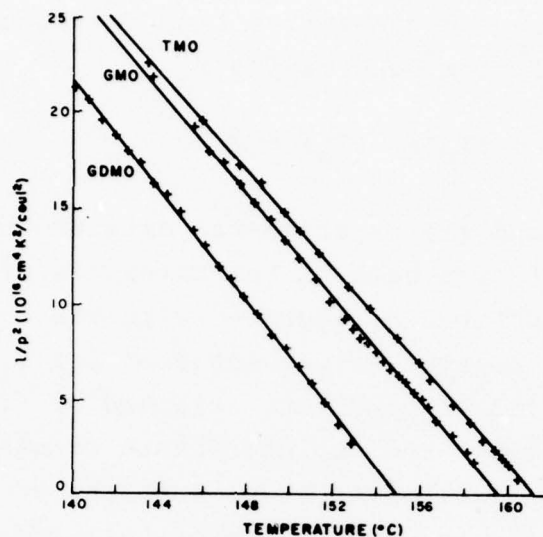


Figure 13. Square of the reciprocal of the pyroelectric coefficient vs. temperature for terbium molybdate (TMO), gadolinium molybdate (GMO) and gadolinium-dysprosium molybdate (GDMO). Crosses are the data points; the straight lines are the theoretically expected linear relationship fit to these data points. The data comes from dynamic measurements of p/c combined with our results for c .

TABLE 3. PARAMETERS K AND T_1 OBTAINED BY FITTING DYNAMIC MEASUREMENTS OF THE PYROELECTRIC COEFFICIENT.

	K ($10^{-8} \text{C/cm}^2 \text{K}^{1/2}$)	T_1 ($^{\circ}\text{C}$)
TMO	1.77	161.3
GMO	1.72	159.6
GDMO	1.66	154.9

2.4.3 Transition Temperatures

Defining $\Delta\epsilon = \epsilon - \epsilon_p$, we can derive from Equations (1) and (4) a useful relationship for determining T_O :

$$\Delta\epsilon(T_C)/\Delta\epsilon(T_O) = 2 \quad (5)$$

Using Equation (5) and the experimental data shown in Figure 12, we have determined T_O for each of the materials studied. The results are given in Table 4, together with the observed transition temperatures T_C and the values obtained for T_1 above. Slightly different values of T_1 are obtained by fitting the pyroelectric coefficient and the dielectric constant, but the differences are not significant in view of the accuracy with which we can determine the sample temperature and the uncertainty in T_C caused by the experimental width of the transition.

TABLE 4. THE CURIE-WEISS TEMPERATURE T_O AND TRANSITION TEMPERATURE T_C AS DETERMINED FROM EQ. (15) AND THE MAXIMUM OF ϵ , RESPECTIVELY. ALSO GIVEN FOR COMPARISON IS T_1 AS FOUND FROM FITTING THE PYROELECTRIC COEFFICIENT \bar{p} OR THE DIELECTRIC CONSTANT ϵ . ALL TEMPERATURES ARE IN $^{\circ}\text{C}$.

	T_O	T_C	T_1 (from \bar{p})	T_1 (from ϵ)
TMO	159.7	161.0	161.3	161.3
GMO	157.0	159.5	159.6	160.2
GDMO	152.6	154.2	154.9	154.7

2.4.4 Influence of an Applied Electric Field

The expected value of the rate of change of the transition temperature with external field can be given in terms of the constants K and K_1 , namely,

$$dT_c/dE = 2K_1/K . \quad (6)$$

Inserting the experimental values for GMO leads to $dT_c/dE = 1.9 \times 10^{-5} \text{ K/V cm}^{-1}$. This value is quite small compared to the result for the proper ferroelectric BaTiO_3 , where $dT_c/dE = 1.6 \times 10^{-3} \text{ K/V cm}^{-1}$, and explains why we have observed no change in T_c in the p or ϵ measurements at fields up to 10 kV/cm.

A general thermodynamic argument based on the Clausius-Clapeyron equation shows that,

$$dT_c/dE = \Delta P/\Delta S, \quad (7)$$

where, ΔP and ΔS are the discontinuous changes in the polarization and entropy, respectively, which occur at the phase transition. Inserting the experimental values (Refs. 2-13, 2-19, 2-30) for GMO ($\Delta P = 4 \times 10^{-8} \text{ C/cm}^2$ and $\Delta S = 2.2 \times 10^{-3} \text{ J/cm}^3\text{K}$), yields $dT_c/dE = 1.8 \times 10^{-5} \text{ K/V cm}^{-1}$, in very good agreement with the result obtained above from Equation (6).

2.4.5 Analysis of Thermal Measurements

The specific heat measurements can be compared to the theoretical expressions for:

- (a) Discontinuity of the entropy at the transition temperature,

$$\Delta S = (3K^2/2K_1) (T_1 - T_c)^{1/2}$$

- (b) Latent heat at the Curie point,

$$\Delta Q = T_c \Delta S = (3K^2 T_c / 2K_1) (T_1 - T_c)^{1/2}$$

- (c) Temperature dependence of the specific heat,

$$c = \begin{cases} c_0 + (K^2/4K_1) T (T_1 - T)^{-1/2} & \text{for } T < T_c \\ c_0 & \text{for } T > T_c \end{cases}$$

The values of K , K_1 , T_1 and T_c are determined above from the analysis of the pyroelectric and dielectric properties. Table 5 summarizes these values, using the T_1 value determined in the dielectric measurements.

A comparison of the predicted values and measured upper bounds for ΔS and ΔQ is given in Table 6.

TABLE 5. PARAMETERS DETERMINED PREVIOUSLY FROM PYROELECTRIC AND DIELECTRIC MEASUREMENTS.

	T_c	T_1	K	K_1
	(K)	(K)	($10^{-8} \text{C/cm}^2 \text{K}^{1/2}$)	($\text{K}^{1/2}$)
TMO	434.2	434.5	1.77	1.25
GMO	432.7	433.4	1.72	1.87
GDMO	427.4	427.9	1.66	1.57

TABLE 6. COMPARISON OF CALCULATED VALUES AND MEASURED UPPER BOUNDS FOR ENTROPY DISCONTINUITY AND THE LATENT HEAT.

	$\Delta S(\text{J/mol K})$		$\Delta Q(\text{J/mol})$	
	Calculated	Measured Upper Bound	Calculated	Measured Upper Bound
TMO	0.40	0.59 ± 0.06	173	255 ± 26
GMO	0.39	0.71 ± 0.07	169	304 ± 30
GDMO	0.36	0.67 ± 0.07	157	288 ± 29

Figure 14 shows experimental results for c in TMO (Isomet #1) as measured (the temperature scale of the experimental data was shifted by 2.5 K to agree with $T_c = 161^\circ\text{C}$ as determined from our dielectric and pyroelectric measurements) together with the behavior calculated, using the data of Table 5 and choosing c_0 to give the best fit. For c_0 we found a constant value of $2.07 \text{ J/cm}^3\text{K}$ over the temperature range $150\text{--}165^\circ\text{C}$. The agreement between the calculated curve and the experimental points is good except in the immediate vicinity of the transition point. In this region an agreement between the theory and the experiment is not expected because the anomaly in the specific heat at the transition is always spread over a small temperature range due to instrumental resolution.

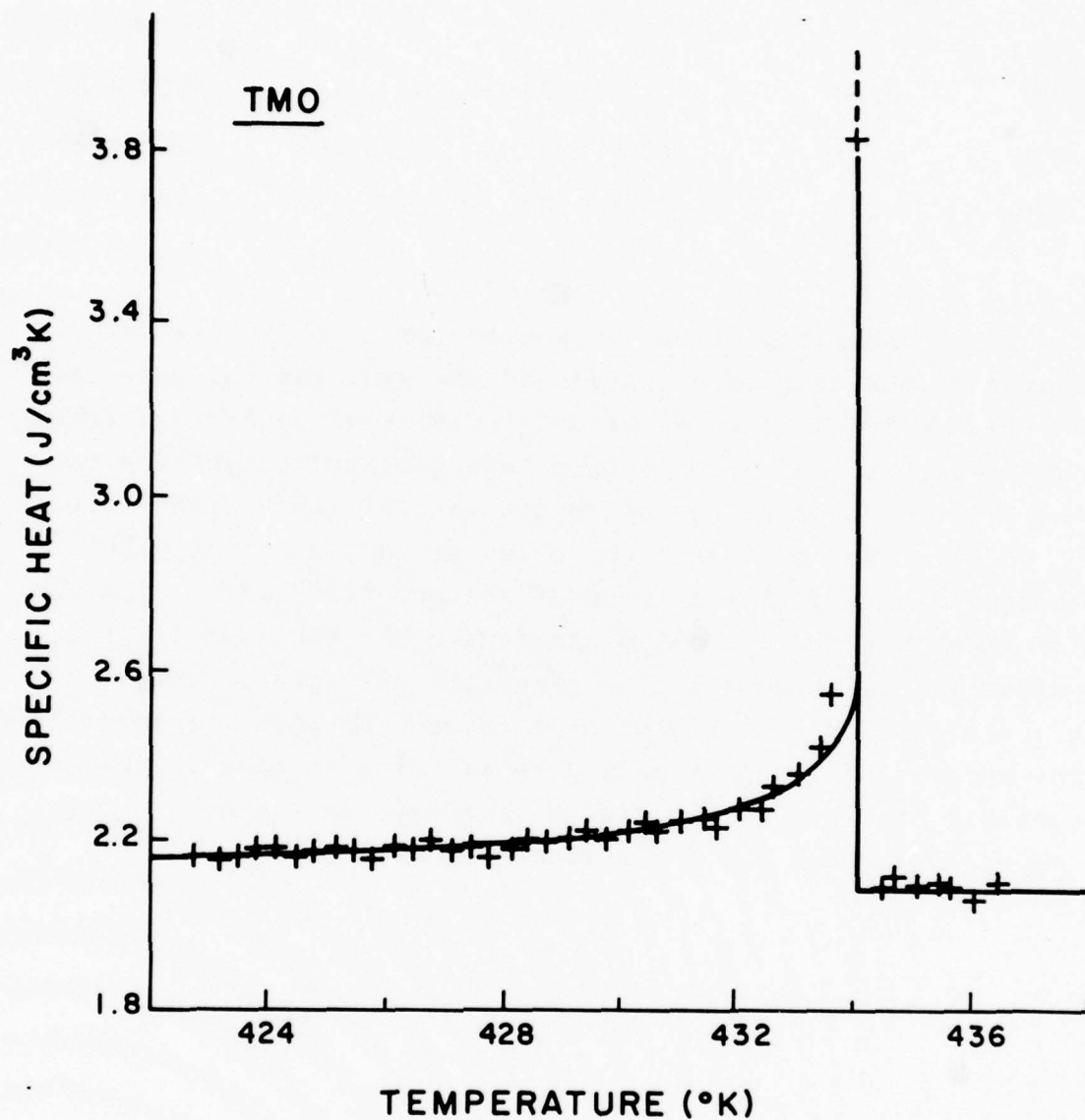


Figure 14. Specific heat of TMO (Isomet #1). Crosses are experimental values previously reported; solid line is theoretically calculated behavior.

2.5 Figures of Merit

The figure of merit of a pyroelectric material used as a vidicon target is $M(1) = p/\epsilon c$, while $M(\frac{1}{2}) = p/\epsilon^{1/2} c$ is the figure of merit for a small-area detector made of that material. We have developed an experimental technique which permits direct measurement of these figures of merit, reducing or completely eliminating the need to calculate products or ratios of independent measurements. Results obtained by this method are reported below for the rare-earth molybdates. To permit comparison with the behavior of a typical proper ferroelectric, we also present data for TGS.

2.5.1 Measurement Method

The measurement method is a modification (Ref. 2-34) of the dynamic technique of Chynoweth (Ref. 2-31), in which we measure voltage rather than current response. A brief analysis of the technique is given below.

Consider a thin plate of pyroelectric material electroded on its major faces which are perpendicular to the polar axis. In parallel to the sample are connected a load resistor R_L and a preamplifier of input capacitance C_i and input resistance R_i . A chopped beam of radiation with a 50% duty factor (Fig. 15a) is incident upon the front electrode and heats the sample. The chopping period τ is assumed to be much shorter than the thermal time constant of the sample. It can be shown that in the steady state, the mean temperature \bar{T} of the sample rises linearly during a radiation pulse and falls linearly between pulses (Fig. 15b). The slopes of the rise and fall are equal (except for sign) and given by $\pm F_0/2cL$, where F_0 = radiation power absorbed per unit area of the sample during a single pulse, and L = thickness of the sample. As a result of the temperature variations, the spontaneous polarization of the material is changed, causing a charge flow through the sample and the load.

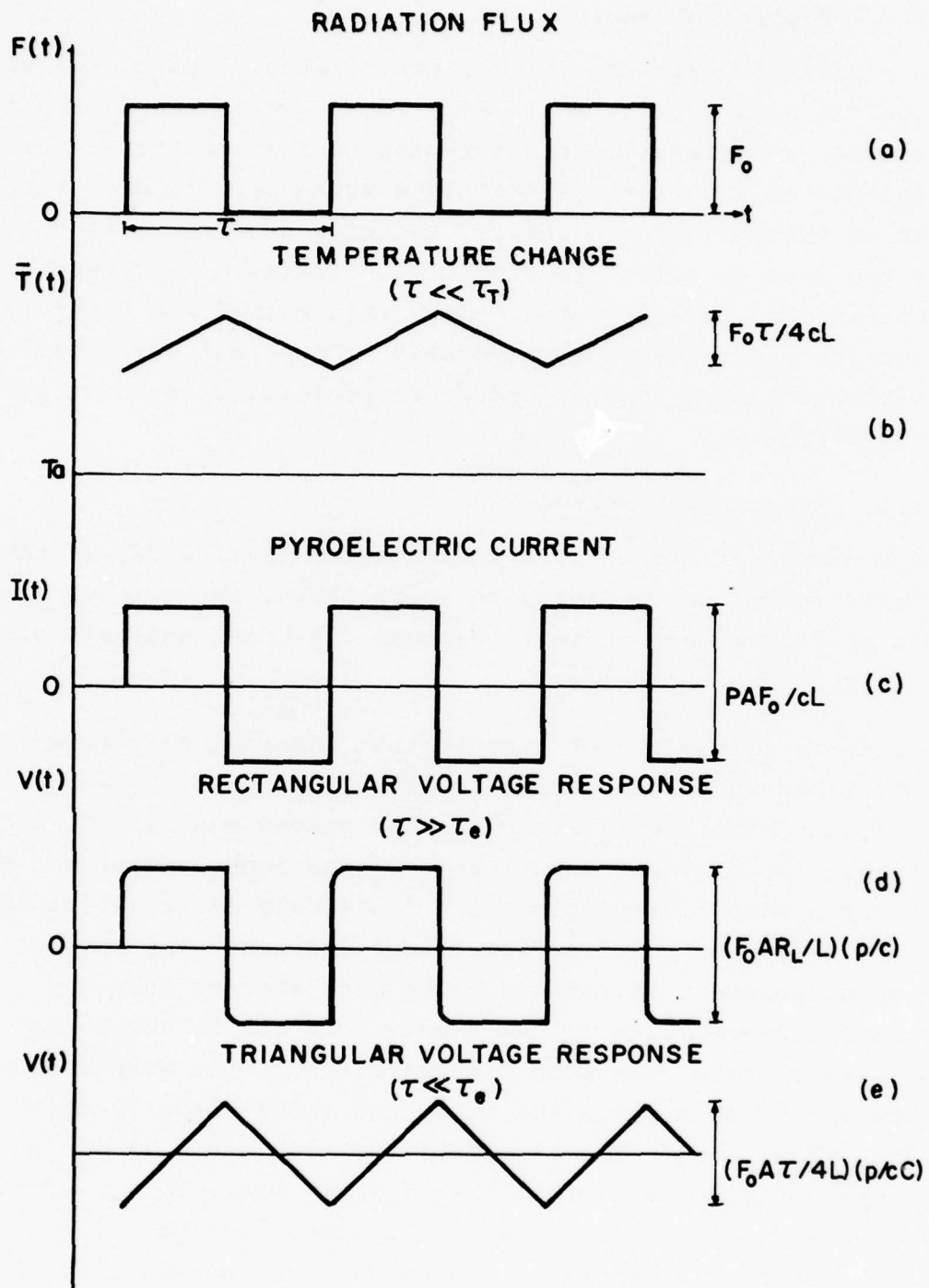


Figure 15. Schematic description of steady state pyroelectric current and voltage responses to rectangular radiation pulses of period much shorter than thermal time constant of sample.

The pyroelectric current (Ref. 2-37) $pA(d\bar{T}/dt)$ consists of positive and negative square pulses (Fig. 15c) of height $pAF_0/2cL$, where A = electrode area. For the voltage $V(t)$ developed across the sample and the load, one obtains the equation:

$$\frac{d(CV)}{dt} + \frac{V}{R} = pA \frac{d\bar{T}}{dt} , \quad (1)$$

where C represents the sum of C_i and the sample capacitance C_s , and R the parallel combination of R_L , R_i , and the sample resistance R_s . Normally R_i and R_s are several orders of magnitude larger than R_L , so that to a good approximation $R = R_L$. Solving Eq. (1) one finds that various response shapes can be obtained depending on the ratio between the electronic time constant of the system $\tau_e = RC$, and the period τ of the radiation pulses. When τ is much greater than τ_e , a rectangular response is obtained (Fig. 15d). In this case the peak-to-peak value V_R of the response is independent of τ and directly proportional to the ratio (p/c) :

$$V_R = (F_0 A R_L / L) (p/c) . \quad (2)$$

When τ is much less than τ_e , a triangular response is obtained (Fig. 15e) for which the peak-to-peak value V_T is proportional to the chopping period τ ,

$$V_T = (F_0 A \tau / 4L) (p/cC) . \quad (3)$$

When the capacitance C_s of the sample dominates, $C \approx C_s = \epsilon_0 \epsilon A / L$, and V_T is directly proportional to M_1 . If C_i is not negligible, M_1 can be expressed in terms of V_T and a correction factor g , which can be calculated from the ratio (V_T/V_R) :

$$M_1 = (4g/F_0 \tau) V_T , \quad (4)$$

where

$$g = [1 - 4R_L C_i \tau^{-1} (V_T/V_R)]^{-1} .$$

Using Eqs. (2) and (4), $M_{1/2}$ can be expressed in the form:

$$M_{1/2} = (2/F_O)(gL/AR_L\tau)^{1/2} (V_R V_T)^{1/2} \quad (5)$$

Equations (4) and (5) form the basis for our direct experimental determinations of the figures of merit.

2.5.2 Experimental Techniques

Thin slices of TGS, GMO, TMO, and GDMO were cut from single crystals normal to the pyroelectric axis. Samples were polished to thicknesses from 0.03 to 0.1 mm and electroded on both faces with evaporated antimony. Attached to the electrodes were 3 mil diameter silver leads by which the samples were suspended. A small sample holder with a LiF window was used, and the sample temperature was measured to ~ 0.2 C with a calibrated thermocouple attached very close to the rear electrode. The sample mount was attached to a heated copper block and placed in a vacuum-tight chamber with a LiF window. Before each measurement, samples were poled with a steady field of 2-5 kV/cm applied during slow cooling through the Curie point and down to room temperature. The radiation source was a Globar with a variable speed chopper (Ithaco 382A). To provide rectangular pulses, the width of the chopper teeth, as well as the distance between them, was much larger than the diameter of the radiation beam.

The measuring circuit consisted of a load resistor ($10^5 - 10^9 \Omega$) and a FET source follower circuit connected in parallel to the sample (Ref. 2-38). The pyroelectric response voltages obtained were displaced on an oscilloscope, and the rms value of the voltage response was measured with a lock-in amplifier (Keithley Autolock 840). The outputs of the lock-in and thermocouple were recorded simultaneously on an x-y recorder.

2.5.3 Experimental Results

Figure 16 shows the temperature dependence of p/c and $p/\epsilon\epsilon_0 c$ in TGS as measured by the dynamic method. The calibration in this measurement was obtained by assuming for the pyroelectric coefficient (Ref. 2-39) $p = 3 \times 10^{-8} \text{ C/cm}^2 \text{ K}$ and for the specific heat (Ref. 2-40) $c = 2.2 \text{ J/cm}^3 \text{ K}$ at 25°C . Comparing the behavior of p/c and $p/\epsilon\epsilon_0 c$ shows that ϵ plays a dominant role in determining the temperature dependence of M_1 ; the increase in the dielectric constant causes a steady drop in M_1 as the transition point is approached.

Figure 17 shows the temperature dependence of $p/\epsilon\epsilon_0 c$ in GMO, TMO, and GDMO. The results for p/c in these materials were presented in Par. 3.3.4. In the molybdates, in sharp contrast to the behavior exhibited by TGS, $p/\epsilon\epsilon_0 c$ increases in the same manner as p/c as the transition point is approached. This result is expected, since at zero stress these materials exhibit only a small increase in dielectric constant near the transition temperature (Par. 3.2.2).

2.5.4 Analysis of Results

The results of Section 2.2 lead to predictions for both figures of merit in the molybdates:

$$M(1) = K/\{2[\epsilon_p + K_1(T_1-T)^{-1/2}] [c_0(T_1-T)^{1/2} + K^2 T/4K_1]\},$$

$$M(\frac{1}{2}) = K/\{2[\epsilon_p + K_1(T_1-T)^{-1/2}]^{1/2} [c_0(T_1-T)^{1/2} + K^2 T/4K_1]\}.$$

In Figures 18 and 19 the calculated values of $M(1)$ and $M(\frac{1}{2})$ are compared with our experimental results for TMO. The crosses in Figure 18 represent the experimental values of $p/\epsilon c$ as measured directly by the dynamic method. In Figure 19 the crosses represent experimental values of $p/\epsilon^{1/2} c$ obtained by taking the square root of the product of the measured values of $p/\epsilon c$ and p/c . The solid lines were calculated using

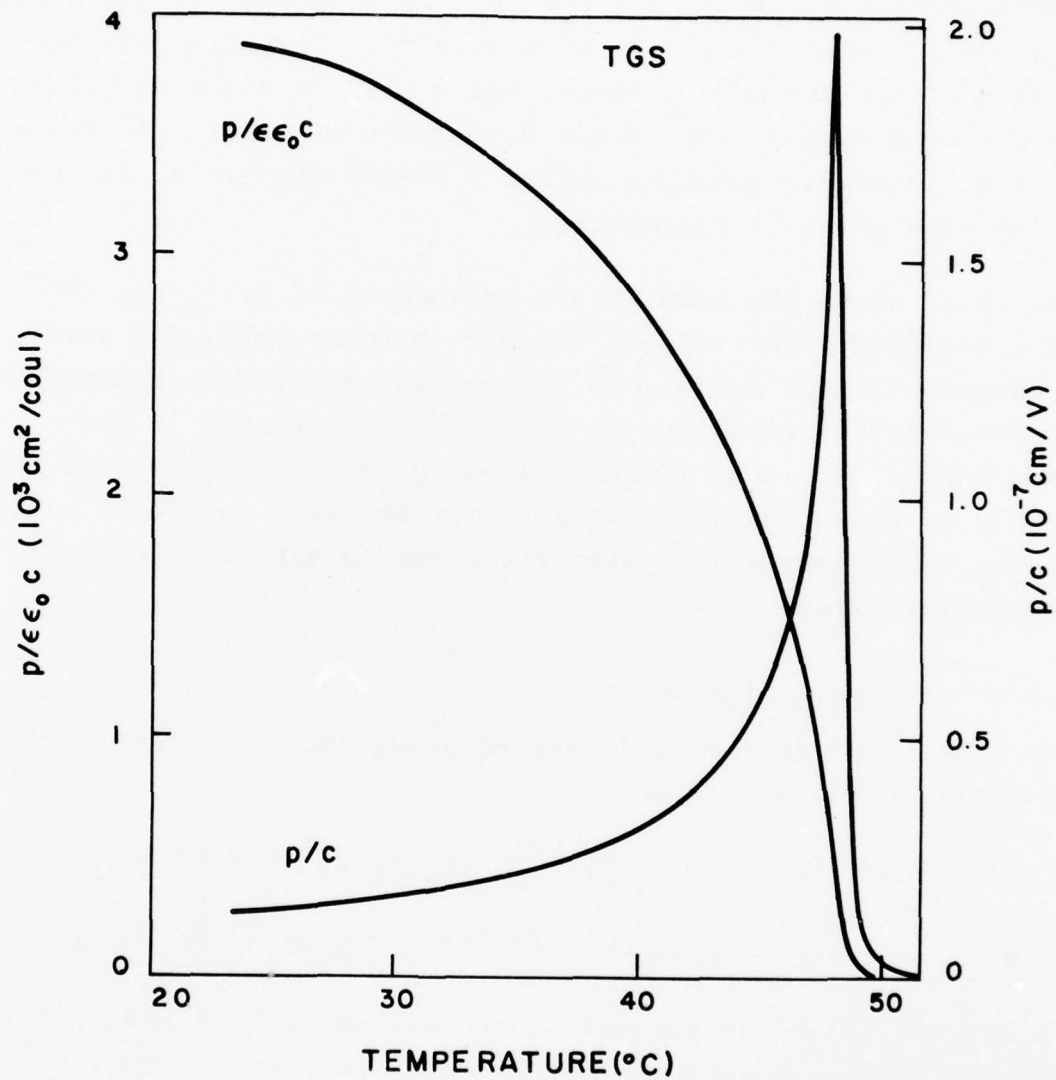
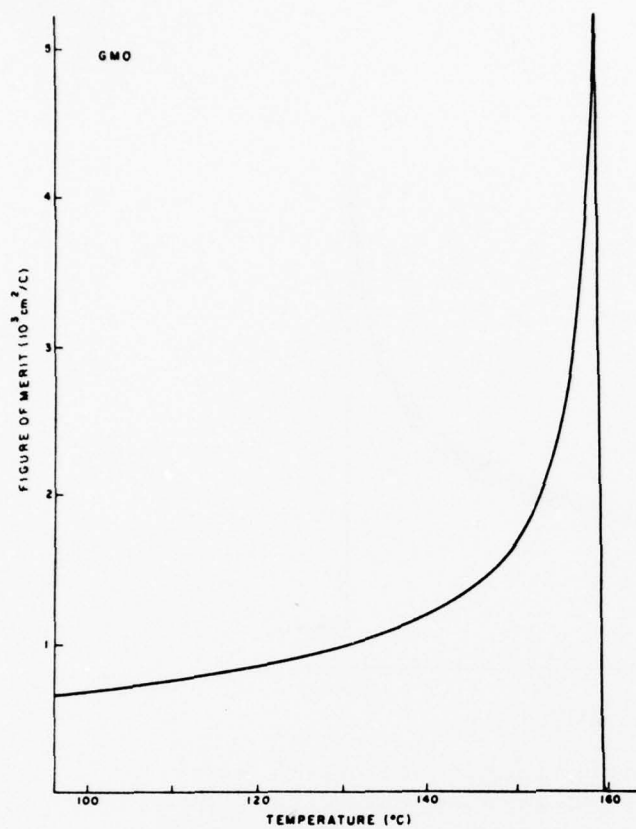
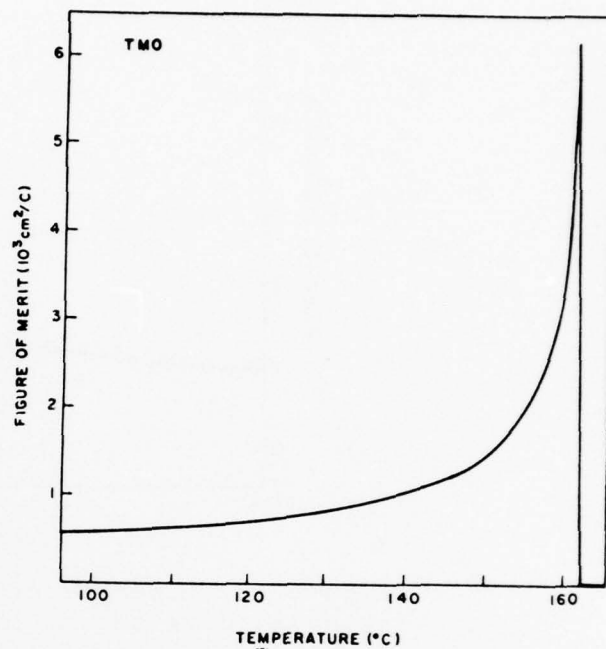


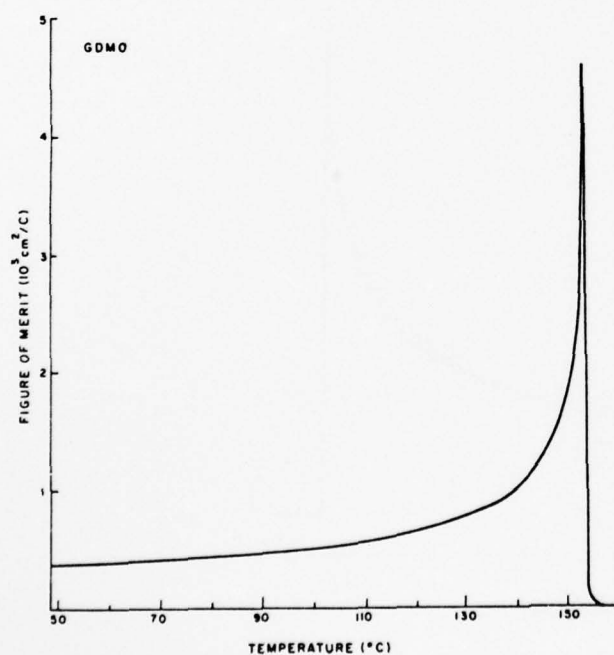
Figure 16. Temperature dependence of $M(1)$ and ratio p/c in TGS as measured by dynamic technique.



(a) GMO



(b) TMO



(c) GDMO

Figure 17. Temperature dependence of $M(1)$ in GMO, TMO and GDMO.

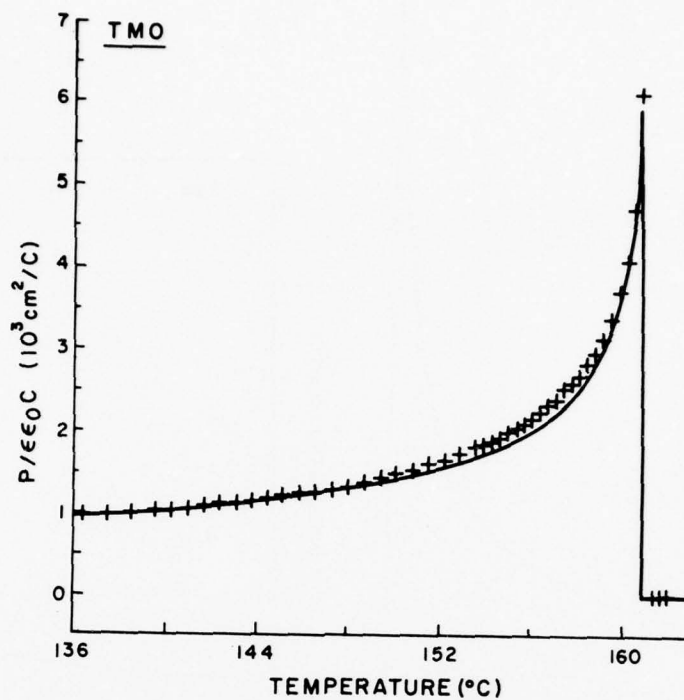


Figure 18. Comparison of measured (crosses) and calculated values of $M(1)$ figure of merit for TMO.

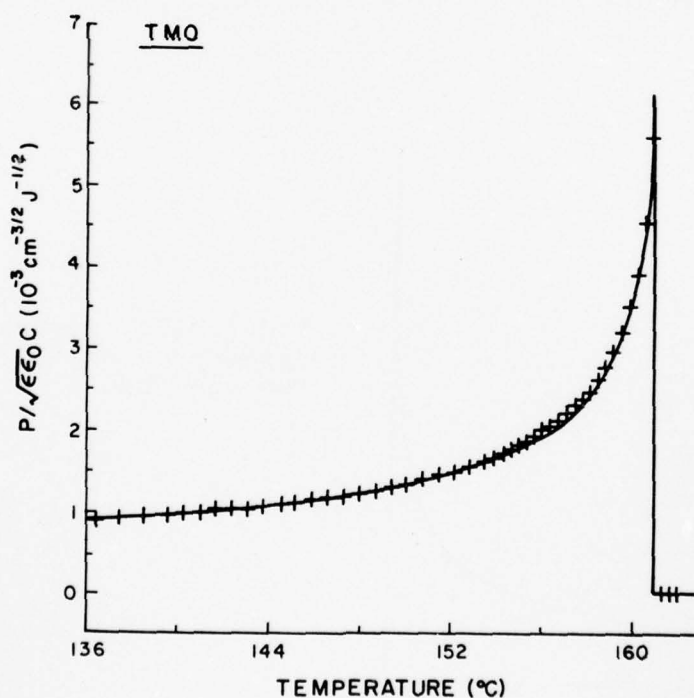


Figure 19. Comparison of measured (crosses) and calculated values of $M(\frac{1}{2})$ figure of merit for TMO.

for K , K_1 , T_1 , and T_c the values given in Table 5. For ϵ_p we used a value of 10 which is $\sim 5\%$ less than the value of 10.6 obtained from independent measurement of ϵ . For c_o we chose the value $1.97 \text{ J/cm}^3 \text{ K}$ which gives a better fit to the specific heat data of TMO #2. Clearly, there is good agreement between theory and experiment for both figures of merit.

2.5.5 Optimization of $M(1)$

It is readily seen from the expression for $M(1)$ obtained in previous section that this figure of merit attains a maximum at T_c unless unrealistically small values of ϵ_p and c_o are assumed. (Even in such a case the value of M_1 at its maximum differs only insignificantly from its value at T_c .) One can evaluate M_1 at T_c and obtain the peak values of the figure-of-merit. This peak value is a function of both the readily measured or estimated quantities ϵ_p , c_o , and T_c and the more difficult to assess quantities $(T_1 - T_c)$, K and K_1 (which are expressible in terms of the free energy parameters). This peak value of the figure of merit can now be optimized with respect to variations in the free energy parameters to give an optimum figure-of-merit,

$$M_1^{\text{opt}} = \frac{1}{4} (\epsilon_p c_o T_c)^{-1/2}. \quad (6)$$

This optimum is attained for values of the free energy parameters such that,

$$T_1 - T_c = K^2 T_c / 4 c_o \epsilon_p, \quad (7a)$$

$$(K/K_1) = (4 c_o / \epsilon_p T_c)^{1/2}. \quad (7b)$$

For the three molybdates examined, the free energy parameters are such that this optimum value is very nearly attained. Thus, this expression for M_1^{opt} provides a useful guide to how large a figure of merit might be realized in the molybdate family.

For materials in the molybdate family, c_o is about 2 J/cm^3 K, and ϵ_p is about 10; therefore, the principal variation in M_1^{opt} stems from variations in T_c . As T_c varies from 160°C down to 40°C , M_1^{opt} only varies from $9.0 \times 10^3 \text{ cm}^2/\text{C}$ up to $10.6 \times 10^3 \text{ cm}^2/\text{C}$. For comparison one should recall that TGS has a figure of merit of $\sim 3.0 \times 10^3 \text{ cm}^2/\text{C}$ at 40°C . (Fig. 16).

2.6 References

- 2-1. V. Dvorak, Phys. Stat. Sol. (b)45, 147 (1971).
- 2-2. V. Dvorak, Phys. Stat. Sol. (b)46, 763 (1971).
- 2-3. A.P. Levanyuk and D.G. Sannikov, Sov. Phys. Sol. State 12, 2418 (1971).
- 2-4. K. Aizu, J. Phys. Soc. Japan 31, 802 (1971).
- 2-5. E. Pytte, Sol. Stat. Commun. 8, 2101 (1970).
- 2-6. B. Dorner, J.D. Axe, and G. Shirane, Phys. Rev. B6, 1950 (1972).
- 2-7. L. Landau, Phys. Z. Sowjet. 8, 113 (1935) and 11, 26 (1937). English translation in "L. Landau, Collected Works", D. ter Haar, editor, Pergamon, 1965.
- 2-8. A.P. Levanyuk and D.G. Sannikov, Sov. Phys. JETP 28, 134 (1969).
- 2-9. A.Z. Rabinovich, Sov. Phys. Sol. State 11, 159 (1969).
- 2-10. F.G. Ullman, B.N. Ganguly and J.R. Hardy, Ferroelectrics 2, 303 (1971).
- 2-11. F.G. Ullman, B.N. Ganguly and J.R. Zeidler, J. Elect. Mat. 1, 425 (1972).
- 2-12. F.G. Ullman, K.M. Cheung, G.A. Rakes and B.N. Ganguly, Ferroelectrics 9, 63 (1975).
- 2-13. E. Sawaguchi and L.E. Cross, J. Appl. Phys. 44, 2541 (1973).
- 2-14. T.E. Keve, S.C. Abrahams, K. Nassau and A.M. Glass, Sol. St. Commun. 8, 1517 (1970).
- 2-15. A.M. Glass - Private Communication 1978.
- 2-16. K. Aizu, J. Phys. Soc. Japan 31, 802 (1971).
- 2-17. S.E. Cummins, Ferroelectrics 1, 11 (1970).
- 2-18. A. Kumada, J. Phys. Soc. Japan 35, 941 (1973).
- 2-19. A. Kumada, Ferroelectrics 7, 145 (1974).
- 2-20. E. Sawaguchi and L.E. Cross, Phys. Stat. Sol. B50, K89 (1972).
- 2-21. H.J. Borchardt and P.E. Bierstedt, Appl. Phys. Lett. 8, 50 (1966).
- 2-22. K. Aizu, A. Kumada, H. Yumoto and S. Ashida, J. Phys. Soc. Japan 27, 511 (1969).

- 2-23. A. Kumada, H. Yumoto and S. Ashida, J. Phys. Soc. Japan 28, Suppl., 351 (1967).
- 2-24. H.J. Borchardt and P.E. Bierstedt, J. Appl. Phys. 38, 2057 (1967).
- 2-25. L.E. Cross, A. Fouskova and S.E. Cummins, Phys. Rev. Lett. 21, 812 (1968).
- 2-26. J. Fousek and C. Konak, Czech. J. Phys. B22, 995 (1972).
- 2-27. A.W. Smith and G. Burns, Phys. Lett. 28A, 501 (1969).
- 2-28. A.M. Shirokov, V.P. Mylov, A.I. Baranov and T.M. Prokhortseva, Sov. Phys. Sol. Stat. 13, 2610 (1972).
- 2-29. M. Midorikawa, Y. Ishibaski and Y. Takagi, J. Phys. Soc. Japan 37, 1583 (1974).
- 2-30. A. Fouskova, J. Phys. Soc. Japan 27, 1699 (1969).
- 2-31. K.M. Cheung and F.G. Ullman, Phys. Rev. B10, 4760 (1974).
- 2-32. R.L. Byer and C.B. Roundy, Ferroelectrics 3, 333 (1972).
- 2-33. A.G. Chynoweth, Phys. Rev. 117, 1235 (1960); J. Appl. Phys. 27, 78 (1956).
- 2-34. M. Simhony and A. Shaulov, App. Phys. Lett. 21, 375 (1972); A. Shaulov and M. Simhony, J. App. Phys. 43, 1440 (1972).
- 2-35. D.C. Ginnings and G.T. Furukawa, J. Amer. Chem. Soc. 75, 522-527 (1953).
- 2-36. K. Nassau, H.J. Levinstein, G.M. Loiacono, J. Phys. Chem. Solids 26, 1805 (1965).
- 2-37. B.R. Holeman, Infrared Phys. 12, 125 (1972).
- 2-38. M. Simhony and A. Shaulov, J. Appl. Phys. 42, 374 (1971).
- 2-39. H.P. Beerman, Ferroelectrics, 2, 123 (1971).
- 2-40. M.J. Tello and J.A. Gonzola, J. Phys. Soc. Japan Suppl. 28, 199 (1970); S.A. Taraskin, B.A. Strukov, and V.A. Meleshina, Sov. Phys. Solid State 12, 1089 (1970).

3. SULFATE FAMILY

Five materials from the family of ferroelectric sulfates were studied: LiNH_4SO_4 , LiND_4SO_4 , LiCsSO_4 , LiKSO_4 and $\text{LiH}_3(\text{SeO}_3)_2$. Lithium ammonium sulfate and its deuterated analogue exhibited similar properties. The high room-temperature value for the figure of merit (about equal to that of TGS at 40°C) suggested further study of related materials. Both lithium cesium sulfate and lithium potassium sulfate were consequently investigated; these materials, however, exhibited distinctly different behaviors which eliminate them for practical pyroelectric applications. Lithium trihydrogen selenite was investigated because of its high value of spontaneous polarization ($\sim 15 \mu\text{C}/\text{cm}^2$) and the fact that the related material $\text{RbH}_3(\text{SeO}_3)_2$ has been identified as an improper ferroelectric. We find no evidence that $\text{LiH}_3(\text{SeO}_3)_2$ is an improper ferroelectric. The measured value of the ratio p/ϵ is about one-fourth that of TGS. While this eliminates $\text{LiH}_3(\text{SeO}_3)_2$ for practical applications, the large value of the spontaneous polarization suggests that related materials might have potentially useful figures of merit.

3.1 Lithium Ammonium Sulfate and Deuterated Lithium Ammonium Sulfate

The room temperature value of the figure-of-merit for these materials is about $3 \times 10^3 \text{ cm}^2/\text{C}$. On the basis of this high value we conclude that further investigation of related materials would be worthwhile.

Pyroelectric and second harmonic generation measurements show the low temperature (below 273 K) phase of these materials to be polar, thus clarifying an ambiguity in the literature.

3.1.1 Growth and Characterization of Materials

Large (3 x 3 x 3 cm) colorless single crystals of LiNH_4SO_4 were grown from aqueous solution containing equimolar concentrations

of $(\text{NH}_4)_2\text{SO}_4$ and $\text{Li}_2\text{SO}_4 \cdot \text{H}_2\text{O}$. The deuterated crystals were grown from D_2O (99.9% D) solutions saturated with previously recrystallized LiND_4SO_4 . The final growth solution had a deuteration level of $97.7 \pm 0.03\%$. The evaporation method of growth was employed using a nitrogen gas flow of $2 \text{ ft}^3/\text{hr}$. The rate of solvent removal was controlled at $2 \text{ cm}^3/\text{day}$. The saturated LiNH_4SO_4 and LiND_4SO_4 solutions were at pH 3.88 and 3.93, respectively. The growth solution was controlled at $318.00 \pm 0.05 \text{ K}$ and stirred at 25 rpm. Single crystals from spontaneously nucleated seeds were always twinned and had a pseudo-hexagonal morphology (Fig. 20). Untwinned sections of these crystals were selected and only c-axis plates were used as seeds for subsequent growth.



Figure 20: Pseudo-hexagonal Morphology of LiNH_4SO_4 (Crossed Polarizers).

There exists some confusion in the literature on the notation of the crystallographic axes for LiNH_4SO_4 . We used the convention $c < a < b$ for the room temperature orthorhombic lattice. Thus the lattice parameters are $a = 8.78 \text{ \AA}$, $b = 9.12 \text{ \AA}$, and $c = 5.26 \text{ \AA}$.

3.1.2 Specific Heat Measurements

Measurements of the temperature dependence of the specific heat were performed with a Perkin-Elmer differential scanning calorimeter Model DSC-2. Sample weights were in the 10 to 40 mg range. Data were recorded at a scan rate of $10^\circ \text{ min}^{-1}$ and a sensitivity of 2 mcal sec^{-1} . The apparatus was calibrated with high purity indium ($T_M = 429.87 \text{ K}$ and $\Delta H = 6.80 \text{ cal g}^{-1}$). The error in H for indium was less than 0.1% while the error in T_M was 0.3 K. The estimated absolute accuracy of these measurements is $\pm 5\%$.

The temperature dependence of the specific heat for LiNH_4SO_4 and LiND_4SO_4 is shown in Figure 21. Upon deuteration of LiNH_4SO_4 , the transition temperature shifts upward 8.2 K; this is at variance with the results of our dielectric and pyroelectric measurements where a shift of only about 2 K is observed. The experimental data for both crystals are summarized in Table 7. A least squares fit of these data over the range 415 K to 445 K yields, for LiNH_4SO_4

$$c_p (\text{cal.g}^{-1}\text{.K}^{-1}) = -0.118 + 1.17 (10^{-3})T,$$

and for LiND_4SO_4

$$c_p (\text{cal.g}^{-1}\text{.K}^{-1}) = 0.054 + 1.01 (10^{-3})T.$$

Figure 22 illustrates a high precision scan of LiNH_4SO_4 ($dT/dt = 0.6^\circ \text{ min}^{-1}$ and 1 mcal/sec sensitivity) which revealed multiple peaking behavior near the ferroelectric transition temperature.

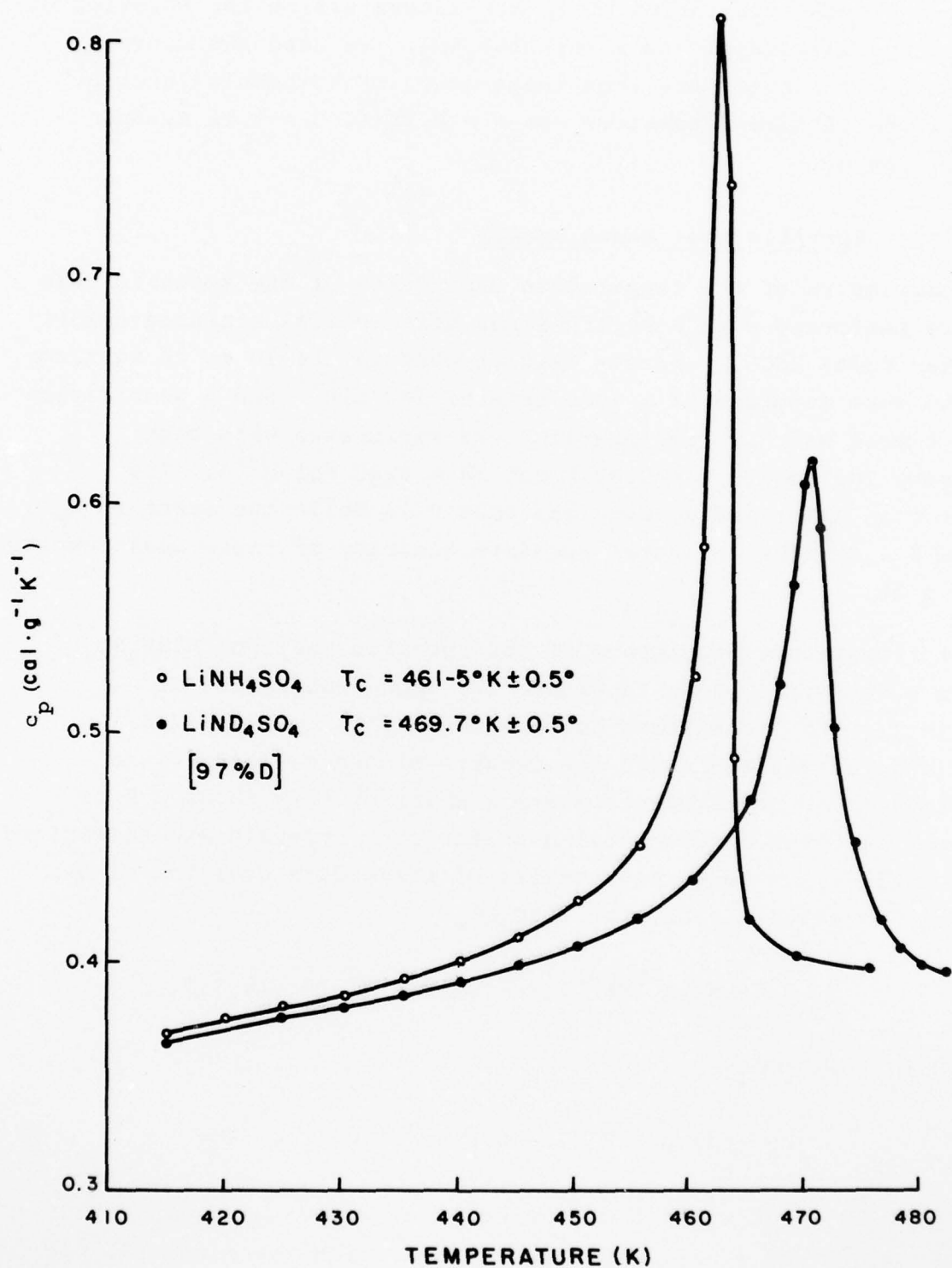


Figure 21. Temperature behavior of c_p in LiNH_4SO_4 and LiND_4SO_4 .

TABLE 7. SPECIFIC HEAT DATA FOR LiNH_4SO_4
AND LiND_4SO_4 .

Temperature °K	c_p (cal.g ⁻¹ °K)	
	LiNH_4SO_4	LiND_4SO_4
412	0.3665 ± 0.0005	0.3632 ± 0.0005
413	0.3674	0.3646
414	0.3692	0.3658
415	0.3695	0.3670
416	0.3701	0.3679
417	0.3719	0.3693
418	0.3733	0.3708
421	0.3750	0.3722
423	0.3771	0.3745
425	0.3798	0.3758
427	0.3819	0.3784
429	0.3843	0.3798
431	0.3867	0.3814
433	0.3899	0.3839
435	0.3928	0.3857
437	0.3957	0.3886
439	0.3992	0.3908
441	0.4023	0.3926

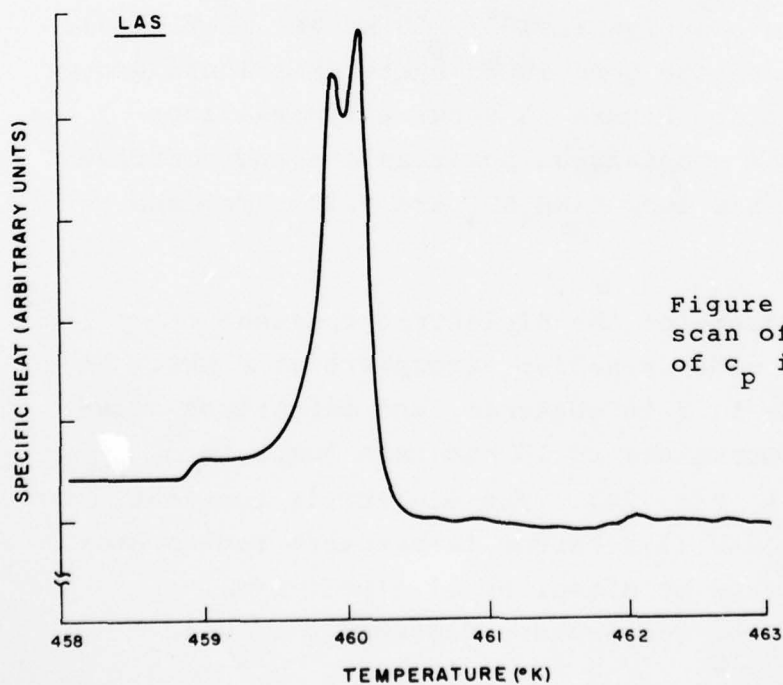


Figure 22. High resolution scan of temperature behavior of c_p in LiNH_4SO_4 .

Similar behavior has been observed in $\text{Gd}_2(\text{MoO}_4)_3$, $\text{Tb}_2(\text{MoO}_4)_3$, $\text{Cr}_3\text{B}_7\text{O}_{13}\text{Cl}$ and $\text{Ni}_3\text{B}_7\text{O}_{13}\text{Br}$, and can be attributed to bulk strains in the crystalline samples (see Par. 2.3.4).

The specific heat measurements also show that both LiNH_4SO_4 and LiND_4SO_4 are stable in air up to at least 548 K. This contradicts an earlier report that LiNH_4SO_4 decomposes at 465 K (Ref. 3-1).

3.1.3 Dielectric Measurements

Samples for electrical measurements were fabricated and their surfaces polished with a water, ethanol and glycerine mixture. A domain structure in the form of narrow stripes were clearly observed with domain boundaries parallel to the (100) planes. Electrodes were formed by deposition of antimony.

(1) High Temperature Phase Transition

In contrast to previous reports, (Refs. 3-2, 3-3) but in agreement with Mitsui et al., (Ref. 3-4) we observed that the polarity of LiNH_4SO_4 can be reversed at room temperature by application of a dc electric field along the c-axis. However, due to the large room temperature coercive field (~ 50 kV/cm) (Ref. 3-4), we were not able to generate good 60 Hz hysteresis loops except at elevated temperatures. Figure 23 shows a typical loop obtained at 437 K. The spontaneous polarization and coercive field estimated from this loop LiNH_4SO_4 are $0.17 \mu\text{C}/\text{cm}$ and 14 kV/cm.

The temperature dependence of the dielectric constant of LiNH_4SO_4 was measured under a helium atmosphere at 8 kHz. At 293 K, a value of $\epsilon_c = 11.2$ is obtained, and then rises slowly with increasing temperature to 13 and then jumps to about 22 at $T_c = 459$ K (Fig. 24). The dielectric constant follows a Curie-Weiss law in a narrow temperature region above T_c as previously reported by Mitsui et al. (Ref. 3-4). Between T_c and 463 K, the temperature dependence of ϵ is

AD-A062 730

PHILIPS LABS BRIARCLIFF MANOR N Y
OPTIMIZED PYROELECTRIC VIDICON THERMAL IMAGER. VOLUME II. IMPRO--ETC(U)
JUL 78 W A SMITH

F/G 17/5

DAAG53-76-C-0053

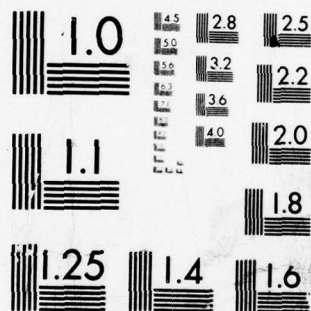
NL

UNCLASSIFIED

2 OF 3

AD
A0 62730





MICROCOPY RESOLUTION TEST CHART
NATIONAL BUREAU OF STANDARDS-1963-A

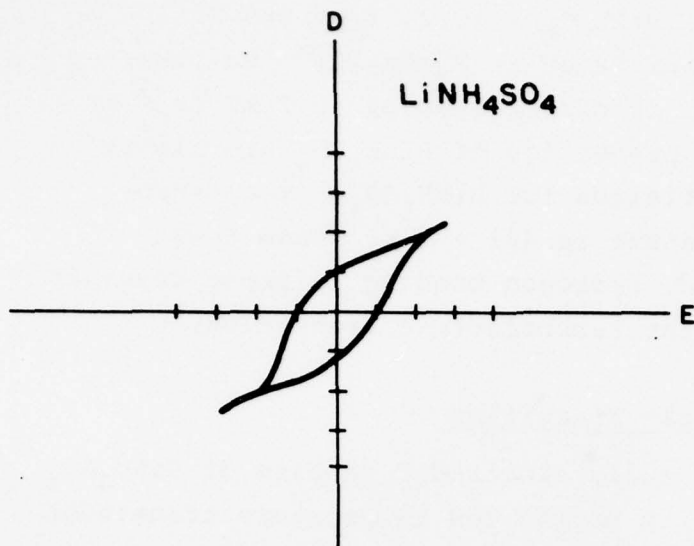


Figure 23. Hysteresis loop of LiNH_4SO_4 at 437 K (c-axis; 60 Hz).

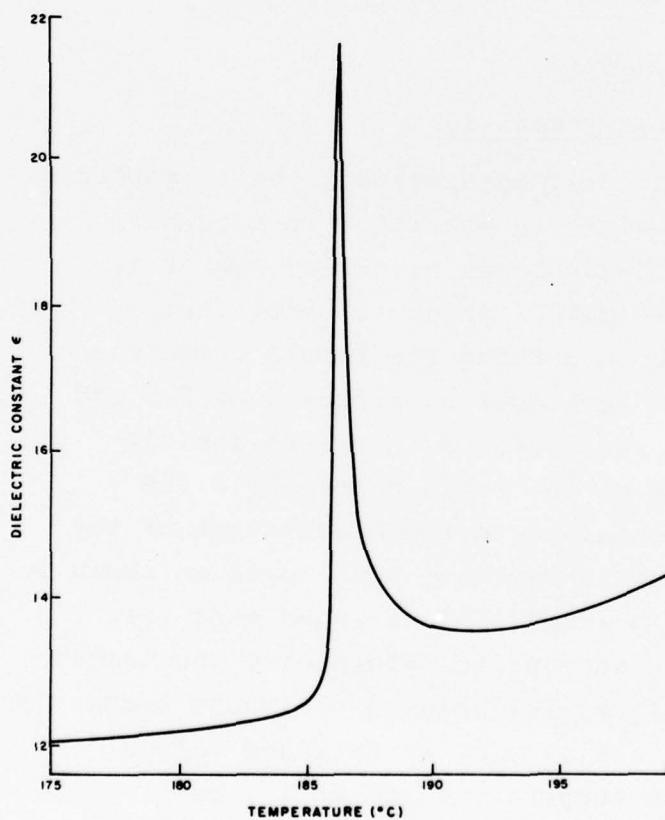


Figure 24. Temperature dependence of dielectric constant in LiNH_4SO_4 .

given by $\epsilon = \epsilon_c + C/(T-T_o)$, with $\epsilon_c = 13.2$, $T_o = 459$ K and $C = 1.8$ K. This is illustrated in Figure 25. We observed no appreciable effects from dc bias fields up to 2 kV cm^{-1} on ϵ_c and T_c . The electrical properties of LiND_4SO_4 are almost identical to the results obtained for LiNH_4SO_4 . The ferroelectric transition temperature is 461 ± 1 K. From these results we conclude that the hydrogen bonding in these crystals is only weakly coupled to the ferroelectric transition.

(2) Low Temperature Phase Transition

The dielectric constant of fully electroded samples of LiND_4SO_4 was measured in the vicinity of the low temperature transition from 80 Hz to 8 kHz. Within 1°C of the low temperature transition the measurement becomes unstable. A step change of the dielectric constant was consistently observed between the upper and lower phases (Fig. 26).

3.1.4 Pyroelectric Measurements

(1) High Temperature Phase Transition

Using the dynamic pyroelectric response method, the temperature dependence of the figure-of-merit ($M = p/\epsilon\epsilon_o c$) in a crystal of LiNH_4SO_4 over a range 20°C – 200°C was measured (Fig. 27). At room temperature, $M \sim 3000 \text{ cm}^2/\text{C}$, which is about that obtained for TGS at 40°C . Upon heating the sample from room temperature up to $\sim 170^\circ\text{C}$, M decreases by a factor of 2.5 and then, as the temperature is increased, M increases rapidly passing through a sharp peak at the Curie point ($T_c = 185 \pm 1^\circ\text{C}$). Similar behavior is obtained in the measurement of the ratio of pyroelectric current to specific heat (p/c) as shown in Figure 28. Comparison of Figures 27 and 28 shows that the influence of the dielectric constant in determining the temperature dependence of M is only appreciable in the phase transition region. From the ratio p/c and $p/\epsilon\epsilon_o c$, we obtained values of 10.5 and 17 for ϵ at room temperature and at T_c , respectively.

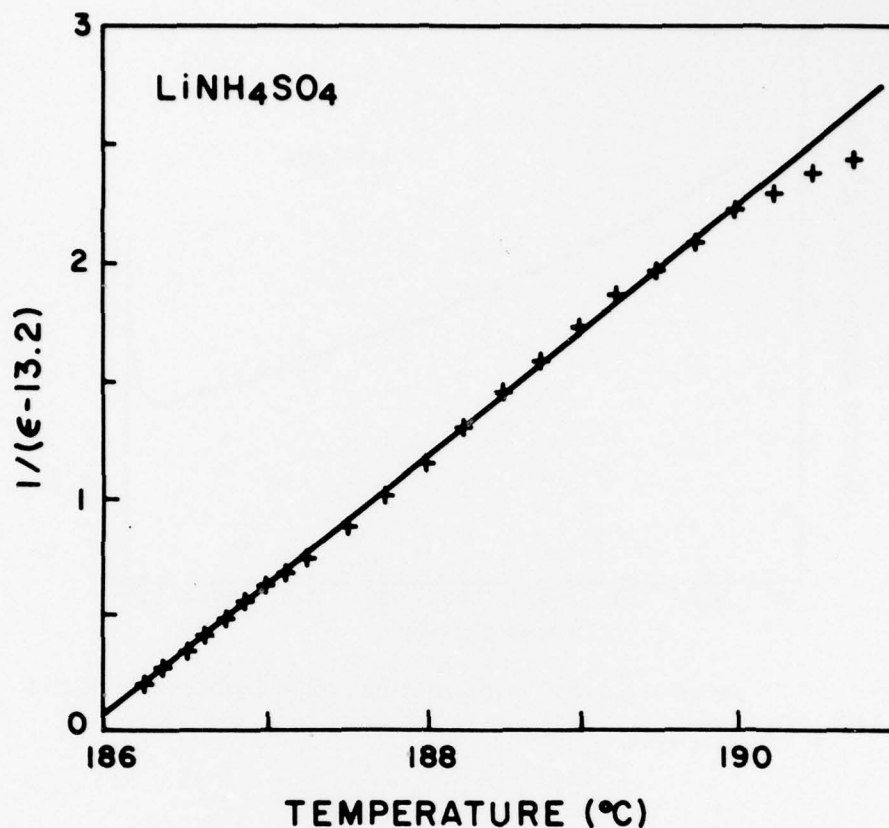


Figure 25. Fit of dielectric constant to Curie-Weiss behavior in high temperature phase of LiNH_4SO_4 .

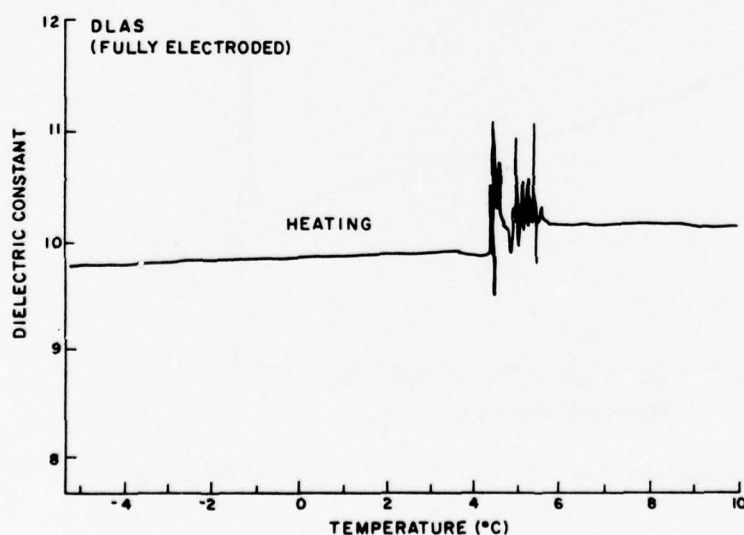


Figure 26. Dielectric constant of fully electroded sample of LiNH_4SO_4 . Near low temperature phase transition ($\sim 4-6^{\circ}\text{C}$) measurement becomes unstable.

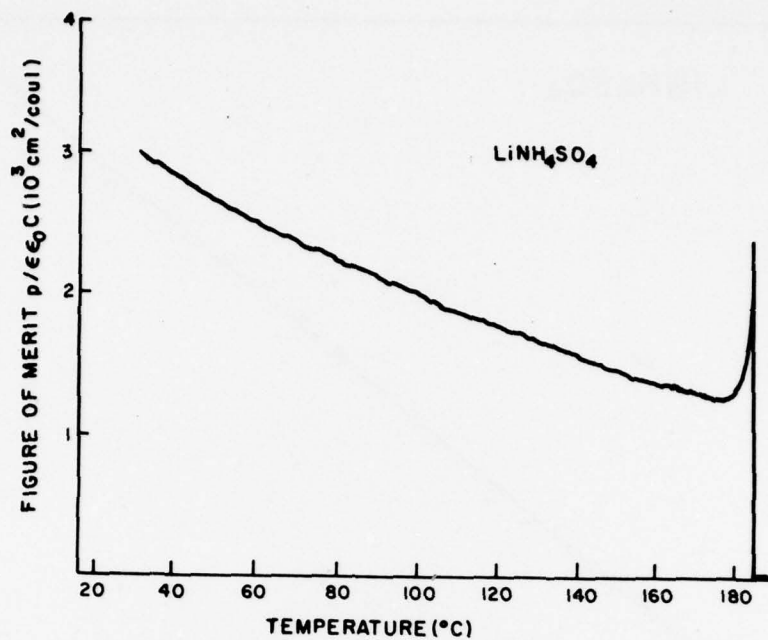


Figure 27. Temperature dependence of figure-of-merit in LiNH_4SO_4 .

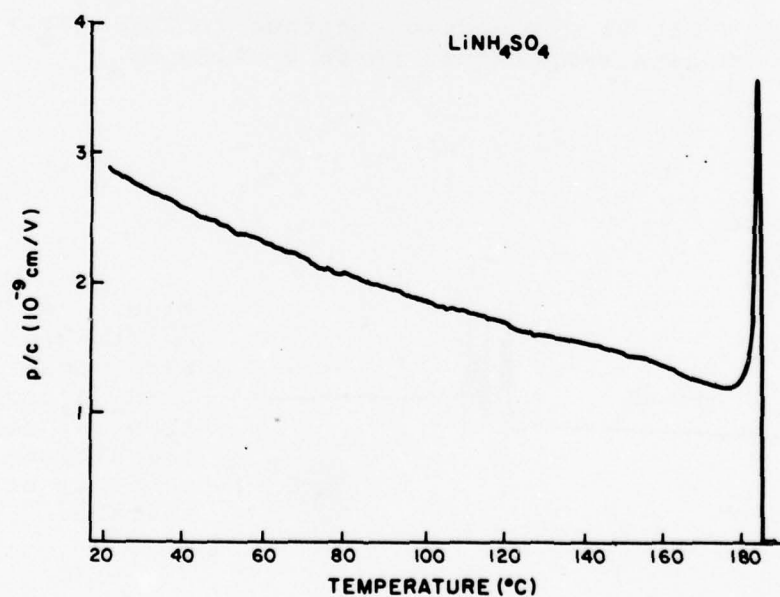


Figure 28. Temperature behavior of p/c in LiNH_4SO_4 .

The application of a bias field (5 kV/cm) along the c-axis was observed to enhance the peak value of p/c by $\sim 35\%$ and induce a small pyroelectric response above T_c . Within our maximum temperature resolution ($\sim 0.2^\circ\text{C}$), we observed no shift in the transition temperature.

Byer-Roundy measurements on c-cut LiNH_4SO_4 samples were also performed in vacuum and helium. In both cases large background currents are observed near T_c . The pyroelectric coefficient at 50°C determined by this method is about $6 \times 10^{-9} \text{ C cm}^{-2} \text{ }^\circ\text{C}^{-1}$. Measurements on "a" and "b" cut samples also exhibit the large background current. This spurious current is a bulk property and could possibly be induced through some defect (i.e., impurity) mechanism or some contact potential.

(2) Low Temperature Phase Transition

The dynamic measurement of the temperature behavior of p/c is shown in Figure 29 for LiNH_4SO_4 . Upon cooling, p/c increases slowly and becomes nearly constant near the transition temperature ($T_t = 5.5^\circ\text{C}$), while the pyroelectric response drops sharply and becomes unstable so that a value for p/c cannot be determined. Below 4°C , the pyroelectric response becomes stable with a value of p/c which is about 20% of the value obtained above 5.5°C . On heating, the pyroelectric response is stable and nearly constant up to 9°C , then increases and becomes unstable. A sharp increase is observed at 11°C after which the response again becomes stable. In the deuterated crystals, the transition is shifted toward lower temperature $T_t = 1.5^\circ\text{C}$ (cooling) and a temperature hysteresis of about 6°C is observed. The lower transition was also examined in both LiNH_4SO_4 and LiND_4SO_4 by measuring the temperature behavior of the pyroelectric current during heating and cooling. The pyroelectric current of a partially electroded sample of LiND_4SO_4 near T_t exhibited the same multiple peaking behavior seen in partially electroded samples of $\text{Gd}_2(\text{MoO}_4)_3$. A fully electroded sample of LiND_4SO_4 resulted in a marked reduction of the number of multiple peaks

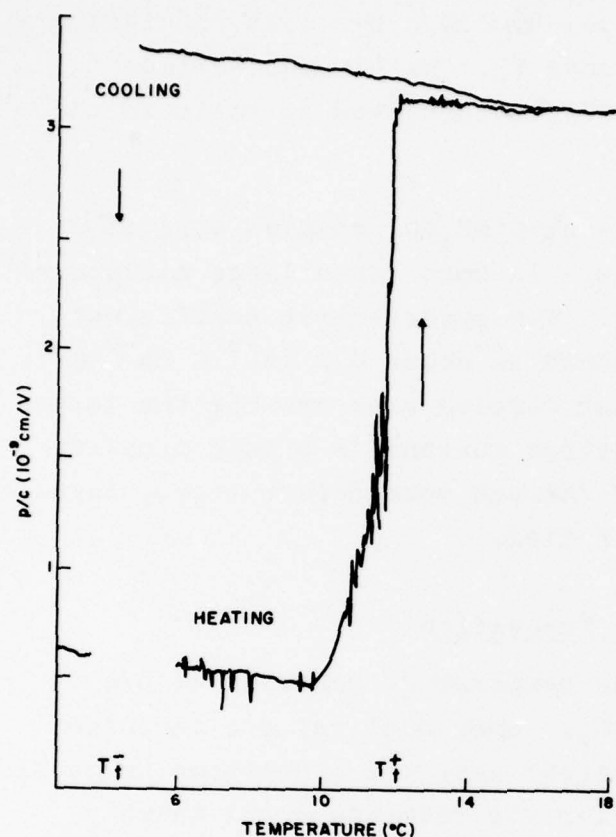


Figure 29. Temperature dependence of p/c , in LiNH_4SO_4 upon heating and cooling through the low temperature phase transition.

but did not completely eliminate this behavior (Figs. 30 and 31). We conclude that the reduction of clamping achieved by the use of full face electrodes coupled with the fact that thermal annealing eliminates the multiple peaking behavior, is conclusive proof that this effect can be attributed to strains present in the bulk crystal. These strains are induced in the crystal during growth and/or during sample fabrication. It is clear that all quantitative measurements should be performed only on suitably annealed samples.

From the sign of the pyroelectric current released near T_c , we deduce that the spontaneous polarization of LiND_4SO_4 on the low temperature side of T_c is smaller than that above T_c . The jump in spontaneous polarization, measured by integration of the pyroelectric current released is $0.27 \mu\text{C}/\text{cm}^{-2}$ ($\pm 10\%$).

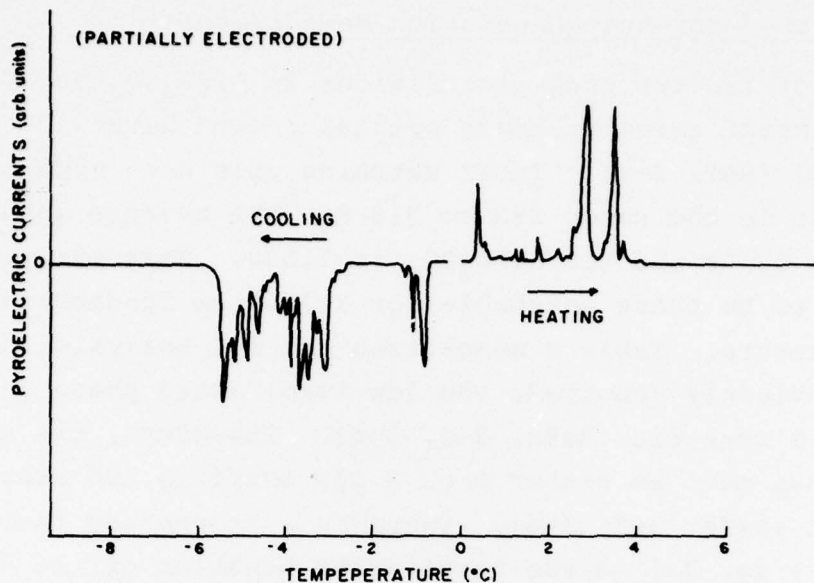


Figure 30. Multiple peaking in the pyroelectric current of partially electroded LiND_4SO_4 as seen during both heating and cooling through the low temperature transition.

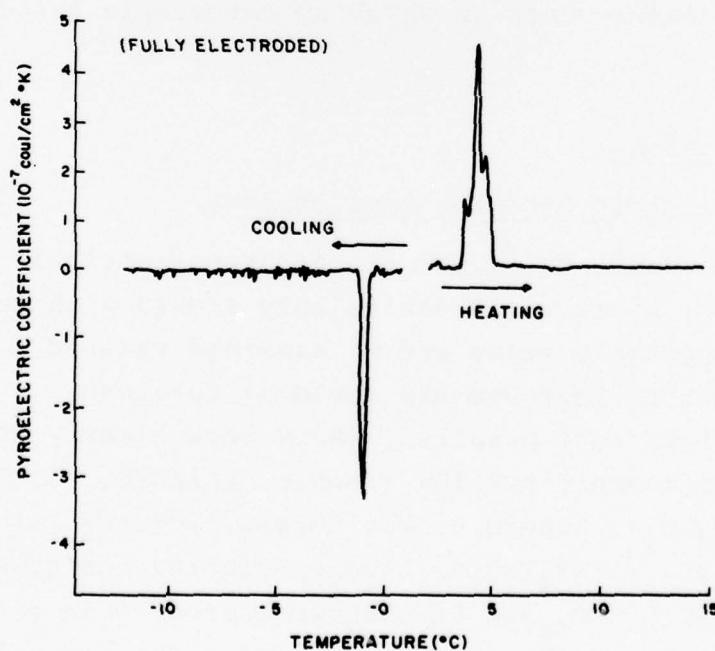


Figure 31. Pyroelectric current of LiND_4SO_4 measured on a fully electroded sample.

3.1.5 Second Harmonic Generation Measurements

The nature of the two phase transitions in LiNH_4SO_4 and LiND_4SO_4 was investigated using standard optical second harmonic techniques (SHG) (Ref. 3-5). Index matching oils were used only for temperatures in the range 293 to 313 K. The average index for LiNH_4SO_4 is 1.496 and for LiND_4SO_4 is 1.500. Both materials were found to be phase matchable for a $1.06 \mu\text{m}$ fundamental at room temperature. Table 8 summarizes the SHG analysis. Contrary to data previously reported, the low temperature phase in both compounds is acentric (Refs. 3-2, 3-4). Therefore, the symmetry of this phase must be either m or 2 and confirms two previous assignments (Refs. 3-3, 3-6). There is a pronounced thermal hysteresis (Fig. 32) in the temperature behavior of the SHG intensity, on the order of 6° for the high temperature transition and 10° at the lower transition. This hysteresis in the low temperature transition is somewhat larger than that observed in our pyroelectric measurements. For the high transition, the observed hysteresis is at variance with our dielectric and pyroelectric measurements in which no detectable hysteresis is observed.

3.1.6 Conclusions

(1) Pyroelectric Detector Applications

The room temperature value for the figure-of-merit is about 70% of that of TGS; moreover it varies only slowly with temperature. This is a respectable value and we examined related materials to see if any further improvements could be obtained. A number of related materials were prepared. Many were clearly centrosymmetric at room temperature for example, $(\text{LiRbSO}_4, \text{LiTlSO}_4, \text{CsNH}_4\text{SO}_4, \text{KNH}_4\text{SO}_4)$; others either formed hydrates (LiNaSO_4) or proved insoluble $(\text{LiNH}_4\text{TeO}_4)$, thus precluding the growth of crystals. Only LiKSO_4 and LiCsSO_4 were studied in detail. Our investigation of these two materials, reported below, shows them to be essentially different from LiNH_4SO_4 .

TABLE 8. OPTICAL SECOND HARMONIC POWDER ANALYSIS
DATA (PARTICLE SIZE: 212-300 μm).

Crystal	Phase	Temperature Interval (K)	\bar{n}_o (5300 Å)	Result	Signal Level Relative $\alpha\text{-SiO}_2$
LiNH_4SO_4	mmm	478 - 505	no oil	-	0.000
	mm2	293 - 455	1.496	+	2.2
	2 or m	170 - 270	no oil	+	0.3
LiND_4SO_4	mmm	478 - 505	no oil	-	0.000
	mm2	293 - 455	1.500	+	2.2
	2 or m	185 - 260	no oil	+	0.3

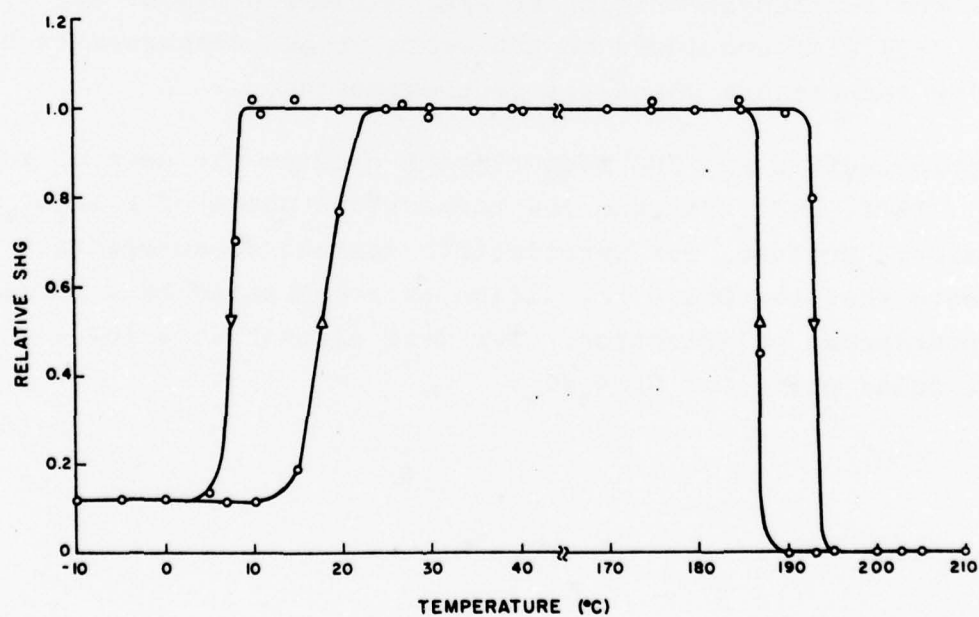


Figure 32. Temperature Behavior of SHG signal in LiND_4SO_4 .

We conclude that further study of related materials is merited on the basis of the high figure-of-merit obtained for LAS and DLAS. However, without even one related material it is difficult to determine precisely what direction should be taken. The neutron scattering analysis of these two materials already in progress might reveal enough about their microscopic structure to suggest plausible directions.

(2) Low Temperature Phase Transition

On cooling, LiNH_4SO_4 is reported to exhibit a first order phase transition from the orthorhombic (C_{2v} -mm2) structure to monoclinic at 10°C . Yuzvak et al. (Ref. 3-3) reported a step-wise increase in spontaneous polarization at this phase transition and assigned the low temperature phase to the polar class 2. A recent study by Poulet and Mathieu (Ref. 3-6) confirmed this polar assignment from measurements of piezoelectric response induced by stress along the two-fold axis below 10°C . However, Mitsui et al. (Ref. 3-4) concluded from the temperature behavior of optical second harmonic generation that the low temperature phase was centrosymmetric class 2/m. Aleksandrova et al. (Ref. 3-2) also concluded on the basis of SHG measurements that the low temperature phase was centrosymmetric.

Our pyroelectric and SHG measurements confirm the data of Yuzvak et al. (Ref. 3-3) that the low temperature phase of LiNH_4SO_4 is polar. However, our pyroelectric current measurements indicate that the phase transition is accompanied by a decrease in spontaneous polarization. Our data also shows a low temperature polar phase for LiND_4SO_4 .

3.2 Lithium Cesium Sulfate and Lithium Potassium Sulfate

On the basis of optical second harmonic generation and pyroelectric measurements on LiCsSO_4 , we resolve the ambiguity in the literature about the space group of this material and conclude that lithium cesium sulfate does not belong to a pyroelectric space group.

Separate measurements of the pyroelectric coefficient, dielectric constant and specific heat of LiKSO_4 yield a figure-of-merit of $1.25 \times 10^3 \text{ cm}^2/\text{C}$. This is less than one-third the figure-of-merit of TGS. We concluded that this material does not have attractive properties for practical applications.

3.2.1 Preparation and Characterization of Materials

The double sulfates LiKSO_4 and LiCsSO_4 were prepared by combining aqueous solutions of the appropriate alkali sulfates (Apache) according to stoichiometry. Single-crystals were grown from aqueous solution via isothermal evaporation at 313 K. Lattice parameters were obtained from X-ray precession diagrams. For LiKSO_4 , the hexagonal unit cell has $a = 5.15 \text{ \AA}$ and $c = 8.63 \text{ \AA}$, and for LiCsSO_4 , the orthorhombic unit cell has $a = 9.45 \text{ \AA}$, $b = 5.45 \text{ \AA}$, and $c = 8.80 \text{ \AA}$. These values are in good agreement with the previously reported work of Bradley (Ref. 3-7) and Hahn et al. (Ref. 3-8).

Flame emission analyses showed 300 and 500 ppm Na impurity in the crystals of LiKSO_4 and LiCsSO_4 , respectively. Atomic absorption analyses showed 300 ppm Rb in the LiCsSO_4 crystals.

3.2.2 Optical Second Harmonic Generation Measurements

Powders ground from single crystal samples of LiKSO_4 and LiCsSO_4 were examined by optical second harmonic analysis (Ref. 3-9) from 260 to 560 K. LiKSO_4 exhibited a temperature invariant ($\pm 10\%$) second harmonic signal on the order of $0.5 \alpha\text{-SiO}_2$. This is consistent with the reported non-centrosymmetric crystal structure, space group $P6_3$, (Ref. 3-7) and indicates the absence

of any phase transitions in the temperature range. In crystals of LiCsSO_4 , no detectable second harmonic at a level of 10^{-3} $\alpha\text{-SiO}_2$ was observed from 260 to 560 K, indicating the absence of a non-centrosymmetric phase in this temperature interval.

3.2.3 Specific Heat Measurements

Single crystals of LiKSO_4 and LiCsSO_4 were examined from 280 to 580 K with a computer-controlled Perkin-Elmer differential scanning calorimeter, Model DSC-2. The instrument calibration, operating parameters, and data refinement were performed as previously described (Ref. 3-10). No phase transitions in either material were observed in agreement with the second harmonic generation experiments.

Two specific heat determinations were made from 300 to 520 K on two different samples of each material. The four measurements on each material agreed within 1%. The resulting mean values are reported as molar heat capacities and are given in Table 9 in intervals of 20 K. Using a least squares curve fit, the temperature dependence of the molar heat capacity of the temperature interval $300 \leq T(\text{K}) \leq 520$ is for LiKSO_4 ,

$$\bar{c}_p (\text{J mol}^{-1} \text{K}^{-1}) = 81.1 + 1.247(10^{-1})T + 7.2(10^{-6})T^2$$

and for LiCsSO_4 ,

$$\bar{c}_p (\text{J mol}^{-1} \text{K}^{-1}) = 63.0 + 1.585(10^{-1})T + 4.8(10^{-6})T^2.$$

The c_p values are considered accurate to $\pm 1.5\%$ relative to the NBS values for sapphire (Ref. 3-11).

The similarities of the molar heat capacities reflect similar interatomic bonding energies in the two materials. The temperature slope of the molar heat capacities are quite different, namely, for LiKSO_4 , $1.32 (10^{-1}) \text{ J mol}^{-1} \text{K}^{-2}$,

TABLE 9. ISOBARIC MOLAR HEAT CAPACITIES OF LiKSO_4 (MW = 142.10) and LiCsSO_4 (MW = 235.91).

T(K)	$C_p \text{ (J/mol}^{-1}\text{K}^{-1}\text{)}$	
	LiKSO_4	LiCsSO_4
300	$119.0 \pm 1.5\%$	$111.0 \pm 1.5\%$
320	121.7	114.0
340	123.8	116.9
360	126.9	120.9
380	128.8	123.6
400	130.7	126.5
420	132.9	128.5
440	135.3	131.5
460	138.0	135.7
480	142.0	139.7
500	145.8	143.2
520	148.0	146.9

and for LiCsSO_4 , $1.60(10^{-1} \text{ J mol}^{-1}\text{K}^{-2})$ over the temperature range measured. This difference can be attributed to dissimilar crystal structures, namely, LiKSO_4 is hexagonal, space group $P6_3$ while LiCsSO_4 is orthorhombic, probable space group Pcmn .

3.2.4 Pyroelectric Measurements

Pyroelectric measurements in LiCsSO_4 were performed by a modification of the Chynoweth technique (Ref. 3-13). In crystals of LiCsSO_4 , all three principal crystallographic directions were studied from room temperature to about 473 K. No pyroelectric response was observed. This result places an upper limit on the pyroelectric coefficient of $10^{-10} \text{ C/cm}^2\text{K}$ suggesting that the structure is non-polar.

For LiKSO_4 , single crystal samples oriented with surfaces normal to [001] were studied by the Byer-Roundy technique (Ref. 3-13). The sample plates were polished on both sides to a thickness of 0.66 mm using 3 μm alumina grit and mineral oil. Both faces of the sample (area 0.32 cm^2) were fully electroded with silver paint. The measurements were performed under a helium atmosphere at a heating rate of 6.5 K min^{-1} . The pyroelectric coefficient was found to be $1.6 \pm 10\% \times 10^{-9} \text{C cm}^{-2} \text{K}^{-1}$ and temperature invariant from 313 to 343 K. The measurement above 343 K was impeded by a large background current. Early work by Ackermann (Ref. 3-14) showed a pyroelectric coefficient of $1.61 \times 10^{-9} \text{C cm}^{-2} \text{K}^{-1}$ at 293 K which rises slowly to $1.78 \times 10^{-9} \text{C cm}^{-2} \text{K}^{-1}$ at 352 K, in reasonable agreement with our measurements.

The application of a dc field of 5 kV cm^{-1} for 1 hour and 2 kV/cm^{-1} for an additional 12 hours did not produce a change in sign of the polarization in LiKSO_4 . This suggests that LiKSO_4 is not ferroelectric in agreement with the observations of Ando (Ref. 3-15).

3.2.5 Dielectric Measurements

The dielectric constant of LiKSO_4 was measured at 8 kHz. For the dielectric constant, ϵ_{33} of LiKSO_4 , we measure a value of $7.2 \pm 10\%$ at room temperature which increases to a value of $7.6 \pm 10\%$ at 473 K. Ando (Ref. 3-15) measured a value of about 6 for ϵ_{33} at 100 kHz over the same temperature interval. This small discrepancy may be attributed to the dispersion of the dielectric constant in LiKSO_4 .

3.2.6 Figure-of-Merit and Conclusions

The absence of a measureable SHG signal and pyroelectric coefficient in LiCsSO_4 indicates that the correct space group is Pcmn and not $\text{Pc}2_1\text{n}$, thus resolving any ambiguity (Ref. 3-8) in the determination of the structure of this material. Since this is not a polar space group we conclude that this material has no pyroelectric effect.

Combining a density of 2.39 gm/cm^3 for LKS obtained from the lattice parameter measurements with the values of the pyroelectric coefficient, dielectric constant and specific heat described above, one obtains a value of $1.25 \times 10^3 \text{ cm}^2/\text{C}$ for the figure-of-merit of LiKSO_4 at room temperature. This value varies only slightly from room temperature up to 70°C . Since this value is less than one-third the figure-of-merit of TGS, we conclude that lithium potassium sulfate does not have attractive properties for practical applications.

3.3 Lithium Trihydrogen Selenite

Lithium trihydrogen selenite $\text{LiH}_3(\text{SeO}_3)_2$ is ferroelectric at room temperature with a very large value of spontaneous polarization ($\sim 15 \mu\text{C}/\text{cm}^2$) (Ref. 3-16). Hydrostatic pressure studies (Ref. 3-17) have shown the Curie point to be 145°C , 35° above the melting point.

Dielectric hysteresis measurements were made on several samples of $\text{LiH}_3(\text{SeO}_3)_2$ using a 60 Hz Sawyer-Tower bridge. Sample to sample variations were very large. Measured values of P_s varied from $7.7 \mu\text{C}/\text{cm}^2$ to $14 \mu\text{C}/\text{cm}^2$. In addition, some hysteresis loops also showed an internal bias of as much as $1.8 \text{ kV}/\text{cm}$. A hysteresis loop representative of one of the better samples is shown in Figure 33.

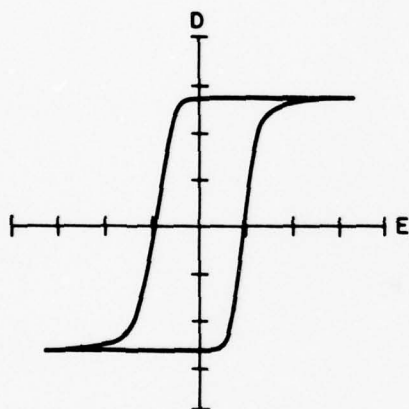


Figure 33. Ferroelectric hysteresis loop for $\text{LiH}_3(\text{SeO}_3)_2$. The vertical axis is $1 \mu\text{C}/\text{division}$ and the horizontal axis is $200/\text{V}$ division. For samples of area $A_2 = 0.227 \text{ cm}^2$ and thickness $t = 0.50 \text{ mm}$, $P_s = 12.1 \mu\text{C}/\text{cm}^2$ and $E_c = 3.8 \text{ kV}/\text{cm}$.

Measured pyroelectric coefficients in the lithium trihydrogen selenite samples were found to be directly related to the degree of poling which could be achieved. These results, shown in Table 10, demonstrate that the samples can have "easy" or "hard" poling directions.

TABLE 10. COMPARISON OF EASY AND HARD POLING DIRECTIONS FOR A $\text{LiH}_3(\text{SeO}_3)_2$ SAMPLE AT 24°C.

Field Direction	P_s $\mu\text{C}/\text{cm}^2$	E_c kV/cm @ 60 Hz	p $\mu\text{C}/\text{cm}^2\text{-K}$
+	7.7	3.2	0.92×10^{-8}
-	11.3	5.0	1.45×10^{-8}

Pyroelectric coefficient and dielectric constant were measured on a sample that showed no bias effects; the sample was poled at high temperature (84°C) and the pyroelectric data taken on cooling without a bias field. The pyroelectric and dielectric data are shown in Figure 34. These data suggest that $\text{LiH}_3(\text{SeO}_3)_2$ might be approaching a proper phase transition. This would be in agreement with a Curie constant 4×10^4 K measured by Samara and Anderson (Ref. 3-17).

The ratio p/ϵ is smaller than that found in TGS-type crystals. The large value of P_s does not produce a correspondingly large pyroelectric current since P_s is relatively constant with temperature in the range of the data, about 100°C below the Curie point. Over the temperature range 40-80°C, the change in P_s (calculated by integrating p) is $1.35 \mu\text{C}/\text{cm}^2$, less than 10% of P_s . TGS by comparison has a change of P_s of $1.2 \mu\text{C}/\text{cm}^2$ for 0-40°C, nearly 35% of P_s .

These results suggest that modifications of lithium trihydrogen selenite might exhibit useful properties for practical applications.

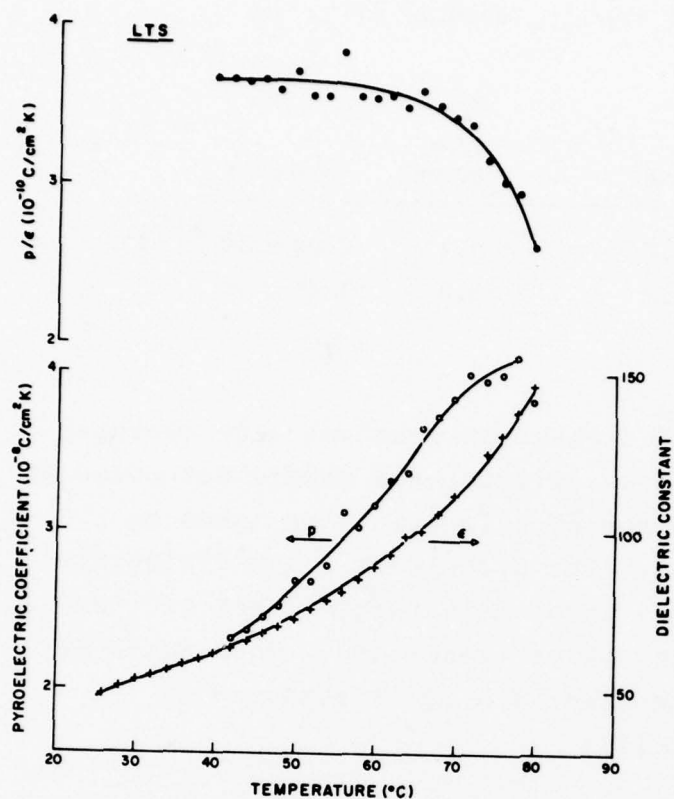


Figure 34. Dielectric constant and pyroelectric coefficient of lithium trihydrogen selenite from room temperature to 80°C .

3.4 References

- 3-1. I.M. Iskornev and I.N. Flerov, Sov. Phys. Solid State 19, 605 (1977).
- 3-2. I.P. Aleksandrova, I.S. Kabanov, S.V. Melnikova, T.I. Chemasova, and V.I. Yuzvak, Sov. Phys. Crystallogr. 22, 182 (1977).
- 3-3. V.I. Yuzvak, L. Zharebtsova, V.B. Shkuryaeva, and I.P. Aleksandrova, Sov. Phys. Crystallogr. 19, 480 (1975).
- 3-4. T. Mitsui, T. Oka, Y. Shiroishi, M. Takashiga, K. Ito and S. Sawada, J. Phys. Soc. Japan 39, 480 (1975).
- 3-5. J.P. Dougherty and S.K. Kurtz, J. Appl. Cryst. 9, 287 (1976).
- 3-6. H. Poulet and J.P. Mathiew, Solid State Comm. 21, 421 (1977).
- 3-7. A.J. Bradley, Phil. Mag. 48, 1225 (1925).
- 3-8. Th. Hahn, G. Lohre and S.J. Chung, Naturwissenschaften 56, 459 (1969).
- 3-9. J.P. Dougherty and S.K. Kurtz, J. Appl. Crystallogr. 9, 145 (1976).
- 3-10. M. Delfino, G.M. Loiacono and J.A. Nicolosi, J. Solid State Chem. 23, 289 (1978).
- 3-11. D.C. Ginnings, and G.T. Furukawa, J. Amer. Chem. Soc. 75, 522 (1953).
- 3-12. A.G. Chynoweth, Appl. Phys. 27, 78 (1956).
- 3-13. R.L. Byer and C.B. Roundy, Ferroelectric 5, 267 (1973).
- 3-14. W. Ackermann, Ann. Phys. (Leipzig) 46, 197 (1915).
- 3-15. R. Ando, J. Phys. Soc. Japan 17, 937 (1962).
- 3-16. R. Pepinsky and K. Vedam, Phys. Rev. 114, 1217 (1959).
- 3-17. G.A. Samara and D.H. Anderson, Sol. State Comm. 4, 653 (1966).

4. PROPIONATES

Initial measurements of the pyroelectric and dielectric properties of dicalcium lead propionate (DLP) reveal the presence of an internal bias field. Annealing samples of dicalcium lead propionate did not eliminate the effects of internal bias fields as reported in the literature; indeed the properties of the samples were severely degraded. Initial measurements on the specific heat of DLP and dicalcium strontium propionate (DSP) show, as expected, no large anomaly at the transition temperature.

A theoretical analysis based on a free energy appropriate to a second-order pseudoproper phase transition was carried out; the predictions agree with our measurements as well as with certain published data. In this analysis, the figure-of-merit has a maximum as a function of temperature which can be expressed in terms of the free-energy parameters. Using data from the literature (which is compatible with our measurements), we can estimate these free-energy parameters and project a maximum figure-of-merit of $4.2 \times 10^3 \text{ cm}^2/\text{C}$ for DSP and $7.3 \times 10^3 \text{ cm}^2/\text{C}$ for DLP.

4.1 Initial Pyroelectric and Dielectric Measurements on DLP

A Byer-Roundy measurement on an as-grown DLP sample was performed in inert gas (helium). The values of the pyroelectric coefficient thus determined were $1.0 \times 10^{-9} \text{ C/cm}^2 \text{ K}$ at 30°C , and $8.5 \times 10^{-9} \text{ C/cm}^2 \text{ K}$ at the peak (Fig. 35). The long tail of the pyroelectric current above $T_c \approx 56^\circ\text{C}$ is probably due to the internal bias field which normally exists in as-grown DLP samples (Ref. 4-1).

Using the dynamic method we measured the temperature dependence of the ratio p/c in an as-grown sample of DLP, applying various dc fields in the direction opposite to the internal bias (Fig. 36). The calibration in this measurement was obtained by setting at 40°C : $p = 2 \times 10^{-9} \text{ C/cm}^2 \text{ K}$, $c = 1.8 \text{ J/cm}^3 \text{ K}$. As the dc field was increased from 0 to 12 kV/cm, the peak in

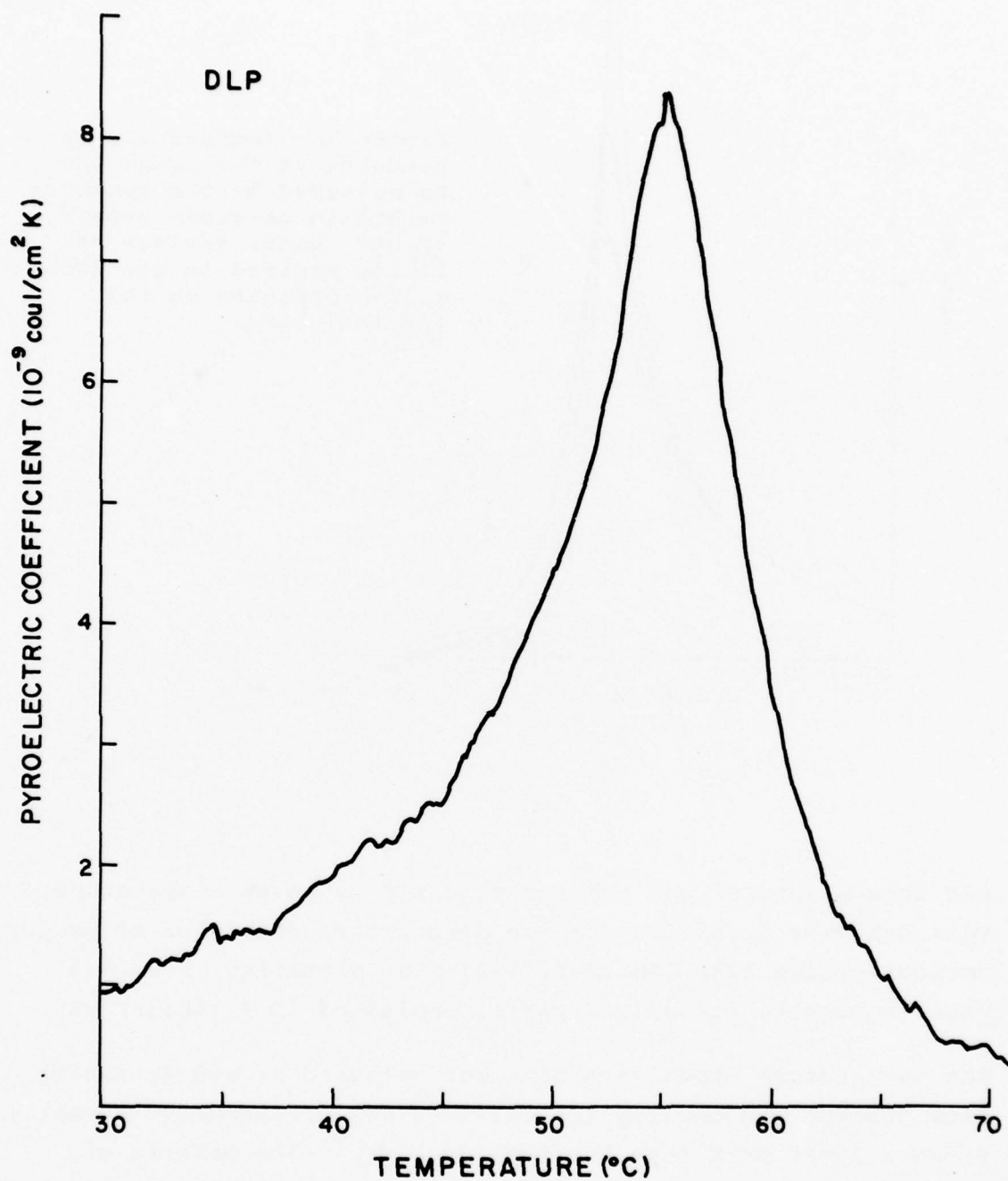


Figure 35. Pyroelectric coefficient of as-grown DLP sample as measured by the Byer-Roundy technique.

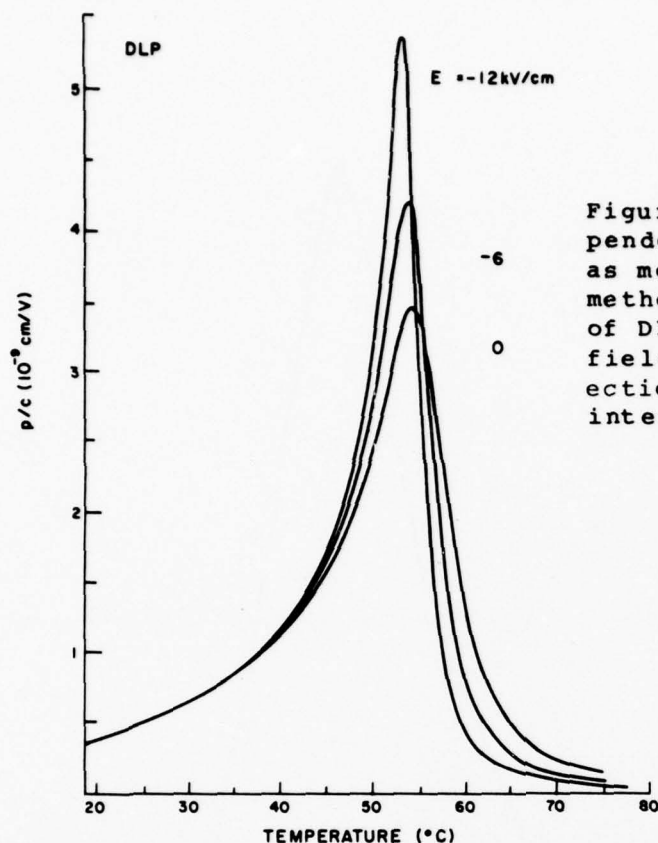


Figure 36. Temperature dependence of the ratio p/c as measured by the dynamic method in as-grown sample of DLP, under various dc fields applied in the direction opposite to the internal bias.

p/c became sharper and shifted slightly to lower temperature. This behavior is similar to the pyroelectric behavior of proper ferroelectrics like TGS (Ref. 4-2) and colemanite (Ref. 4-3) under a biasing field, and can be explained in a similar way.

The temperature dependence of ϵ was measured at 800 Hz during slow heating and cooling (Fig. 37). The heating curve normally shows a lower peak than the cooling curve. The effects of external dc fields applied in the same direction as the internal bias field (+ 3 kV/cm) and opposite the internal bias (- 3 kV/cm) are shown in Figure 38.

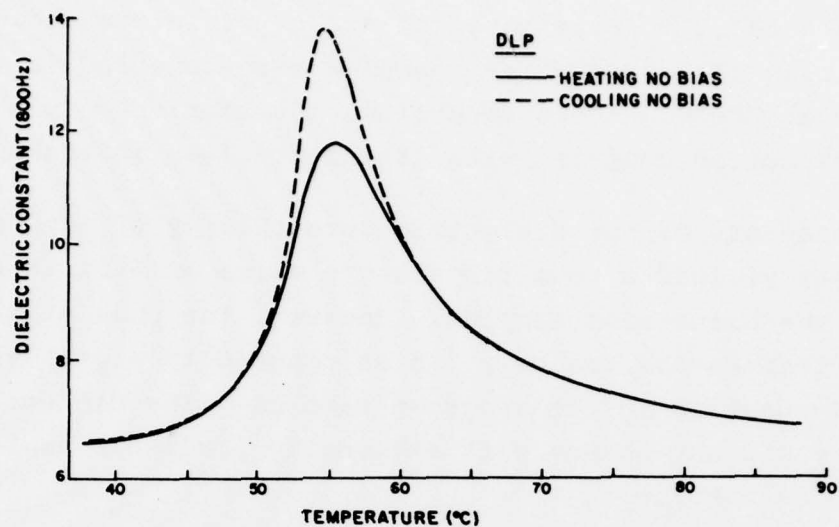


Figure 37. Temperature dependence of dielectric constant of as-grown DLP.

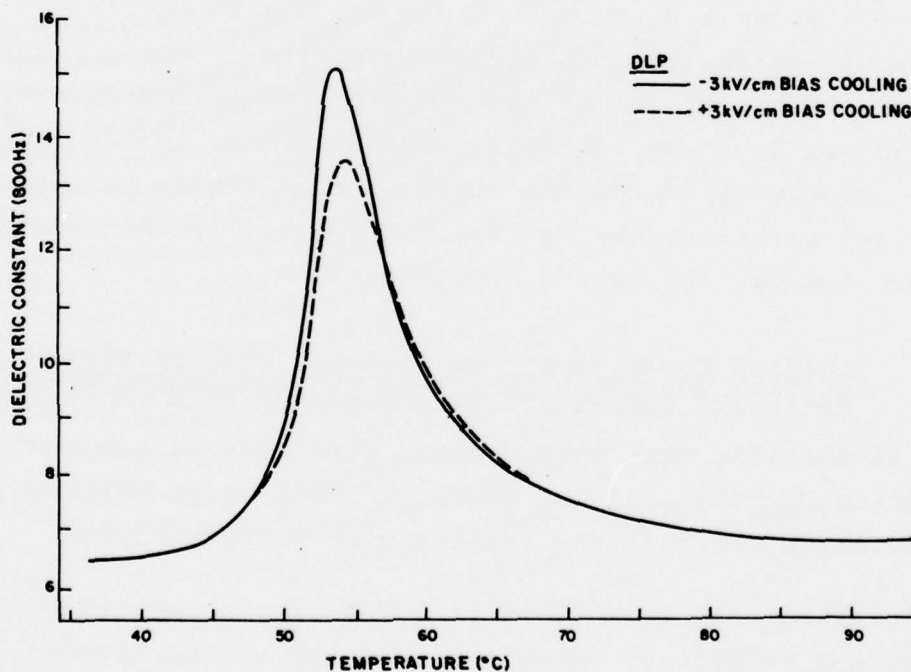


Figure 38. Temperature dependence of dielectric constant of as-grown DLP under dc field of 3 kV/cm applied in the direction of the internal bias (+) and opposite to the internal bias (-).

4.2 Annealing Experiments on Dicalcium Lead Propionate

In an attempt to eliminate the effect of internal bias fields in dicalcium lead propionate, samples were annealed in air for 24 hours at 200°C. After annealing, the sample had a light tan discoloration compared with its water-clear initial appearance.

Measurements of the dielectric permittivity of the annealed samples yielded a room-temperature value of 6.9, in agreement with the unannealed samples. However, the peak at the transition temperature was only 7.5 as opposed to a peak value of 12-14 observed in the as-grown samples. The dielectric permittivity did not change with externally applied bias fields as large as 5 kV/cm.

Measurements of the pyroelectric coefficient by the Byer-Roundy technique revealed no detectable pyroelectric current in the annealed samples.

Thus, the annealing procedures did not simply eliminate the effect of internal bias fields as reported in the literature. Rather, the properties of the samples were seriously degraded. Two explanations are possible, namely, either chemical impurities in the samples produced the observed degradation or the proper annealing technique was not fully described in the literature. We lean towards the latter hypothesis.

4.3 Initial Measurements of Specific Heat of Dicalcium Strontium Propionate and Dicalcium Lead Propionate

Initial specific heat measurements were made on samples of $\text{Ca}_2 \text{Sr}(\text{CH}_3\text{CH}_2\text{COO})_6$ and $\text{Ca}_2 \text{Pb}(\text{CH}_3\text{CH}_2\text{COO})_6$ which were obtained from outside sources; the samples were visibly flawed.

Measurements made from 270 K to 360 K with an accuracy of about 5% did not reveal any anomalous behavior at the ferroelectric-paraelectric phase transition temperature (283 K for DSP and 331 K for DLP). This is consistent with the expectation that the anomaly in the specific heat is quite small (1-4%) for these materials.

The molar heat capacity of dicalcium strontium propionate has the form:

$$c_p \text{ (J/molK)} = -375.9 + 3.10 T \quad 290K \leq T \leq 360K.$$

Roughly the same magnitude with a similar linear temperature dependence was obtained for the lead salt. For DSP at 310 K, the value for the specific heat is 21% lower than that reported by Nakamura, et al. (Ref. 4-4).

4.4 Analysis of the Pyroelectric Behavior of DLP above T_c

According to Takashige et al. (Ref. 4-1), the dielectric constant of unbiased DLP crystals obeys a modified Curie-Weiss law:

$$\epsilon = \epsilon_c + C/(T - T_o) \quad (1)$$

with $\epsilon_c = 4$ and $C = 69$ K. Based on this result, the pyroelectric behavior of as-grown DLP above T_c can be analyzed in the following way.

From a few degrees above T_c and upwards, where nonlinearities in the dielectric constant can be neglected, it can be assumed that the polarization induced by the biasing field E_b is,

$$P = \epsilon_o (\epsilon - 1) E_b = \epsilon_o [(\epsilon_c - 1) + C/(T - T_o)] E_b, \quad (2)$$

where $\epsilon_o = 8.85 \times 10^{-14}$ F/cm, E_b is expressed in V/cm and P is in C/cm². The pyroelectric coefficient is thus,

$$p = -dP/dT = \epsilon_o C E_b / (T - T_o)^2. \quad (3)$$

It follows that plotting $p^{-1/2}$ versus T one should obtain a linear plot with a slope given by $(\epsilon_o C E_b)^{-1/2}$. Figure 39 shows $p^{-1/2}$, obtained by the Byer-Roundy measurement of p , as a function of T . The agreement with the expected behavior is reasonably good. The value obtained for E_b , using $C = 69$ K, is about 15 kV/cm in agreement with the value estimated by Takashige et al. (Ref. 4-1), from their dielectric measurements.

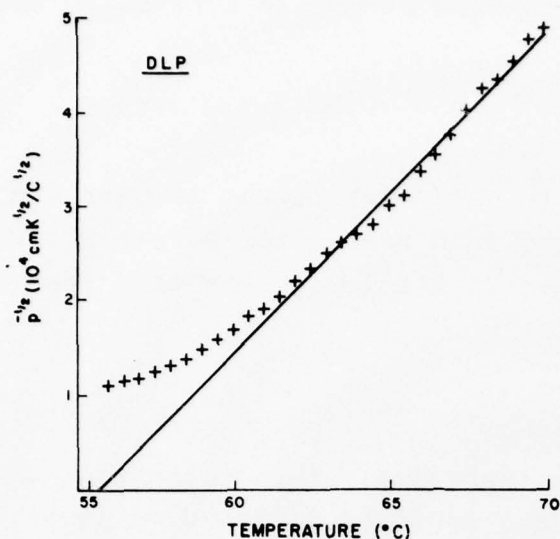


Figure 39. Square root of the reciprocal of the pyroelectric coefficient vs. temperature for as-grown sample of DLP.

4.5 Analysis of Propionates as Second-Order Pseudo-proper Ferroelectrics

Both dicalcium lead propionate (DLP) and dicalcium strontium propionate (DSP) exhibit two phase transitions, and the structures of the two crystals are reported to be identical in each of the corresponding phases (Ref. 4-1). It is the high-temperature transition (occurring at 54°C and 8.5°C in DLP and DSP, respectively) which is of interest here. The remarkable resemblance, visible in the measurements reported above and elsewhere (Ref. 4-1), between the dielectric behavior of the propionates at these transitions and that of ordinary ferroelectrics at second-order phase transitions has led to the suggestion (Ref. 4-5) that these are pseudoproper ferroelectrics, i.e., that the order parameter has the same symmetry as the polarization so that a linear coupling between the two is possible (Ref. 4-6). If in fact no increase in the size of the unit cell occurs at the transition, this view is consistent with the observed reduction in point group symmetry from 422 (D_4) to 4 (C_4), since it has been shown (Ref. 4-7) that this symmetry change can be induced by the one-dimensional, polar representation A_2 of 422. If the order parameter η is one-dimensional and the transition is second

order (so that terms of order η^6 and higher can be neglected), the thermodynamic potential can be written in the form:

$$\Phi(\eta, P) = \Phi_0(T) + \frac{\alpha_0(T-T_0)}{2} \eta^2 + \frac{\beta}{4} \eta^4 + \frac{\chi^{-1}}{2} P^2 + a\eta P - EP \quad (4)$$

where α_0 , β , χ^{-1} and a are taken, as usual, to be temperature independent. In the discussion of this thermodynamic potential it is necessary to avoid the restriction $E = 0$, since the experimental results for unannealed DLP show strong effects due to internal bias fields.

The equilibrium values of $\eta(E, T)$ and $P(E, T)$ are determined from the equations:

$$\begin{aligned} \partial\Phi/\partial\eta &= \alpha_0(T-T_0)\eta + \beta\eta^3 + aP = 0 \\ \partial\Phi/\partial P &= \chi^{-1}P + a\eta - E = 0 \end{aligned} \quad (5)$$

Thus, the temperature and field dependence of the polarization is readily given in terms of the temperature and field dependence of the order parameter,

$$P = \chi E - a\chi\eta(E, T) \quad (6)$$

while $\eta(E, T)$ is in turn obtained from the solution of the cubic equation:

$$\left(\frac{a\chi}{K}\right)^2 \eta(E, T)^3 + (T-T_1)\eta(E, T) + (C/a\chi)E = 0 \quad (7)$$

where we have introduced the notation,

$$T_1 = T_0 + a^2\chi/\alpha_0, \quad K = a\chi(\alpha_0/\beta)^{1/2} \quad \text{and} \quad C = a^2\chi^2/\alpha_0.$$

In terms of the function $\eta(E, T)$ determined by this equation, one can obtain the dielectric constant,

$$\epsilon(E, T) = 1 + \chi + \frac{C}{[T-T_1 + 3(a\chi/K)^2\eta^2(E, T)]}, \quad (8)$$

the pyroelectric coefficient,

$$p(E,T) = \frac{a\chi\eta(E,T)}{[T-T_1 + 3(a\chi/K)^2\eta^2(E,T)]} \quad (9)$$

and the specific heat,

$$c(E,T) = C_0 + \frac{T(a\chi)^2/C\eta^2(E,T)}{[T-T_1 + 3(a\chi/K)^2\eta^2(E,T)]} \quad (10)$$

For the special case $E = 0$ when all internal bias fields have been annealed out, Equation (7) can be easily solved for $\eta(0,T)$; and we obtain in that case for the spontaneous polarization,

$$P_s = \begin{cases} K(T_1-T)^{1/2} & ; \quad T \leq T_1 \\ 0 & ; \quad T > T_1 \end{cases} \quad (11)$$

By least-square fitting of the P_s data of Takashige et al. (Ref. 4-1) between 37 and 49°C, we found for K the value $K = 3.1 \times 10^{-8} \text{ C/cm}^2 \text{ K}^{1/2}$. Similarly where $E = 0$ the dielectric constant takes the form,

$$\epsilon = \begin{cases} 1+\chi + C/(T-T_1) & ; \quad T < T_1 \\ 1+\chi + C/2(T_1-T) & ; \quad T > T_1 \end{cases} \quad (12)$$

The dielectric measurements of Takashige et al. (Ref. 4-1) confirm that the dielectric constant of unbiased DLP crystals has this form with $1 + \chi = 4$ and $C \approx 69 \text{ K}$.

With C and K thus determined, one has enough information to theoretically determine the pyroelectric coefficient,

$$p = \begin{cases} K/2 (T_1-T)^{-1/2} & ; \quad T < T_1 \\ 0 & ; \quad T > T_1 \end{cases} \quad (13)$$

and the specific heat,

$$c = \begin{cases} c_0 + K^2 T / 2C & ; \quad T < T_1 \\ c_0 & ; \quad T > T_1 \end{cases} \quad (14)$$

As expected (Ref. 4-6), the results obtained here are identical to those for a proper ferroelectric with a second-order transition (Ref. 4-3). Only the anomalously small Curie constant, $C = f^2 \chi_0^2 / \beta$, produced by the weak coupling between η and P , serves to demonstrate the "almost non-polar" character of the structural instability and to provide a quantitative meaning to the distinction between proper and pseudoproper transitions. No qualitative distinction based on symmetry is possible (Ref. 4-6).

4.6 Projected Figure of Merit

While the comparison of our experimental results with the predictions given above is still in progress, one can examine the consequences of this analysis for the figure-of-merit $M(1) = p/\epsilon c$ in unbiased crystals. Using the expressions in Equations (12), (13) and (14) above, we can express the figure-of-merit as,

$$M(1) = (K/2) (T_1 - T)^{-1/2} [(1 + \chi + (C/2) (T_1 - T)^{-1})^{-1} (c_0 + K^2 T / 2C)^{-1} \quad (15)$$

The maximum of $M(1)$ as a function of temperature occurs at a temperature T_m , such that,

$$(T_1 - T_m) - C/\epsilon - (K^2/cC) (T_1 - T_m)^2 = 0. \quad (16)$$

As we shall show shortly, the third term in this equation is negligible in the propionates, so T_m is simply given by,

$$T_m = T_0 - C/[2 (1 + \chi)] \quad (17)$$

In this approximation we can also take $c = c_0$ when evaluating $M(1)$ at $T = T_m$. The resulting maximum value of $M(1)$ is,

$$M_{\max} = (K/2c_o) (2(1+\chi)C)^{-1/2} \quad (18)$$

Note that M_{\max} has no natural optimum with respect to the parameters which characterize the phase transition: increasing K or decreasing C will always increase M_{\max} .

Table 11 summarizes the experimental values (Refs. 4-1, 4-8, 4-9) of the parameters required to evaluate M_{\max} and to justify the approximation which led to Equation (18). The results of the calculation are given in Table 12. The ratio $K^2/2C$ is a

TABLE 11. EXPERIMENTAL VALUES USED IN CALCULATION OF M_{\max} .

	<u>DLP</u>	<u>DSP</u>
$K(10^{-8} \text{ C/cm}^2 \text{ K}^{1/2})$	3.1	5.6
$C(K)$	69 ^a	73.2 ^b
$T_1 (\text{°C})$ ^a	54	8.5
$1 + \chi$	4 ^a	4 ^b
$c_o (\text{J/cm}^3 \text{ K})$ ^c	1.8	1.8

(a) Ref. 4-1

(b) Ref. 4-9

(c) Ref. 4-8

TABLE 12. PROJECTED PARAMETERS FOR PROPIONATES.

	<u>DLP</u>	<u>DSP</u>
$K^2/2C (10^{-5} \text{ J/cm}^3 \text{ K}^2)$	5.5	24
$c-c_o (10^{-2} \text{ J/cm}^3 \text{ K, at } T=T_c)$	1.8	6.8
$T_1 - T_m (K)$	8.6	9.1
$M_{\max} (10^3 \text{ cm}^2/C)$	4.2	7.3

measure of the strength of the specific heat anomaly $c-c_0$ and we find it to be very small. In fact the maximum value of $c-c_0$ found at T_c is just 1% of c_0 in DLP and less than 4% of c_0 in DSP. This is consistent with the results of Nakamura et al. (Ref. 4-8) for DSP and with our own preliminary measurements. Clearly, we are justified in neglecting the third term on the right-hand side of Equation (16) and in using Equation (18) for M_{\max} . The next entries in Table 12 show that T_m occurs close enough to T_0 (roughly 9 K below in both materials) so that having neglected higher-order terms in the thermodynamic potential probably has not seriously affected our results.

Finally, the values obtained for M_{\max} are quite substantial, namely, 4.2×10^3 and 7.3×10^3 cm²/C for DLP and DSP, respectively. Note for comparison the value reported earlier for triglycine sulfate (TGS) at 40°C of slightly less than 4×10^3 cm²/C.

4.7 References

- 4-1. M. Takashige, H. Iwamura, S. Hirotsu, and S. Sawada, *Ferroelectrics* 11, 431 (1976).
- 4-2. A. Shaulov and M. Simhony, *J. Appl. Phys.* 47, 1 (1976).
- 4-3. E. Fatuzzo, *J. Appl. Phys.* 31, 1029 (1960).
- 4-4. N. Nakamura, H. Suga, H. Chihara and S. Beki, *Bull. Chem. Soc. Japan* 38, 1779-1787 (1965).
- 4-5. J. Kobayashi, Y. Enomoto and Y. Sato, *Phys. Stat. Sol.* (b) 50, 335 (1972).
- 4-6. V. Dvorak, *Ferroelectrics* 7, 1 (1974).
- 4-7. V. Janovec, V. Dvorak and J. Petzelt, *Czech. J. Phys.* B 25, 1362 (1975).
- 4-8. N. Nakamura, H. Suga, H. Chihara and S. Seki, *Bull. Chem. Soc. Jpn.* 38, 1779 (1965).
- 4-9. K. Deguchi and E. Nakamura, *Phys. Rev. Letters* 37, 1642 (1976).

5. BORACITES

Initial dielectric and pyroelectric measurements were performed on samples of boracites obtained from Plessey Company. Major difficulties in fully poling these samples were encountered. The measurements are consistent with the data reported by Plessey Company and with the resulting expectations of a high figure-of-merit for Ni-Br boracite.

Specific heat measurements were made on samples of Zn-Br, Cr-Cl, Fe-I, Ni-Br and Cu-Cl boracite. In addition, infrared vibrational spectra, electronic spectra, and second harmonic measurements were performed on some of the samples in order to better characterize the material. A number of initial observations can be made:

- The cubic-orthorhombic phase transition appears to be strongly first order. This is indicated by the large latent heat of the transition, a detectable thermal hysteresis, and the discontinuous jump in the second harmonic intensity at the transition.
- The different members of the boracite family may be structurally dissimilar. This is indicated by large differences in the molar heat capacity of Fe-I and Cr-Cl boracite in the cubic phase. Large differences in the molar latent heats also support this conclusion.

5.1 Initial Dielectric and Pyroelectric Measurements on Boracites

5.1.1 Poling of Samples

Figure 40 shows an SEM image of a sample of Ni-Br boracite fabricated by the Plessey Company. The electrodes are silver epoxy. Measurements made on such samples show them to be very difficult to fully pole, as has been reported. On cooling

through the transition temperature with a bias field as large as 4.3 kV/cm, the pyroelectric current contains many large spikes characteristic of domain switching even a few degrees below the transition temperature. When such a bias field is removed well below the transition, the sample would on occasion switch into a polarization state opposite to that impressed by the bias field. These difficulties in poling confirm the experiment at

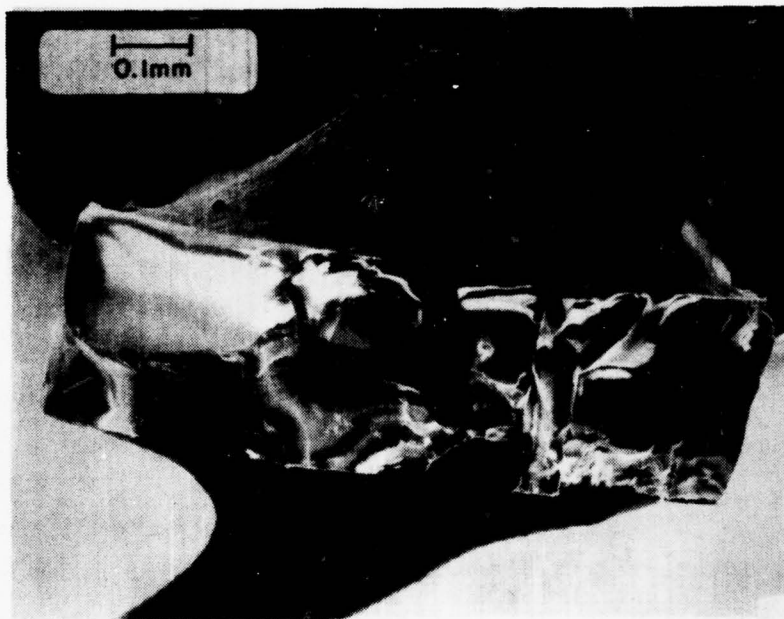


Figure 40. An electroded sample of Ni-Br boracite fabricated by the Plessey Co.

Plessey where 50 Hz hysteresis loops could not be obtained with fields as large as 30 kV/cm in Ni-Br boracite. Indeed, even after resorting to a high voltage pulse poling technique, they observe coercive fields between 50 kV/cm and 80 kV/cm only 5°C below the transition temperature.

In view of the previous experience with other improper ferroelectrics which are also ferroelastic, (see Section 2) it seems probable these poling difficulties are associated with the

mechanical boundary conditions. Thus, both growth-induced stresses and the effect of the electrodes play major roles in determining the orientation of polarization.

The application of a bias field should, nevertheless, improve the state of poling by properly orienting those portions of the sample not dominated by mechanical effects. Such bias fields were accordingly used in the measurements of the dielectric permittivity. Unfortunately, in the measurements of pyroelectric current, the leakage currents produced by the bias fields made reliable measurements on biased samples unattainable.

5.1.2 Ni-Br Boracite: Initial Pyroelectric Measurements

A typical measurement of the pyroelectric coefficient of an unbiased sample of Ni-Br boracite is shown in Figure 41. The measurements were made during cooling with no external bias field applied. The poling state is that "spontaneously" assumed by the sample and is probably determined by the mechanical boundary conditions. The temperature region from 123°C to the transition temperature at 126°C contains many large spikes indicative of an incompletely poled sample. The significance of this graph is not the absolute magnitude of the pyroelectric coefficient but rather the substantial increase in pyroelectric coefficient that occurs as the transition temperature is approached. The value at 123°C (3° below the transition temperature) is about six times the value at 90°C.

An estimate of the degree of poling can be obtained by comparing the approximately constant value of $0.26 \times 10^{-8} \text{ C/cm}^2 \text{ K}$ (the pyroelectric coefficient in the temperature range of 88°C-100°C) to the constant value of $1 \times 10^{-8} \text{ C/cm}^2 \text{ K}$ reported by Plessey for Ni-Br boracite in the 10°C-40°C temperature range. If the enhancement by a factor of six which we observe near the transition is superimposed on the low temperature value for the pyroelectric coefficient measured at Plessey, a figure-of-merit substantially better than that of DTGFB would be attained by

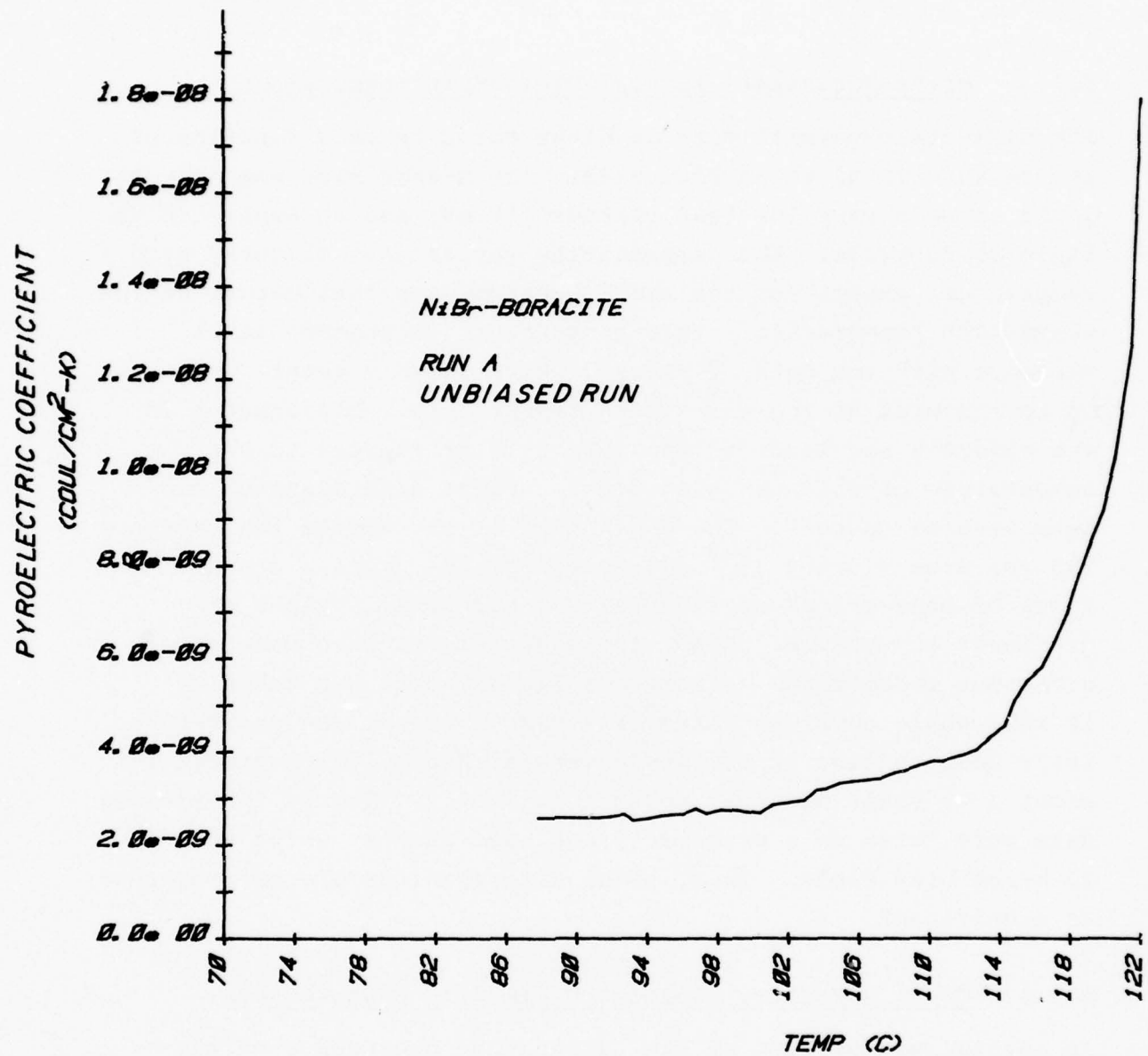


Figure 41. Pyroelectric coefficient vs. temperature for Ni-Br boracite.

Ni-Br boracite as much as 3 K below its transition temperature. It is to be emphasized that this is projection, not a measurement.

5.1.3 Ni-Br Boracite: Initial Dielectric Measurements

The dielectric permittivity of Ni-Br boracite as a function of temperature is given in Figure 42. The measurement was made at 1 MHz using a very low test voltage (10 mV) and an applied bias field of 20 kV/cm. The permittivity varies only slightly with temperature except for the small upwards step that occurs at the transition temperature. This temperature dependence is at variance with the data of Plessey which shows a smooth increase up to the peak at the transition temperature. Differences in the absolute magnitude of the permittivity as well as the temperature of the peak also occur. These discrepancies can have several sources. The small size of the sample (thickness = 260 μm ; area = $3.6 \times 10^{-3} \text{ cm}^2$; see Fig. 40) gives a capacitance of only 0.3 pF at its maximum; such small values are difficult to measure. Also, the measurements were made under different conditions. First, the Plessey data was taken at 10 kHz, while ours was taken at 1 MHz. Second, the characteristic test voltage of Plessey's General Radio 1615-A bridge is about 1 V; while our test voltage is 0.01 V. Third, the Plessey data were taken on a presumably unbiased sample, while we used a 20 kV/cm bias field. Thus, these discrepancies are not regarded as significant.

5.1.4 Cu-Cl Boracite: Initial Dielectric Measurements

An initial measurement of the temperature dependence of the dielectric permittivity for an unbiased sample of Cu-Cl boracite is shown in Figure 43. The measurements were made at 1 MHz using a probe field of 10 mV with no bias applied to the sample. The measured values agree with the Plessey report within the estimated experimental accuracy.

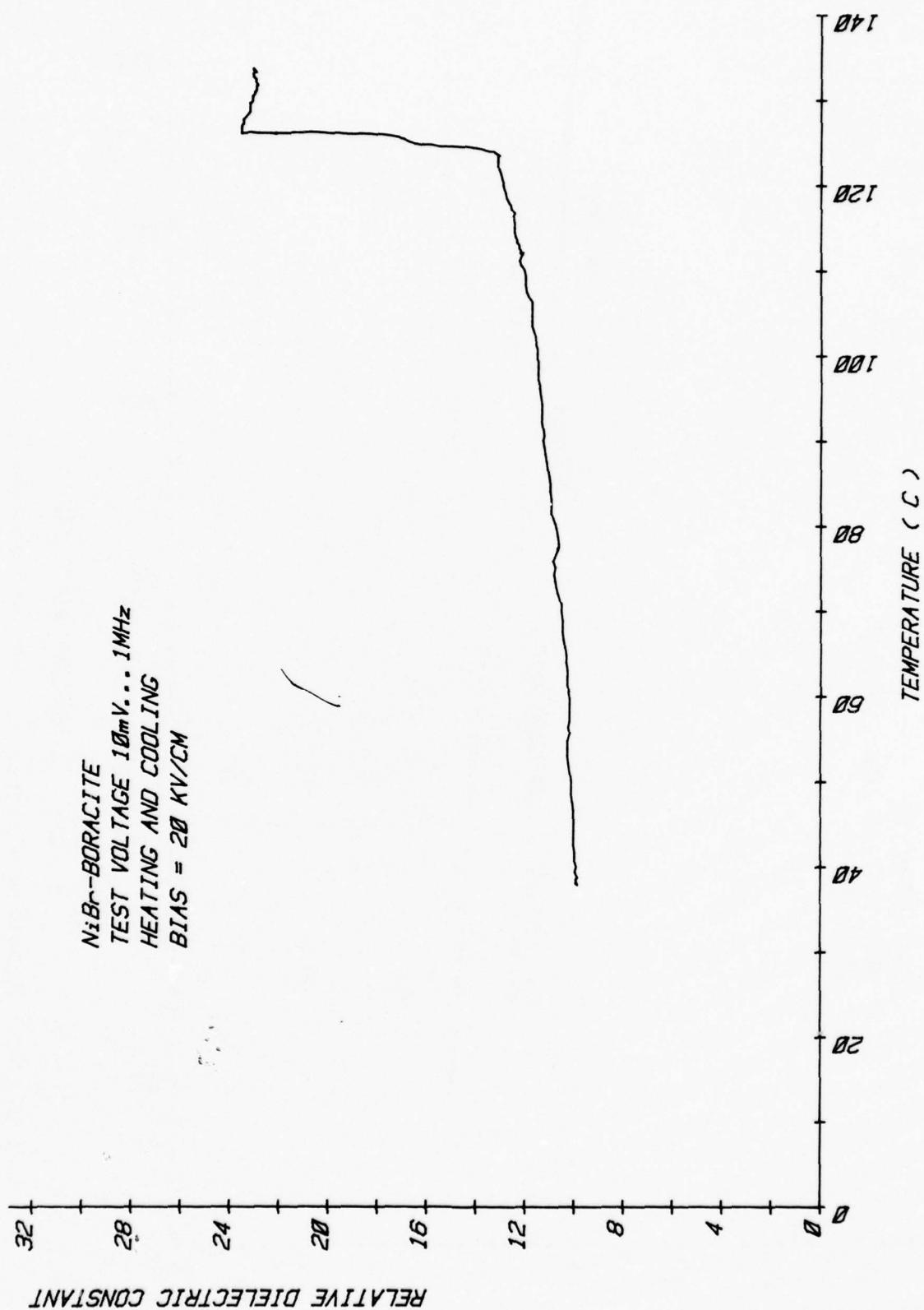


Figure 42. Relative dielectric constant vs. temperature for Ni-Br boracite.

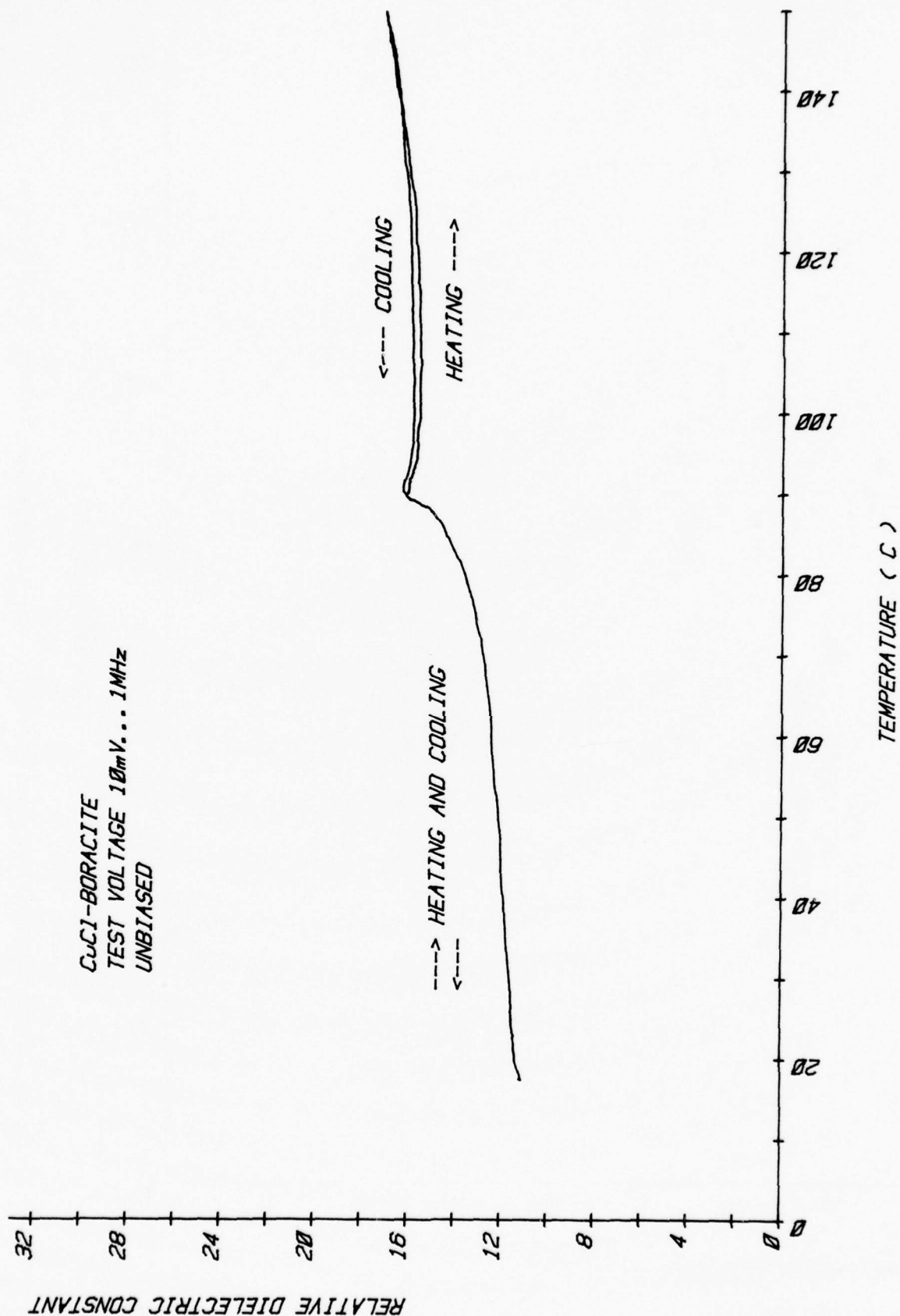


Figure 43. Relative dielectric constant vs. temperature for Cu-Cl boracite.

5.2 Specific Heat Measurements

Calorimetric data were obtained with a Perkin-Elmer differential scanning calorimeter Model DSC-2 interfaced to a Tektronix programmable calculator Model 31. The system is equipped with an Autoscan zero mini-computer for automatic baseline corrections. Single crystal samples, typically between 5 and 50 mg, were weighed with a precision of 1 (10^{-4}) and run under a nitrogen atmosphere. In all cases, open aluminum sample pans were employed with the largest crystal facet parallel to the bottom of the pan to assure good thermal contact. The instrument was calibrated relative to the melting point and enthalpy of fusion of 5N indium metal; $T_M = 429.87$ K and $\Delta H_f = 3266.8$ J mol $^{-1}$ and of 6N lead metal; $T_M = 600.65$ K and $\Delta H_f = 4768.1$ J mol $^{-1}$. Both the melting point and enthalpy of fusion were found to be independent of heating and cooling rates from 0.625 to 20 K min $^{-1}$ and reproducible to $\pm 0.02\%$ and $\pm 0.75\%$, respectively. Initial specific heat determinations were done at 5 K min $^{-1}$ over a large temperature range in each boracite (typically 200 K) to obtain the temperature dependence of the heat capacity. The integration intervals was 0.4 K. Detailed specific heat data were obtained at integration intervals of 0.078 K at heating rates of 1.25 K min $^{-1}$ in the vicinity of the phase transition. The raw data was further refined by normalization to the NBS values of sapphire using a sapphire standard run under the same operating conditions.

The temperature dependence of the heat capacity near the $\bar{4}3m - mm2$ phase transition of some of the boracites is shown in Figures 44 - 48. These curves were obtained in a heating mode only and are the result of averaging at least two runs on at least two different samples. The standard deviation of the specific heat for each data point is on the order of 4%. The transition temperature T_c is taken to be the peak in the heat capacity. The peak in the heat capacity at the transition was found to be asymptotic as a function of decreasing the heating rate at a constant integration interval. For example, in Zn-Br

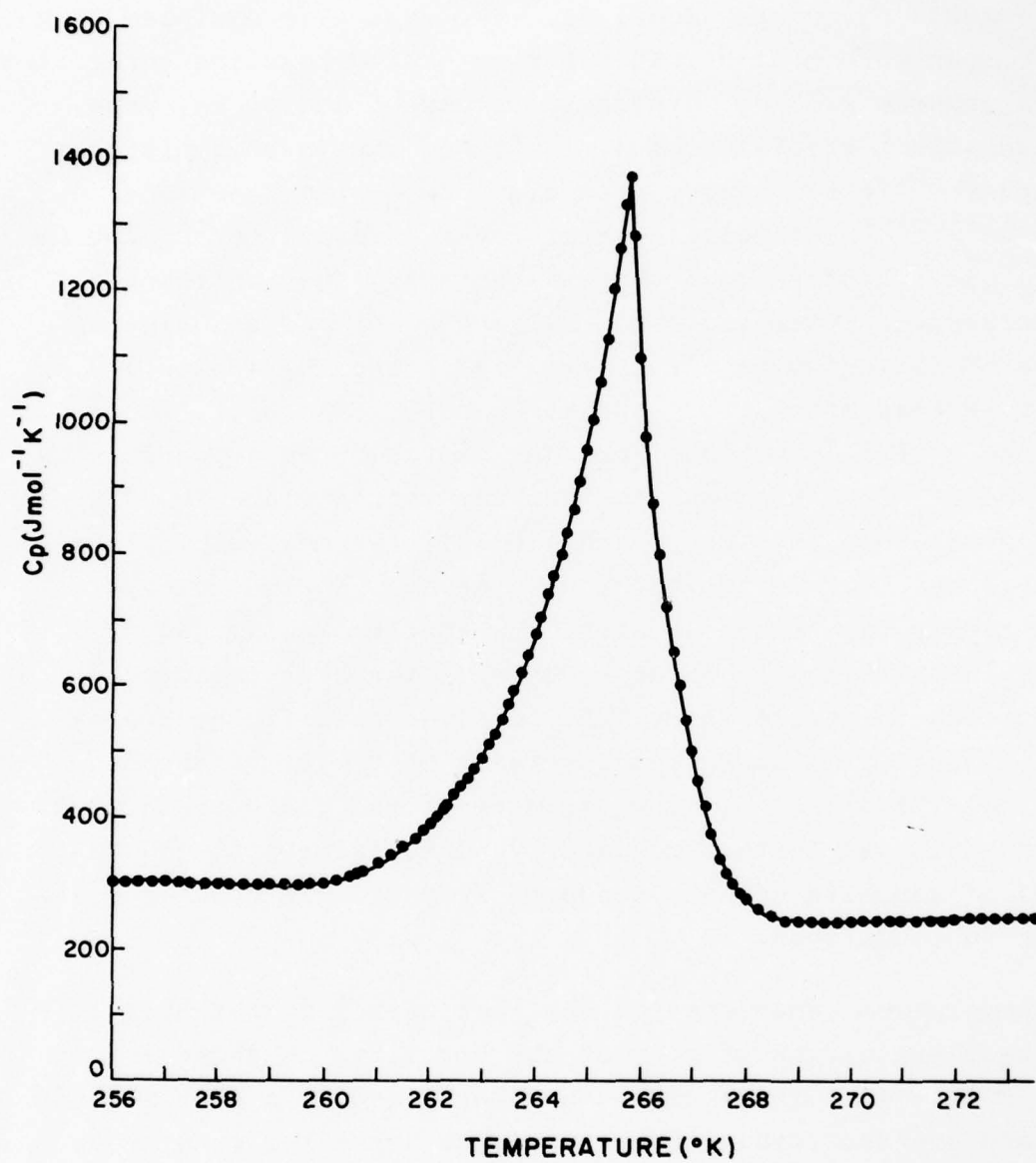


Figure 44. Isobaric molar heat capacity of Cr-Cl boracite in the vicinity of the 43m-mm2 phase transition.

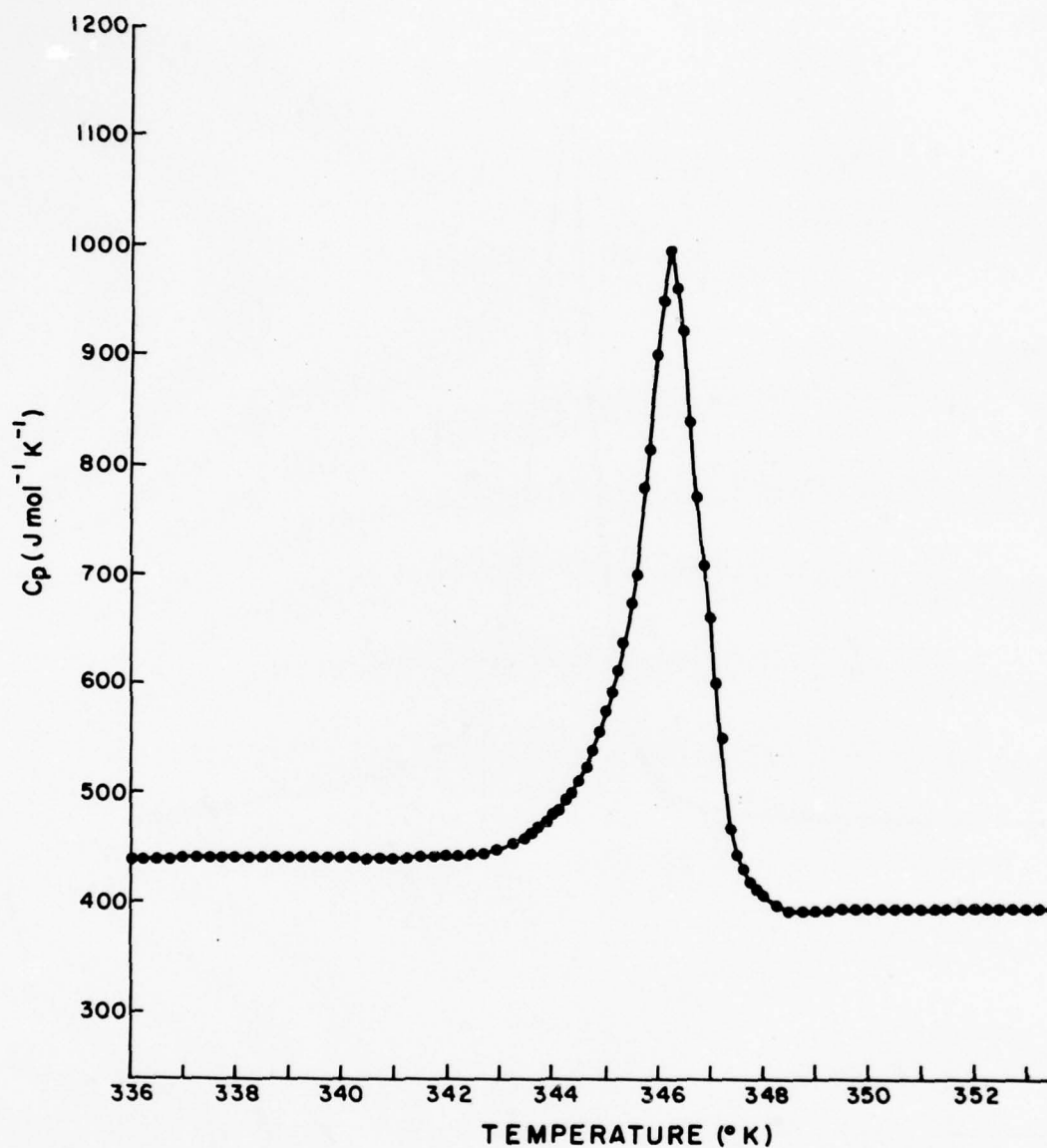


Figure 45. Isobaric molar heat capacity of Fe-I boracite in the vicinity of the $\bar{4}3m$ - $mm2$ phase transition.

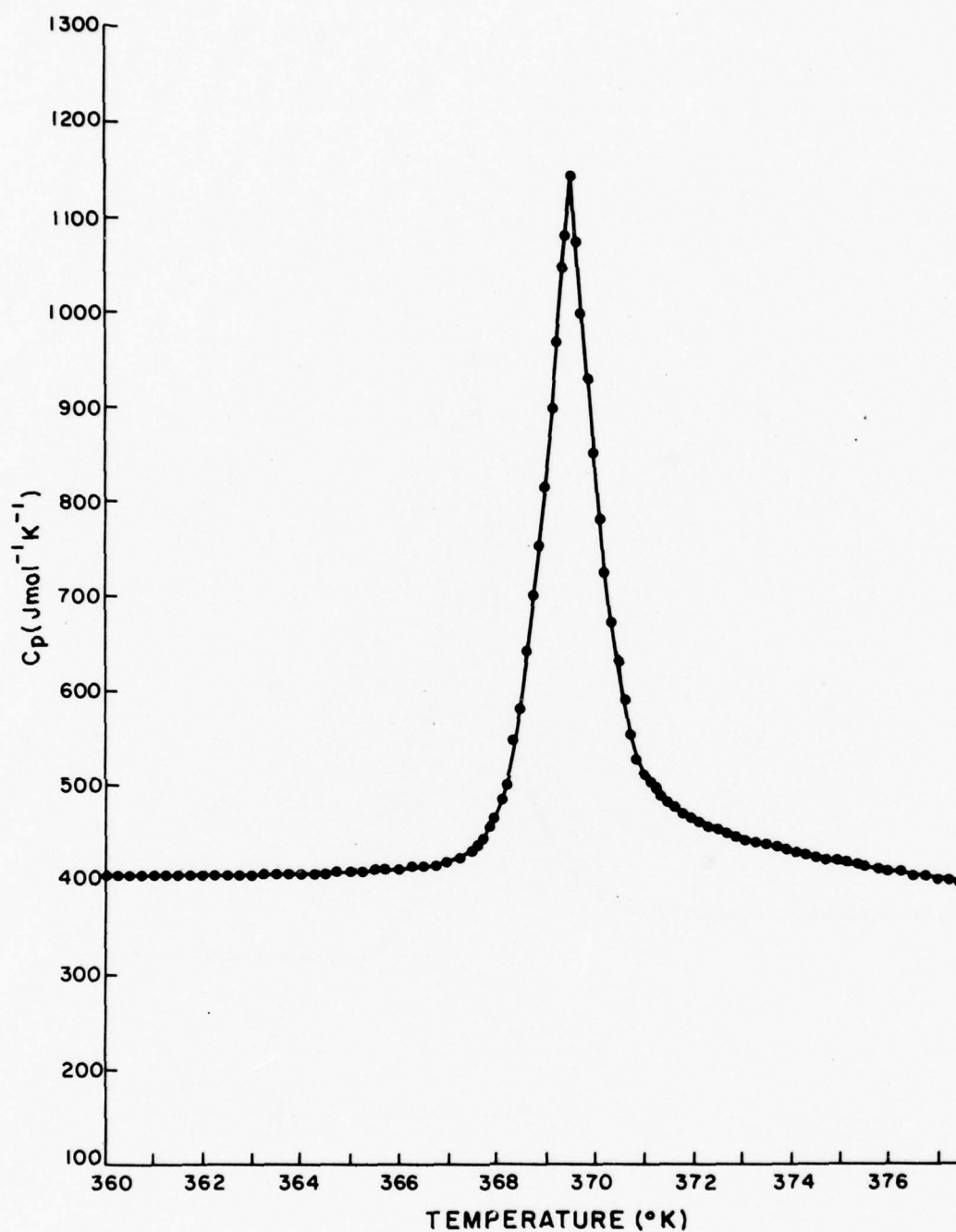


Figure 46. Isobaric molar heat capacity of Cu-Cl boracite in the vicinity of the 43m-mm2 phase transition.

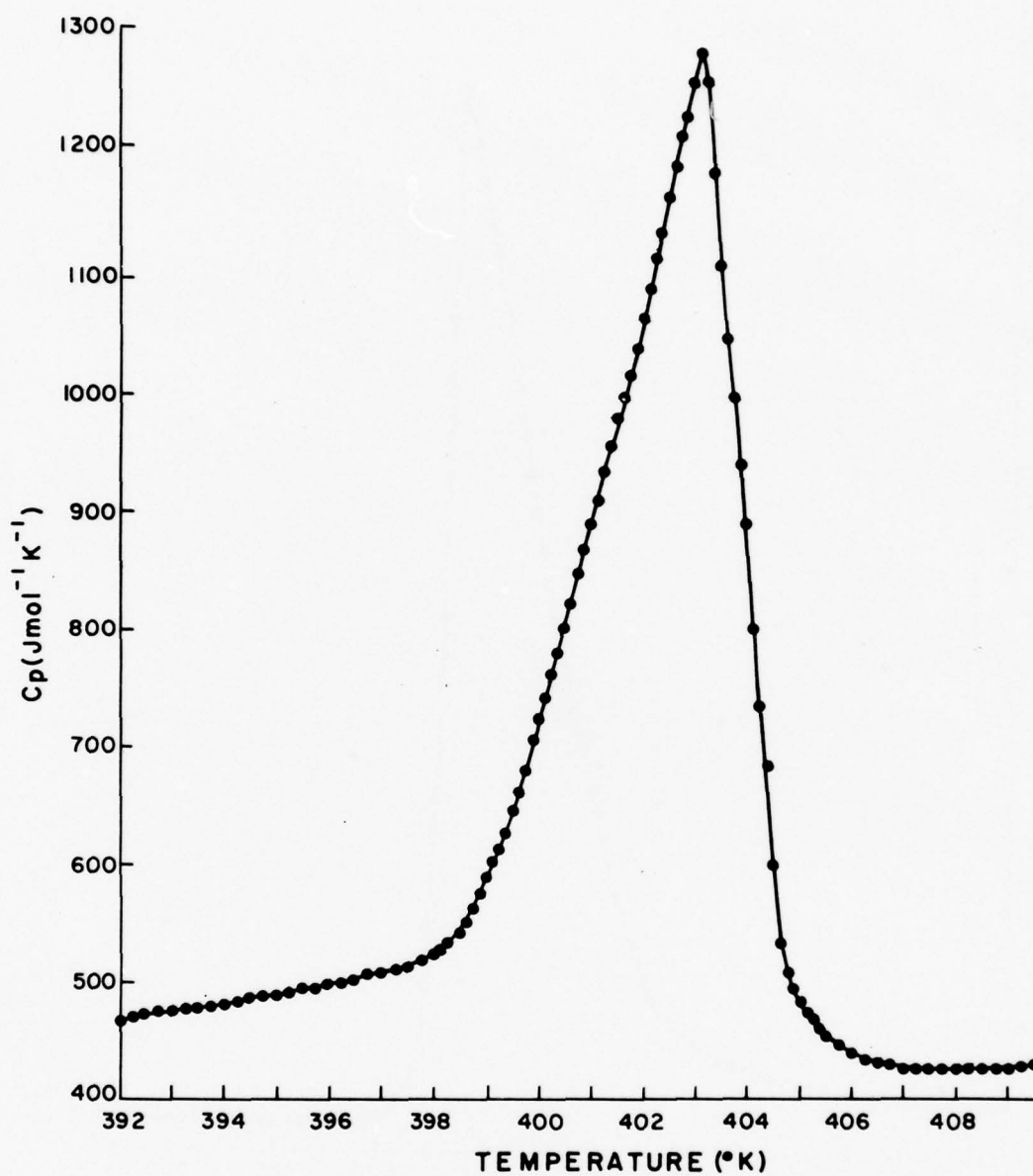


Figure 47. Isobaric molar heat capacity of Ni-Br boracite in the vicinity of the 43m-mm2 phase transition.

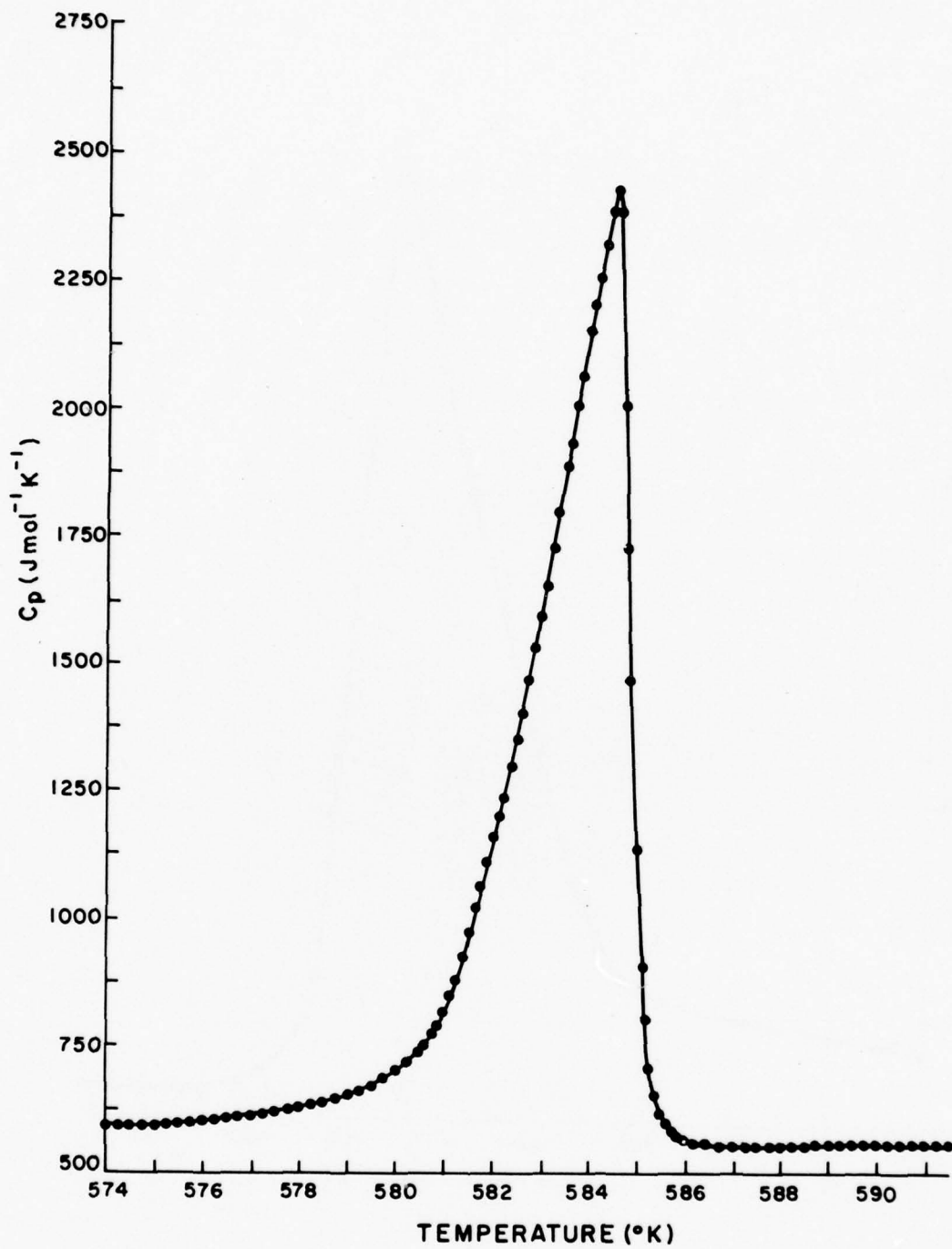


Figure 48. Isobaric molar heat capacity of Zn-Br boracite in the vicinity of the 43m-mm2 phase transition.

boracite it is $1660 \text{ J mol}^{-1} \text{ K}^{-1}$ at 5 K min^{-1} and $2406 \pm 8 \text{ J mol}^{-1} \text{ K}^{-1}$ at both 1.25 K min^{-1} and 0.62 K min^{-1} . Similar results were obtained for the Fe-I boracite, and this behavior is assumed to occur in the other boracites. Consequently, specific heat curves were recorded at 1.25 K min^{-1} in order to minimize any instrumental broadening of the specific heat peak in the vicinity of the transition.

Table 13 is a summary of the thermodynamic values associated with the $\bar{4}3m - mm2$ phase transitions in the boracites. The enthalpies of the phase transitions were obtained by direct computer integration on cooling and heating and by graphical integration on heating only of the heat capacity curves. All three ΔH values were in agreement to within $\pm 3\%$.

The integration is performed by extrapolating a line from the heat capacity curve in the low temperature phase to a line in the high temperature phase. This is done over a temperature interval as small as 6 K in Fe-I and as large as 17 K in Ni-Br. The entropy of the transition is calculated by dividing ΔH by T_c . This assumes that the transition occurs over a small enough temperature interval so that the error in this approximation is minimal. Thus the values of ΔH and ΔS are upper bounds on the true latent heat and entropy discontinuity at T_c , as they contain contributions also from the rise in the heat capacity just below the transition temperature.

Several conclusions can be made from these specific heat curves and computed thermodynamic values. The sharp peak in the specific heat, the large latent heat of transition, and the thermal hysteresis, although somewhat small, clearly show that the $\bar{4}3m - mm2$ phase transition is first order. The anomalously large ΔH values of the Zn-Br boracite relative to the other boracites may reflect the existence of boracite polytypes.

TABLE 13: THERMODYNAMIC VALUES FOR THE 43m-mm2 PHASE TRANSITION IN BORACITE CRYSTALS.

Boracite	T_C (K)	ΔT (K)	ΔH (J mol. ⁻¹)	ΔS (J mol. ⁻¹ K ⁻¹)
Cr-Cl	265.8 \pm 0.2	1.6 \pm 0.4	1966 \pm 14	7.40 \pm 0.09
Fe-I	346.2 \pm 0.2	3.4 \pm 0.4	962 \pm 7	2.78 \pm 0.04
Cu-Cl	369.7 \pm 0.2	3.7 \pm 0.4	1211 \pm 7	3.28 \pm 0.05
Ni-Br	398.4 \pm 0.2	2.1 \pm 0.4	2950 \pm 20	7.41 \pm 0.09
Zn-Br	584.6 \pm 0.2	3.2 \pm 0.4	4050 \pm 20	6.95 \pm 0.04

Schmid et al. (Ref. 5-1) have previously reported the heat capacity of Fe-I boracite measured also by differential scanning calorimetry. Their results are generally in good agreement with ours except for a serious discrepancy concerning the latent heat of the transition. For Fe-I boracite Schmid et al. (Ref. 5-1) measure $\Delta H = 3100 \pm 300$ J mol.⁻¹ whereas we obtain $\Delta H = 962 \pm 7$ J mol.⁻¹. Aside from errors in measurement or calculation, this discrepancy may be explained by assuming either different materials were measured or that polytypes of Fe-I boracite exist. This is in agreement with the suggestion of Nelmes (Ref. 5-2) that at least three distinguishable orthorhombic polytypes exist.

During the course of this investigation some boracite samples were observed to exhibit multiple peaking at the phase transition. An example of multiple peaking in the heat capacity of Cr-Cl and Ni-Br boracites are shown in Figures 49 and 50. The general behavior was reproducible in any given sample with small fluctuations occurring in the varying specific heat peaks. More importantly the ΔH values of each successive determination were in agreement to within $\pm 3\%$. In the case of Cr-Cl and Ni-Br boracite no single peak samples were observed whereas Zn-Br and Fe-I boracite were

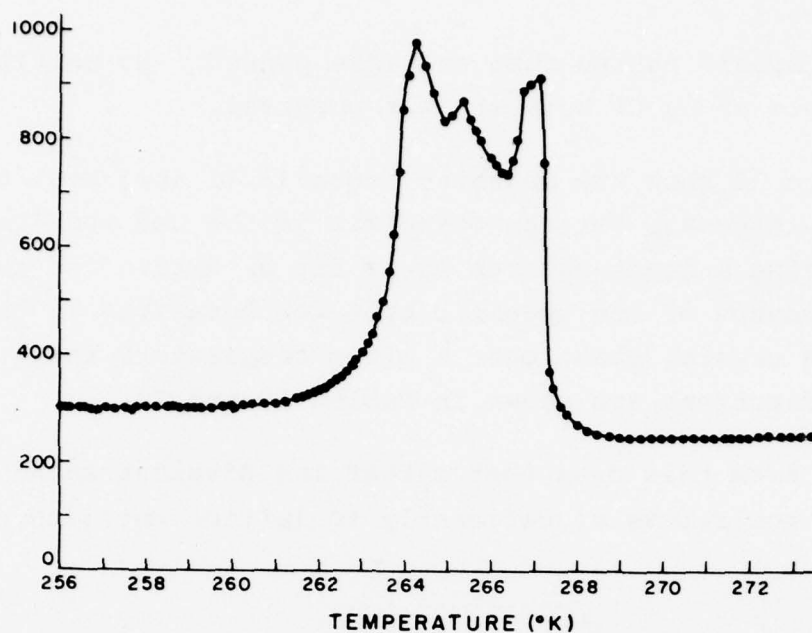


Figure 49. Multiple peaking of isobaric molar heat capacity in Cr-Cl boracite at 43m-mm2 phase transition.

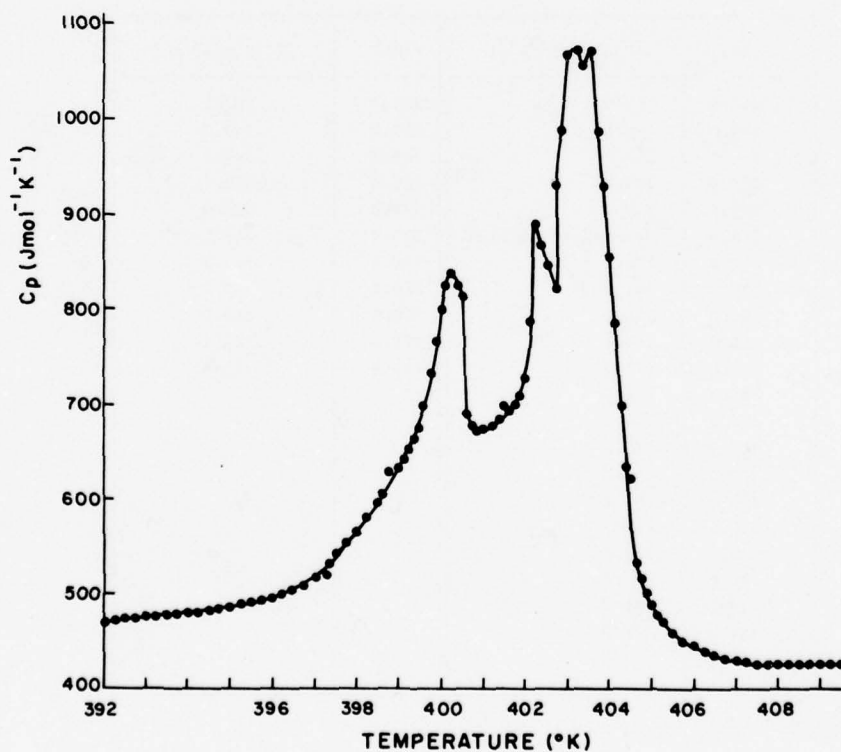


Figure 50. Multiple peaking of isobaric molar heat capacity in Ni-Br boracite at 43m-mm2 phase transition.

more often single peaked than multiple peaked. No multiple peaked sample of Cu-Cl boracite was observed.

Tables 14 to 18 show the measured isobaric (1 atm) heat capacities in 5 K intervals for the boracites in the mm2 and $\bar{4}3m$ phases. Using a least-squares curve fit we derive the temperature dependence of the specific heat for boracites in their appropriate crystal phase over a given temperature range. The resulting functions are shown in Tables 19 and 20.

It appears from this data that either the divalent metal and/or the halide contribute significantly to lattice energies of boracites.

TABLE 14. MOLAR HEAT CAPACITY AT CONSTANT PRESSURE OF Cr-Cl BORACITE IN THE mm2 AND $\bar{4}3m$ PHASES (MW = 475.10).

T(K)	C_p (J mol ⁻¹ K ⁻¹)	T(K)	C_p (J mol ⁻¹ K ⁻¹)
240.0	269.6 ± 1.0	350.0	299.2
245.0	278.5	355.0	303.2
250.0	286.9	360.0	306.7
255.0	300.0	365.0	310.1
260.0	318.9	370.0	312.5
265.8	$\bar{4}3m$ -mm2 transition	375.0	315.1
270.0	260.6	380.0	317.3
275.0	262.8	385.0	318.1
280.0	265.2	390.0	319.3
285.0	268.4	395.0	320.1
290.0	271.3	400.0	321.4
295.0	272.5		
300.0	274.7		
305.0	278.1		
310.0	280.7		
315.0	283.1		
320.0	285.3		
325.0	288.2		
330.0	291.6		
335.0	292.2		
340.0	294.6		
345.0	297.0		

TABLE 15. MOLAR HEAT CAPACITY AT CONSTANT PRESSURE OF Fe-I IN THE mm2 AND 43m PHASES (MW = 578.10).

T (K)	C_p (J mol ⁻¹ K ⁻¹)	T (K)	C_p (J mol ⁻¹ K ⁻¹)
270.0	354.8 ± 1.3	380.0	399.4
275.0	361.6	385.0	404.7
280.0	367.9	390.0	408.8
285.0	376.6	395.0	412.7
290.0	383.4	400.0	414.3
295.0	387.5	405.0	418.1
300.0	395.2	410.0	421.8
305.0	403.2	415.0	424.8
310.0	411.2	420.0	427.7
315.0	418.7	425.0	430.1
320.0	427.7	430.0	432.7
325.0	433.2	435.0	435.2
330.0	436.6	440.0	436.9
335.0	444.6		
340.0	446.8		
346.2	43m-mm2 transition		
350.0	372.0		
355.0	374.9		
360.0	380.5		
365.0	385.8		
370.0	391.1		
375.0	396.0		

TABLE 16. MOLAR HEAT CAPACITY AT CONSTANT PRESSURE OF Cu-Cl BORACITE IN THE mm2 AND 43m PHASES (MW = 509.75).

T (K)	C_p (J mol ⁻¹ K ⁻¹)	T (K)	C_p (J mol ⁻¹ K ⁻¹)
270.0	206.1 ± 1.0	380.0	392.9
275.0	216.5	385.0	391.2
280.0	227.0	390.0	393.5
285.0	237.2	395.0	397.3
290.0	248.9	400.0	399.1
295.0	259.9	405.0	403.1
300.0	270.8	410.0	406.7
305.0	281.2	415.0	409.7
310.0	292.4	420.0	412.9
315.0	302.8	425.0	415.9
320.0	313.6	430.0	418.5
325.0	323.1	435.0	421.4
330.0	337.0	440.0	423.0
335.0	341.7	445.0	424.4
340.0	351.3	450.0	425.9
345.0	370.0		
350.0	372.0		
355.0	390.9		
360.0	407.4		
365.0	427.8		
369.7	43m-mm2 transition		
375.0	425.7		

TABLE 17. MOLAR HEAT CAPACITY AT CONSTANT PRESSURE OF Ni-Br BORACITE IN THE mm2 AND 43m PHASES (MW = 539.69).

T(K)	C_p (J mol ⁻¹ K ⁻¹)	T(K)	C_p (J mol ⁻¹ K ⁻¹)
270.0	239.3 ± 0.9	380.0	417.3
275.0	247.5	385.0	425.7
280.0	255.6	390.0	428.1
285.0	263.8	395.0	503.5
290.0	271.8	398.4	43m-mm2 transition
295.0	280.0	405.0	467.2
300.0	288.0	410.0	415.5
305.0	296.1	415.0	417.3
310.0	304.5	420.0	420.0
315.0	312.3	425.0	423.2
320.0	320.3	430.0	425.7
325.0	328.5	435.0	429.0
330.0	336.7	440.0	430.6
335.0	344.9	445.0	432.7
340.0	353.0	450.0	434.5
345.0	361.1	455.0	436.0
350.0	369.1	460.0	437.4
355.0	377.1	465.0	439.2
360.0	385.0	470.0	440.6
365.0	393.8		
370.0	401.7		
375.0	410.5		

TABLE 18. MOLAR HEAT CAPACITY AT CONSTANT PRESSURE OF Zn-Br BORACITE IN THE mm2 AND 43m PHASES (MW = 559.70).

T(K)	C_p (J mol ⁻¹ K ⁻¹)	T(K)	C_p (J mol ⁻¹ K ⁻¹)
455.0	401.7 ± 1.4	565.0	566.8
460.0	409.2	570.0	574.2
465.0	416.7	575.0	581.7
470.0	424.5	584.6	43m-mm2 transition
475.0	431.8	590.0	585.2
480.0	439.2	595.0	588.5
485.0	436.5	600.0	592.1
490.0	454.2	605.0	595.3
495.0	461.8	610.0	599.0
500.0	469.2	615.0	602.1
505.0	476.8	620.0	605.6
510.0	484.1	625.0	609.0
515.0	491.5	630.0	612.5
520.0	499.0	635.0	615.5
525.0	506.7	640.0	619.0
530.0	514.5	645.0	622.5
535.0	521.7	650.0	625.9
540.0	529.0		
545.0	536.7		
550.0	544.0		
555.0	551.7		
560.0	559.2		

TABLE 19. LEAST SQUARES FIT MOLAR HEAT CAPACITY FUNCTIONS FOR BORACITES IN THE mm2 PHASE.

Boracite	Temperature Interval	C_p (J mol ⁻¹ K ⁻¹)
Cr-Cl	$240 \leq T(K) \leq 260$	$C_p = -3.097 (10^2) + 24.0 (10^{-1}) T$
Fe-I	$270 \leq T(K) \leq 340$	$C_p = -0.157 (10^2) + 13.0 (10^{-1}) T$
Cu-Cl	$270 \leq T(K) \leq 355$	$C_p = -3.776 (10^2) + 21.6 (10^{-1}) T$
Ni-Br	$270 \leq T(K) \leq 385$	$C_p = -1.986 (10^2) + 16.2 (10^{-1}) T$
Zn-Br	$455 \leq T(K) \leq 575$	$C_p = -1.849 (10^2) + 15.0 (10^{-1}) T$

TABLE 20. LEAST SQUARES FIT MOLAR HEAT CAPACITY FUNCTIONS FOR BORACITES IN THE 43m PHASE.

Boracite	Temperature Interval	C_p (J mol ⁻¹ K ⁻¹)
Cr-Cl	$270 \leq T(K) \leq 400$	$C_p = 1.374 (10^2) + 4.588 (10^{-1}) T$
Fe-I	$350 \leq T(K) \leq 440$	$C_p = 1.184 (10^2) + 7.353 (10^{-1}) T$
Cu-Cl	$385 \leq T(K) \leq 450$	$C_p = 1.741 (10^2) + 5.654 (10^{-1}) T$
Ni-Br	$410 \leq T(K) \leq 470$	$C_p = 2.411 (10^2) + 4.279 (10^{-1}) T$
Zn-Be	$590 \leq T(K) \leq 650$	$C_p = 1.849 (10^2) + 6.784 (10^{-1}) T$

5.3 Infrared Vibrational Spectra

Solid-state infrared vibrational spectra were recorded on a Perkin-Elmer infrared spectrophotometer, Model 283, with AgCl optics. Scanning time was $150 \text{ cm}^{-1} \text{ min}^{-1}$ at a response time of 2 sec using slit program 7. Single crystal samples ground with an agate mortar and pestle were run as mulls containing approximately 12 mg of material. Fluorolube mulls were examined from 4000 to 13000 cm^{-1} while nujol mulls were employed from 1300 to 400 cm^{-1} . The sample temperature in front of the beam was found to vary from 36 to 38°C . Therefore, all samples are noted as being recorded at $37 \pm 1^\circ\text{C}$, neglecting temperature fluctuations due to black body radiation.

The infrared vibrational spectra in the solid-state from 1600 to 400 cm^{-1} are shown in Figures 51 - 56 for the boracites. The main absorption maxima are given in Table 21. From 5000 to 1600 cm^{-1} no absorptions were observed except for probable combinations and overtones. More importantly no absorption which could be attributed to OH was found. It is concluded that (with the possible exception of CuCl which has not been studied above 1300 cm^{-1}) no boracite contained hydrated water or hydroxyl-substituted halogens in amounts greater than 0.5% by weight.

General inspection of the spectra reveal some interesting facts. The spectrum of Cr-Cl is taken in the $\bar{4}3m$ while the other spectra are taken in the orthorhombic phase. It appears that the spectra of Cu-Cl and Ni-Br are the same, forming one type while Fe-I and Zn-Br exhibit two other types of spectra. Interestingly, the spectra of "dark green" and "light green" Cu-Cl boracite were identical within our resolution.

The absorption at 1401 and 1348 cm^{-1} in Zn-Br and at 1385 and 1338 cm^{-1} in Ni-Br are attributed to the degenerate stretch $\bar{\nu}_3$ for BO_3 with D_{3h} site symmetry. The latter absorption is for B^{10} while the former is for B^{11} on the approximate ratio of 1:4 corresponding to the natural isotope ratio of 18:82.

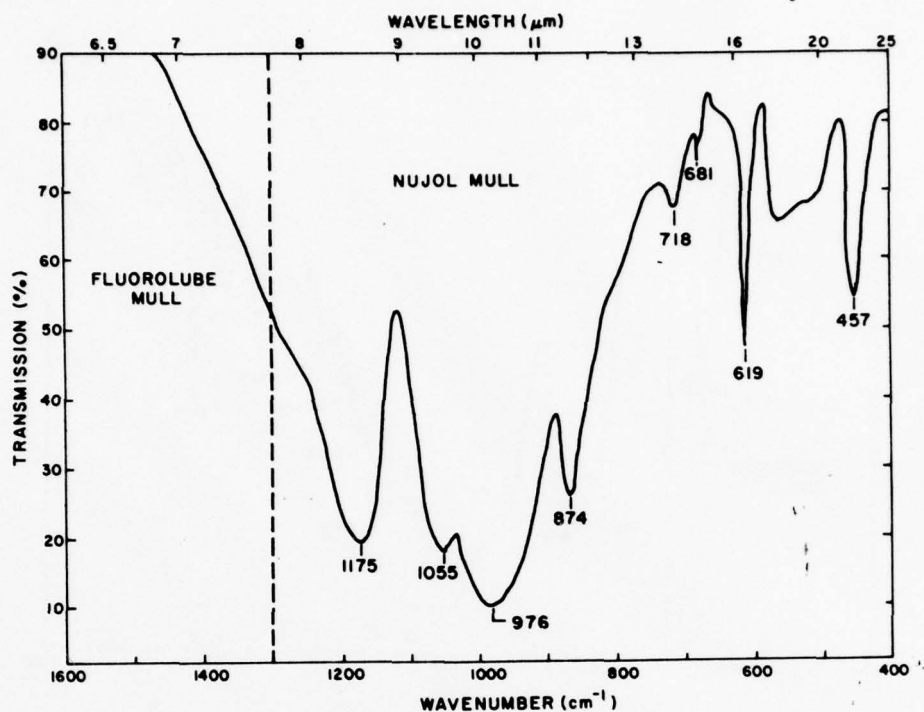


Figure 51. Solid-state infrared vibrational spectrum of 43m $\text{Cr}_3\text{B}_7\text{O}_{13}\text{Cl}$.

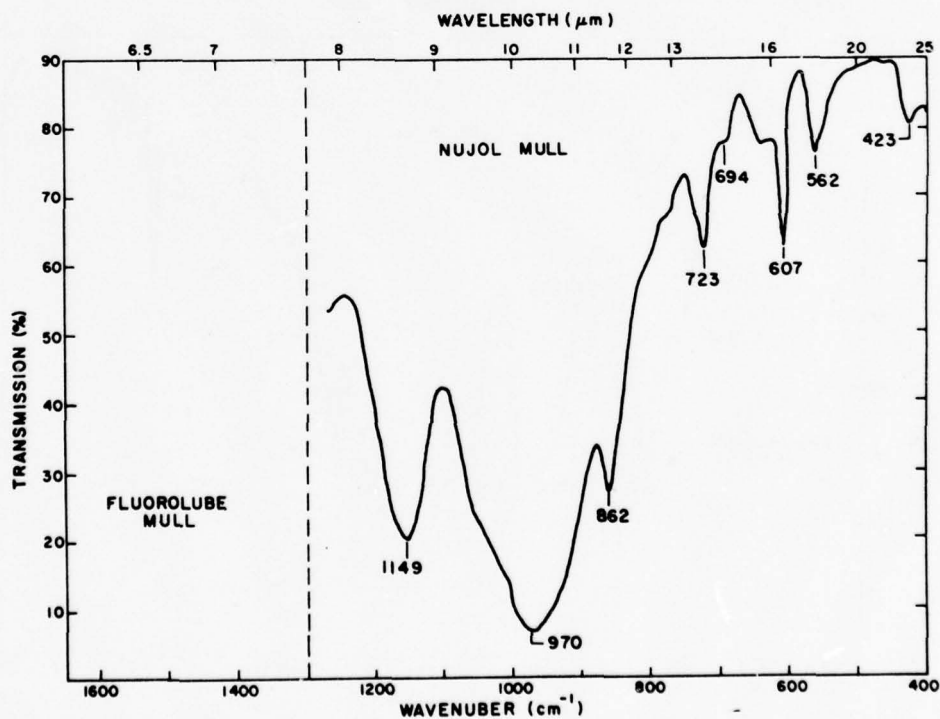


Figure 52. Solid-state infrared vibrational spectrum of mm2 $\text{Fe}_3\text{B}_7\text{O}_{13}\text{I}$.

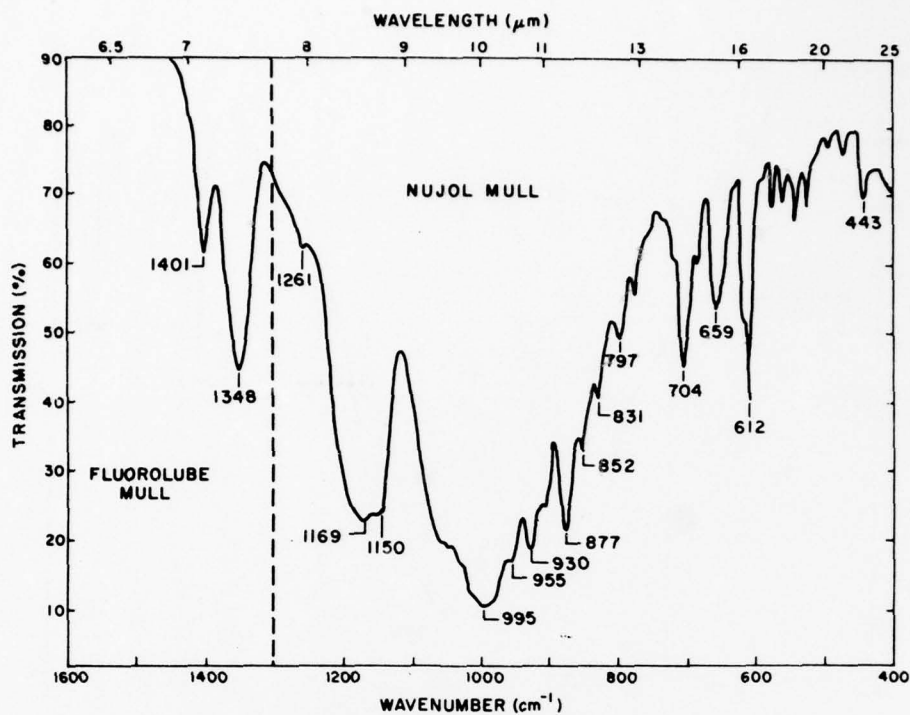


Figure 53. Solid-state infrared vibrational spectrum of mm2 $\text{Zn}_3\text{B}_7\text{O}_{13}\text{Br}$.

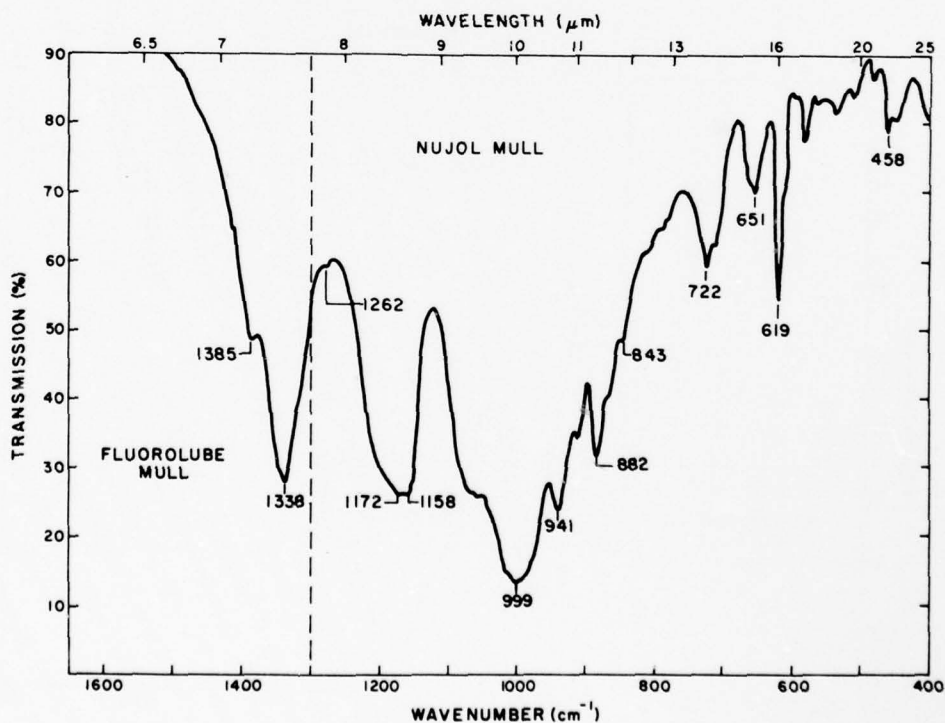


Figure 54. Solid-state infrared vibrational spectrum of mm2 $\text{Ni}_3\text{B}_7\text{O}_{13}\text{Br}$.

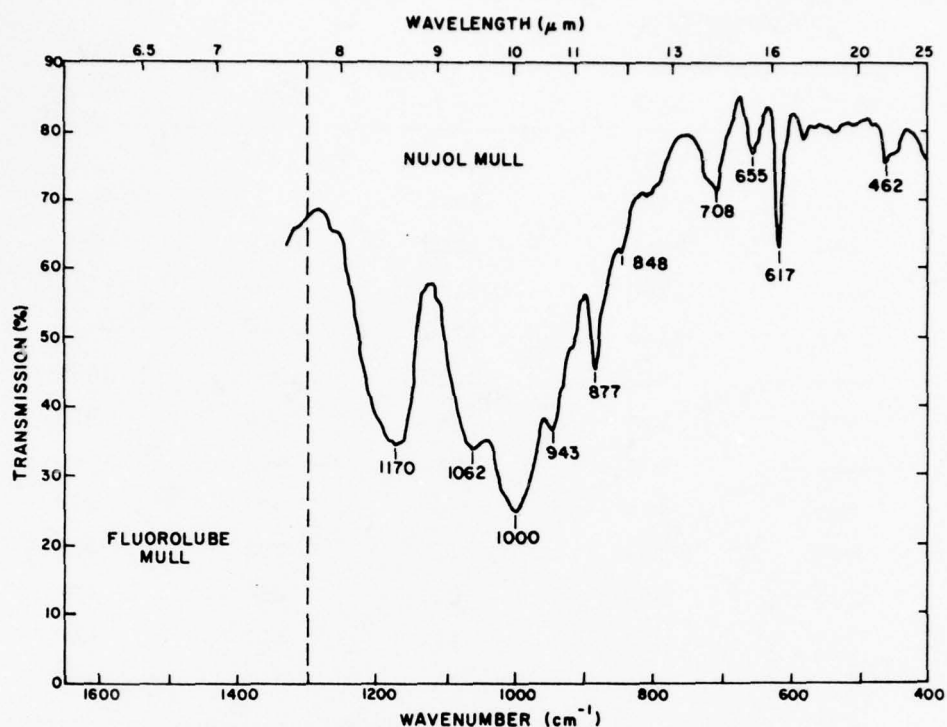


Figure 55. Solid-state infrared vibrational spectrum of mm2 $\text{Cu}_3\text{B}_7\text{O}_{13}\text{Cl}$.

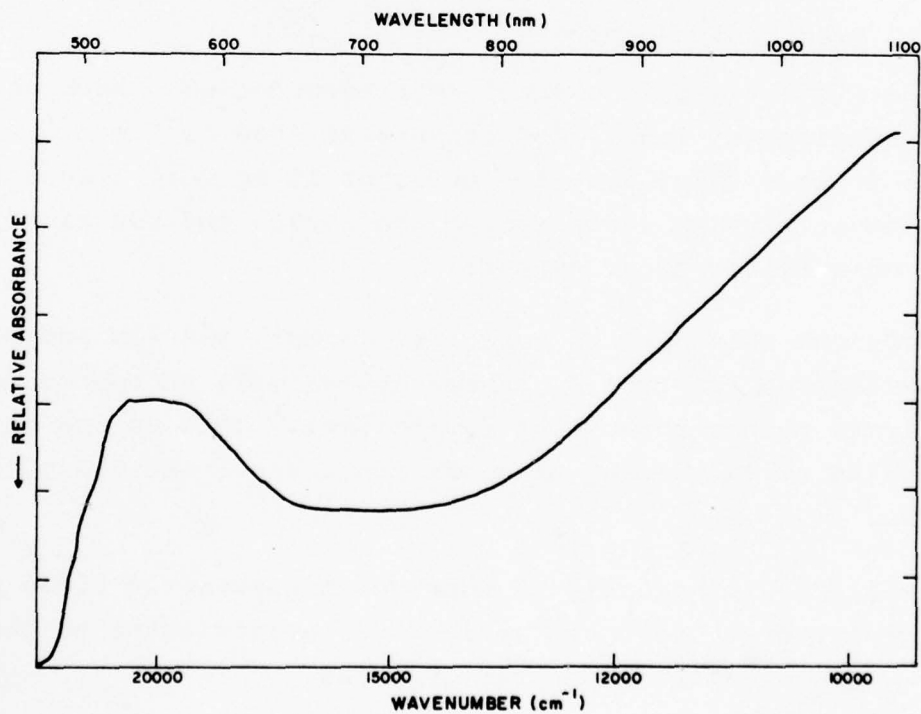


Figure 56. Solid-state electronic spectrum of 43m $\text{Cr}_3\text{B}_7\text{O}_{13}\text{Cl}$.

TABLE 21. INFRARED ABSORPTIONS OF BORACITES
(FUNDAMENTALS IN cm^{-1}).

Fe-I	Zn-Br	Ni-Br	Cu-Cl	Cr-Cl
	1401	1385		----
	1348	1338		----
----	1261	1262	1261	----
----	1169	1172	1170	1175
1149	1150	1158	----	----
----	1047	1058	1062	1055
970	995	999	1000	976
----	930	941	943	----
862	877	882	877	874
723	704	722	708	718
----	659	651	654	681
607	612	619	617	619
423	443	458	462	457

5.4 Electronic Spectra

Solid-state electronic spectra were recorded on a Beckman UV-Vis spectrophotometer model DK-2 scanned at $2000 \text{ cm}^{-1} \text{ min}^{-1}$.

Single crystal samples on the order of 10 mg were ground to a fine powder with an agate mortar and pestle and run as nujol mulls on a filter paper support.

The divalent metal ion of boracites in both the $\bar{4}3m$ and $mm2$ crystal phases has true D_{4h} symmetry but will be approximated by a trans pseudo-octahedral environment. This is due to a broadening of the widths of bands involving transitions to T and E terms.

For cubic Cr-Cl (Fig. 56) we observe an asymmetric broad absorption centered at 14000 cm^{-1} which can be attributed to the ${}^5E_g \rightarrow {}^5T_{2g}$ transition in the Cr^{++} ion.

Figure 57 shows the electronic absorption spectra from two different samples of orthorhombic Cu-Cl boracite denoted "light green" and "dark green". Both of these samples exhibit a broad absorption band centered in the 12000 cm^{-1} to 13000 cm^{-1} region which can be attributed to the ${}^2E_g \rightarrow {}^2T_{2g}$ transition in the Cu^{++} ion. This broad absorption band in the "light green" sample is shifted about 650 cm^{-1} towards higher energies than the corresponding absorption in the "dark green" sample. This shift is outside the range of experimental uncertainties and is much more than one would expect from impurities or mild distortions. We take this shift to be evidence for the existence of polytypes or substantial variations in stoichiometry in Cu-Cl boracite.

Finally, it should be noted that no evidence for multiple oxidation states in either crystal was observed.

5.5 Second Harmonic Generation in Ni-Br Boracite

Optical second harmonic generation (SHG) was performed with a second harmonic analyzer (SHA) (Ref. 5-3) at $1.06\text{ }\mu\text{m}$. Powders of random size, $\leq 212\text{ }\mu\text{m}$, ground from single crystals in an agate mortar and pestle were examined as monolayer samples between two coverglasses. A chromel-alumel thermocouple was placed near the sample as a means of monitoring the temperature. Temperature fluctuations were less than $\pm 3^\circ\text{C}$.

The results of the SHG measurements on $\overline{4}3m - mm2$ phase transition on Ni-Br boracite are shown in Figure 58. The normalized second harmonic intensity is on the order of $0.1\text{ }\alpha\text{-SiO}_2$ at room temperature. The phase transition is observed to occur at $400 \pm 4\text{ K}$ which is in good agreement with the specific heat determination of $398.4 \pm 0.4\text{ K}$. No thermal hysteresis was measured due to temperature fluctuations; however, the discontinuous jump in the second harmonic intensity, $I^{2\omega}$, supports the claim of a first-order transition. Both phases are seen to be noncentrosymmetric in accordance with crystal point group assignments in other boracites. The lack of structural data on Ni-Br boracite precludes a definitive assignment of the crystal phases.

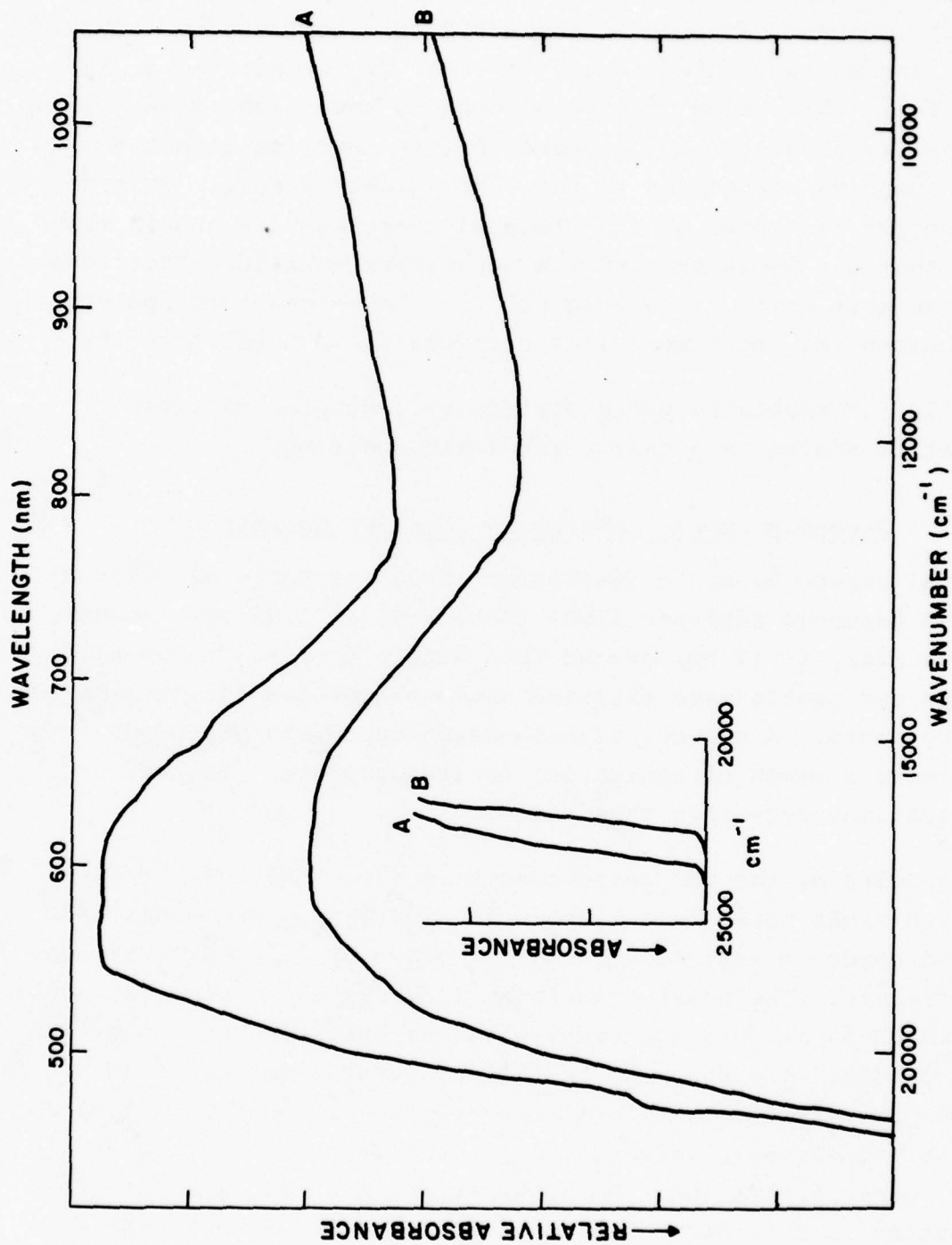


Figure 57. Solid-state electronic spectra of mm2, a) "light green" and b) "dark green" $\text{Cu}_3\text{B}_7\text{O}_{13}\text{Cl}$.

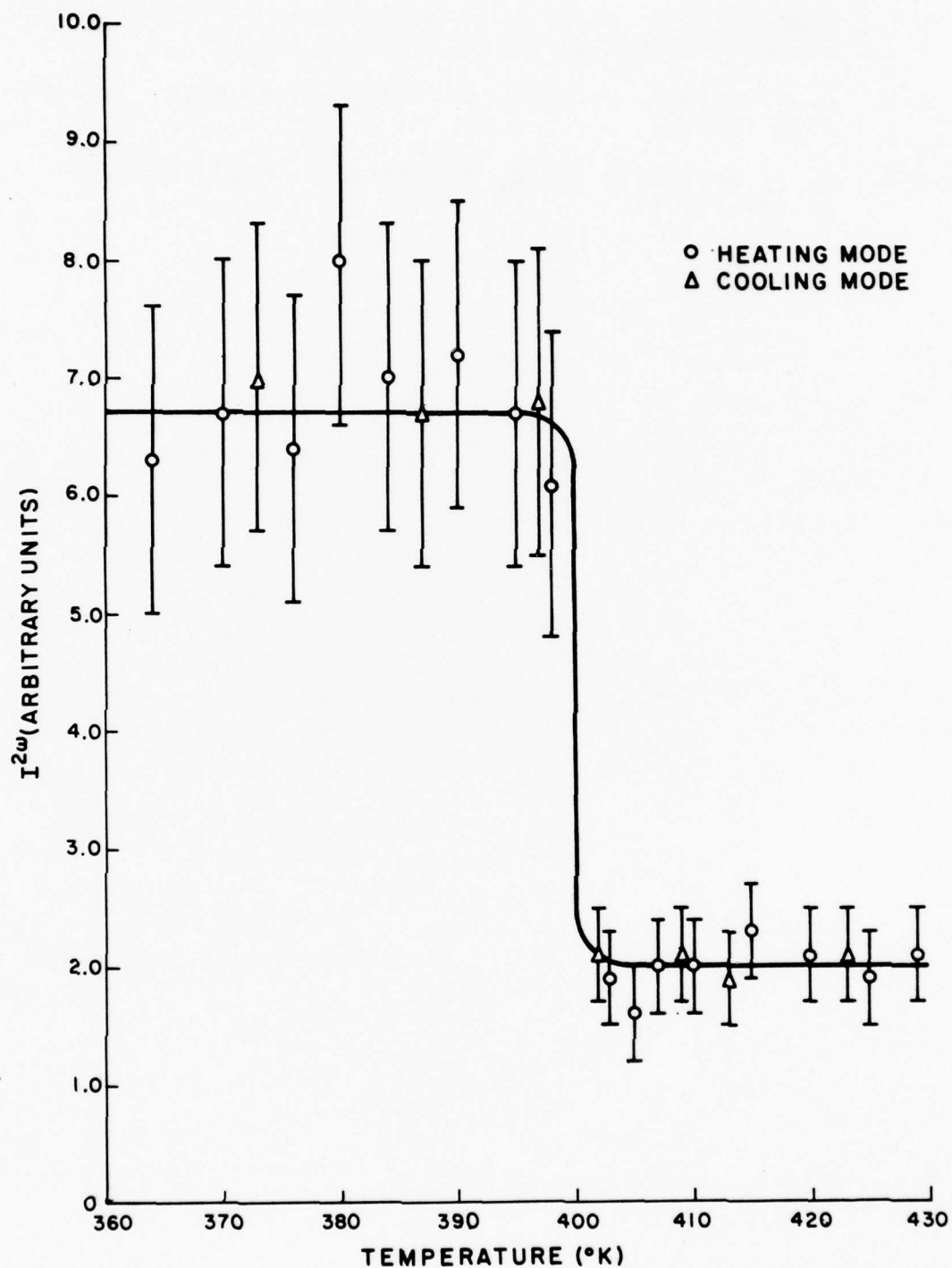


Figure 58. Temperature dependence of the second harmonic intensity of $\text{Ni}_3\text{B}_7\text{O}_{13}\text{Br}$ at the 43m - mm2 phase transition.

5.6 References

- 5-1. H. Schmid, P. Chan, L. A. Petermann, F. Teufel and M. Mandly, *Ferroelectrics* 13, 351 (1976).
- 5-2. R. J. Nelmes, *J. Phys. C: Solid State Phys.* 7, 3840-3854 (1974).
- 5-3. J. P. Dougherty and S. K. Kurtz, *J. Appl. Crystal.* 9, 145 (1976).

6. LITERATURE SURVEY

6.1 Basic References

There are three recent review papers on the subject of improper ferroelectrics. The most comprehensive review of the theory appears in:

A. P. Levanyuk and D. G. Sannikov 1974
Improper Ferroelectrics
Soviet Physics: Uspekhi 17, 199-214.

Particular attention is given to contributions made in the Soviet literature, some of which are not available in English translation. The authors performed the first theoretical analysis of the dielectric properties of improper ferroelectrics in 1968 and continue to actively contribute to the field. Significantly more attention is paid to experimental observations in:

V. Dvořák 1974
Improper Ferroelectrics
Ferroelectric 7, 1-9

This author is responsible for suggesting the name "improper ferroelectrics" for this class of materials. The name seems to have gained acceptance, although papers continue to appear occasionally referring to a weak, atypical, complex, faint, partial, or extrinsic ferroelectrics. The most recent review is presented by:

Y. Ishibashi and Y. Takagi 1976
Improper Ferroelectric Phase Transitions
Japan. J. Appl. Phys. 15, 1621-1636.

In this review, attention is focused on a number of unresolved questions, both experimental and theoretical.

Much of the theory of improper ferroelctrics rests on Landau's theory of continuous phase transitions. The original papers,

L. Landau 1937A
Zur Theorie der Phasenumwandlung I
Phys. Z. Sowjet 11, 26.

and

L. Landau 1937B
Zur Theorie der Phasenumwandlung II
Phys. Z. Sowjet 11, 545

here appeared in English translation in:

L. D. Landau, Collected Works
D. ter Haar, Editor
Pergamon, 1965.

These are still the best exposition of this theory. The first theoretical suggestion that an improper ferroelectric might occur appears in,

V. L. Indenbom 1960
Phase Transitions Without Change in the Number of
Atoms in the Unit Cell of the Crystal
Soviet Physics: Crystallograph 5, 106-115.

This paper basically analyzes the crystallographic point groups to determine all possible phase transitions consistent with the Landau theory in which the unit cell does not change during the transition. An even more detailed analysis of precisely the same problem is given by,

V. Janovec, D. Dvořák and J. Petzelt 1975
Symmetry Classification and Properties of
Equi-Translational Structural Phase Transitions
Czech. J. Phys. B25, 1362-1396.

This paper tabulates a wealth of information. An extension of these two analyses to include transitions in which the unit cell changes has been performed for the special case of improper ferroelectrics which however are not simultaneously ferro-elastic. This partial extension is reported in:

P. Tolédano and J. C. Tolédano 1976
Order-Parameter Symmetries for Improper
Ferroelectric Nonferroelastic Transitions
Phys. Rev. B14, 3097-3109.

6.2 Experimental Literature On Boracites

The boracite family of compounds ($X_3B_7O_{13}Y$, where X is a divalent metal and Y a halogen) is known to contain a large number of ferroelectric materials, some of which have been identified as improper ferroelectrics. The large number of compounds and the many interesting properties of these materials has led to a large experimental literature. In Table 22 this literature is classified in terms of physical properties and the particular material. In Table 23 the properties of the observed ferroelectric transitions are summarized. All references are to papers listed in Appendix B.

TABLE 22. EXPERIMENTAL LITERATURE ON BORACITES

Dielectric Constant

Mg-Cl:	Jona 1959; Sonin & Zheludev 1963; Bochkov, Gavrilova et al. 1975; Albers et al. 1976.
Cr-Cl:	Bochkov & Drozhdin 1975
Fe-Cl:	Bochkov et al. 1973
Fe-Br:	Bochkov et al. 1973
Fe-I :	Schmid et al. 1976
Co-Cl:	Bochkov et al. 1973
Co-Br:	Ascher et al. 1964
Co-I :	Ascher et al. 1964; Smutny & Fousek 1970; Smutný et al. 1974 B; Smutny & Konak 1975; Drozhdin et al 1975.
Ni-Cl:	Jona 1959; Ascher et al. 1964.
Ni-Br:	Ascher et al. 1964
Ni-I :	Ascher et al. 1966; Smutny et al. 1974 A; Smutný et al. 1974 B.
Cu-Br:	Drozhdin et al. 1975.
Zn-Cl:	Jona 1959; Bochkov et al. 1973.
Cd-Cl:	Jona 1959.

Spontaneous Polarization

Mg-Cl:	Bochkov, Gavrilova et al. 1975; Fridkin et al. 1974; Torre et al. 1972.
Cr-Cl:	Bochkov & Drozhdin 1975; Fridkin et al. 1974.
Fe-Br:	Fridkin et al. 1974
Fe-I :	Schmid et al. 1976
Co-I :	Smutný & Fousek 1970; Smutny & Konak 1975; Drozhdin et al. 1975.
Ni-I :	Miyashita & Murakami 1970
Cu-Br:	Drozhdin et al. 1975

TABLE 22. EXPERIMENTAL LITERATURE ON BORACITES (CONT'D)

Crystal Structure

Review: Nelmes 1974 - A review of the properties of boracites with an emphasis on the structural studies of boracites.

X-Ray Studies:

Ito et al. 1951 - structure of Mg-Cl ($\bar{4}3m-mm2$).

Kobayashi and Mizutani 1970 - lattice strains of Fe-I strains and parameters of Fe-I.

Schmid 1970 - trigonal boracites.

Dowty and Clark 1972 - atomic displacements.

Kobayashi et al. 1972 - Fe-I at low temperatures.

Torre et al. 1972 - structural basis of ferroelectricity

Felix et al. 1974 - x-ray diffuse scattering for boracite

Nelmes and Thornley 1974 - Cr-Cl, full 3-diam. structure

Thornley and Nelmes 1974 - Cr-Cl

Nelmes and Thornley 1976 - Ni-I

Thornley et al. 1974 - Cu-Cl

Mossbauer Investigations:

Schmid and Trooster 1967 - Fe-Cl, Fe-Br and Fe-I.

Trooster 1969

EPR Spectra:

Rivera et al 1976A - Mg-Cl(Mn^{2+})

Rivera et al 1976B - Zn-Cl(Mn^{2+})

Neutron Scattering:

Thornley et al. 1976

Domain Studies

Ascher et al. 1964 - Ni-Cl domain wall motion

Kobayashi et al. 1968 - Fe-I

Schmid 1969 - Ni-Cl, Ni-Br

Bochkov, Gavrilova et al. 1975 - Mg-Cl

Drozhdin et al. 1975 - Cu-Br

TABLE 22. EXPERIMENTAL LITERATURE ON BORACITES (CONT'D)

Thermal Measurements

The Latent Heat of the Transition:

Bochkov et al. 1973 - Fe-Cl, Fe-Br, Co-Cl, Zn-Cl.

Bochkov, Gavriola et al. 1975 - Mg-Cl

Specific Heat:

Smutný 1972 - Co-I

Schmid et al. 1976 - Fe-I

Pyroelectricity

Bochkov and Drozhdin 1975 - Cr-Cl

Torre et al. 1972 - Mg-Cl

Optical and Electrooptical Properties

Schmid and Trooster 1967 - optical study of phase transitions

Kobayashi, Mizutani, Hara et al. 1970 - optical refractive index of Fe-I

Pisarev et al. 1970 - crystal field theory and optical absorption

Fridkin et al. 1974 - temperature dependence of the optical absorption edge

Smutný and Konak 1975 - Co-I

Raman Spectroscopy

Lockwood 1976 A - Cr-Cl

Lockwood 1976 B - Cr-Cl, Mn-Cl

Piezoelectricity

Mg-Cl: Sonin and Zheludev 1963; Torre et al. 1972;
Albers et al. 1976

Fe-I: Kobayashi and Mizutani 1970;
Kobayashi, Mizutani, Hara et al. 1970

Co-I: Smutný and Albers 1972

TABLE 22. EXPERIMENTAL LITERATURE ON BORACITES (CONT'D)

DC Resistivity

Sonin and Zheludev 1963 - Mg-Cl

Smutný et al. 1974 A - Ni-I

Schmid et al. 1976 - Fe-I

Crystal Growth

Jona 1959; Schmid 1965; Schmid 1969;

Nassau and Shiever 1972

Ferromagnetoelectricity of Ni-I Boracite

Ascher et al. 1966

Miyashita and Murakami 1970

The Effect of Hydrostatic Pressure on the Ferroelectric Phase Transition Temperature

Fousek et al. 1972 - Co-I

TABLE 23. OBSERVED FERROELECTRIC TRANSITIONS IN BORACITES

Boracite	Phase Transition	Transition Temperatures($^{\circ}\text{C}$)	Nature of Transition	Ref.
Mg-Cl	$\bar{4}3m\text{-mm}2$	265	1	2
Cr-Cl	$\bar{4}3m\text{-mm}2$	-9	1	2
Fe-Cl	$\bar{4}3m\text{-mm}2$	320	1	1
	-m	225	1	1
	-3m	203	1	1
Fe-Br	$\bar{4}3m\text{-mm}2$	222	1	1
	-3m	130	1	1
Fe-I	$\bar{4}3m\text{-mm}2$	72		
		-55 - -70		6,7
Co-Cl	$\bar{4}3m\text{-mm}2$	350	1	1
	-m	265	2	2
	-3m	195	2	2
Co-Br	$\bar{4}3m\text{-mm}2$	185		
Co-I	$\bar{4}3m\text{-mm}2$	-76	1	3,4,5
		-235		3
Ni-Cl	$\bar{4}3m\text{-mm}2$	337	1	3
Ni-Br	$\bar{4}3m\text{-mm}2$	125		
Ni-I	$\bar{4}3m\text{-mm}2$	-209		
Cu-Cl	$\bar{4}3m\text{-mm}2$	92		
Cu-Br	$\bar{4}3m\text{-mm}2$	-53	1	4
		-248		
Zn-Cl	$\bar{4}3m\text{-mm}2$	430	1	1
	-m	291	1	2
	-3m	199	1	2
Cd-Cl	$\bar{4}3m\text{-mm}2$	525		
Mg-Br		21		3
Mn-Cl		407		3
Mn-Br		291-294		3
Mn-I		139		3
Zn-Br		312		3
Zn-I		413		3
Cd-Br		462		3
Cd-I		342		3

References : (1) Bochkov et al 1973 (2) Fridkin et al 1974
 (3) Ascher et al 1964 (4) Drozhdin et al 1975
 (5) Fousek et al 1972 (6) Kobayashi et al 1972
 (7) Schmid & Trooster 1967

6.3 Experimental Literature on Molybdates

Most members of the molybdate family [chemical composition: $R_2(MoO_4)_3$ where R is a rare earth] have been shown to be ferroelectric. Among these, gadolinium molybdate and terbium molybdate have been clearly established as improper ferroelectrics; it is expected that the other molybdates will also be identified as improper ferroelectrics when studied in detail.

In addition to ferroelectricity, the molybdates also exhibit ferroelasticity. The resulting nonlinear thermal, electrical and mechanical properties of the molybdates have provided a fruitful field for experimental study. This rather extensive literature has been classified in Table 24. Papers cited in the table are listed in Appendix B.

TABLE 24. MOLYBDATES EXPERIMENTS

BRILLOUIN SCATTERING (GMO)

Itoh & Nakamura 1973 ; Itoh & Nakamura 1974 ;
Luspin & Hauret 1976 A&B

CALORIMETRIC MEASUREMENTS

GMC : Nassau et al 1965 ; Fouskova 1969 ;
Cheung & Ullman 1974 ; Megumi et al 1974
TMC : Keve et al 1970

CRYSTAL GROWTH

Borchardt & Bierstedt 1967 ; Drobyshhev et al 1969 ;
Keve et al 1970 ; Bohm & Kürsten 1971

CRYSTAL STRUCTURE

X-Ray Studies : Bernstein 1965 ; Nassau et al 1965 ;
Aizu et al 1969 ; Drobyshhev et al 1969 ;
Jamieson et al 1969 ; Nassau et al 1969 ;
Newnham et al 1969 ; Kvapil & John 1970 ;
Prewitt 1970 ; Keve et al 1971 ; Brixner et al 1972 ;
Jeitschko 1972 ; Kobayashi et al 1972 ;
Megumi et al 1974

Neutron Scattering : Axe et al 1971 ; Dorner et al 1972

DIELECTRIC CONSTANTS

GMO : Borchardt & Bierstedt 1967 ; Cross et al 1968 ;
Aizu et al 1969 ; Smith & Burns 1969 ;
Fousek & Koňák 1972B
TMC : Borchardt & Bierstedt 1967 ; Keve et al 1970

DOUBLE HYSTERESIS LOOP

Kumada 1973 ; Kumada 1974 ;
Sawaguchi & Cross 1972

TABLE 24. MOLYBDATE EXPERIMENTS (CONT'D)

DOMAIN STRUCTURES & ANTI-PHASE BOUNDARIES

Borchardt & Bierstedt 1966 ; Cummins 1970 ; Kumada 1970 ;
Kumada et al 1970 ; Bohm & Kürsten 1971 ; Barkley et al 1972 ;
Kumada 1972 ; Kürsten & Bohm 1972 ; Shepherd & Barkley 1972 ;
Suzuki 1972 ; Barkley & Jeitschko 1973 ;
Bohm & Kürsten 1973 ; Flippen & Haas 1975 ;
Kürsten et al 1973 ; Meleshina et al 1974 ; Flippen 1975

EFFECT OF HYDROSTATIC PRESSURE ON PHASE TRANSITION IN GMO

Shirokov et al 1972

ELASTIC PROPERTIES

GMO : Cross et al 1968 ; Epstein et al 1970 ;
Chizhikov et al 1971 ; Höchli 1972 ;
Courdille & Dumas 1973 ; Scheiding 1973 ;
Courdille & Dumas 1974 ; Esayan et al 1974 ;
Esayan et al 1975
TMO : Dorner et al 1972

ELECTROOPTIC PROPERTIES (GMO)

Smith & Burns 1969 ; Nakamura et al 1971 ;
Fousek & Koňák 1972 A&B ; Kobayashi & Ascher 1972 ;
Kumada 1972 ; Kobayashi & Miyazaki 1975 ;
Anistratov et al 1976 ; Kojima et al 1976 ;
Theophanous 1976

OPTICAL PROPERTIES

Refractive Indices & Birefringence :

(GMO) Aizu et al 1969 ; Smith & Burns 1969 ; Cummins 1970 ;
Nakamura et al 1971 ; Fousek & Koňák 1972A ;
Kobayashi & Ascher 1972 ; Shaldin et al 1973 ;
Fousek & Glogarová 1975 ; Anistratov et al 1976 ;
Kojima et al 1976
(TMO) Keve et al 1970 ; Shaldin et al 1973
(Nd₂(MoO₄)₃) Nassau et al 1965

TABLE 24. MOLYBDATES EXPERIMENTS (CONT'D)

Transmission Spectra : Nassau et al 1965 ; Petzelt 1971 ;
Petzelt & Dvořák 1971 ; Zeidler & Ullman 1973
Ferroelectric Laser Host : Borchardt 1963 ;
Borchardt & Bierstedt 1966
Optical Device Application : Kumada 1970 ; Kumada 1972
Second Harmonic Generation : Miller et al 1971

PHOTOELASTICITY (GMO)

Esayan et al 1974 ; Esayan et al 1975 ;
Fousek & Glogarová 1975 ; Martynov et al 1975 ;
Anistratov et al 1976

PIEZOELECTRICITY

Aizu et al 1969 ; Cummins 1970 ; Kobayashi et al 1972 ;
Scheiding & Schmidt 1972 ; Scheiding 1973 ;
Agishev et al 1976

PYROELECTRICITY

GMO : Rabinovich 1969 ; Ullman et al 1971 ;
Ullman et al 1972 ; Ullman et al 1975
TMO : Keve et al 1970

RAMAN SPECTROSCOPY (GMO)

Fleury 1970 ; Shepherd 1971 ; Shepherd & Barkley 1972 ;
Ullman et al 1973 ; Ganguly et al 1975 A&B ;
Ganguly et al 1976 ; Shigenari et al 1976 ;
Takagi et al 1976

SPONTANEOUS POLARIZATION

GMO : Borchardt & Bierstedt 1966 ; Borchardt & Bierstedt 1967 ;
Aizu et al 1969 ; Cummins 1970 ;
Kumada et al 1970 ; Sawaguchi & Cross 1973
TMO : Borchardt & Bierstedt 1967 ; Keve et al 1970

SURFACE ACOUSTIC WAVE VELOCITY ON GMO : Toda et al 1973

$\text{NaFe}(\text{MoO}_4)_2$ - A NEW FERROELASTIC : Dudnik & Stolpakova 1976

6.4 Experimental Literature on Ferroelectric Sulfates

Tables 25 and 26 summarize the results of our search of the experimental literature on ammonium sulfate, $(\text{NH}_4)_2 \text{SO}_4$, and related materials. The following classes of materials are included:

- (1) $(\text{NH}_4)_2 \text{SO}_4$ analogs: $(\text{NH}_4)_2 \text{X}$, with $\text{X} = \text{SO}_4, \text{BeF}_4, \text{SeO}_4$
- (2) Bisulfates: $\text{NH}_4 \text{HSO}_4, \text{RbHSO}_4, (\text{NH}_4)_3 \text{H}(\text{SO}_4)_2$
- (3) ABX compounds with $\text{A} = \text{Li}, \text{Na}$; $\text{B} = \text{Na}, \text{K}, \text{Rb}, \text{NH}_4, \text{Cs}, \text{N}_2\text{H}_5$; $\text{X} = \text{BeF}_4, \text{SO}_4, \text{SeO}_4$
- (4) Langbeinites: $(\text{M}^{1+})_2 (\text{M}^{2+})_2 (\text{SO}_4)_3$ with
 $\text{M}^{1+} = \text{K}, \text{Rb}, \text{Tl}, \text{NH}_4$; $\text{M}^{2+} = \text{Zn}, \text{Co}, \text{Mn}, \text{Mg}, \text{Cd}$

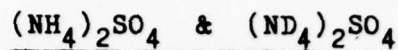
Among the langbeinites, only $(\text{NH}_4)_2 \text{Cd}_2 (\text{SO}_4)_3$ and $\text{Tl}_2 \text{Cd}_2 (\text{SO}_4)_3$ have been identified as ferroelectric. Table 25 lists all known ferroelectrics among these classes, gives the space group (or, in parentheses, the point group) of each phase if known, and the temperatures of all reported phase transitions. Ferroelectric phases have been characterized as pseudoproper when a Curie-Weiss law is obeyed in a small region above the transition temperature and as improper where there is no Curie-Weiss behavior and only a small dielectric anomaly. In Table 26 the literature is classified according to the material and physical property studied, all references are to papers listed in Appendix B.

TABLE 25. THE FERROELECTRIC SULFATE FAMILY.

Abbr.	Formula	Name	Symmetry	$T_c (^{\circ}\text{C})$	Order of Transition	Character
AS	$(\text{NH}_4)_2\text{SO}_4$	Ammonium Sulfate	Pna	-50	1	Paraelectric
APB	$(\text{NH}_4)_2\text{BeF}_4$	Ammonium Fluoberyllate	$\text{Pna}2_1$ (mm) (2/m)	-90 -96	2 1	Pseudo-Proper Ferroelectric Paraelectric
AHS	NH_4HSO_4	Ammonium Hydrogen Sulfate (Ammonium Bisulfate)	$\text{Pn}2_1/a$ $\text{P}2_1/c$ Pc P1	-3 -119	2 1	Improper Ferroelectric Paraelectric, Ferroelastic Pseudo-Proper Ferroelectric Paraelectric, Piezoelectric
RHS	RbHSO_4	Rubidium Hydrogen Sulfate (Rubidium Bisulfate)	$\text{P}2_1/c$ Pc	-15	2	Paraelectric Pseudo-Proper Ferroelectric
	$(\text{NH}_4)_3\text{H}(\text{SO}_4)_2$	Triammonium Hydrogen Sulfate		-8 -132 -140	2 2 1	Paraelectric Anti-ferroelectric Paraelectric
LAS	LiNH_4SO_4	Lithium Ammonium Sulfate	Pmc $\text{Pc}2_1/n$ (2/m)	187 10	1 1	Paraelectric Pseudo-Proper Ferroelectric Anti-ferroelectric (?)
LHS	$\text{Li}(\text{Mg}_2\text{H}_5)\text{SO}_4$ $\text{LiNH}_4\text{SO}_4 \cdot 2\text{H}_2\text{O}$	Lithium Hydrasium Sulfate Sodium Ammonium Sulfate Dihydrate	$\text{Pbn}2_1$ $\text{P}2_1^2 2_1^2$	-172 -181		Paraelectric Pseudo-Proper Ferroelectric Ferroelectric
	$\text{NaNH}_4\text{SeO}_4 \cdot 2\text{H}_2\text{O}$	Sodium Ammonium Selenate Dihydrate	$\text{P}2_1^2 2_1^2$	-93	2	Paraelectric Pseudo-Proper Ferroelectric
	RbLiSO_4	Rubidium Lithium Sulfate	orthorhombic 188 monoclinic 166 $\text{P}2_1/n$	203		Paraelectric Anti-ferroelectric Ferroelectric Paraelectric
CAS	$(\text{NH}_4)_2\text{Cd}_2(\text{SO}_4)_3$	Dicadmium Diammonium Sulfate	23 2	-181	1	Paraelectric Improper Ferroelectric
CTS	$\text{Ti}_2\text{Cd}_2(\text{SO}_4)_3$	Dicadmium Dithallium Sulfate	$\text{P}2_1^3$ $\text{P}2_1$ P1 $\text{P}2_1^2 2_1^2$	-143 -146 -175		Paraelectric Improper Ferroelectric Improper Ferroelectric Paraelectric, Ferroelastic

TABLE 26. THE FERROELECTRIC SULFATE FAMILY.

LITERATURE GUIDE



CALORIMETRIC MEASUREMENTS

Hoshino et al 1958

CRYSTAL STRUCTURE

Neutron Diffraction : Hamilton 1969 ; Schlemper & Hamilton 1966

NMR : Blinc et al 1972 ; Kydon et al 1967 ; Miller et al 1962 ;

O'Reilly & Tsang 1967 ; O'Reilly & Tsang 1969

X-Ray Scattering : Okaya et al 1958

DIELECTRIC CONSTANTS

Anistratov & Martynov 1970 ; Hoshino et al 1958 ;

Ikeda et al 1973 ; Kamiyoshi 1957 ; Ohshima & Nakamura 1966 ;

Sawada et al 1975 ; Yoshihara et al 1976

ELASTIC PROPERTIES

Hoshino et al 1958 (Thermal Expansion) ;

Ikeda et al 1973 (Elastic Compliance Coefficient, Electrostrictive Constant) ; Makita et al 1976 (Mechanical Twins) ;

Nakanishi et al 1973 (Elastic Softening) ;

Sawada et al 1976 (Mechanical Twins)

ELECTROOPTIC PROPERTIES

Anistratov & Martynov 1970 ; Fousek & Koňák 1976

INFRARED SPECTROSCOPY

Belousov et al 1975 ; Jain et al 1973 ;

KumaraAcharya & Narayanan 1973 ; Petzelt et al 1974 ;

Schutte & Heyns 1970 ; Torrie et al 1972

OPTICAL PROPERTIES

Anistratov 1972 ; Anistratov & Martynov 1970 ;

Fousek & Koňák 1976 ; Strukov 1962

PYROELECTRICITY

Sawada et al 1975

RAMAN SPECTROSCOPY

KumaraAcharya & Narayanan 1973 ; Torrie et al 1972 ;

Unruh & Ayere 1976

TABLE 26. THE FERROELECTRIC SULFATE FAMILY (CONT'D)

SPONTANEOUS POLARIZATION

Hoshino et al 1958 ; Ikeda et al 1973 ;
Matthias & Remeika 1956 ; Sawada et al 1975 ;
Unruh 1970 ; Unruh & Ayere 1976

THEORIES

Ikeda et al 1973 ; Jain & Bist 1974 ; Sawada et al 1973



CALORIMETRIC MEASUREMENTS

Hoshino et al 1958 ; Strukov et al 1973

CRYSTAL STRUCTURE

NMR : Aleksandrova & Shcherbakov 1970 ; Burns 1961 ;
Miller et al 1962
X-Ray : Makita & Yamauchi 1974 ; Okaya et al 1958

DIELECTRIC CONSTANTS

Hoshino et al 1958 ; Ohshima & Nakamura 1966 ;
Pepinsky & Jona 1957 ; Strukov et al 1962 ;
Strukov et al 1973

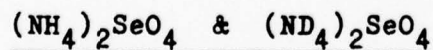
OPTICAL & ELECTROOPTIC PROPERTIES

Anistratov 1972 ; Koňák & Matras 1976

SPONTANEOUS POLARIZATION

Pepinsky & Jona 1957 ; Strukov et al 1962

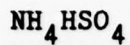
THEORIES : Dvorak et al 1975



INFRARED & RAMAN SPECTROSCOPY

Sankaranarayanan & Krishnan 1972

TABLE 26. THE FERROELECTRIC SULFATE FAMILY (CONT'D)



CALORIMETRIC MEASUREMENTS

Alexandrov et al 1976 ; Flerov et al 1975 ;
Pepinsky et al 1958

CRYSTAL STRUCTURE

Miller et al 1962 (NMR) ; Nelmes 1972 (X-Ray) ;
Watton et al 1976 (NMR)

DIELECTRIC CONSTANTS

Alexandrov et al 1976 ; Flerov et al 1975 ; Pepinsky et al 1958 ;
Strukov et al 1962 ; Tamaki et al 1976

DOMAIN STUDIES : Kondo et al 1974

EFFECT OF HYDROSTATIC PRESSURE ON PHASE TRANSITION

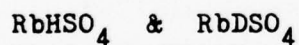
Polandov et al 1969

OPTICAL PROPERTIES : Alexandrov et al 1976

SPONTANEOUS POLARIZATION

Alexandrov et al 1976 ; Flerov et al 1975 ;
Pepinsky et al 1958 ; Strukov et al 1962

THEORIES : Aizu 1974 ; Kondo et al 1975



DIELECTRIC CONSTANT & SPONTANEOUS POLARIZATION

Alexandrov et al 1976 ; Pepinsky & Vedam 1960

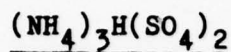
SPECIFIC HEAT & OPTICAL PROPERTIES

Alexandrov et al 1976

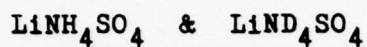
EFFECT OF HYDROSTATIC PRESSURE ON THE PHASE TRANSITIONS

Gesi & Ozawa 1975

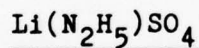
TABLE 26. THE FERROELECTRIC SULFATE FAMILY (CONT'D)



CRYSTAL STRUCTURE : Watton et al 1976 (NMR)
 DIELECTRIC CONSTANTS : Gesi 1976 ; Pepinsky et al 1958
 SPECIFIC HEAT : Gesi 1976

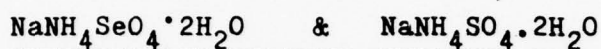


CRYSTAL STRUCTURE
 Aleksandrov et al 1975 ; Dollase 1969 (X-Ray) ;
 Yuzvak et al 1975 (NMR)
 DIELECTRIC CONSTANTS & SPONTANEOUS POLARIZATION
 Mitsui et al 1975 ; Yuzvak et al 1975
 DOMAIN STUDIES : Hildmann et al 1975
 ELASTIC CONSTANTS : Aleksandrov et al 1975
 INFRARED & RAMAN SPECTROSCOPY : KumaraAcharya & Narayanan 1973
 OPTICAL & ELECTROOPTIC PROPERTIES : Anistratov & Mel'nikova 1975



CALORIMETRIC MEASUREMENTS : Pepinsky et al 1958
 CONDUCTIVITY : Howell et al 1967 ; Schmidt et al 1971
 CRYSTAL STRUCTURE
 Neutron Scattering : Padmanabhan & Balasubramanian 1967
 X-Ray : Brown 1964 ; Van den Hende & Boutin 1964
 NMR : Cuthbert & Petch 1963 ; Knispel & Petch 1971
 DIELECTRIC CONSTANTS
 Pepinsky et al 1958 ; Schmidt et al 1971

TABLE 26. THE FERROELECTRIC SULFATE FAMILY (CONT'D)



CRYSTAL STRUCTURE

NMR : Aleksandrova et al 1972 ; Shirokov et al 1975

DIELECTRIC CONSTANTS

Aleksandrov et al 1971 ; Makita & Sekido 1965 ;

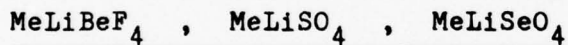
Shirokov et al 1975 ; Zaitseva et al 1975

ELASTIC & PIEZOELECTRIC PROPERTIES : Zaitseva et al 1975

INFRARED & RAMAN SPECTROSCOPY : KumaraAcharya & Narayanan 1973

OPTICAL & ELECTROOPTIC PROPERTIES : Anistratov & Mel'nikova 1975

PYROELECTRICITY : Makita & Sekido 1965



Me = K, Rb, Tl, NH_4 , Cs (except NH_4LiSO_4)

CRYSTAL STRUCTURE

Chung & Hahn 1972 ; Hahn et al 1969 ;

LeRoy & Aleonard 1970 ; LeRoy & Aleonard 1972

DIELECTRIC CONSTANTS : Shiroishi et al 1976 (RbLiSO_4)

OPTICAL & ELECTROOPTIC PROPERTIES

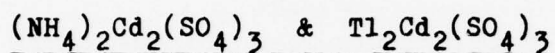
Anistratov & Mel'nikova 1975 ($\text{LiNH}_4\text{SeO}_4$)

INFRARED & RAMAN SPECTROSCOPY

Rao et al 1976 (LiKSO_4) ;

Sankaranarayanan & Krishnan 1972 ($\text{LiNH}_4\text{SeO}_4$)

TABLE 26. THE FERROELECTRIC SULFATE FAMILY (CONT'D)



CRYSTAL STRUCTURE : Ikida & Yasuda 1975 (CTS, X-Ray)

DIELECTRIC CONSTANTS

CAS : Glogarová & Fousek 1973 ; Glogarová et al 1972 ;
Jona & Pepinsky 1956 ; Ohshima & Nakamura 1966

CTS : Ěrezina & Glogarová 1972 ; Ikida & Yasuda 1975

DOMAIN STUDIES

CAS : Glogarová & Fousek 1973 ; Glogarová et al 1972

CTS : Ěrezina & Glogarová 1972

ELASTIC PROPERTIES

CAS : Glogarová et al 1972

CTS : Ikida & Yasuda 1975

INFRARED & RAMAN SPECTROSCOPY

CAS : KumaraAcharya & Narayanan 1973

OPTICAL & ELECTROOPTIC PROPERTIES

CAS : Glogarová & Fousek 1973 ; Glogarová et al 1972 ;
Koňák & Fousek 1974 ; Koňák et al 1974

SPONTANEOUS POLARIZATION

CAS : Glogarová & Fousek 1973

THEORIES : Dvořák 1972 & 1974

APPENDIX A

Intuitive Physical Overview of Theoretical Concepts
used in Study of Improper Ferroelectrics

1. THEORY

This Appendix contains intuitive physical overviews of the theoretical concepts used in the study of improper ferroelectrics. There are two languages in wide-spread use. One is provided by Landau's macroscopic theory of continuous phase transitions and the other originates with the microscopic soft-mode analysis of structural phase transitions. Using these ideas we distinguish between three different types of extrinsic (or improper in the larger sense) ferroelectrics. Since all known improper ferroelectrics also exhibit ferroelasticity, we also summarize the relationship between the full free energy and the reduced free energy which is applicable to stress-free measurements.

1.1 Landau Theory of Continuous Phase Transitions

Landau's theory is basically a macroscopic thermodynamic analysis applicable to any continuous, so-called second-order phase transition. In a second-order phase transition, the transition temperature marks the point where the system's properties begin to change; there is no sudden jump in the system's properties at the transition temperature, as occurs in the so-called first-order transitions.* While the Landau analysis is strictly applicable only to such gradual or continuous phase transitions, it can be extended to the first-order transitions in which the discontinuities exhibited at the transition temperature are small.

1.1.1 Free Energy Considerations

The first ingredient of the Landau theory is to exploit the hypothesized continuity of the phase transition by expanding the relevant thermodynamic free energy Φ as a power series in the so-called order parameter, η . "Order parameter" is the generic name for the property which distinguishes the two phases of the system. For example, in an ordinary ferroelectric, the order parameter is just the electric polarization. The order parameter is chosen so that it vanishes in one phase (the high

symmetry or prototypic phase) and gradually begins to appear at the transition temperature, thus making the transition to the new phase (the low symmetry or ferroic phase). This expansion of the free energy ϕ , which is assumed to be valid both above and below the transition temperature, has, in general, the form:

$$\begin{aligned} \phi(n, p, T) = & \phi_0(p, T) + n\phi_1(p, T) + n^2\phi_2(p, T) + \\ & + n^3\phi_3(p, T) + n^4\phi_4(p, T) \dots \end{aligned} \quad (1)$$

where p denotes the pressure and perhaps other thermodynamic properties which are not involved in the transition.

This free energy, of course, embodies a complete description of the thermodynamic behavior of the system; its consequences are deduced in a number of ways. For example: the order parameter n takes the value that gives a minimum for ϕ ; the inverse susceptibility χ^{-1} (in the ferroelectric case, the dielectric stiffness) is just the curvature of ϕ at that minimum $\chi^{-1} = \partial^2\phi/\partial n^2$; the entropy $S = -\partial\phi/\partial T$, and heat capacity $C = -T\partial^2\phi/\partial T^2$ are contained in the temperature dependence of the free energy.

Landau's analysis reveals that if the free energy ϕ , given in Equation (1), is, in fact, to describe a second-order transition additional requirements must be met. First, the odd degree terms must vanish; second, the coefficient of the second degree term must change sign at the transition temperature; and third, the coefficient of the fourth degree term must be positive. We shall see below that these requirements amount to substantive restrictions on the nature of the order parameter and the nature of the high symmetry and low symmetry phases of the system. At this point, let us just review the general features of the phase transition, assuming that these requirements are fulfilled.

The free energy for a second order transition then, has the form:

$$\phi(\eta, T) = \phi_0 + a(T - T_c)\eta^2 + B\eta^4 \quad (2)$$

where $B > 0$, T_c is the transition temperature and $a > 0$ if the high symmetry phase is also the high temperature phase. (This is usually, but now always, the case). In Figure 1, ϕ is plotted as a function of the order parameter η for a number of different temperatures. Figure 2 depicts the temperature dependence of the order parameter and inverse susceptibility deduced from this free energy. (In the case of a proper ferroelectric, these correspond to the electric polarization and the dielectric stiffness, respectively.) From Figure 1 we see that for $T > T_c$, the minimum of ϕ is at $\eta = 0$ and χ^{-1} , the curvature of ϕ at the minimum is quite large. As the temperature is reduced, the minimum remains at $\eta = 0$ and the curvature χ^{-1} vanishes. As the temperature is reduced below T_c , the central minimum bifurcates into two symmetric minima which gradually move further from the origin, with their curvature increasing concomitantly.

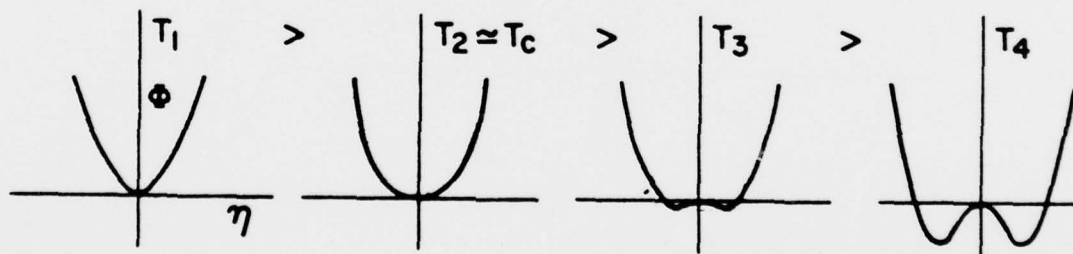
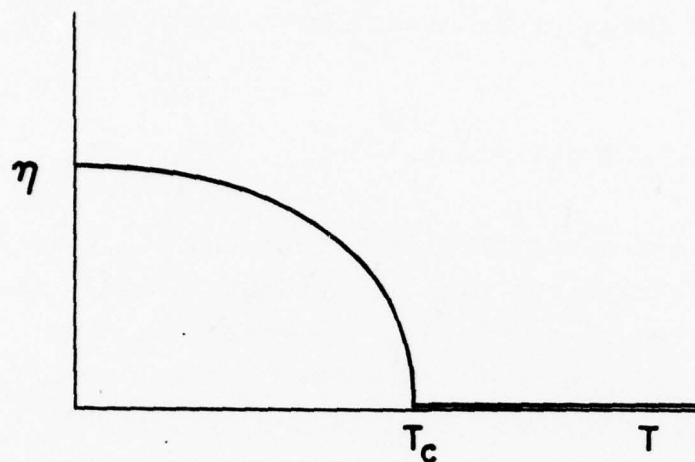
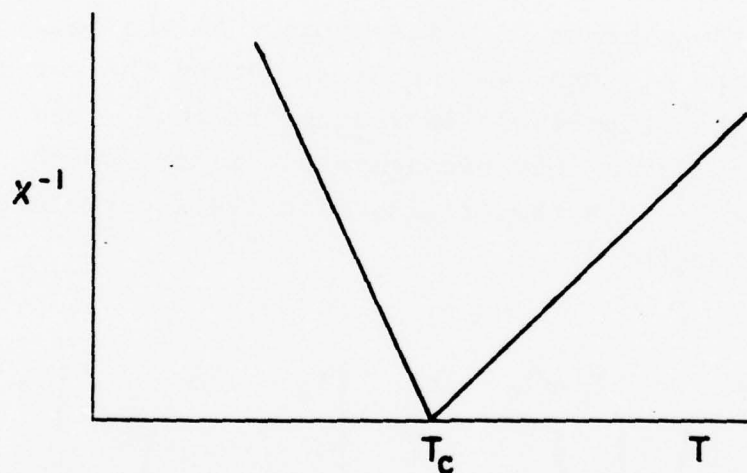


Figure 1: Free energy $\phi(\eta, T)$ vs. order parameter η for various temperatures above and below critical temperature T_c where a second-order phase transition occurs.



(a)



(b)

Figure 2: (a) Temperature dependence of the magnitude of the order parameter η for a system which undergoes a second-order phase transition at T_c . The graph gives the value of η at the absolute minimum of the free energy which is shown in Fig. 1. Below T_c , η varies as $(T_c - T)^{1/2}$. (b) Temperature dependence of the inverse susceptibility χ^{-1} , for a system which undergoes a second-order phase transition at T_c . This graph gives the value of the curvature of the free energy (shown in Fig. 1) at its absolute minimum.

Landau's analysis of second-order phase transitions can be extended to describe first-order transitions which are nearly of second order. Such weak first-order transitions are describable by a free energy of the form:

$$\phi = \phi_0 + a(T - T_c)\eta^2 + B\eta^4 + C\eta^6 \quad (3)$$

where $C > 0$, and B is negative but small. Figure 3 depicts the free energy at various temperatures, while Figure 4 exhibits the temperature dependence of the order parameter and inverse susceptibility. The order parameter makes a small jump at the transition temperature and the susceptibility does not diverge at T_c , although it exhibits the characteristic Curie behavior $\chi = C/(T - T_0)$ with $(T_0 < T_c)$ in the high symmetry phase.

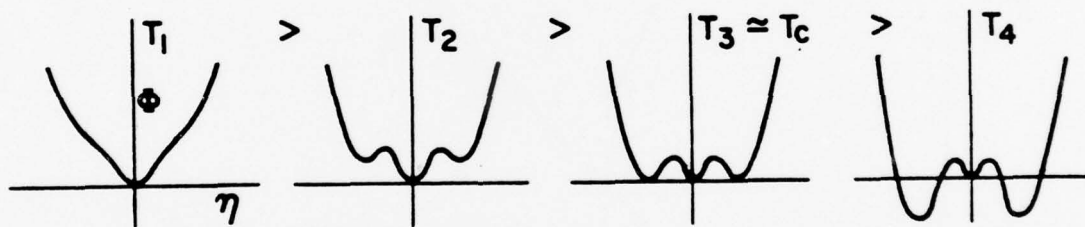
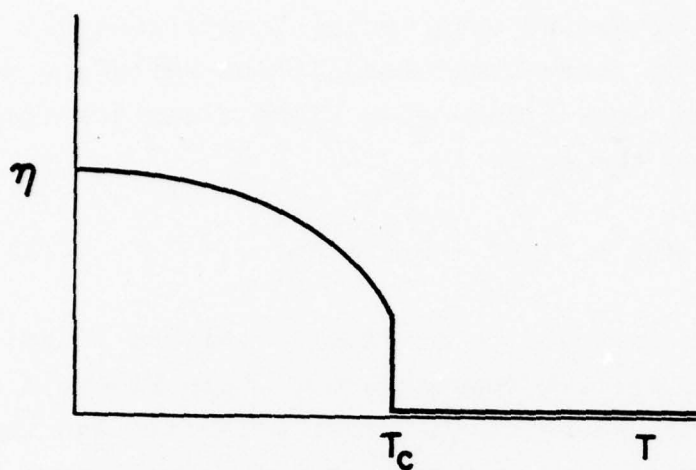
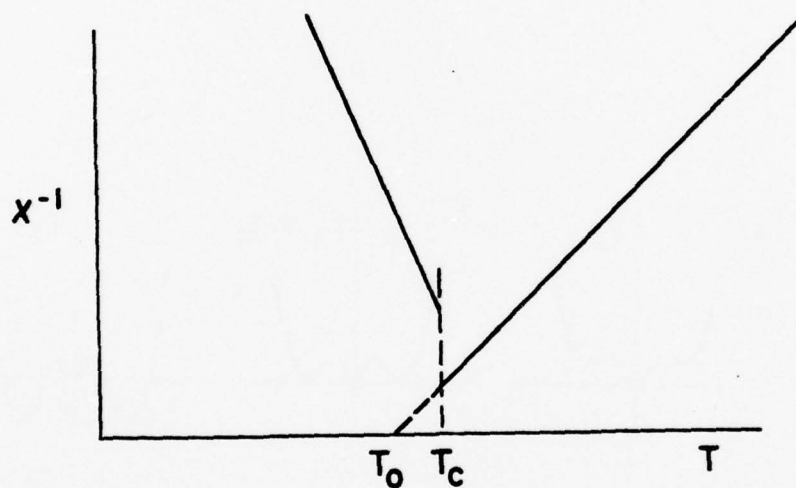


Figure 3: Free energy $\phi(\eta, T)$ vs. order parameter η for various temperatures above and below critical temperature T_c where a first-order phase transition occurs.



(a)



(b)

Figure 4: (a) Temperature dependence of the magnitude of the order parameter η for a system which undergoes a first-order phase transition at T_c . The graph gives the value of η at the absolute minimum of the free energy which is shown in Fig. 3. (b) Temperature dependence of the inverse susceptibility χ^{-1} , for a system which undergoes a first-order phase transition at T_c . This graph gives the value of the curvature of the free energy (shown in Fig. 3) at its absolute minimum.

1.1.2 Order Parameter Symmetry

The second major ingredient of the Landau theory of second-order phase transitions is an analysis of the symmetry properties of the order parameter and how these relate to the overall symmetry of the system both above and below the transition temperature. Let us first consider the high symmetry phase ($n = 0$) of the system precisely at the transition temperature. This phase can be characterized by the electric charge density function $\rho(r)$. Since the charge density embodies an entire description of the material, one could in principle, calculate the free energy ϕ from $\rho(r)$. Of course, one cannot in practice perform such a calculation but we can symbolize the dependence by writing $\phi[\rho(r)]$. Moreover, since the charge density function reflects the spatial distribution of all the electrons and nuclei which make up the material, it should be left invariant by all the crystallographic symmetries (rotations, reflections, translations, etc.) possessed by the high symmetry phase of the system.

As the temperature changes and the system undergoes its phase transition into the new ($n \neq 0$) phase, the electric charge density function will change continuously from $\rho(r)$ to $\rho(r) + \delta\rho(r)$. For a second-order phase transition, the electric charge density will not change abruptly at the transition temperature; rather $\delta\rho(r)$ will start from zero at the transition temperature and gradually increase in magnitude as the temperature moves further into the new ($n \neq 0$) phase. What changes abruptly at the transition temperature is not the magnitude, but rather the symmetry of the charge density function. As we shall see below, for a second-order phase transition, $\delta\rho(r)$ must necessarily possess fewer crystallographic symmetries than $\rho(r)$. So, as soon as the temperature moves an infinitesimal amount into the new ($n \neq 0$) phase, $\delta\rho(r)$ becomes non-zero and the macroscopic crystallographic symmetry of the system is reduced. (This provides the reason for naming the $n \neq 0$ phase the low symmetry phase, and the $n = 0$ phase the high symmetry phase.)

Since $\delta\rho(r)$ brings about this reduction in symmetry, it is instructive to analyze $\delta\rho(r)$ in terms of the symmetry of the high symmetry phase. We shall decompose $\delta\rho(r)$ into a sum of functions $\phi_i^{(n)}(r)$ which possess special properties from the point of view of the crystallographic symmetries of the high symmetry phase, namely:

$$\delta\rho(r) = \sum_n \left(\sum_i C_i^{(n)} \phi_i^{(n)}(r) \right) \quad (4)$$

where the size of the coefficients $C_i^{(n)}$ of the normalized functions $\phi_i^{(n)}$ determine the magnitude of $\delta\rho(r)$ at a given temperature (clearly all $C_i^{(n)} = 0$ at the transition temperature). The real-valued functions $\phi_i^{(n)}(r)$ are chosen so as to transform according to a physically irreducible representation of the symmetry group of the high temperature phase. That is, when acted upon by a symmetry transformation of the high temperature phase, a given function, $\phi_i^{(n)}(r)$ transforms into some linear combination of the other functions $\phi_1^{(n)}(r), \phi_2^{(n)}(r) \dots$ which have the same index n .

For example, $\phi_1^{(2)}(r)$ may become equal to $(2\phi_1^{(2)}(r) - \phi_2^{(2)}(r) + \phi_3^{(2)}(r))/\sqrt{6}$ when its argument $(r) = (x, y, z)$ is replaced by $(x, y, -z)$, i.e., when it is transformed according to a mirror reflection in the x - y plane. In addition, this decomposition of $\delta\rho(r)$ in terms of families of real-valued functions which transform solely among themselves is assumed to be complete, in the sense that a set of functions with given index n cannot be further decomposed into two subsets of real-valued functions which transform solely among themselves when acted upon by the symmetry operations of the high temperature phase (Ref. 1).

Ref. 1: It is sometimes possible to further decompose a physically irreducible representation by allowing the introduction of complex-valued functions. (In such a case we drop the adjective, physically, and call them simply, irreducible representations.) Since we are decomposing an intrinsically real function $\delta\rho(r)$, we do not carry the decomposition further than the physically irreducible representations.

In summary, the index n labels the different physically irreducible representations while the subscript i distinguishes among the different independent functions belonging to a particular physically irreducible representation; the number of linearly independent functions in any one such family is the dimension of that physically irreducible representation.

It is possible to view Equation (4) from two different perspectives. Up to this point, we have regarded the coefficients $C_i^{(n)}$ as constant and the functions $\phi_i^{(n)}(r)$ as transforming under symmetry operations. An equally valid perspective is to regard the functions $\phi_i^{(n)}(r)$ as fixed and then allow the coefficients $C_i^{(n)}$ to transform among themselves under the action of the symmetry operations. Henceforth, we shall employ the second perspective exclusively: The coefficients $C_i^{(n)}$ are regarded as transforming according to the irreducible representations of the symmetry group of the ($n = 0$) phase.

The reason so much attention is focused on these coefficients is simply that the coefficient $C_i^{(n)}$ are just the components of the order parameter.

Each separate set of coefficients with a given index n , ($C_1^{(n)}$, $C_2^{(n)}$...), is taken to constitute a separate order parameter, distinguishable from all others by the way it transforms under the symmetry operations of the high symmetry phase. Clearly there are as many different kinds of order parameters as there are different physically irreducible representations of the symmetry group of the high symmetry phase.

While a plethora of order parameters is thus logically possible, it would be extremely unlikely if more than one order parameter were to have precisely the same transition temperature. This restriction to phase transitions describable by a single order parameter amounts to a substantive restriction on the kind of symmetry change that may take place in a second-order phase transition.

For the case of only one order parameter, we may drop the index n and write Equation (4) as,

$$\delta\rho(r) = \sum_i C_i \phi_i(r). \quad (5)$$

It is conventional abuse of language for "order parameter" to refer to both the entire array of coefficient $\eta \sim (C_1, C_2, \dots)$ and to the magnitude of these components $\eta = (\sum_i C_i^2)^{1/2}$. The expansion of the free energy as a power series in the order parameter takes the form:

$$\begin{aligned} \phi[\rho + \sum_i C_i \phi_i] &= \phi_0 + \phi_1 p_1(C_i) + \phi_2 p_2(C_i) + \\ &\dots + \phi_n p_n(C_i) + \dots \end{aligned} \quad (6)$$

where $p_n(C_i)$ is a polynomial of the n^{th} degree in the components of the order parameter. (Hence, the magnitude of $p_n(C_i)$ goes as η^n). Since the free energy must be an invariant quantity under the crystallographic symmetry transformations, each term which appears in the expansion must likewise be invariant. A given order parameter has specified transformation properties under the crystallographic symmetries of the high symmetry phase, so it is either possible or not possible to construct an invariant polynomial of some desired degree ($p_n(C_i)$). Thus the transformation properties of the order parameter will determine whether a given term will actually appear in the expansion (6). Moreover, it is unreasonable to expect that a term which is allowed by the symmetry of the order parameter would not appear. In summary, then, it is the symmetry of the order parameter which determines which terms appear in the free energy expansion.

We have seen in Par. 1.1.1, that the odd degree terms must not appear in a free energy which is to describe a second-order

phase transition. This requirement places further substantive restrictions on the possible order parameters which describe a continuous phase transition. In fact, the requirement that the first degree term not appear, rules out continuous phase transitions except those which reduce the symmetry of the initial phase. (This fact has already been assumed implicitly in the preceeding discussion.)

In summary, then, the Landau analysis of continuous phase transitions severely limits the allowable transitions, to those describable by a single order parameter which possesses no odd degree invariants. It is surprising how far-reaching these relatively simple requirements are.

1.2 Soft Modes and Structural Phase Transitions

The soft mode perspective provides a more intuitive microscopic picture of the order parameter which describes a continuous phase transition in a crystal. Here basically one identifies the order parameter with the amplitude of some optical phonon. Such a description is valid for a purely structural transition involving the atomic positions; it is a less fruitful approach for transitions in which the electrons play a significant role.

To appreciate the insights that this perspective does provide, let us consider an idealized crystal and focus our attention on the motion of some single atom within each unit cell. The net force acting on the atom has two major contributions; first, a local potential provided by all the other atoms within the same unit cell, which causes the atom to perform some oscillatory motion about its equilibrium position; and second, an interaction with the similar atoms in neighboring cells which couple these oscillatory motions together. There are two complimentary perspectives from which to view a crystal. In the first, one focuses on the oscillation of individual atoms and the interaction among these individual oscillators - as described above. In the second, one focuses on the traveling-wave collective oscillations of all the atoms together - the optical phonons. When all the local and interaction potentials are harmonic, the running waves of atomic oscillations are the true normal modes of oscillation for the crystal, i.e., each traveling wave has a characteristic wavelength and frequency and does not interact with all the other traveling waves of atomic oscillation. When the local or interaction potentials are not harmonic, the traveling wave oscillations are not true normal modes of the crystal - they interact and scatter off each other. Nevertheless, these optical phonons provide a fruitful way of analyzing the collective motion of all the atoms within the crystal.

Each optical phonon is characterized by its wavelength as a running wave λ (or equivalently its wave number, $k = 2\pi/\lambda$), the frequency of the collective oscillation, ν , (or equivalently, its angular frequency $\omega = 2\pi\nu$) and the amplitude a_k of the oscillation (see Fig. 5a).

Two particular optical phonons are of interest for structural phase transitions. First the infinite wavelength (i.e., $k = 0$) phonon which describes the in-phase oscillations of all the atoms up and down together (called the zone center or Γ point phonon; see Fig. 5b). Second, the phonon with wavelength of two lattice spacings (i.e., $k = \pi/a$) which describes the out-of-phase oscillations where the position of neighboring atoms are always anti-correlated, (called the zone edge or zone boundary phonon, see Fig. 5c).

In a structural phase transition, the equilibrium positions of certain atoms within each unit cell shift. In the "soft mode" picture of such a transition, we focus attention on the optical phonon whose spatial pattern of oscillation corresponds to the spatial pattern of the atomic shifts. For example, in a structural transition in which a central atom is displaced from the center of each unit cell in one particular direction, one would focus attention on the zone center phonon which describes the in-phase oscillation of these central atoms in that particular direction (see Fig. 5b). In the high symmetry phase, these central atoms are all oscillating together about the centers of their respective cells at some finite frequency.

As the transition temperature is approached, the oscillation slows down, i.e., its frequency approaches zero as shown in Figure 6 and 7a. It is this slowing down of the optical phonon that is referred to as the "softening" of this optical mode. As the crystal passes through the transition temperature into the low symmetry phase, this soft mode is described as "freezing in". Of course, this does not mean that the oscillations cease; rather, it means that the center about which each atom

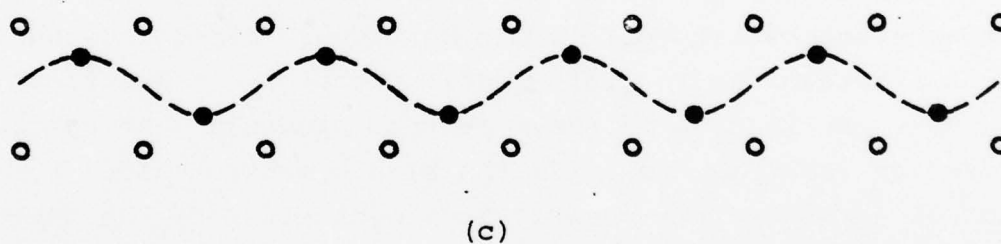
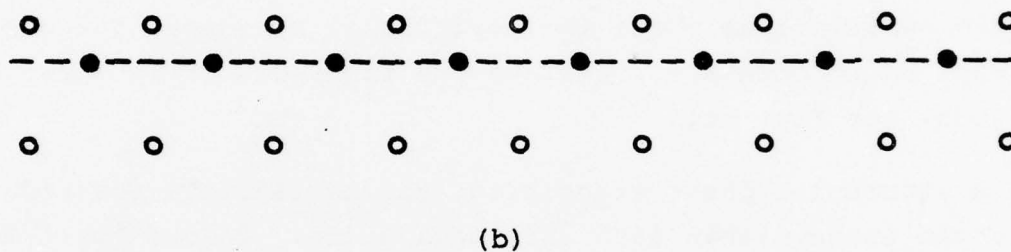
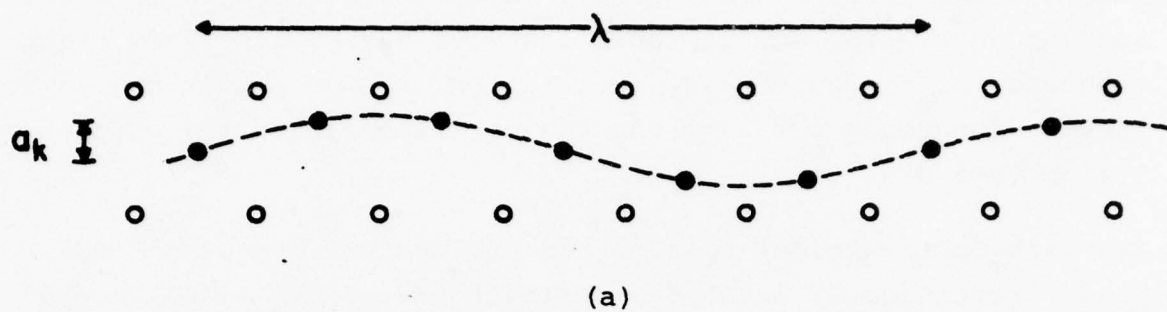


Figure 5: (a) Idealized depiction of a typical optical phonon, i.e., collective running wave oscillation of all of the central atoms in the unit cell. The wavelength λ is six lattice spacings a , so the wavenumber is $k = 2\pi/6a$. One should imagine that the solid atoms are all oscillating about the center of their cells at same frequency ω_k . The magnitude of this collective oscillation is given by a_k . (b) Idealized depiction of a zone center ($\lambda = \infty$, $k = 0$) phonon. All of the atoms move up and down together. (c) Idealized depiction of a zone boundary ($\lambda = 2a$, $k = \pi/a$) phonon.....

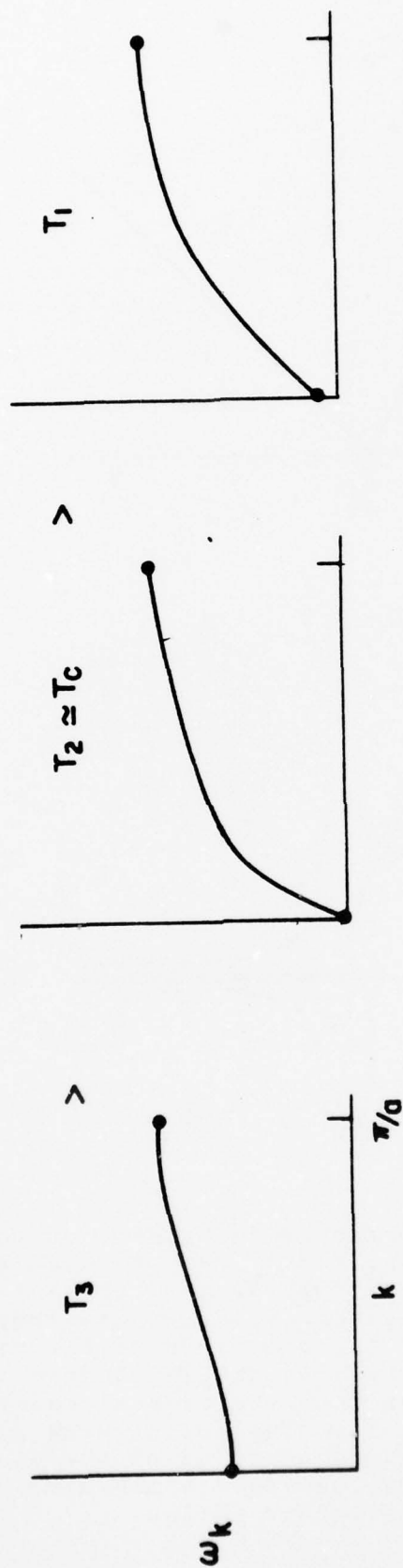


Figure 6: Temperature dependence of the dispersion curve (i.e. frequencies ω_k of the optical phonons at each wavenumber k) for a system which under goes a structural transition at T_c corresponding to the "freezing in" of a zone center phonon.

AD-A062 730

PHILIPS LABS BRIARCLIFF MANOR N Y
OPTIMIZED PYROELECTRIC VIDICON THERMAL IMAGER. VOLUME II. IMPRO--ETC(U)
JUL 78 W A SMITH

F/G 17/5

DAA653-76-C-0053

NL

UNCLASSIFIED

3 OF 3

AD
A0 62730



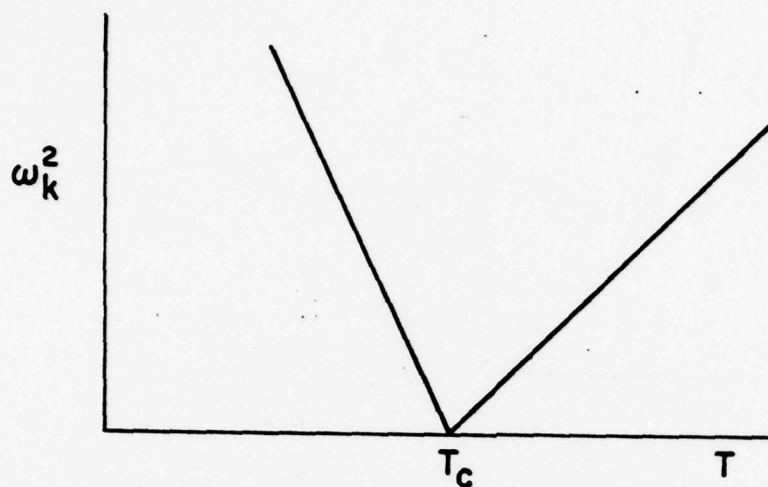
END
DATE
FILMED

3 --79

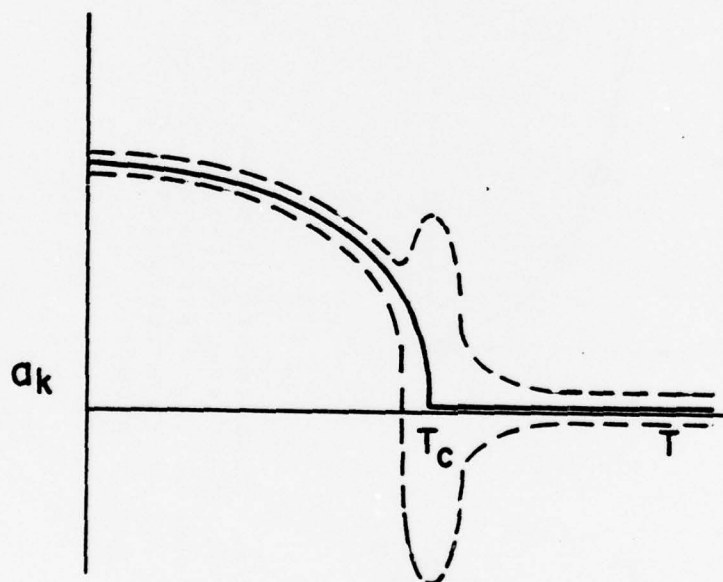
DDC



MICROCOPY RESOLUTION TEST CHART
NATIONAL BUREAU OF STANDARDS-1963-A



(a)



(b)

Figure 7: (a) Temperature dependence of the frequency of the zone center phonon which softens as the consequence of a structural phase transition at T_c . (b) Heuristic depiction of the temperature dependence of the amplitude of the oscillatory motion of an atom which is displaced from its equilibrium position when the crystal undergoes a phase transition at T_c . The solid curve gives the temporally averaged position of the atom; the dashed curves are the envelope which marks the extremes of its oscillatory motion.

oscillates has shifted in a spatial pattern which mirrors the spatial pattern of the oscillatory motion (see Fig. 7b).

It is possible to establish a relatively strong link between this soft mode description and the Landau order parameter description. In the limit of a purely harmonic crystal lattice where the optical phonons are true normal modes of the system, one can classify the spatial pattern of atomic displacements of each normal mode according to the crystallographic symmetries. In fact, one can identify each optical phonon by the physically irreducible representation under which it transforms. Thus, its behavior under the crystallographic symmetry transformations enable one to link a particular optical phonon to the particular order parameter which transforms according to the same physically irreducible representation.

1.3 Extrinsic Ferroelectrics

The figure-of-merit for a pyroelectric detector material is $p/\epsilon c$, where $p = (\partial P/\partial T)$ is the pyroelectric coefficient, $\epsilon = (\partial P/\partial E) + 1$ is the dielectric constant, and c is the volume specific heat. In an intrinsic (or proper) ferroelectric for temperatures where the pyroelectric coefficient is large, the dielectric constant is also large. This is readily understood since in an intrinsic ferroelectric the same structural deformation of the material that is temperature dependent also carries the ferroelectric polarization. In a regime where this structural deformation is easily changed by adding microscopic thermal energy (i.e., $p = \partial P/\partial T$ is large), this structural deformation is also easily changed by an external electric field (i.e., $\epsilon = \partial P/\partial E$ is large) which can couple directly to the structural deformation via its electric polarization. Thus, in an intrinsic ferroelectric the pyroelectric and dielectric response are fundamentally related since they owe their origin to the same microscopic structural deformation. Moreover, and unfortunately, the relationship is such that a large pyroelectric coefficient implies a large dielectric constant, thereby producing a reduced detector figure-of-merit.

In an extrinsic ferroelectric, there are two structural deformations taking place simultaneously. The deformation which is temperature sensitive (called the primary or soft mode) carries no electric polarization itself. It is, however, coupled to a secondary deformation which carries the electric polarization. The description of an extrinsic ferroelectric must include both the magnitude of the primary deformation (the order parameter, η) and the magnitude of the secondary ferroelectric deformation (the polarization, P). Since the thermal and electric response of the material are embodied in separate microscopic features of an extrinsic ferroelectric, one no longer has the tight coupling between the pyroelectric coefficient and dielectric constant¹

which occurs in intrinsic ferroelectrics. The precise relationship of the thermal and dielectric response depends upon the coupling between the primary soft deformation and the secondary ferroelectric deformation. While this coupling can vary considerably, an analysis of the symmetry of the order parameter and the polarization enables one to classify all extrinsic ferroelectrics into three distinct classes.

(a) Improper Ferroelectrics. The primary order parameter η which softens at the transition temperature completely describes the reduction in crystal symmetry at the phase transition. The order parameter η transforms under the crystallographic symmetries differently than does the electric polarization P . The η - P interaction contributes to the free energy a term of the form $\eta^2 P$ or $\eta^3 P$. Such materials have dielectric properties which are dramatically different from ordinary ferroelectrics. Gadolinium molybdate is the best known example of such a material.

(b) Pseudoproper Ferroelectrics. The primary order parameter η also completely describes the symmetry reduction at the transition. However, in this case η transforms under the crystallographic symmetries in the same fashion as the electric polarization (although it is not the polarization). The η - P interaction will then contribute a term ηP to the free energy. The dielectric behavior of such a material is qualitatively indistinguishable from an ordinary ferroelectric. KDP provides the best studied example of a ferroelectric transition of this type.

(c) Triggered Ferroelectrics. The primary order parameter η does not completely account for the symmetry reduction at the transition (thus the transition is necessarily of first order). The transformation properties of η under the crystallographic symmetries are different from those of the electric polarization and are such that the lowest order η - P interaction contributes a term $\eta^2 P^2$ to the free energy. Such a material would have dielectric properties quite different from ordinary ferroelectrics, but no example of such a transition has been identified.

1.4 Ferroelasticity and the Reduced Free Energy

All known improper ferroelectrics also exhibit ferroelasticity. It is possible, however, to formulate the theory and perform measurements in such a fashion that one does not have to deal with the ferroelasticity explicitly. An improper ferroelectric requires a minimum of three thermodynamic coordinates to specify its state, viz., temperature (T), macroscopic polarization (P), and the order parameter describing the soft mode which undergoes the phase transition [η -(C_1, C_2, \dots)]. For an improper ferroelectric which is also ferroelastic, an additional thermodynamic coordinate, x , the strain field, must also be specified to describe the thermodynamic state of the system. The free energy describing such a system has the form,

$$\begin{aligned} \Phi(\eta, P, x, T) = & \Phi_0 + \frac{1}{2} a_0 (T - T_c) \eta^2 + \frac{1}{4} \eta^2 f_4 + \frac{1}{6} \eta^6 f_6 \\ & + \frac{1}{2} \eta^2 P g_2 + \frac{1}{2} \eta^2 x h_2 \\ & + \frac{1}{2} A P^2 + B x P + \frac{1}{2} C x^2 \end{aligned} \quad (7)$$

where, f_n , g_n , and h_n are temperature independent polynomials of degree n in the direction cosines, $\gamma_i = C_i / \eta$ of the order parameter whose magnitude is $\eta = (\sum_i C_i^2)^{1/2}$.

On the first line are the usual free-energy terms describing a continuous phase transition for η . The terms in the second line describe the interaction of η with P and x . The terms in the last line provide the stabilization of P and x and a possible direct interaction between these two coordinates.

In studying the pyroelectric and dielectric properties of such a material, the ferroelastic features are not of direct interest. Since no external stresses are applied to the sample, one can

use the condition $\partial\phi/\partial x = 0$ to eliminate the strain coordinate x from the free energy $\phi(\eta, P, x, T)$ to give a reduced free energy $\phi'(\eta, P, T)$ which only depends on the thermodynamic coordinates of interest. This reduced free energy takes the form,

$$\begin{aligned} \phi'(\eta, P, T) = & \phi_0 + \frac{1}{2} a_0 (T - T_C) \eta^2 + \frac{1}{4} \eta^2 f_4' + \frac{1}{6} \eta^2 f_6 \\ & + \frac{1}{2} \eta^2 P g_2' + \frac{1}{2} A' P^2 \end{aligned} \quad (8)$$

where, $f_4' = f_4 - (h_2)^2 / 2C$,

$A' = A - B^2/C$, and

$$g_2' = g_2 - h_2 B/C. \quad (9)$$

Thus, the reduced free energy in Equation (8) has the same form as the complete free energy given in Equation (7) if all terms containing the strain were omitted. While the form of the reduced free energy is the same as for an improper ferroelectric which is not ferroelastic, the renormalization of the parameters given by Equation (9), which is brought about by the presence of ferroelasticity, alters the physical meaning of these free energy parameters.

APPENDIX B

Bibliography of Improper Ferroelectrics

1. P. K. Acharya and P. S. Narayanan, Indian J. Pure & Appl. Phys. 11, 514 (1973)
Vibration Spectra of Ferroelectric Sulfates: Part I - $(\text{NH}_4)_2\text{SO}_4$, LiNH_4SO_4 , $\text{NaNH}_4\text{SO}_4 \cdot 2\text{H}_2\text{O}$, and $(\text{NH}_4)_2\text{Cd}_2(\text{SO}_4)_3$
2. P. K. Acharya and P. S. Narayanan, Indian J. Pure & Appl. Phys. 11, 519 (1973)
Vibration Spectra of Ferroelectric Sulfates: Part II - RbHSO_4 , NH_4HSO_4 and $(\text{NH}_4)_3\text{H}(\text{SO}_4)_2$
3. B. A. Agishev, I. A. Deryugin, V. V. Lemanov and N. K. Yushin, Sov. Phys. Sol. State 18, 638 (1976)
Electroacoustic Interaction in Piezoelectrics
4. K. Aizu, Phys. Rev 146, 423 (1966)
Possible Species of Ferroelectrics
5. K. Aizu, J. Phys. Soc. Japan 27, 387 (1969)
Possible Species of "Ferroelastic" Crystals and of Simultaneously Ferroelectric and Ferroelastic Crystals
6. K. Aizu, Phys. Rev. B 2, 754 (1970)
Possible Species of Ferromagnetic, Ferroelectric, and Ferroelastic Crystals
7. K. Aizu, J. Phys. Soc. Japan 28, 717 (1970)
Considerations of Partially Ferroelastic and Partially Antiferroelastic Crystals and Partially Ferroelectric and Partially Antiferroelectric Crystals
8. K. Aizu, J. Phys. Soc. Japan 31, 802 (1971)
Inferred Temperature-Dependences of Electrical, Mechanical and Optical Properties of Ferroelectric-Ferroelastic $\text{Gd}_2(\text{MoO}_4)_3$
9. K. Aizu, J. Phys. Soc. Japan 31, 1521 (1971)
Inferred Mechanism of the Phase Transformation of a Peculiar Ferroelectric-Ferroelastic Crystal: NaNH_4 Tartrate
10. K. Aizu, J. Phys. Soc. Japan 32, 135 (1972)
Conjectured Mechanism of the Phase Transformation of a Peculiar Ferroelectric-Ferroelastic Crystal: $(\text{NH}_4)_2\text{Cd}_2(\text{SO}_4)_3$
11. K. Aizu, J. Phys. Soc. Japan 32, 1287 (1972)
Electrical, Mechanical and Electromechanical Orders of State Shifts in Nonmagnetic Ferroic Crystals
12. K. Aizu, J. Phys. Soc. Japan 33, 629 (1972)
General Consideration of Ferroelectrics and Ferroelastics such that the Electric Susceptibility or Elastic Compliance is Temperature Independent in the Prototypic Phase

13. K. Aizu, J. Phys. Soc. Japan 33, 1390 (1972)
Presentation and Discussion of Examples of Ferroelectrics and Ferroelastics Having the Index of Faintness Unequal to the Cell Multiplicity
14. K. Aizu, J. Phys. Soc. Japan 35, 180 (1973)
Evaluation of the Faintness Indices for All of the Zero-Wavenumber Vibrational Modes Whose Oversoftening Causes Ferroelectricity or Ferroelasticity
15. K. Aizu, J. Phys. Soc. Japan 36, 937 (1974)
Mechanism of the Sequence of Phase Transitions [Orthorhombic - Monoclinic Nonferroelectric - Monoclinic Ferroelectric] in NH_4HSO_4
16. K. Aizu, J. Phys. Soc. Japan 38, 1592 (1975)
General Considerations of Homophone Sequences of Phase Transitions
17. K. Aizu, J. Phys. Soc. Japan 39, 1422 (1975)
A General and Unified Theory of the Homophone Sequences of Transitions in which the Soft Modes are Doubly Degenerate
18. K. Aizu, A. Kumada, H. Yumoto, and S. Ashida, J. Phys. Soc. Japan 27, 511 (1969)
Simultaneous Ferroelectricity and Ferroelasticity of $\text{Gd}_2(\text{MoO}_4)_3$
19. J. Albers, R. W. Sailer and H. E. Mueser, Phys. Stat. Sol. A 36, 189 (1976)
Dielectric, Elastic, and Piezoelectric Properties of Mg-Cl Boracite
20. K.S. Aleksandrov, I. P. Aleksandrova, L. I. Zherebtsova, A. I. Kruglik, A. I. Krupnyi, S. V. Mel'nikova, V. E. Shneider and L. A. Shuvalov, Bull. Acad. Sci. USSR Phys. Ser. 39, 943 (1975)
Lithium Ammonium Sulfate: the First Pyroelectric Ferroelastic
21. K. S. Aleksandrov, I. P. Aleksandrova, L. I. Zherebtsova, M. P. Zaitseva and A. T. Anistratov, Ferroelectrics 2, 1 (1972)
Investigation of Ferroelectricity in $\text{NaNH}_4\text{SeO}_4 \cdot 2\text{H}_2\text{O}$ and $\text{NaH}_4\text{SO}_4 \cdot 2\text{H}_2\text{O}$
22. K. S. Aleksandrov, A. T. Anistratov, D. X. Blat, L. I. Zherebtsova, V. I. Zinenko, I. M. Iskornev, S. V. Melnikova and I. N. Flerov, Ferroelectrics 12, 191 (1976)
Properties of NH_4HSO_4 and RbHSO_4 Single Crystals near Their Curie Points
23. K. S. Aleksandrov, A. T. Anistratov, A. I. Krupnyi, V. G. Martynov, Yu. A. Popkov, and V. I. Fomin, Sov. Phys. Crystallogr. 21, 296 (1976)
Mandelstam-Brillouin and Ultrasonic Studies of Phase Transitions in the $(\text{NH}_4)_2\text{BeF}_4$ Crystal
24. I. P. Aleksandrova and V. N. Shcherbakov, Sov. Phys. Crystallogr. 14, 608 (1970)
The Nuclear Magnetic Resonance of D^2 in the $(\text{ND}_4)_2\text{BeF}_4$ Crystal

25. I. P. Aleksandrova, V. I. Yuzvak and V. F. Shabanov, J. de Physique 33 Suppl., C2-63 (1972)
Mechanisms of Ferroelectric Phase Transition in Crystals with Reorientating Structural Groups
26. A. T. Anistratov, Rev. Phys. Appl. 7, 77 (1972)
Optical Properties of Ferroelectrics. Digressions from Phenomenological Theory
27. A. T. Anistratov and V. G. Martynov, Sov. Phys. Crystallogr. 15, 256 (1970)
The Ferroelectric Transition in $(\text{NH}_4)_2\text{SO}_4$ the Dielectric, Optical and Electrooptical Properties in the Neighborhood of the Curie Point
28. A. T. Anistratov, V. G. Martynov and S. V. Mel'nikova, Sov. Phys. Solid State 17, 1964 (1976)
Optical Properties of Gadolinium Molybdate near an Improper Ferroelectric Transition
29. A.T. Anistratov and S. V. Mel'nikova, Bull. Acad. Sci. USSR Phys. Ser. 39, 144 (1975)
The Optical and Electrooptical Properties of Crystals Belonging to the $\text{Me}^+\text{NH}_4\text{RO}_4 \cdot n\text{H}_2\text{O}$ Group
30. E. Ascher, J. Phys. Soc. Japan 28 Suppl., 7 (1970)
The Interactions between Magnetization and Polarization: Phenomenological Symmetry Considerations on Boracites
31. E. Ascher, H. Rieder, H. Schmid, and H. Stoessel, J. App. Phys. 37, 1404 (1966)
Some Properties of Ferromagnetoelectric Nickel-Iodine Boracite, $\text{Ni}_3\text{B}_7\text{O}_{13}\text{I}$
32. E. Ascher, H. Schmid and D. Tar, Sol. State Commun. 2, 45 (1964)
Dielectric Properties of Boracites and Evidence for Ferroelectricity
33. J. D. Axe, B. Dorner, and G. Shirane, Phys. Rev. Lett. 26, 519 (1971)
Mechanism of the Ferroelectric Phase Transition in Rare-Earth Molybdates
34. J. R. Barkley, L. H. Brixner, E. M. Hogan and R. K. Waring, Jr., Ferroelectrics 3, 191 (1972)
Control and Application of Domain Wall Motion in Gadolinium Molybdate
35. J. R. Barkley and W. Jeitschko, J. Appl. Phys. 44, 938 (1970)
Antiphase Boundaries and their Interactions with Domain Walls in Ferroelastic-Ferroelectric $\text{Gd}_2(\text{MoO}_4)_3$
36. M. V. Belousov, V. A. Kamyshev and A. A. Shultin, Bull Acad. Sci. USSR Phys. Ser. 39, 744 (1975)
The Vibrational Spectrum and the Nature of the Phase Transition in an Ammonium Sulfate Crystal

37. J. L. Bernstein, Z. Krist. 122, 3 (1965)
The Unit Cell and Space Group of Gadolinium Molybdate and Scandium Tungstate
38. A. S. Bhalla, ?J. Electrochem. Soc. ??? 170 (1970)
Crystallographic Assignment of the Domains in Single Crystals of Gadolinium Molybdate (GMO)
39. R. Blinc, M. Mali, R. Osredkar, A. Prelesnik, J. Seliger and I. Zupancic, Chem. Phys. Lett 14, 49 (1972)
¹⁴N Quadrupole Coupling in Paraelectric (NH₄)₂SO₄
40. R. Blinc, J. Stepisnik, and I. Zupancic, Phys. Rev. 176, 732 (1968)
Nuclear-Magnetic-Resonance Study of the Ferroelectric Transitions in NaH₃(SeO₃)₂ and NaD₃(SeO₃)₂
41. B. G. Bochkov, V. I. Bugakov, N. D. Gavrilova, V. A. Koptsik and V. K. Novik, Sov. Phys. Crystallogr. 17, 1093 (1973)
Dielectric and Thermal Anomalies in Trigonal Boracites
42. B. G. Bochkov, S. M. Bugrov, N. D. Gavrilova, V. A. Koptsik and V. K. Novik, Sov. Phys. Crystallogr. 20, 524 (1976)
The Domain Structure of Trigonal Boracites
43. B. G. Bochkov and S. N. Drozhdin, Sov. Phys. Crystallogr. 19, 811 (1975)
Anomalous Ferroelectric Transition in the Boracite Cr₃B₇O₁₃Cl
44. B. G. Bochkov, N. D. Gavrilova, V. K. Novik and V. A. Koptsik, Sov. Phys. Crystallogr. 20, 404 (1975)
Dielectric Properties of the Boracite Mg₃B₇O₁₃Cl
45. J. Bohm and H. D. Kuersten, Krist. Tech. 6, 213 (1971)
Zuechtung und Morphologie von Einkristallen aus Gadoliniummolybdat, einer ferroelektrischen und ferroelastischen Substanz
46. J. Bohm and H. D. Kuersten, Phys. Stat. Sol. A 19, 179 (1973)
Domaenen II. Art in ferroelektrischem Gadoliniummolybdat
47. H. J. Borchardt, J. Chem. Phys. 38, 1251 (1963)
Rare-Earth Phosphors
48. H. J. Borchardt, U. S. Patent 3,328,311 (1967)
Selected Luminescent Molybdates and Tungstates of Sc, La, Eu, Gd, and Lu
49. H. J. Borchardt, U. S. Patent 3,437,432 (1969)
Single Crystals
50. H. J. Borchardt and P. E. Bierstedt, Appl. Phys. Lett. 8, 50 (1966)
Gd₂(MoO₄)₃: A Ferroelectric Laser Host
51. H. J. Borchardt and P. E. Bierstedt, J. App. Phys. 38, 2057 (1967)
Ferroelectric Rare-Earth Molybdates

52. L. L. Boyer and J. R. Hardy, Sol. State Commun. 11, 555 (1972)
Ferroelectric Domains and the Condensed Soft Mode In Gadolinium Molybdate
53. L. L. Boyer and J. R. Hardy, Phys. Rev. B 8, 2205 (1973)
Lattice Dynamics of a Rigid-Ion Model for Gadolinium Molybdate
54. B. Brezina and M. Glogarova, Phys. Stat. Sol. A 11, K39 (1972)
New Ferroelectric Langbeinite $Tl_2Cd_2(SO_4)_3$
55. L. H. Brixner, Mat. Res. Bull. 7, 879 (1972)
Pi-GMO: Another Modification of $Gd_2(MoO_4)_3$
56. L. H. Brixner, P. E. Bierstedt, A. W. Sleight and M. S. Liciš, Mat. Res. Bull. 6, 545 (1971)
Precision Parameters of Some $Ln_2(MoO_4)_3$ -type Rare Earth Molybdates
57. I. D. Brown, Acta Cryst. 17, 654 (1964)
The Crystal Structure of Lithium Hydrazinium Sulfate
58. G. Burns, Phys. Rev. 123, 64 (1961)
Nuclear Magnetic Resonance in $(NH_4)_2(BeF_4)_x(SO_4)_{1-x}$ and Other Ferroelectric Systems
59. T. I. Chekmasova, I. S. Kabanov and V. I. Yuzvak, Phys. Stat. Sol. A 44, K155 (1977)
The Pressure-Temperature Phase Diagram of $LiNH_4SO_4$
60. K. M. Cheung and F. G. Ullman, Phys. Rev. B 10, 4760 (1974)
Specific Heat of Gadolinium Molybdate at the Ferroelectric Transition
61. S. I. Chizhikov, N. G. Sorokin, B. I. Ostrovskii and V. A. Meleshina, JETP Letters 14, 333 (1971)
Anomalous Absorption of Elastic Waves in Phase Transition in Gadolinium Molybdate
62. S. J. Chung and Th. Hahn, Mat. Res. Bull. 7, 1209 (1972)
Tetrahedral-Framework Structures of NH_4LiBeF_4 and $CsLiBeF_4$
63. L. A. Coldren, R. A. Lemons, A. M. Glass and W. A. Bonner, Appl. Phys. Lett. 30, 506 (1977)
Electronically Variable Delay Using Ferroelastic-Ferroelectrics
64. J. M. Courdille and J. Dumas, Phys. Rev. B 8, 1129 (1973)
Electric Field Effect on the Elastic Constant near the Gadolinium Molybdate Phase Transition
65. J. M. Courdille and J. Dumas, Ferroelectrics 7, 135 (1974)
Electric Field Effect on the c_{11} Elastic Constant near the G. M. O. Phase Transition

66. L. E. Cross, A. Fouskova, and S. E. Cummins, Phys. Rev. Lett. 21, 812 (1968)
Gadolinium Molybdate, a New Type of Ferroelectric Crystal
67. S. E. Cummins, Ferroelectrics 1, 11 (1970)
Electrical, Optical, and Mechanical Behavior of Ferroelectric $\text{Gd}_2(\text{MoO}_4)_3$
68. J. D. Cuthbert and H. E. Petch, Can. J. Phys. 41, 1629 (1963)
Nuclear Magnetic Resonance Study of Ferroelectric Lithium Hydrazinium Sulfate, $\text{Li}(\text{N}_2\text{H}_5)\text{SO}_4$
69. W. A. Dollase, Acta Cryst B25, 2298 (1969)
 NH_4LiSO_4 : A Variant of the General Tridymite Structure
70. J. F. Dorrian, R. E. Newnham, D. K. Smith, and M. I. Kay, Ferroelectrics 3, 17 (1971)
Crystal Structure of $\text{Bi}_4\text{Ti}_3\text{O}_{13}$
71. B. Dorner, J. D. Axe and G. Shirane, Phys. Rev. B 6, 1950 (1972)
Neutron Scattering Study of the Ferroelectric Phase Transformation in $\text{Tb}_2(\text{MoO}_4)_3$
72. E. Dowty and J. R. Clark, Sol. St. Commun. 10, 543 (1972)
Atomic Displacements in Ferroelectric Trigonal and Orthorhombic Boracite Structures
73. L. A. Drobyshchev, Yu. Ya. Tomashpol'skii, A. I. Safonov, G. N. Antonov, S. A. Fedulov, and Yu. N. Venevtsev, Sov. Phys. Cryst. 13, 964 (1969)
Production and X-Ray Study of $\text{Gd}_2(\text{MoO}_4)_3$ Ceramic and Single Crystals
74. S. N. Drozhdin, B. G. Bochkov, N. D. Gavrilova, T. V. Popova, V. A. Koptsik and V. K. Novik, Sov. Phys. Crystallogr. 20, 526 (1975)
Ferroelectric Properties of Cu-Br- and Co-I-Boracites
75. E. F. Dudnik and T. M. Stolpakova, Sov. Phys. Solid State 17, 2228 (1976)
 $\text{NaFe}(\text{MoO}_4)_2$ - A New Ferroelastic
76. V. Dvorak, J. Phys. Soc. Japan 28 Suppl., 252 (1970)
On the Phase Transition in KH_2PO_4 and the Role of the Depolarization Energy in It
77. V. Dvorak, Phys. Stat. Sol. B 45, 147 (1971)
The Origin of the Structural Phase Transition in $\text{Gd}_2(\text{MoO}_4)_3$
78. V. Dvorak, Phys. Stat. Sol. B 46, 763 (1971)
A Thermodynamic Theory of Gadolinium Molybdate
79. V. Dvorak, Czech. J. Phys. B 21, 1250 (1971)
A Thermodynamic Theory of the Cubic-Orthorhombic Phase Transition in Boracites

80. V. Dvorak, Phys. Stat. Sol. B 51, K129 (1972)
Improper Ferroelectric Phase Transition in Rubidium Tri-Hydrogen Selenite
81. V. Dvorak, Phys. Stat. Sol. B 52, 93 (1972)
Structural Phase Transitions in Langbeinites
82. V. Dvorak, J. de Physique 33, C2 (1972)
Boracites - An Example of Improper Ferroelectrics
83. V. Dvorak, Phys. Stat. Sol. B 55, K59 (1973)
On the Dielectric Anomaly in Improper Ferroelectrics
84. V. Dvorak, Ferroelectrics 7, 1 (1974)
Improper Ferroelectrics
85. V. Dvorak, Phys. Stat. Sol. B 66, K87 (1974)
On the Phase Transition in Langbeinites
86. V. Dvorak and Y. Ishibashi, J. Phys. Soc. Japan 41, 548 (1976)
Two-Sublattice Model of Ferroelectric Phase Transitions
87. V. Dvorak, A. P. Levanyuk and D. G. Sannikov, Bull. Acad. Sci. USSR Phys. Ser. 39, 659 (1975)
Discussion of Different Versions of the Description of Phase Transitions in Ammonium Fluorberyllate
88. V. Dvorak and J. Petzelt, Czech. J. Phys. B 21, 1141 (1971)
Symmetry Aspect of the Phase Transition in Boracites
89. V. Dvorak and J. Petzelt, Phys. Lett. 35A, 209 (1971)
Soft Mode Behavior in Improper Ferroelectrics
90. D. J. Epstein, W. V. Herrick and R. F. Turek, Sol. St. Commun. 8, 1491 (1970)
Elastic Constants of Gadolinium Molybdate
91. S. Kh. Esayan, B. D. Laikhtman and V. V. Lemanov, Sov. Phys. JETP 41, 342 (1975)
Elastic and Photoelastic Properties of Gadolinium Molybdate Crystals near a Phase Transition
92. S. Kh. Esayan, Kh. S. Bagdasarov, V. V. Lemanov, T. M. Polkhovskaya and L. A. Shuvalov, Sov. Phys. Solid State 16, 85 (1974)
Scattering of Light by Acoustic Waves in Gadolinium Molybdate Crystals
93. P. Felix, M. Lambert, R. Comes and H. Schmid, Ferroelectrics 7, 131 (1974)
X-Ray Diffuse Scattering Study of Boracites
94. E. Ferroni and P. Orioli, Zeits. Krist. 111, 362 (1959)
Zur Kristallstruktur von $\text{PbCa}_2(\text{CH}_3\text{CH}_2\text{COO})_6$

95. I. N. Flerov, V. I. Zinenko, L. I. Zhrebtsova, I. M. Iskornev and D. Kh. Blat, Bull. Acad. Sci. USSR Phys. Ser. 39, 752 (1975)
Investigation of Phase Transitions in Ammonium Acid Sulfate
96. P. A. Fleury, Sol. St. Commun. 8, 601 (1970)
Anomalous Phonon Behavior near the Phase Transition in Ferroelastic-Ferroelectric $\text{Gd}_2(\text{MoO}_4)_3$
97. R. B. Flippen, J. Appl. Phys. 46, 1068 (1975)
Domain Wall Dynamics in Ferroelectric/Ferroelastic Molybdates
98. R. B. Flippen and C. W. Haas, Sol. St. Commun. 13, 1207 (1973)
Nonplanar Domain Walls in Ferroelastic $\text{Gd}_2(\text{MoO}_4)_3$ and $\text{Pb}_3(\text{PO}_4)_2$
99. J. Fousek and M. Glogarova, Sol. St. Commun. 17, 97 (1975)
Elastooptic Effect and Sources of the Spontaneous Birefringence in $\text{Gd}_2(\text{MoO}_4)_3$
100. J. Fousek and C. Konak, Czech. J. Phys. B 22, 995 (1972)
Electrooptical Properties of Ferroelectric $\text{Gd}_2(\text{MoO}_4)_3$
101. J. Fousek and C. Konak, Phys. Stat. Sol. B 52, K13 (1972)
Induced and Spontaneous Birefringence in Improper Ferroelectric $\text{Gd}_2(\text{MoO}_4)_3$
102. J. Fousek and C. Konak, Ferroelectrics 12, 185 (1976)
Birefringent and Electro-optical Properties of $(\text{NH}_4)_2\text{SO}_4$
103. J. Fousek, F. Smutny, C. Frenzel and E. Hegenbarth, Ferroelectrics 4, 23 (1972)
Ferroelectric Transition in Co-I-Boracite Under Pressure
104. A. Fouskova, J. Phys. Soc. Japan 27, 1699 (1969)
The Specific Heat of $\text{Gd}_2(\text{MoO}_4)_3$
105. A. Fouskova and L. E. Cross, J. Appl. Phys. 44, 2834 (1970)
Dielectric Properties of Bismuth Titanate
106. A. Fouskova and J. Fousek, Phys. Stat. Sol. A 32, 213 (1975)
Continuum Theory of Domain Walls in $\text{Gd}_2(\text{MoO}_4)_3$
107. V. M. Fridkin, K. A. Verkhovskaya and B. G. Bochkov, Phys. Stat. Sol. A 22, 759 (1974)
Optical Absorption Edge in Improper Ferroelectrics in the Phase Transition Region
108. B. N. Ganguly, F. G. Ullman, R. D. Kirby and J. R. Hardy, Phys. Rev. B 12, 3783 (1975)
Effect of Uniaxial Stress on the Unstable $A_1(\text{TO})$ Phonon in Ferroelectric Gadolinium Molybdate

109. B. N. Ganguly, F. G. Ullman, R. D. Kirby and J. R. Hardy, Sol. St. Commun. 17, 533 (1975)
Optic-Mode Coupling in Ferroelectric Gadolinium Molybdate
110. B. N. Ganguly, F. G. Ullman, R. D. Kirby and J. R. Hardy, Phys. Rev. B 13, 1344 (1976)
Raman Spectrum of Gadolinium Molybdate at 80K
111. K. Gesi, Phys. Stat. Sol. A 15, 653 (1973)
"Improper" Ferroelectric Properties of NaNO_2 and $\text{AgNa}(\text{NO}_2)_2$
112. K. Gesi, Phys. Stat. Sol. A 33, 479 (1976)
Dielectric Study on the Phase Transitions in Triammonium Hydrogen Disulfate $(\text{NH}_4)_3\text{H}(\text{SO}_4)_2$
113. K. Gesi, J. Phys. Soc. Japan 40, 483 (1976)
Phenomenological Theory of an Isomorphous Transition in Polar Crystals - Application to the II-III Transition in Ferroelectric $\text{Ca}_2\text{Pb}(\text{C}_2\text{H}_5\text{COO})_6$
114. K. Gesi and K. Ozawa, J. Phys. Soc. Japan 38, 459 (1975)
Effect of Hydrostatic Pressure on the Phase Transitions in Ferroelectric RbHSO_4 and RbDSO_4
115. K. Gesi and K. Ozawa, J. Phys. Soc. Japan 39, 1026 (1975)
Effect of Hydrostatic Pressure on the Phase Transitions in Ferroelectric $\text{Ca}_2\text{Sr}(\text{C}_2\text{H}_5\text{COO})_6$ and $\text{Ca}_2\text{Pb}(\text{C}_2\text{H}_5\text{COO})_6$
116. V. L. Ginzburg, Sov. Phys. Sol. St. 2, 1824 (1960)
Some Remarks on Phase Transitions of the Second Kind and the Microscopic Theory of Ferroelectric Materials
117. V. V. Gladkii, V. K. Magataev and I. S. Zheludev, Ferroelectrics 13, 343 (1976)
Improper Ferroelectric Phase Transition in the Crystal $\text{RbH}_3(\text{SeO}_3)_2$
118. M. Glogarova and J. Fousek, Phys. Stat. Sol. A 15, 579 (1973)
Dielectric, Optical, and Domain Properties of the Improper Ferroelectric $(\text{NH}_4)_2\text{Cd}_2(\text{SO}_4)_3$
119. M. Glogarova, J. Fousek and B. Brezina, J. de Physique, Suppl. 33, C2-75 (1972)
Properties of Ferroelectric $\text{Cd}_2(\text{NH}_4)_2(\text{SO}_4)_3$
120. L. V. Gorbatiy, V. I. Ponomarev and D. M. Kheiker, Sov. Phys. Crystallogr. 21, 165 (1976)
Refinement of the Crystal Structure of Ammonium Trihydroselenite $\text{NH}_4\text{H}_3(\text{SeO}_3)_2$ at -150°C
121. Yu. M. Gufan, Sov. Phys. Sol. St. 13, 175 (1971)
Phase Transitions Characterized by a Multicomponent Order Parameter
122. Yu. M. Gufan and V. P. Sakhnenko, Sov. Phys. Sol. St. 14, 1660 (1973)
Theory of Phase Transitions in Boracites

123. Yu. M. Gufan and V. P. Sakhnenko, Sov. Phys. JETP 36, 1009 (1973)
Features of Phase Transitions Associated with Two- and Three-Component
Order Parameters
124. Yu. M. Gufan and L. A. Shuvalov, Sov. Phys. Solid State 17, 381 (1975)
Group-Theoretical Analysis of the Phase Transition in Ferroelectric
Crystals $\text{RbH}_3(\text{Se})_3$
125. C. Haas, Phys. Rev. 140, A863 (1965)
Phase Transitions in Ferroelectric and Antiferroelectric Crystals
126. Th. Hahn, G. Lohre and C. J. Chung, Naturwissenschaften 56, 459 (1969)
A New Tetrahedral Framework Structure in Sulfates and Fluoberyllates
127. K. Hamano, Jap. J. Appl. Phys. 5, 865 (1966)
Piezoelectric Property of Ferroelectric Dicalcium Strontium Propionate
128. W. C. Hamilton, J. Chem. Phys. 50, 2275 (1969)
Comment on the Order-Disorder Transition in Ferroelectric Ammonium
Sulfate
129. B. O. Hildmann, Th. Hahn, L. E. Cross and R. E. Newnham, Appl. Phys.
Lett. 27, 103 (1975)
Lithium Ammonium Sulfate, A Polar Ferroelastic Which Is Not
Simultaneously Ferroelectric
130. U. T. Hoechli, Phys. Rev. B 6, 1814 (1972)
Elastic Constants and Soft Optical Modes in Gadolinium Molybdate
131. J. Holakovsky, Phys. Stat. Sol. B 56, 615 (1973)
A New Type of the Ferroelectric Phase Transition
132. S. Hoshino, K. Vedam, Y. Okaya and R. Pepinsky, Phys. Rev. 112, 405
(1958)
Dielectric and Thermal Study of $(\text{NH}_4)_2\text{SO}_4$ and $(\text{NH}_4)_2\text{BeF}_4$ Transitions
133. F. L. Howell, R. R. Knipsel, and V. H. Schmidt, Bull. Am. Phys. Soc. 12,
924 (1967)
Deuteron NMR Spectrum and Electrical Conductivity in
 LiND_5SO_4
134. T. Ikeda, K. Fujibayashi, T. Nagai and J. Kobayashi, Phys. Stat. Sol. A
16, 279 (1973)
Elastic Anomaly in $(\text{NH}_4)_2\text{SO}_4$
135. T. Ikeda and G. Yasuda, Jap. J. Appl. Phys. 14, 1287 (1975)
The Phase Transition of Ferroelectric $\text{Tl}_2\text{Cd}_2(\text{SO}_4)_3$
136. V. L. Indenbom, Sov. Phys. Crystallogr. 5, 106 (1960)
Phase Transitions without Change in the Number of Atoms in the Unit Cell
of the Crystal

137. Z. Iqbal and C. W. Christoe, *Ferroelectrics* 12, 177 (1976)
Raman Scattering Study of Phase Transition in Ammonium Sulfate
138. Y. Ishibashi and V. Dvorak, *J. Phys. Soc. Japan* 41, 1650 (1976)
Domain Walls in Improper Ferroelectrics
139. Y. Ishibashi and Y. Takagi, *J. Phys. Soc. Japan* 37, 1349 (1974)
A Simple Model for Phase Transition in $\text{Ca}_2\text{Sr}(\text{C}_2\text{H}_5\text{CO}_2)_6$
140. Y. Ishibashi and Y. Takagi, *Jap. J. Appl. Phys.* 15, 1621 (1976)
Improper Ferroelectric Phase Transitions
141. T. Ito, N. Morimoto and R. Sadanaga, *Acta Cryst.* 4, 310 (1951)
The Crystal Structure of Boracite
142. S. Itoh and T. Nakamura, *Phys. Lett.* 44A, 461 (1973)
Brillouin Scattering Study of $\text{Gd}_2(\text{MoO}_4)_3$ Using a Double Fabry-Perot Interferometer
143. S. Itoh and T. Nakamura, *Sol. St. Commun.* 15, 195 (1974)
Brillouin Linewidth and Anomalous Damping of Acoustic Phonons near the Phase Transition in $\text{Gd}_2(\text{MoO}_4)_3$
144. N. R. Ivanov, I. T. Tukhtasunov and L. A. Shuvalov, *Sov. Phys. Crystallogr.* 15, 647 (1971)
Phase Transformation and Thermo-Optical and Electro-Optical Effect in $\text{RbD}_3(\text{SeO}_3)_2$ Crystals
145. Y. S. Jain and H. D. Bist, *Sol. St. Commun.* 15, 1229 (1974)
Comments on the Paper "The Origin of the Ferroelectric Phase Transition in Ammonium Sulfate"
146. Y. S. Jain, H. D. Bist and G. C. Upreti, *Chem. Phys. Lett.* 22, 572 (1973)
The Ferroelectric Phase Transition in Ammonium Sulfate
147. P. B. Jamison, S. C. Abrahams and J. L. Bernstein, *J. Chem. Phys.* 50, 86 (1969)
Crystal Structure of the Transition-Metal Molybdates and Tungstates. V. Paramagnetic Alpha- $\text{Nd}_2(\text{MoO}_4)_3$
148. V. Janovec, *Czech. J. Phys. B* 22, (1972)
Group Analysis of Domains and Domain Pairs
149. V. Janovec, V. Dvorak and J. Petzelt, *Czech. J. Phys.* B25 (1975)
Symmetry Classification and Properties of Equi-Translational Structural Phase Transitions
150. W. Jeitschko, *Acta Cryst. B* 28, 60 (1972)
A Comprehensive X-ray Study of the Ferroelectric-Ferroelastic and Paraelectric-Paraelastic Phases of $\text{Gd}_2(\text{MoO}_4)_3$

151. F. Jona, J. Phys. Chem. 63, 1750 (1959)
Preparation and Dielectric Properties of Synthetic Boracite-Like Compounds
152. F. Jona and R. Pepinsky, ?Phys. Rev.? ???, 1577 (1953?4)
Dielectric Properties of Some Double Tartrates
153. F. Jona and R. Pepinsky, Phys. Rev. 103, 1126 (1956)
Ferroelectricity in the Langbeinite System
154. K. Kamiyoshi, J. Chem. Phys. 26, 218 (1957)
Effect of Electric Field on the Phase Transition of Ammonium Sulfate
155. E. T. Keve, S. C. Abrahams, and J. L. Bernstein, J. Chem. Phys. 54, 3185 (1971)
Ferroelectric Ferroelastic Paramagnetic Beta-Gd₂(MoO₄)₃ Crystal Structure of the Transition-Metal Molybdates and Tungstates. VI
156. E. T. Keve, S. C. Abrahams, K. Nassau and A. M. Glass, Sol. St. Commun. 8, 1517 (1970)
Ferroelectric Ferroelastic Paramagnetic Terbium Molybdate Beta-Tb₂(MoO₄)₃
157. D. E. Khmel'nitskii, Sov. Phys. JETP 34, 1125 (1972)
Complex Phase Transitions in Crystals
158. D. E. Khmel'nitskii and V. L. Shneerson, Sov. Phys. Solid State 15, 1226 (1973)
Phonon Spectrum and Kinetic Phenomena in Extrinsic Ferroelectrics of the Displacive Type
159. R. R. Knispel and H. E. Petch, Can. J. Phys. 49, 870 (1971)
Proton Rotating Frame Relaxation in Lithium Hydrazinium Sulfate, Li(N₂H₅)SO₄
160. J. Kobayashi and E. Ascher, Phys. Lett. 38A, 47 (1972)
An Explanation of Anomalous Optical Behavior of the Improper Ferroelectric Gd₂(MoO₄)₃
161. J. Kobayashi, Y. Enomoto and Y. Sato, Phys. Stat. Sol. B 50, 335 (1972)
A Phenomenological Theory of Dielectric and Mechanical Properties of Improper Ferroelectric Crystals
162. J. Kobayashi and M. Miyazaki, Phys. Lett. 55A, 193 (1975)
Anomalous Electrooptic Behavior of Ferroelectric Gd₂(MoO₄)₃
163. J. Kobayashi and L. Mizutani, Phys. Stat. Sol. A 2, K89 (1970)
Latent Lattice Strain in the Ferroelectric State of Iron-Iodine Boracite
164. J. Kobayashi, I. Mizutani, H. Hara, N. Yamada, O. Nakada, A. Kumada and H. Schmid, J. Phys. Soc. Japan 28 Suppl., 67 (1970)
Optical Properties of Ferroelectric Boracite

165. J. Kobayashi, I. Mizutani, H. Schmid and H. Schachner, Phys. Rev. B 1 3801 (1970)
X-Ray Study on the Lattice Strains of Ferroelectric Iron Iodine Boracite $\text{Fe}_3\text{B}_7\text{O}_{13}\text{I}$
166. J. Kobayashi, Y. Sato and T. Nakamura, Phys. Stat. Sol. A 14, 259 (1972)
X-Ray Study on Thermal Expansion of Ferroelectric $\text{Gd}_2(\text{MoO}_4)_3$
167. J. Kobayashi, Y. Sato and H. Schmid, Phys. Stat. Sol. A 10, 259 (1972)
X-Ray Study on Phase Transitions of Ferroelectric Iron Iodine Boracite $\text{Fe}_3\text{B}_7\text{O}_{13}\text{I}$ at Low Temperatures
168. J. Kobayashi, H. Schmid and E. Ascher, Phys. Stat. Sol. 26, 277 (1968)
Optical Study on the Ferroelectric Orthorhombic Phase of Fe-I-Boracite
169. S. Kojima, K. Ohi and T. Nakamura, J. Phys. Soc. Japan 41, 162 (1976)
Temperature Dependence of Electrooptic Coefficient and Spontaneous Birefringence of Ferroelectric Gadolinium Molybdate
170. C. Konak and J. Fousek, Ferroelectrics 7, 141 (1974)
Induced Spontaneous Birefringence in Improper Ferroelectric $\text{Cd}_2(\text{NH}_4)_2(\text{SO}_4)_3$
171. C. Konak, J. Fousek and N. R. Ivanov, Ferroelectrics 6, 235 (1974)
Birefringent and Electrooptical Properties of Improper Ferroelectric $\text{Cd}_2(\text{NH}_4)_2(\text{SO}_4)_3$
172. C. Konak and J. Matras, Czech. J. Phys. B 26, 577 (1976)
Birefringent and Electrooptical Properties of $(\text{NH}_4)_2\text{BeF}_4$
173. T. Kondo, Y. Ishibashi and Y. Takagi, J. Phys. Soc. Japan 37, 1708 (1974)
Domain Observation in Ammonium Hydrogen Sulfate Crystals
174. T. Kondo, Y. Ishibashi and Y. Takagi, J. Phys. Soc. Japan 39, 1326 (1975)
The Phase Transition in Ammonium Hydrogen Sulfate
175. A. Kumada, J. Japan Soc. Appl. Phys. 39 Suppl., 258 (1970)
Function and Applications of $\text{Gd}_2(\text{MoO}_4)_3$
176. A. Kumada, Ferroelectrics 3, 115 (1972)
Optical Properties of Gadolinium Molybdate and Their Device Applications
177. A. Kumada, J. Phys. Soc. Japan 35, 941 (1973)
Observation of Double Hysteresis Loops in $\text{Gd}_2(\text{MoO}_4)_3$
178. A. Kumada, Ferroelectrics 7, 145 (1974)
Observation of Double Hysteresis Loops in $\text{Gd}_2(\text{MoO}_4)_3$
179. A. Kumada, H. Yumoto and S. Ashida, J. Phys. Soc. Japan 28 Suppl., 351 (1970)
Ferroelectric-Ferroelastic Crystal: $\text{Gd}_2(\text{MoO}_4)_3$

180. H. D. Kuersten and J. Bohm, Krist. Tech. 7, 957 (1972)
Die Domänenstruktur von Gadoliniummolybdat (GMO)
181. H. D. Kuersten, J. Bohm, C. Scheiding and H. Blumberg, Krist. Tech. 8, 303 (1973)
Zu einigen Eigenschaften des polaren Gadoliniummolybdates (I) Optische Untersuchungen zum Umschaltverhalten
182. J. Kvapil and V. John, Phys. Stat. Sol. 39, K15 (1970)
Structural Study of $Gd_2(MoO_4)_3$ Crystals
183. D. W. Kydon, M. Pintar and H. E. Petch, J. Chem. Phys. 47, 1185 (1967)
Deuteron Relaxation Times in Ferroelectric Ammonium Sulfate
184. L. Landau, Phys. Z. Sowjet. 8, 113 (1935)
Zur Theorie der Anomalien der spezifischen Waerme
English trans. in: "L. D. Landau, Collected Works" D. ter Haar, editor, Pergamon, 1965
On the Theory of Specific Heat Anomalies
185. L. Landau, Phys. Z. Sowjet. 11, 26 (1937)
Zur Theorie der Phasenumwandlungen I
English trans. in: "L. D. Landau, Collected Works" D. ter Haar, editor, Pergamon, 1965
On the Theory of Phase Transitions
186. L. Landau, Phys. Z. Sowjet. 11, 545 (1937)
Zur Theorie der Phasenumwandlungen II %
English trans. in: "L. D. Landau, Collected Works," D. ter Haar, editor, Pergamon, 1965
On the Theory of Phase Transitions
187. J. Le Roy and S. Aleonard, Mat. Res. Bull. 5, 409 (1970)
Orthofluoroberyllates Complexes de Lithium de Formule $MeLiBeF_4$
188. J. Le Roy and S. Aleonard, Acta Cryst. B28, 1383 (1972)
Structure des Orthofluoroberyllates de Lithium $MLiBeF_4$
189. A. P. Levanyuk and D. G. Sannikov, Sov. Phys. JETP 28, 134 (1969)
Anomalies in Dielectric Properties in Phase Transitions
190. A. P. Levanyuk and D. G. Sannikov, Sov. Phys. Solid State 12, 2418 (1971)
Phenomenological Theory of the Ferroelectric Phase Transition in Gadolinium Molybdate
191. A. P. Levanyuk and D. G. Sannikov, Sov. Phys. Usp. 17, 199 (1974)
Improper Ferroelectrics
192. A. P. Levanyuk and D. G. Sannikov, Sov. Phys. Solid State 17, 327 (1975)
Theory of Structural Phase Transitions in Boracites

193. D. J. Lockwood, Sol. St. Commun. 18, 115 (1976)
Observation of Soft Modes in the Raman Spectrum of Ferroelectric $\text{Cr}_3\text{B}_7\text{O}_{13}\text{Cl}$
194. D. J. Lockwood, Ferroelectrics, 13, 353 (1976)
Raman Spectral Study of the Ferroelectric Phase Transition in Boracites
195. Y. Luspín and G. Hauret, Phys. Stat. Sol. B 76, 551 (1976)
Study of the Velocity and Damping of Acoustic Waves Obtained by Brillouin Scattering in the Paraelastic Phase in GfO
196. Y. Luspín and G. Hauret, Ferroelectrics 13, 347 (1976)
Brillouin Scattering Spectra and Phonon-Phonon Interactions in Paraelastic GfO
197. Y. Makita, A. Sawada and Y. Takagi, J. Phys. Soc. Japan 41, 167 (1976)
Twin Plane Motion in $(\text{NH}_4)_2\text{SO}_4$
198. Y. Makita and T. Sekido, J. Phys. Soc. Japan 20, 954 (1965)
Dielectric Properties of A New Ferroelectric, $\text{NaNH}_4\text{SO}_4 \cdot 2\text{H}_2\text{O}$, near Its Curie Temperature
199. Y. Makita and S. Suzuki, J. Phys. Soc. Japan 36, 1215 (1974)
Super-Lattice Structure of $\text{RbH}_3(\text{SeO}_3)_2$ below the Ferroelectric Transition Temperature
200. Y. Makita and Y. Takagi, J. Phys. Soc. Japan 13, 367 (1958)
Ferroelectric and Optical Properties of $\text{Na}(\text{K}-\text{NH}_4)$ -tartrate Mixed Crystals
201. Y. Makita and Y. Yamauchi, J. Phys. Soc. Japan 37, 1470 (1974)
Super-Lattice Structure of Ferroelectric $(\text{NH}_4)_2\text{BeF}_4$ in the Nonferroelectric Phase below 182 K
202. V. G. Martynov, K. S. Aleksandrov, A. T. Anistratov and T. M. Polkhovskaya, Sov. Phys. Crystallogr. 19, 753 (1975)
Photoelasticity of Gadolinium Molybdate
203. B. T. Matthias and J. P. Remeika, Phys. Rev. 103, 262 (1956)
Ferroelectricity in Ammonium Sulfate
204. B. T. Matthias and J. P. Remeika, Phys. Rev. 107, 1727 (1957)
Ferroelectricity of Dicalcium Strontium Propionate
205. K. Megumi, H. Tumoto, S. Ashida, S. Akiyama and Y. Furuhashi, Mat. Res. Bull. 9, 391 (1974)
Phase Equilibrium Diagram for the System Gd_2O_3 - MoO_3
206. V. A. Meleshina, V. L. Indenbom, Kh. S. Bagdasarov and T. M. Polkhovskaya, Sov. Phys. Crystallogr. 18, 764 (1974)
Domain Boundaries, Antiphase Boundaries and Dislocations in Gadolinium Molybdate Single Crystals

207. H. Miki, J. Phys. Soc. Japan 34, 1314 (1973)
X-Ray Diffraction Study of the Upper Phase Transition in $\text{NaH}_3(\text{SeO}_3)_2$
208. R. C. Miller, W. A. Nordland and K. Nassau, Ferroelectrics 2, 97 (1971)
Nonlinear Optical Properties of $\text{Gd}_2(\text{MoO}_4)_3$ and $\text{Tb}_2(\text{MoO}_4)_3$
209. S. R. Miller, R. Blinc, M. Brenman and J. S. Waugh, Phys. Rev. 126, 528 (1962)
Nuclear Spin-Lattice Relaxation in Some Ferroelectric Ammonium Salts
210. T. Mitsui, T. Oka, Y. Shiroishi, M. Takashige, K. Iio and S. Sawada, J. Phys. Soc. Japan 39, 845 (1975)
Ferroelectricity in NH_4LiSO_4
211. T. Miyashita and T. Murakami, J. Phys. Soc. Japan 29, 1092 (1970)
The Coexistence of the Spontaneous Electric Polarization and Magnetization in Ni-I Boracite
212. E. Nakamura and M. Hosoya, J. Phys. Soc. Japan 23, 844 (1967)
Dielectric Critical Slowing-Down in Ferroelectric $\text{Ca}_2\text{Sr}(\text{C}_2\text{H}_5\text{CO}_2)_6$
213. T. Nakamura, T. Kondo and A. Kumada, Phys. Lett. 36A, 141 (1971)
Spontaneous Birefringence and Electrooptic Response in $\text{Gd}_2(\text{MoO}_4)_3$
214. N. Nakamura, H. Suga, H. Chihara and S. Seki, ? Bulletin ? 38, 1779 (1965)
Phase Transitions in Crystalline Divalent Metal Dicalcium Propionates. I. Calorimetric and Dielectric Investigations of Strontium- and Lead Dicalcium Propionates
215. N. Nakanishi, Y. Murakami, M. Tobioki, H. Sugiyama and S. Kachi, J. Phys. Soc. Japan 35, 947 (1973)
Elastic Properties of $(\text{NH}_4)_2\text{SO}_4$ in the Paraelectric Region
216. K. Nassau, P. B. Jamieson and J. W. Shiever, J. Phys. Chem. Solids 30, 1225 (1969)
The Neodymium Molybdate-Tungstate System
217. K. Nassau, H. J. Levinstein and G. M. Loiacono, J. Phys. Chem. Solids 26, 1805 (1965)
A Comprehensive Study of Trivalent Tungstates and Molybdates of the Type $\text{L}_2(\text{MO}_4)_3$
218. K. Nassau and J. W. Shiever, J. Crystal Growth 16, 59 (1972)
Modified Technique for the Growth of Boracite Crystals
219. R. J. Nelmes, Ferroelectrics 4, 133 (1972)
The Structure of Ammonium Hydrogen Sulfate in its Ferroelectric Phase and the Ferroelectric Transition
220. R. J. Nelmes, J. Phys. C: Solid State Phys. 7, 3840 (1974)
Structural Studies of Boracites. A Review of the Properties of Boracites

221. R. J. Nelmes and F. R. Thornley, J. Phys. C: Solid State Phys. 7, 3855 (1974)
Structural Studies of Boracites. The Cubic Phase of Chromium Chlorine Boracite, $\text{Cr}_3\text{B}_7\text{O}_{13}\text{Cl}$
222. R. J. Nelmes and F. R. Thornley, Ferroelectrics, 13, 355 (1976)
Can Optically Uniaxial Ni-I-Boracite Be Structurally Cubic?
223. R. E. Newnham, H. A. McKinstry, C. W. Gregg and W. R. Stitt, Phys. Stat. Sol. 32, K49 (1969)
Lattice Parameters of Ferroelectric Rare Earth Molybdates
224. H. Ohshima and E. Nakamura, J. Phys. Chem. Solids 27, 481 (1966)
Dielectric Properties of Ferroelectric $(\text{NH}_4)_2\text{SO}_4$, $(\text{NH}_4)_2\text{BeF}_4$ and $(\text{NH}_4)_2\text{Cd}_2(\text{SO}_4)_3$ at 10 kc/s and 3.3 kMc/s
225. Y. Okaya, K. Vedam and R. Pepinsky, Acta Cryst. 11, 307 (1958)
Non-Isomorphism of Ferroelectric Phases of Ammonium Sulfate and Ammonium Fluoberyllate
226. D. E. O'Reilly and T. Tsang, J. Chem. Phys. 46, 1291 (1967)
Deuteron Magnetic Resonance and Proton Relaxation Times in Ferroelectric Ammonium Sulfate
227. D. E. O'Reilly and T. Tsang, J. Chem. Phys. 46, 1301 (1967)
First-Order Ferroelectric Transition in $(\text{NH}_4)_2\text{SO}_4$
228. D. E. O'Reilly and T. Tsang, J. Phys. Chem. 50, 2274 (1969)
Order-Disorder Transition in Ferroelectric Ammonium Sulfate
229. T. Osaka, Y. Makita and K. Gesi, J. Phys. Soc. Japan 38, 292 (1975)
Pyroelectricity of Dicalcium Lead Propionates Associated with Its Phase Transitions
230. V. M. Padmanabhan and R. Balasubramanian, Acta Cryst 22, 532 (1967)
A Neutron Diffraction Study of the Crystal Structure of Lithium Hydrazinium Sulfate
231. R. Pepinsky and F. Jona, Phys. Rev. 105, 344 (1957)
New Ferroelectric Crystal Containing No Oxygen
232. R. Pepinsky and K. Vedam, Phys. Rev. 114, 1217 (1959)
 $\text{LiH}_3(\text{SeO}_3)_2$: New Room-Temperature Ferroelectric
233. R. Pepinsky and K. Vedam, Phys. Rev. 117, 1502 (1960)
Ferroelectric Transition in Rubidium Bisulfate
234. R. Pepinsky, K. Vedam, S. Hoshino and Y. Okaya, Phys. Rev. 111, 1508 (1958)
Ammonium Hydrogen Sulfate: A New Ferroelectric with Low Coercive Field

235. R. Pepinsky, K. Vedam, Y. Okaya and S. Hoshino, Phys. Rev. 111, 1467 (1958)
Room-Temperature Ferroelectricity in Lithium Hydrazinium Sulfate, $\text{Li}(\text{N}_2\text{H}_5)\text{SO}_4$
236. J. Petzelt, Sol. St. Commun. 9, 1485 (1971)
New Type of Far-Infrared Soft Mode in Ferroelectric Gadolinium Molybdate
237. J. Petzelt and V. Dvorak, Phys. Stat. Sol. B 46, 413 (1971)
New Type of Ferroelectric Soft Mode in Gadolinium Molybdate
238. J. Petzelt, J. Grigas and I. Mayerova, Ferroelectrics 6, 225 (1974)
Far Infrared Properties of the Pseudoproper Ferroelectric Ammonium Sulfate
239. R. V. Pisarev, V. V. Druzhinin, N. N. Nesterova, S. D. Prochorova and G. T. Andreeva, J. Phys. Soc. Japan 28 Suppl., 71 (1970)
Crystal Field Theory and Optical Absorption of Ferroelectric Boracites
240. I. N. Polandov, V. P. Mylov and B. A. Strukov, Sov. Phys. Solid State 10, 1754 (1969)
The P-T Diagram of the Ferroelectric Crystal NH_4HSO_4
241. C. T. Prewit, Sol. St. Commun. 8, 2037 (1970)
X-Ray Diffraction Study of $\text{Gd}_2(\text{MoO}_4)_3$
242. E. Pytte, Sol. St. Commun. 8, 2101 (1970)
Model for Ferroelectric $\text{Gd}_2(\text{MoO}_4)_3$
243. A. Z. Rabinovich, Sov. Phys. Solid State 11, 159 (1969)
The Barkhausen Effect in Gadolinium Molybdate
244. J. K. M. Rao, Sov. Phys. Crystallogr. 17, 432 (1972)
Room-Temperature Crystal Structure of the Ferroelectric Sodium Trideuteroselenite
245. T. R. Rao, M. L. Bansal, V. C. Sahni and A. P. Roy, Phys. Stat. Sol. B 75, K31 (1976)
Study of the Internal Modes of SO_4^{2-} in LiKSO_4
246. J.-P. Rivera, H. Bill and R. Lacroix, Ferroelectrics 13, 361 (1976)
I. EPR of Mn^{2+} in the Ferroelectric and Paraelectric Phases of Natural (Mg-Cl) Boracite
247. J.-P. Rivera, H. Bill and R. Lacroix, Ferroelectrics 13, 363 (1976)
II. EPR of Mn^{2+} in the Three Ferroelectric Phases of Zn-Cl Boracite, a Model for the Monoclinic Phase with Bigger Cell is Proposed
248. V. N. Sankaranarayanan and R. S. Krishnan, Proc. Indian Acad. Sci. A 76, 267 (1972)
Raman and Infrared Spectra of Ammonium Selenate and Lithium Ammonium Selenate

249. A. Sawada, S. Ohya, Y. Ishibashi and Y. Takagi, J. Phys. Soc. Japan 38, 1408 (1975)
Ferroelectric Phase Transition in $(\text{NH}_4)_2\text{SO}_4\text{-K}_2\text{SO}_4$ Mixed Crystals
250. A. Sawada, Y. Makita and Y. Takagi, J. Phys. Soc. Japan 41, 174 (1976)
The Origin of Mechanical Twins in $(\text{NH}_4)_2\text{SO}_4$
251. A. Sawada and Y. Takagi, J. Phys. Soc. Japan 31, 952 (1971)
Superstructure in the Ferroelectric Phase of Ammonium Rochelle Salt
252. A. Sawada and Y. Takagi, J. Phys. Soc. Japan 33, 1071 (1972)
Mechanism of Ferroelectric Phase Transition in Ammonium Rochelle Salt
253. A. Sawada, Y. Takagi and Y. Ishibashi, J. Phys. Soc. Japan 34, 748 (1973)
The Origin of the Ferroelectric Phase Transition in Ammonium Sulfate
254. E. Sawaguchi and L. E. Cross, Phys. Stat. Sol. B 50, K89 (1972)
Double Hysteresis Loops and First Order Phase Transitions in Ferroelectric Crystals
255. E. Sawaguchi and L. E. Cross, J. Appl. Phys. 44, 2541 (1973)
Spontaneous Polarization of $\text{Gd}_2(\text{MoO}_4)_3$
256. C. Scheiding and G. Schmidt, Phys. Stat. Sol. B 53, K95 (1972)
Piezoelectric d_{36} Coefficient of Gadolinium Molybdate
257. C. Scheiding, G. Schmidt and H. D. Kuersten, Krist. Tech. 8, 311 (1973)
Zu einigen Eigenschaften des polaren Gadoliniummolybdats (II) Morphische piezoelektrische und elastische Koeffizienten
258. E. O. Schlemper and W. C. Hamilton, J. Chem. Phys. 44, 4498 (1966)
Neutron-Diffraction Study of the Structures of Ferroelectric and Paraelectric Ammonium Sulfate
259. H. Schmid, J. Phys. Chem. Solids 26 973 (1965)
Die Synthese von Boraziten mit Hilfe Chemischer Transportreaktionen
260. H. Schmid, Growth of Crystals 7, 25 (1969)
Twinning and Sector Growth in Nickel Boracites Grown by Transport Reactions
261. H. Schmid, Phys. Stat. Sol. 37, 209 (1970)
Trigonal Boracites - A New Type of Ferroelectric and Ferromagnetoelectric that Allows No 180° Electric Polarization Reversal
262. H. Schmid, P. Chan, L. A. Petermann, F. Teufel and M. Maendly, Ferroelectrics 13, 351 (1976)
Spontaneous Polarization, Dielectric Constant, D.C. Resistivity and Specific Heat of Orthorhombic Boracite $\text{Fe}_3\text{B}_7\text{O}_{13}\text{I}$

263. H. Schmid and J. M. Trooster, Sol. St. Commun. 5, 31 (1967)
Mossbauer Effect and Optical Evidence for New Phase Transitions in Fe-Cl-, Fe-Br-, Fe-I-, Co-Cl- and Zn-Cl- Boracite
264. V. H. Schmidt, J. E. Drumheller and F. L. Howell, Phys. Rev. B 4, 4582 (1971)
Dielectric Properties of Lithium Hydrazinium Sulfate
265. C. J. H. Schutte and A. M. Heyns, J. Chem. Phys. 52, 864 (1970)
Low-Temperature Studies. IV. The Phase Transitions of Ammonium Sulfate Ammonium-d₄ Sulfate; the Nature of Hydrogen Bonding and the Reorientation of the NX₄⁺ Ions
266. Yu. V. Shaldin, D. A. Belogurov and T. M. Prokhortseva, Sov. Phys. Solid State 15, 936 (1973)
Anisotropy of the Nonlinear Refractive Index of Single Crystals of Gadolinium and Terbium Molybdate
267. I. W. Shepherd, Sol. St. Commun. 9, 1857 (1971)
Wavenumber Dependent Relaxation of an Optical Phonon in Gadolinium Molybdate
268. I. W. Sheperd and J. R. Barkley, Sol. St. Commun. 10, 123 (1972)
Investigation of Domain Wall Structure in Gd₂(MoO₄)₃ by Raman Scattering
269. T. Shigenari, Y. Takagi and Y. Wakabayashi, Sol. St. Commun. 18, 1271 (1976)
Raman Scattering from Soft Modes in the Ferroelectric Phase of Gd₂(MoO₄)₃
270. Y. Shiozaki, Ferroelectrics 2, 245 (1971)
Satellite X-Ray Scattering and Structural Modulation of Thiourea
271. Y. Shiroishi, N. Nakata and S. Sawada, J. Phys. Soc. Japan 40, 911 (1976)
Ferroelectricity in RbLiSO₄
272. A. M. Shirokov, I. P. Aleksandrova, V. I. Yuzak, A. I. Baranov and V. L. Serebryannikov, Bull. Acad. Sci. USSR Phys. Ser. 39, 947 (1975)
Dielectric and NMR Studies on the High-Pressure Phase Transition in the Ferroelectric NaNH₄SeO₄·2H₂O
273. A. M. Shirokov, V. P. Mylov, A. I. Baranov and T. M. Prokhortseva, Sov. Phys. Solid State 13, 2610 (1972)
Effect of Hydrostatic Pressure on Phase Transition in Gadolinium Molybdate
274. L. A. Shuvalov, N. R. Ivanov, N. V. Gordeeva and L. F. Kirpichnikova, Sov. Phys. Crystallogr. 14, 554 (1970)
New Crystals Belonging to the Family of Alkali Trihydroselenites: the Ferroelectric RbH₃(SeO₃)₂ and the Linear Dielectric NH₄H₃(SeO₃)₂

275. L. A. Shuvalov, N. R. Ivanov, L. F. Kirpichnikova and N. V. Gordeyeva, Phys. Lett. 33A, 490 (1970)
Isotopic Non-Isomorphism of $\text{Rb}(\text{H}_{1-x}\text{D}_x)_3(\text{SeO}_3)_2$ Crystals
276. L. A. Shuvalov, N. R. Ivanov, L. F. Kirpichnikova and N. M. Shchagina, Sov. Phys. Crystallogr. 17, 851 (1973)
Dielectric Properties of Crystals of the System $\text{Na}(\text{D}_x\text{H}_{1-x})_3(\text{SeO}_3)_2$ and Refinement of its xT Phase Diagram
277. A. W. Smith and G. Burns, Phys. Lett. 28A, 501 (1969)
Optical Properties and Switching in $\text{Gd}_3(\text{MoO}_4)_3$
278. F. Smutny, Phys. Stat. Sol. A 9, K109 (1972)
The Specific Heat Anomaly of Ferroelectric Co-I-Boracite, $\text{Co}_3\text{B}_7\text{O}_{13}\text{I}$
279. F. Smutny and J. Albers, Phys. Stat. Sol. B 49, K149 (1972)
Piezoelectric Properties of Co-I Boracite, $\text{Co}_3\text{B}_7\text{O}_{13}\text{I}$
280. F. Smutny and J. Fousek, Phys. Stat. Sol. 40, K13 (1970)
Ferroelectric Transition in Co-I-Boracite
281. F. Smutny, J. Fousek and M. Kotrbova, Czech. J. Phys. B 24, 231 (1974)
Low-Frequency Dielectric Dispersion in $\text{Ni}_3\text{B}_7\text{O}_{13}\text{I}$
282. F. Smutny, J. Fousek and M. Kotrbova, Ferroelectrics 7, 143 (1974)
Dielectric Permittivity Behavior of $\text{Ni}_3\text{B}_7\text{O}_{13}\text{I}$ and $\text{Co}_3\text{B}_7\text{O}_{13}\text{I}$ Single Crystals
283. F. Smutny and C. Konak, Phys. Stat. Sol A 31, 151 (1975)
Dielectric, Optical and Electrooptical Properties of Cobalt-Iodine Boracite ($\text{Co}_3\text{B}_7\text{O}_{13}\text{I}$)
284. G. Soda and T. Chiba, J. Phys. Soc. Japan 26, 723 (1969)
Hydrogen-Bond Network and Ferroelectric Transition in Sodium Trihydrogen Selenite, $\text{NaD}_3(\text{SeO}_3)_2$ by Nuclear Magnetic Resonance Study
285. A. S. Sonin and I. S. Zheludev, Sov. Phys. Crystallogr. 8, 217 (1963)
The Dielectric Properties of Single Crystal Boracite
286. B. A. Strukov, Sov. Phys. Crystallogr. 6, 511 (1962)
The Temperature Dependence of Birefringence in Crystals of Ammonium Sulfate and Ammonium Fluoberyllate
287. B. A. Strukov, N. D. Gavriluk and V. A. Koptsik, Sov. Phys. Crystallogr. 6, 625 (1962)
Some Aspects of the Ferroelectric Phase Transition in $(\text{NH}_4)_2\text{BeF}_4$
288. B. A. Strukov, V. A. Koptsik and V. D. Ligasova, Sov. Phys. Solid State 4, 977 (1962)
Experimental Investigation of the Ferroelectric Properties of Ammonium Bisulfate in the Vicinity of the High Temperature Phase Transition

289. B. A. Strukov, T. L. Skomorokhova, V. A. Koptsik, A. A. Boiko and A. N. Izailenko, Sov. Phys. Crystallogr. 18, 86 (1973)
Thermal Properties of Ammonium Fluoroberyllate over a Wide Temperature Range
290. K. Suzuki, Sol. St. Commun. 11, 937 (1972)
Observation of Diffracted Light from Domain Walls in $Gd_2(MoO_4)_3$
291. Y. Takagi and Y. Makita, J. Phys. Soc. Japan 13, 272 (1958)
Ferroelectricity of $NaNH_4$ -Tartrate
292. Y. Takagi, Y. Wakabayashi and T. Shigenari, J. Phys. Soc. Japan 41, 719 (1976)
Raman Scattering of Longitudinal Modes in $Gd_2(MoO_4)_3$ Crystals
293. M. Takashige, S. Hirotsu and S. Sawada, J. Phys. Soc. Japan 38, 904 (1975)
Optical Rotary Power and $60^\circ C$ Phase Transition of $Ca_2Pb(C_2H_5CO_2)_6$
294. M. Takashige, H. Iwamura, S. Hirotsu and S. Sawada, Ferroelectrics 11, 431 (1976)
Dielectric and Optical Properties of Ferroelectric Dicalcium Lead Propionate
295. A. Tamaki, T. Fujimura and K. Kamiyoshi, J. Chem Phys. 65, 4867 (1976)
Critical Slowing Down of Dielectric Relaxation in Ferroelectric NH_4HSO_4
296. N. G. Theophanous, IEEE J. Quant. Elect. ??, 507 (1976)
A $gd_2(MoO_4)_3$ Longitudinal Electrooptic Modulator at 6328 Å
297. F. R. Thornley and R. J. Nelmes, Ferroelectrics 7, 139 (1974)
The Crystal Structure of Chromium Chlorine Boracite, $Cr_3B_7O_{13}Cl$
298. F. R. Thornley, R. J. Nelmes and N. S. J. Kennedy, Ferroelectrics 13, 357 (1976)
Structural Studies of Cu-Cl-Boracite
299. M. Toda, S. Tosima E. Shima and T. Iwasa, Appl. Phys. Lett. 22, 476 (1973)
Surface Acoustic Wave Velocities on $Gd_2(MoO_4)_3$
300. P. Toledano and J.-C. Toledano, Phys. Rev B 14, 3097 (1976)
Order-Parameter Symmetries for Improper Ferroelectric Nonferroelastic Transitions
301. L. P. Torre, S. C. Abrahams and R. L. Barns, Ferroelectrics 4, 291 (1972)
Ferroelectric and Ferroelastic Properties of Mg-Cl-Boracite
302. B. H. Torrie, C. C. Lin, O. S. Binbrek and A. Anderson, J. Chem. Phys. Solids 33, 697 (1972)
Raman and Infrared Studies of the Ferroelectric Transition in Ammonium Sulfate

303. A. B. Tovbis, T. S. Davydova and V. I. Simonov, Sov. Phys. Crystallogr. 17, 81 (1972)
Crystal Structure of Rubidium Trihydroselenite $\text{RbH}_3(\text{SeO}_3)_2$
304. J. M. Trooster, Phys. Stat. Sol. 32, 179 (1969)
Mossbauer Investigation of Ferroelectric Boracites
305. Y. Uesu, T. Tanaka and J. Kobayashi, Ferroelectrics 7, 246 (1974) X-Ray Dilatometric Study of the Phase Transition of the Improper Ferroelectrics KH_2PO_4 and KD_2PO_4
306. F. G. Ullman, K. M. Cheung, G. A. Rakes and B. N. Ganguly, Ferroelectrics 9, 63 (1975)
Re-examination of the Pyroelectric Current Anomaly in Gadolinium Molybdate
307. F. G. Ullman, B. N. Ganguly and J. R. Hardy, Ferroelectrics 2, 303 (1971)
Pyroelectric Effect in Gadolinium Molybdate (GMO)
308. F. G. Ullman, B. N. Ganguly and J. R. Zeidler, J. Elect. Mat. 1, 425 (1972)
Pyroelectric Detection Properties of Gadolinium Molybdate (GMO)
309. F. G. Ullman, B. J. Holden, B. N. Ganguly and J. R. Hardy, Phys. Rev. B 8, 2991 (1973)
Raman Spectrum of Gadolinium Molybdate Above and Below the Ferroelectric Transition
310. H.-G. Unruh, Sol. St. Commun. 8, 1951 (1970)
The Spontaneous Polarization of $(\text{NH}_4)_2\text{SO}_4$
311. H.-G. Unruh and O. Ayere, Ferroelectrics 12, 181 (1976)
Raman and Dielectric Measurements on Ferrielectric Ammonium Sulfate
312. V. G. Vaks and N. E. Zein, Ferroelectrics 6, 251 (1974)
The Model of Phase Transitions in Sodium Trihydrogen Selenite, $\text{NaH}_3(\text{SeO}_3)_2$
313. J. H. Van den Hende and H. Boutin, Acta Cryst. 17, 660 (1964)
The Crystal Structure of Ferroelectric Lithium Hydrazinium Sulfate
314. V. M. Varikash, S. N. Drozhdin, T. A. Zarembovskaya and V. K. Novik, Sov. Phys. Crystallogr. 20, 267 (1975)
Ferroelectric Properties of Dicalcium Strontium Propionate in the Interval 4.2-300 K
315. K. Vedam, Y. Okaya and R. Pepinshy, Phys. Rev. 119, 1252 (1960)
Crystal Structure of Ferroelectric $\text{LiH}_3(\text{SeO}_3)_2$
316. A. Watton, E. C. Reynhardt and H. E. Petch, J. Chem. Phys. 65, 4370 (1976)
NMR Investigation of Ammonium Ion Motions in Two Ammonium Bisulfates

317. A. Yoshihara, T. Fujimura and K. I. Kamiyoshi, Phys. Stat. Sol. A 34, 369 (1976)
Phase Transition of Ammonium Sulfate
318. V. I. Yuzvak, L. I. Zherebtsova, V. B. Shkuryaeva and I. P. Aleksandrova, Sov. Phys. Crystallogr. 19, 480 (1975)
Dielectric and NMR Investigations of Phase Transition in Lithium Ammonium Sulfate
319. M. P. Zaitseva, A. I. Krupnyi, Yu. I. Kokorin and V. S. Krasikov, Bull. Acad. Sci. USSR Phys. Ser. 39, 954 (1975)
Elastic and Electromechanical Parameters of Sodium Ammonium Selenate Dihydrate near the Ferroelectric Transition
320. J. R. Zeidler and F. G. Ullman, Phys. Rev. B 8, 3371 (1973)
Temperature and Polarization Dependence of the Optical Absorption Edge of Gadolinium Molybdate

DISTRIBUTION LIST

1. Texas Instruments
13500 N. Central Expressway
Dallas, Texas 75222
2. Honeywell, Inc.
Corporate Research Center
Hopkins, Minnesota 55343
3. Barnes Engineering
30 Commerce Road
Stamford, Conn. 06902
ATTN: R. Astheimer
4. R.C.A.
Government and Commercial
Systems
1901 N. Moore Street
Arlington, VA 22209
ATTN: D. Reid
5. Westinghouse Corporation
Defense and Space Center
P.O. Box 1521
Baltimore, MD 21203
6. ITT
Electron Tube Division
3700 E. Pontiac Street
Fort Wayne, Indiana 46803
ATTN: E. Eberhart
7. General Electric Company
777 Fourteenth Street, N.W.
Washington, D.C. 20005
ATTN: D. Hunter
8. Hughes Aircraft Company
Industrial Products Division
2020 Oceanside Blvd.
Oceanside, CA 92054
ATTN: J. Koda
9. Inrad Corporation
406 Paulding Drive
Northvale, New Jersey 07647
ATTN: Dr. W. Ruderman
10. Teltron Inc.
Baltic Mews Industrial Park
2 Riga Lane
P.O. Box 416
Douglassville, PA 19518
ATTN: A. Mengel
11. Systems Research Laboratories
Inc.
2800 Indian Ripple Road
Dayton, Ohio 45440
ATTN: R. Holmes
12. Lockheed Missles & Space Inc.
1111 Lockheed Way
Sunnyvale, CA 94088
13. U.S. Naval Weapons Center
China Lake, CA
ATTN: W. Woodworth
14. Prof. Frank G. Ullman
Dept. of Electrical Engineering
University of Nebraska
Lincoln, Nebraska 68588
15. Prof. Paul M. Raccah
Univ. of Illinois at
Chicago Circle
P.O. Box 4348
Chicago, Illinois 60680